ARCTIC SEA ICE AND LARGE-SCALE ATMOSPHERIC TELECONNECTIONS ASSOCIATED WITH GREENLAND BLOCKING

by

Christopher S. Hinojosa, B.A.

A thesis submitted to the Graduate Council of
Texas State University in partial fulfillment
of the requirements for the degree of
Master of Science
with a Major in Geography
August 2020

Committee Members:

Yanan Li, Chair

Thomas Ballinger

Nathan Currit

FAIR USE AND AUTHOR'S PERMISSION STATEMENT

Fair Use

Duplication Permission

DEDICATION

This work is dedicated to my parents, Elvira Hinojosa-Almaguer and Vicente Almaguer, for their endless patience, support, and love.

ACKNOWLEDGEMENTS

A special thank you to my thesis committee members for helping to make this document possible and guiding me through the long and sinuous road of academia. Your wisdom, time, and efforts are much appreciated. To the family, friends, peers, and professors who have provided encouragement and support, I am very grateful to all of you.

TABLE OF CONTENTS

Page

ACKNOWLEDGEMENTS v

LIST OF TABLES ix

LIST OF FIGURES x

LIST OF ABREVIATIONS xvi

ABSTRACT xviii

CHAPTER

1. INTRODUCTION 1

2. LITERATURE REVIEW 6

2.1 SEA ICE 6
2.2 GREENLAND BLOCKING 8
2.3 TELECONNECTIONS 11
2.4 INCREASED EXTREME WEATHER IN MIDLATITUDES 15
2.5 GAPS AND LIMITATIONS 16

3. RESEARCH OBJECTIVES 20

4. DATA AND METHODS 21

4.1. DATA 21
4.1.1. SEA ICE 21
4.1.2. GREENLAND BLOCKING INDEX 22
4.1.3. WEB-BASED REANALYSIS INTERCOMPARISON TOOL 22
4.2. METHODS 23
4.2.1. PART 1: MULTIDECADAL CORRELATION ANALYSIS 23
4.2.2. PART 2: MONTHLY COMPOSITE ANALYSIS 26
4.3. CONCEPTUAL FRAMEWORK 27

5. RESULTS PART 1: MULTIDECADAL CORRELATION ANALYSIS 29

5.1 VARIABLE ASSESSMENTS 29
5.2 REGIONAL ASSESSMENTS OF ATLANTIC AND PACIFIC 38
5.2.1 SIE VERSUS GBI 38
5.2.2 SIA VERSUS GBI 47

6. RESULTS PART 2: MONTHLY COMPOSITE ANALYSIS 89

6.1 INITIAL PROCESSING 89
6.2 BAFFIN BAY 91
6.2.1 MAXIMUM SIE VERSUS MINIMUM GBI 91
6.2.1.1 CONTEMPORARY ANALYSIS 91
6.2.1.2 LEAD-1 ANALYSIS 97
6.2.1.3 LEAD-2 ANALYSIS 102
6.2.2 MINIMUM SIE VS. MAXIMUM GBI 108
6.2.2.1 CONTEMPORARY ANALYSIS 108
6.2.2.2 LEAD-1 ANALYSIS 113
6.2.2.3 LEAD-2 ANALYSIS 118
6.3 BEAUFORT SEA 124
6.3.1 MAXIMUM SIE VS. MINIMUM GBI 124
6.3.1.1 CONTEMPORARY ANALYSIS 124
6.3.1.2 LEAD-1 ANALYSIS 127
6.3.1.3 LEAD-2 ANALYSIS 131
6.3.2 MINIMUM SIE VS. MAXIMUM GBI 134
6.3.2.1 CONTEMPORARY ANALYSIS 134
6.3.2.2 LEAD-1 ANALYSIS 137
6.3.2.3 LEAD-2 ANALYSIS 141

7. DISCUSSION AND CONCLUSIONS 234

7.1 DISCUSSION PART 1: MULTIDECADAL CORRELATION ANALYSIS 234
7.2 DISCUSSION PART 2: MONTHLY COMPOSTIE ANALYSIS 241
7.2.1 BAFFIN BAY ANALYSIS 241
7.2.1.1 MAXIMUM SIE VERSUS MINIMUM GBI COMPOSITES 241
7.2.1.2 MINIMUM SIE VERSUS MAXIMUM GBI COMPOSITES 244
7.2.2 BEAUFORT SEA ANALYSIS 247
7.2.2.1 MAXIMUM SIE VERSUS MINIMUM GBI COMPOSITES 247

7.2.2.2 MINIMUM SIE VERSUS MAXIMUM GBI COMPOSITES 248
7.3. CONCLUSIONS 250

APPENDIX SECTION 255

LITERATURE CITED 266

LIST OF TABLES

Table **Page**

1. Decadal averages and differences for SIE for the Atlantic sector 58

2. Decadal averages and differences for SIE for the Pacific sector 58

3. Decadal averages and differences for SIA for the Atlantic sector 59

4. Decadal averages and differences for SIA for the Pacific sector 59

5. Decadal averages and differences for GBI 60

6. The top 10 values for maximum SIE and minimum GBI for Baffin Bay in January, March, October, and December 146

7. The top 10 values for minimum SIE and maximum GBI for Baffin Bay in January, March, October, and December 171

8. The top 10 values for maximum SIE and minimum GBI for the Beaufort Sea in May, June, and August 196

9. The top 10 values for minimum SIE and maximum GBI for the Beaufort Sea in May, June, and August 215

LIST OF FIGURES

Figure **Page**

1. Map of the Arctic region 5

2. The Greenland Blocking Index (GBI) domain is shown by the solid black line, with the latitude for the Arctic Circle given for reference 19

3. Conceptual model for Arctic-North American mid-latitude teleconnection with the GBI pattern 28

4. Raw GBI time series plots are shown for months comprising a) winter (DJF), b) spring (MAM), c) summer (JJA), and d) autumn (SON) 60

5. Detrended GBI time series plots are shown for months comprising a) winter (DJF), b) spring (MAM), c) summer (JJA), and d) autumn (SON) 61

6. Raw SIE time series plots are shown for the Atlantic sector for a) winter (DJF), b) spring (MAM), c) summer (JJA), and d) autumn (SON) 61

7. Detrended SIE time series plots are shown for the Atlantic sector for a) winter (DJF), b) spring (MAM), c) summer (JJA), and d) autumn (SON) 62

8. Raw SIE time series plots are shown for the Pacific sector for a) winter (DJF), b) spring (MAM), c) summer (JJA), and d) autumn (SON) 63

9. Detrended SIE time series plots are shown for the Pacific sector for a) winter (DJF), b) spring (MAM), c) summer (JJA), and d) autumn (SON) 64

10. Raw SIA time series plots are shown for the Atlantic sector for a) winter (DJF), b) spring (MAM), c) summer (JJA), and d) autumn (SON) 65

11. Detrended SIA time series plots are shown for the Atlantic sector for a) winter (DJF), b) spring (MAM), c) summer (JJA), and d) autumn (SON) 66

12. Raw SIA time series plots are shown for the Pacific sector for a) winter (DJF), b) spring (MAM), c) summer (JJA), and d) autumn (SON) 67

13. Detrended SIA time series plots are shown for the Pacific sector for a) winter (DJF), b) spring (MAM), c) summer (JJA), and d) autumn (SON) 68

14. Correlation results for SIE against GBI at 3 month lag (a-n) 69

15. Correlation results for SIE against GBI at 2 month lag (a-n) 70

16. Correlation results for SIE against GBI at 1 month lag (a-n) 71

17. Correlation results for contemporary SIE against GBI (a-n) 72

18. Heatmap showing contemporary monthly correlation coefficients for raw SIE versus GBI 73

19. Heatmap showing contemporary monthly correlation coefficients for detrended SIE versus GBI 73

20. Correlation results for SIE against GBI at 1 month lead (a-n) 74

21. Heatmap showing all correlation coefficients for SIE versus GBI at lead-1 for raw values 75

22. Heatmap showing all correlation coefficients for SIE versus GBI at lead-1 for detrended values 75

23. Correlation results for SIE against GBI at 2 month lead (a-n) 76

24. Heatmap showing all correlation coefficients for SIE versus GBI at lead-2 for raw values 77

25. Heatmap showing all correlation coefficients for SIE versus GBI at lead-2 for detrended values 77

26. Correlation results for SIE against GBI at 3 month lead (a-n) 78

27. Correlation results for SIA against GBI at 3 month lag (a-n) 79

28. Correlation results for SIA against GBI at 2 month lag (a-n) 80

29. Correlation results for SIA against GBI at 1 month lag (a-n) 81

30. Correlation results for contemporary SIA against GBI (a-n).....82

31. Heatmap showing contemporary monthly correlation coefficients for raw SIA versus GBI.....83

32. Heatmap showing contemporary monthly correlation coefficients for detrended SIA versus GBI 83

33. Correlation results for SIA against GBI at 1 month lead (a-n).....84

34. Heatmap showing all correlation coefficients for SIA versus GBI at lead-1 for raw values 85

35. Heatmap showing all correlation coefficients for SIA versus GBI at lead-1 for detrended values.....85

36. Correlation results for SIA against GBI at 2 month lead (a-n).....86

37. Heatmap showing all correlation coefficients for SIA versus GBI at lead-2 for raw values 87

38. Heatmap showing all correlation coefficients for SIA versus GBI at lead-2 for detrended values.....87

39. Correlation results for SIA against GBI at 3 month lead (a-n).....88

40. Baffin Bay contemporary January composites for maximum SIE and minimum GBI.....147

41. Baffin Bay contemporary March composites for maximum SIE and minimum GBI.....149

42. Baffin Bay contemporary October composites for maximum SIE and minimum GBI.....151

43. Baffin Bay contemporary December composites for maximum SIE and minimum GBI.....153

44. Baffin Bay lead-1 February composites for maximum SIE and minimum GBI 155

45. Baffin Bay lead-1 April composites for maximum SIE and minimum GBI 157

46. Baffin Bay lead-1 November composites for maximum SIE and minimum GBI.....159

47. Baffin Bay lead-1 January composites for maximum SIE and minimum GBI 161

48. Baffin Bay lead-2 March composites for maximum SIE and minimum GBI 163

49. Baffin Bay lead-2 May composites for maximum SIE and minimum GBI 165

50. Baffin Bay lead-2 December composites for maximum SIE and minimum GBI 167

51. Baffin Bay lead-2 February composites for maximum SIE and minimum GBI 169

52. Baffin Bay contemporary January composites for minimum SIE and maximum GBI.....172

53. Baffin Bay contemporary March composites for minimum SIE and maximum GBI.....174

54. Baffin Bay contemporary October composites for minimum SIE and maximum GBI.....176

55. Baffin Bay contemporary December composites for minimum SIE and maximum GBI.....178

56. Baffin Bay lead-1 February composites for minimum SIE and maximum GBI 180

57. Baffin Bay lead-1 April composites for minimum SIE and maximum GBI 182

58. Baffin Bay lead-1 November composites for minimum SIE and maximum GBI.....184

59. Baffin Bay lead-1 January composites for minimum SIE and maximum GBI 186

60. Baffin Bay lead-2 March composites for minimum SIE and maximum GBI 188

61. Baffin Bay lead-2 May composites for minimum SIE and maximum GBI 190

62. Baffin Bay lead-2 December composites for minimum SIE and maximum GBI 192

63. Baffin Bay lead-2 February composites for minimum SIE and maximum GBI 194

64. Beaufort Sea contemporary May composites for maximum SIE and minimum GBI.....197

65. Beaufort Sea contemporary June composites for maximum SIE and minimum GBI.....199

66. Beaufort Sea contemporary August composites for maximum SIE and minimum GBI.....201

67. Beaufort Sea lead-1 June composites for maximum SIE and minimum GBI 203

68. Beaufort Sea lead-1 July composites for maximum SIE and minimum GBI.....205

69. Beaufort Sea lead-1 September composites for maximum SIE and minimum GBI.....207

70. Beaufort Sea lead-2 July composites for maximum SIE and minimum GBI.....209

71. Beaufort Sea lead-2 August composites for maximum SIE and minimum GBI 211

72. Beaufort Sea lead-2 October composites for maximum SIE and minimum GBI.....213

73. Beaufort Sea contemporary May composites for minimum SIE and maximum GBI.....216

74. Beaufort Sea contemporary June composites for minimum SIE and maximum GBI.....218

75. Beaufort Sea contemporary August composites for minimum SIE and maximum GBI.....220

76. Beaufort Sea lead-1 June composites for minimum SIE and maximum GBI 222

77. Beaufort Sea lead-1 July composites for minimum SIE and maximum GBI.....224

78. Beaufort Sea lead-1 September composites for minimum SIE and maximum GBI.....226

79. Beaufort Sea lead-2 July composites for minimum SIE and maximum GBI 228

80. Beaufort Sea lead-2 August composites for minimum SIE and maximum GBI 230

81. Beaufort Sea lead-2 October composites for minimum SIE and maximum GBI.....232

LIST OF ABBREVIATIONS

Abbreviation	Description
AA	Arctic Amplification
AO	Arctic Oscillation
CAA	Canadian Archipelago
ESRL	Earth System Research Laboratory
GB	Greenland Block(ing)
GBI	Greenland Blocking Index
GHG	Greenhouse Gas(es)
GrIS	Greenland Ice Sheet
GPH	Geopotential height
GPH500	500 mb geopotential height
IPCC	Intergovernmental Panel on Climate Change
LH	Latent Heat
mb	Millibar
MSLP	Mean Sea Level Pressure
NA	North America(n)
NAM	Northern Annular Mode
NAO	North Atlantic Oscillation
NCAR	National Center for Atmospheric Research

NCEI	National Center for Environmental Information
NCEP	National Center for Environmental Prediction
NH	Northern Hemisphere
NOAA	National Oceanic and Atmospheric Administration
NSIDC	National Snow and Ice Data Center
PW	Precipitable water
SAT	Surface Air Temperature(s)
SH	Sensible Heat
SLR	Sea Level Rise
SIA	Sea Ice Area
SIC	Sea Ice Concentration
SIE	Sea Ice Extent
SSV	Statistically Significant Value(s)
SST	Sea Surface Temperature(s)
T2m	Two-meter air temperature
US	United States
WRIT	Web-based Reanalysis Intercomparison Tool

ABSTRACT

Sea ice is a critical component of the cryosphere (regions of the Earth where water exists as ice) as it helps to maintain Earth's heat and energy balance, in part, through reflecting incoming shortwave radiation during summer back into space. Due to global warming, Arctic (≥60°N) temperatures are increasing at twice the rate of the rest of the world, a phenomenon known as Arctic Amplification (AA), and because of this, both the Arctic sea ice and atmosphere have experienced greater variability and extreme conditions. Sea ice extent (SIE) and area (SIA) have steadily diminished since the 1970s, but more persistent and accelerated rates of sea ice loss have been observed since the mid-1990s. The loss of sea ice has affected the Arctic climate, but also has implications for regions of the Northern Hemisphere (NH), including the mid-latitudes (30°–60°N). Atmospheric circulation changes have been observed and associated with the loss of sea ice. These changes have been linked with increased extreme weather such as cold air outbreaks over regions of North America (NA), and more frequent blocking episodes over Greenland and the North Atlantic Ocean.

The goal of this research was to assess the potential for Arctic sea ice influence on mid-latitude weather extremes via Greenland blocking. This study is comprised of two parts: the first tested monthly associations between regional Arctic SIE and SIA, and the Greenland blocking time series (as represented by the Greenland Blocking Index; GBI); and the second examined GBI linkages with anomalous weather patterns across NA in those years with extreme sea ice and GBI conditions. Statistical associations from part

one were further analyzed in part two through composites of synoptic atmospheric circulation variables (i.e. geopotential height, surface air pressure and temperature, and precipitable water) to draw physical associations to the co-variability of sea ice, blocking patterns, and southward climate conditions over NA.

It was found that two Arctic marginal seas, Baffin Bay and the Beaufort Sea, produced the greatest and second greatest number of months with statistically significant associations, respectively. The composite analyses for minimum sea ice and maximum GBI for both Baffin Bay and the Beaufort Sea produced greater instances of anomalously negative values for geopotential height, and surface air pressure and temperature in the mid-latitude region, while precipitable water shows a more mixed response; and greater instances of anomalously positive values for regions of the Arctic for all variables. This study concluded that there are not only statistical links between changing sea ice patterns over certain Arctic marginal seas with increased Greenland blocking episodes, but also that those years of sea ice and blocking extremes can affect mid-latitude weather variables in some months of the year.

1. INTRODUCTION

The effects of global warming are widespread and have implications for how the climate forecasting community creates weather and climate models tuned for future predictions and change. The quality and quantity of data used for analysis are especially important as well as the interpretation of a global warming signal versus natural atmospheric noise. Although global warming is affecting every region of the globe, warmer surface air temperature (SAT) trends and moisture incursion into the Arctic can initiate longer melt periods and a later freeze-up of sea ice, disrupting seasonal trends. The years 2018–2019 and 2015–2016 (October–September) had the first and second warmest annual SAT on record on land, respectively, at +1.9°C (relative to 1981-2010 climatology) since observations began in 1900, and all years between 2014–2019 exceeded previous records (Overland et al., 2019).

The Arctic (≥60°N, **Figure 1**) is one of a few regions on Earth with year-round sea ice. Due to its location, the Arctic receives more of the sun's weaker, oblique rays throughout the year relative to the low (0°–30°N) and mid-latitudes (30°–60°N), and because of this decreased intensity of insolation, some areas see consistently low temperatures, and persistent snow and ice throughout the year. The cold Arctic region, in tandem with the tropical belt around Earth's equatorial region, creates a temperature gradient, and the cold northern air and warm southerly air are transferred equatorward and poleward, respectively, through low-pressure systems to maintain climatological heat and

energy balance across the planet.

Global warming has caused Arctic temperatures to increase at twice the rate of the rest of the world, a phenomenon called Arctic Amplification (AA). Higher Arctic SAT brought on by AA have weakened the regulatory temperature gradient and created a wavier jet stream, which is associated with slower moving winds and therefore weather systems in the Northern Hemisphere (NH) (Dethloff et al. 2019). Additionally, Francis and Vavrus (2012) noted that weakened zonal winds and increased wave amplitudes contribute to slower moving upper-level Rossby waves and therefore longer persistence in weather systems. Although the scientific debate over the long-term effects of AA on remote weather and climate patterns is ongoing, both in situ and remotely sensed data are collected at daily intervals to aid in analysis of the highly sensitive Arctic region (Barnes and Screen 2015).

Anthropogenic pollution, including the release of greenhouse gases (GHG) such as carbon dioxide (CO_2) and methane (CH_4), has led to the increased retention of longwave radiation within the Earth's atmosphere. This trapped radiation heats the atmosphere causing various effects on weather processes including higher tropospheric air temperatures, which have the potential to disrupt stratospheric conditions (IPCC 2014). This overall warming effect has led to a substantial reduction of perennial snow, and sea and land ice in the Arctic, Antarctic, and high-altitude regions (e.g. Stroeve and Notz 2018; Box et al. 2019). Without the highly reflective (high albedo) snow- and ice-covered surfaces, less insolation is reflected away from Earth back into space. An initial warming of the Arctic can melt snow and ice, exposing darker land and ocean surfaces, which absorb more insolation, which then leads to a further amplification of warming and

melting through a positive feedback (Serreze and Barry 2011).

The AA phenomenon had been first recognized during the 20th century as a possibility, but improvements in models and analysis techniques allowed for the determination of a clear signal during the 1990s (around the same time accelerated rates of sea ice loss were observed) as the effects of highly concentrated GHG emerged from natural climate variability. The AA signal has persisted and intensified from the 1990s through present (Screen et al. 2014). Without sea ice, the relatively warm ocean water is exposed to the cold Arctic atmosphere, allowing for heat transfer from the surface into the atmosphere. These exchanges are most pronounced in autumn and winter months when the Arctic atmosphere is coldest and the oceans are relatively warmer; however, summer conditions may act to precondition the Arctic environment. During summer, low sea ice conditions allow excessive heat exchange from the ocean to the atmosphere, which can delay sea ice freeze onset in the autumn season that follows (Serreze and Barry 2011). Ice formation occurs when the excess heat is transferred from the ocean surface to the atmosphere and latent heat (LH) is released, which allows ocean surface temperatures to drop to the freezing point. This two-way interaction between sea ice and the atmosphere is crucial for understanding potential climatological disruptions.

Ongoing alterations to the Arctic region will likely produce other climatological changes that may ripple through the larger Earth system. For this reason, it is essential that potential linkages are monitored to detect the possibility of an association with the changing Arctic system, such as the atmospheric response to changing sea ice regimes, which may provide insights into additional local and remote effects. Therefore, exploring the causes and effects of meteorological and climatological phenomena in the changing

Earth system can help society better plan for a world with increased atmospheric extremes, while advancing atmospheric scientists' ability to understand and predict complex cryosphere-atmosphere linkages and processes in the climate system. Those who might be interested in this research include an array of scientists and stakeholders concerned with the broad effects of regional Arctic change.

Figure 1. Map of the Arctic region. The 14 marginal seas used in analyses of this study are labeled (excluding Pacific Ocean and Atlantic Ocean) and shown by the boundaries delineated by black lines.

2. LITERATURE REVIEW

2.1 SEA ICE

Paleo-reconstructions provide evidence that current sea ice extent conditions in the Arctic are at their lowest in the last 1400 years (Walsh et al. 2019). As a result of AA, the composition of the Arctic region has changed dramatically over the last few decades with consistent decreases in multi-year ice (ice that survives the summer melt season), receding sea ice extent (SIE), and diminished sea ice area (SIA) (Kwok and Rothrock 2009). Ice thickness has decreased by more than 50% from the 1958–1976 period to the 2003–2008 period, and older thicker ice has decreased from 45% in 1985 to 21% in 2017. Observations of SIE have shown decreases in all months of all regions of the Arctic, with the September (end of summer and climatological minimum) monthly average trend for the entire Arctic at -12.9 ± 2.2% per decade relative to the 1981–2010 average (Overland et al. 2019). In 1985, the oldest ice (>4 years) made up about 16% of the ice pack, while the March (end of winter and climatological maximum) ice pack of 2018 was comprised of only about 0.9% of old ice; the extent of the oldest ice has declined from 2.54 M km^2 to 0.13 M km^2 between 1985 and 2018, a 95% reduction. Much of the sea ice that remains at the end of the winter season is first-year ice. Approximately 77% of the March 2018 ice pack was composed of first-year ice. This ice is thinner, more mobile, weaker, and more easily melted and broken apart relative to sea ice cover in the 1970s and 1980s (Overland et al. 2018).

Several passive microwave satellite-based sensors have observed Arctic sea ice

coverage and have allowed for the generation of consistent SIE and SIA records, such as those available from the National Snow and Ice Data Center (NSIDC), which provides data for 14 marginal seas, including: Central Arctic, Greenland Sea, Baffin Bay, Hudson Bay, Beaufort Sea, Chukchi Sea, East Siberian Sea, Laptev Sea, Kara Sea, Barents Sea, Sea of Okhotsk, Bering Sea, Canadian Archipelago, and Gulf of St. Lawrence (**Figure 1**; boundaries are adapted from Meier et al. 2007).

Passive microwave radiation penetrates through clouds, rain, and dust, and can be captured during the day and night. These types of sensors have the advantage of being optimized to distinguish sea ice from liquid water. Active microwave sensors are also used to detect sea ice; however, the reflected energy varies according to the physical properties of the sea ice (such as thickness, salinity, and grain size), making these radar images difficult to interpret.

Satellite imagery has revealed striking examples of global warming's effect on the Arctic. Recent unprecedented loss (i.e. since 2007) of both perennial and seasonal sea ice locally affects the heat, energy, and moisture budget of the Arctic climate (Serreze and Barry 2011), but also that of the larger NH. In 2012, the month of September experienced a 50% reduction in sea ice extent (about 3.41 M km^2) compared to the 1979–2000 mean extent (Budikova et al. 2017). While each marginal sea has shown losses in SIE and SIA, some have experienced more than others. For instance, the Beaufort Sea, Chukchi Sea, and East Siberian Sea regions have seen the steepest sea ice declines during summer months (Onarheim et al. 2018).

In addition to Arctic sea ice change, the Greenland Ice Sheet (GrIS) has also experienced significant ice loss from warming air temperatures with implications for

regional oceanographic patterns, ecology, human settlements, as well as large-scale weather and climate (Richter-Menge, et al. 2019). The GrIS (including its peripheral glaciers) lost an estimated $2.9 \pm 0.5 \times 10^3$ Gt of mass between 1991 and 2011, which is approximately equivalent to 8 mm of global mean sea level rise (SLR), and this trend is expected to continue (van den Broeke et al. 2017). Although melt of the GrIS can occur through various pathways, atmospheric high pressure blocking patterns have been shown to amplify melt events (Hanna et al. 2014; Hanna et al. 2018a; Tedesco and Fettweis 2020).

2.2 GREENLAND BLOCKING

In meteorology, "block" is a large, quasi-stationary mid-to-high latitude anticyclone that persists for a few days (e.g. Hann et al. 2018a). Blocks indicate higher geopotential heights (GPH), which promote anti-cyclonic ridging of the upper atmosphere, and tend to be collocated with subsidence and clear skies atop the core region of high pressure (McLeod et al. 2018). Greenland blocks (GB) refer to a domain-average of the large-scale atmospheric pressure at 500 mb (~5500 meters above sea level) over the Greenland region at 60–80° N, 20–80° W, and are measured by the Greenland Blocking Index (GBI) (**Figure 2**). Daily observations of the GBI region have been collected since 1948, and extended reanalysis based on reconstructed boundary conditions has allowed for the creation of an extended time series back to 1851, which have both shown an increase in variability and extremes of the GBI; most notably, sustained positive periods have been shown for 1870–1900 and from 1990 to present, and a cluster of extremely high GBI episodes since 2000 (Brönnimann et al. 2011; Hanna et al. 2013; Hanna et al. 2014; Hanna et al. 2018b).

The winds around a Greenland block (GB), winds tend to be anticyclonic, which can advect warm, moist air from the southeast out of the North Atlantic and cold, dry air from the northwest out of the Arctic toward Greenland depending on the spatial configuration and center of the block (e.g. Ballinger et al. 2018a). It has been found that with persistent and frequent Arctic blocking patterns, there is more frequent advection of warm and moist air masses from the middle and low latitudes into higher latitude regions, including over Greenland, which induce GrIS melt and affect the surface energy balance (e.g. Herman et al. 2020; Mattingly et al. 2020). Blocks can also cause southward (more meridional) deviation and slowing of the prevailing westerly winds of the polar jet stream, while also advecting warm, moist air masses from the subpolar North Atlantic that can increase air and surface temperatures and melt sea and land ice. GBI variability has been associated with an increase in mid-tropospheric circulation anomalies that bring warmer temperatures to the GrIS region; warmer temperatures expand the air mass situated above Greenland, thereby increasing geopotential height, which could then influence larger circulation patterns including the configuration of the North Atlantic polar jet stream (Hanna et al., 2018b). In addition, blocking patterns can warm the upper-ocean mixed layer and increase SST, which act to delay sea ice freeze onset during late autumn, a critical time for decreasing air and ocean surface temperatures concurrent with seasonal ice coverage formation and advance (Ballinger et al 2018b).

A study by Hanna et al. (2016) produced a long term GBI time series from 1851 to 2015 revealing increased variability in modern GBI values compared to historical trends, which has persisted through present. This increase in GBI variability is most apparent in summer and winter months, with mixed signals inconsistent with time in

autumn and spring seasons. The study plotted seasonal GBI trends showing several periods of variability, including a decreasing trend around 1910–1920, an increase around 1930–1940, another decrease around 1980–1990, and an increasing trend since the early 1990s. More specifically, monthly analysis showed the month of December had its lowest and highest ten GBI values since 2001, while June had four of its ten highest GBI values since 2007 and the second highest on record in 2012.

Additionally, regional sea ice loss has been shown to influence the movement (or lack of movement) of Greenland blocks, which can then affect upstream (westward), downstream (eastward), and southward surface and atmospheric conditions depending on the season in which the blocking takes place. Chen and Luo (2017) noted that westward moving GB tends to affect upstream conditions, bringing strong cold anomalies over NA, specifically the eastern US; and stationary GB produces strong cold anomalies over northern Europe and eastern Asia, but weak cold anomalies over NA. Overland and Wang (2019) examined late winter Greenland blocking episodes as they relate to NA climate and noted that the atmospheric response varies by month, which in turn affects the polar jet stream differently through either tropospheric or stratospheric pathways. November through December were found to have a regional tropospheric pathway for Arctic-mid-latitude weather associations due to delayed sea ice freeze up, and January through March were found to have a more hemispheric pathway affecting the polar vortex movement in the stratosphere (delayed into late winter). AA is strongest over the Arctic Ocean in the autumn and winter, especially if more darker ocean surface was exposed during the summer season, warming the ocean and increasing the likelihood of anomalous heat fluxes as temperatures begin to cool during autumn; and spring and

summer show weaker AA shifting over land areas and the GrIS (Hanna et al. 2017;Cohen et al. 2020).

2.3 TELECONNECTIONS

Several studies have associated pan-Arctic sea ice loss to Greenland climate and overlying atmospheric circulation (e.g. blocking), and these works suggest forcing by local and remote factors (Serreze and Barry 2011; Vihma 2014; Walsh 2014; Liu et al. 2016; Jensen et al. 2016; McLeod and Mote 2016). In recent years, December GBI values showed an increase in variability, and in turn was found to be related to an increase in variability of both the North Atlantic Oscillation (NAO) and Arctic Oscillation (AO) for the same month (Hanna et al. 2015; Overland and Wang 2015). Both the NAO and AO describe a change in the latitudinal pressure gradient and subsequent changes in atmospheric circulation (Meleshko et al. 2018). These two oscillation patterns can potentially affect sea ice variability and the GBI as they influence SST and SAT in the GrIS region. Such surface and atmospheric temperature changes may be more prominent during the end of summer and early autumn when open water conditions (with little to no sea ice) and accumulated solar heat are at their maximum, but this also depends on other atmospheric factors including the vertical temperature gradient, columnar water content, and cloud cover. These local-scale physical feedbacks brought on by larger-scale atmospheric circulation patterns can influence the interactions between GB and surface air temperatures, which then alter wind-driven sea ice movement, surface heat fluxes, and oceanic heat transport (Wu and Wang 2020).

Depending on the time of year and strength and positioning of a blocking pattern, earlier than usual ice melt can occur on the GrIS and the surrounding bodies of water,

which causes warming of the air and ocean through turbulent heat transfer. The ensuing melt can also be a function of an ice-albedo feedback maximized under clear, sunny skies during the melt season. In the case of the latter process in late spring and summer, heat from the sun directly strikes the darker open ocean at the ice edge, within low ice pack concentration areas and in leads (narrow, linear fissures) and polynyas (local, quasi-periodic fractures in sea ice). That downward solar radiation then heats the upper ocean and SAT, melting more ice. Some work has suggested that early melt season blocking can precondition the seasonal ice pack for anomalous melt out, initiating an early onset to the warm season ice-albedo feedback (Ballinger et al. 2018b).

The effect of sea ice loss on atmospheric temperature and pressure varies spatiotemporally and by ice thickness within the Arctic basin. Depending on season and location, both sensible heat (SH) and LH fluxes can be more or less turbulent, inducing heat transfer between surface and atmosphere; but SH and LH fluxes are limited where thicker sea ice creates a buffer between the sea and overlying air. Polynyas can increase SH and LH fluxes by inducing strong temperature gradients between warm ocean surfaces and cold air above, creating an unstable boundary layer (Taylor et al. 2018). Screen (2017) examined the effect of sea ice loss on area-mean heat flux for the Arctic region and found that atmospheric forcing results in various responses to near surface air temperature, precipitation, 500 mb GPH, and 700 mb zonal winds. The study noted that for southern Arctic marginal seas such as the Sea of Okhotsk, Bering Sea, and Labrador Sea, there is an in-phase response between sea ice loss and atmospheric forcing with no lag or lead. Higher latitude seas such as the East Siberian Sea, Laptev Sea, Beaufort Sea, and Chukchi Sea regions showed the greatest forcing emerges following summer sea ice

loss (ice loss leads autumn and winter forcing). Additionally, in the Barents Sea, Kara Sea, Canadian Archipelago, Baffin Bay, and Hudson Bay regions, autumn and winter sea ice loss forces greater variability of the atmosphere in the summer (summer atmospheric response lags autumn and winter ice loss). The atmospheric forcing includes higher SAT and precipitation local to areas of sea ice loss, and lower SAT (over most land areas) and mixed precipitation over various mid- to low latitude regions (though there are some much smaller warming signals noted for these regions as well). The study also mentioned mid-tropospheric (500 mb) geopotential height and zonal wind responses and noted greater instances of lower geopotential heights mostly over mid-latitudes (with very few higher geopotential heights in these regions) and generally weaker winds following sea ice loss.

Atmospheric responses to sea ice changes vary in magnitude as well with only some regions, such as the Barents and Kara Seas, influencing atmospheric dynamics like the NAO phase and its larger-scale atmospheric circulation counterpart the Northern Annular Mode (NAM; also known as the AO) (Screen 2017). Arctic sea ice variability can affect NAO and AO phases as well, thereby altering high and low pressure systems, which can potentially increase GB by contributing to planetary wave formation and propagation. Chen and Luo (2017) found that sea ice loss in the Baffin region (including Davis Strait and Labrador Sea) was linked to increases in the duration of the GB pattern, which helped sustain a slow-moving, wavy jet stream that supported extreme cold weather in NA.

In addition to the large scale hemispheric patterns, several studies have looked at the effects of prolonged physical alteration of ice cover in the Arctic region, which has

been observed to disrupt energy exchanges within the Arctic atmosphere and ocean, at varying spatial and temporal scales (Serreze and Berry 2011). Changes in seasonal SIE and SIA have the potential to produce long-term, interannual impacts within and beyond the Arctic climate system. Several studies have included the use of lead and lag analyses to better assess the effect of persistence that could be indicative of a teleconnection between sea ice variables and other physical and atmospheric phenomena. Blanchard-Wrigglesworth et al. (2011) used monthly SIE and SIA observational records, as well as one advanced climate model, to run lagged correlations to assess mechanisms for persistence against the more comprehensive sea ice model output. They found that after plotting their results, both observational and model correlation values started off at a peak (with zero lag), then dropped within a few months only to rise again, then fell again to near-zero after about 15 months. This reemergence of memory within the Arctic system has been observed by others as well (Alexander et al. 1999; Francis et al. 2009) indicating a potential for lasting effects after particularly anomalously low SIE and SIA values. Francis et al. (2009) examined SIE and other atmospheric observations and found that varying ice conditions during the Arctic summer are associated with large-scale atmospheric features including a warmer, less stable lower troposphere, increased cloud cover, and a weakened polar jet stream due to the slackening of the poleward thickness gradient. Petty et al. (2018) used lead correlation analysis and a simplified linear regression model to ascertain September SIE predictability from previous monthly sea ice conditions (i.e. melt onset and sea ice concentration (SIC) values derived from passive microwave observations) and found that SIC data produced the highest predictability skill for detrended SIE, with the most robust correlations belonging to the previous June–

August period. Walsh et al. (2019) used lagged correlation analysis for SIE and a sea ice severity index to determine if ice conditions across subregions of the Arctic could portend Pan-Arctic ice extent or summer ice conditions for the Beaufort Sea region. They found correlation values decreased as the lag increased, though it varied by marginal sea, with several regions reaching near-zero correlation by 3–4 months including the Beaufort, Chukchi, and East Siberian seas. In addition, this study concluded that the removal of trend within the sea ice data resulted in little predictive skill beyond lags of one to two months due to the relatively simple statistical method used.

2.4 INCREASED EXTREME WEATHER IN MIDLATITUDES

Costly and devastating extreme weather patterns across the United States (US) have increased in frequency, magnitude, and duration (IPCC 2014; Overland et al. 2018). These anomalous events seem to coincide with Arctic changes and have incited debate over which weather extremes might be the result of a forced teleconnection (a pattern of atmospheric variability that persists over large distances) and which are related to natural, chaotic climate dynamics (Barnes and Screen, 2015). Attributing an Arctic influence on mid-latitude weather requires separating the Arctic warming signal from internal climate variability through the analysis of high and mid-latitude atmospheric circulation patterns and often involves complex climate modeling exercises with different surface boundary conditions (Budikova et al. 2017). Additionally, Cohen et al. (2020) noted that decadal global SST variability can also lead to uncertainty in distinguishing the influence of AA on the mid-latitudes. The complexity of mid-latitude weather depends on the background state of the global climate system, which makes it difficult to link AA and mid-latitude weather through episodic events like heavy snow fall and cold air outbreaks.

Extreme weather across the North American (NA) continent may be related to changes in the Northwest Atlantic Arctic (i.e. Greenland region), and yet linkage studies between Arctic change, GBI variability, and anomalous weather phenomena in NA are sparse. A study by Cohen et al. (2018) analyzed 12 cities across the US and found that high geopotential height anomalies across the Arctic were more effective than stratospheric warming at producing extreme winter weather for the northeastern and mid-west portions of the country. Overland and Wang (2019) found that warmer Arctic temperatures and loss of sea ice are related to a repositioning of the center of the polar vortex from the larger Arctic region to the Greenland region. This atmospheric shift creates a trough/ridge/trough pattern from eastern Siberia eastward toward Greenland, which extends into both the troposphere and stratosphere, bringing warm temperatures and drought conditions to the west coast of the US and cold temperatures and sometimes precipitation to the eastern and central US by advecting cold Arctic air into NA.

Although the IPCC Report (2014) suggests increased instances of anomalous weather are likely due to global warming for the NH mid-latitude regions, it will be helpful to identify the drivers and impacts of the changes. The changing Northwest Atlantic atmospheric circulation may potentially affect storm tracks and extreme weather prediction for heavily populated areas such as NA and Europe. Through examining the rapid changes in the Arctic, researchers can better describe and constrain the physical processes of global forecast models used to predict extreme weather outbreaks and implement climate mitigation technologies against natural disasters.

2.5 GAPS AND LIMITATIONS

Arctic-mid-latitude teleconnections have been studied at length (Cohen et al.

2014; Francis et al. 2017; Cohen et al. 2020), but there is limited research on the Greenland Block as a pathway by which changing Arctic sea ice regimes could affect extreme weather in NA (Chen and Luo 2017). This research intended to fill the gap by identifying those Arctic marginal seas which produce the greatest monthly correlations of sea ice and GBI values, and from those marginal seas and months, then identifying the effects of years with extreme sea ice and GBI values to determine the atmospheric response over NA through four weather variables.

Several aspects pose limitations to the scope of this study such as data availability, the simplistic statistical and compositing methods, and the inability to rule out larger climate fluctuations as the primary drivers of teleconnections. The biggest limitation for the data used within this study is the lack of more extensive observational records and the lack of models, which can better assess complex surface-atmosphere interactions. A spatially and temporally consistent passive microwave satellite record of sea ice coverage began only in late 1978, but digitization of additional observational data, including ship reports have aided in the production of longer-term records (e.g. Walsh et al. 2017). More long-term and high-resolution satellite-derived product of sea ice would help study Arctic long-term climates, nevertheless, the data currently available are still sufficient for synoptic-scale decadal analysis (Walsh et al. 2017).

Another hurdle for researchers is the inherent dynamic nature of the climate system. Natural fluctuations of weather phenomena are inevitable and are difficult to rule out on when assessing the possible influence of oceanic and atmospheric teleconnection patterns on areas within the Arctic as well as linking high and mid-latitude environments. Several studies have pointed to various pathways by which Arctic change can disrupt

mid-latitude weather; these paths include: a reduced meridional temperature gradient, wavier jet streams, a weakened stratospheric vortex, and slower moving planetary waves (Barnes and Screen, 2015).

Even the best climate predictions possess uncertainty and need to be constantly updated with observations to reflect the real world. This thesis evaluates linkages between observational data streams but does not use climate model experiments to disentangle underlying complex surface-atmosphere processes behind these associations. Studying Arctic climate is important to understand how quickly this regulatory, sensitive region is changing, which may give hints to other urgent Earth system changes such as when and where tipping points might occur based on analysis of extreme events.

Various physical changes such as increased air temperatures, thawing permafrost, an increased hydrologic cycle (including humidity, precipitation, rainfall, and river discharge), increased biomass, wildfires, and changes in snow cover (amount, duration) have all been noted as contributors to a rapidly changing Arctic system. Tracking these and other Arctic change indicators underscores why continuous observation of the Arctic region and its interactions with lower latitudes is necessary in order to confidently establish internal drivers and potential teleconnection patterns (Box et al. 2019).

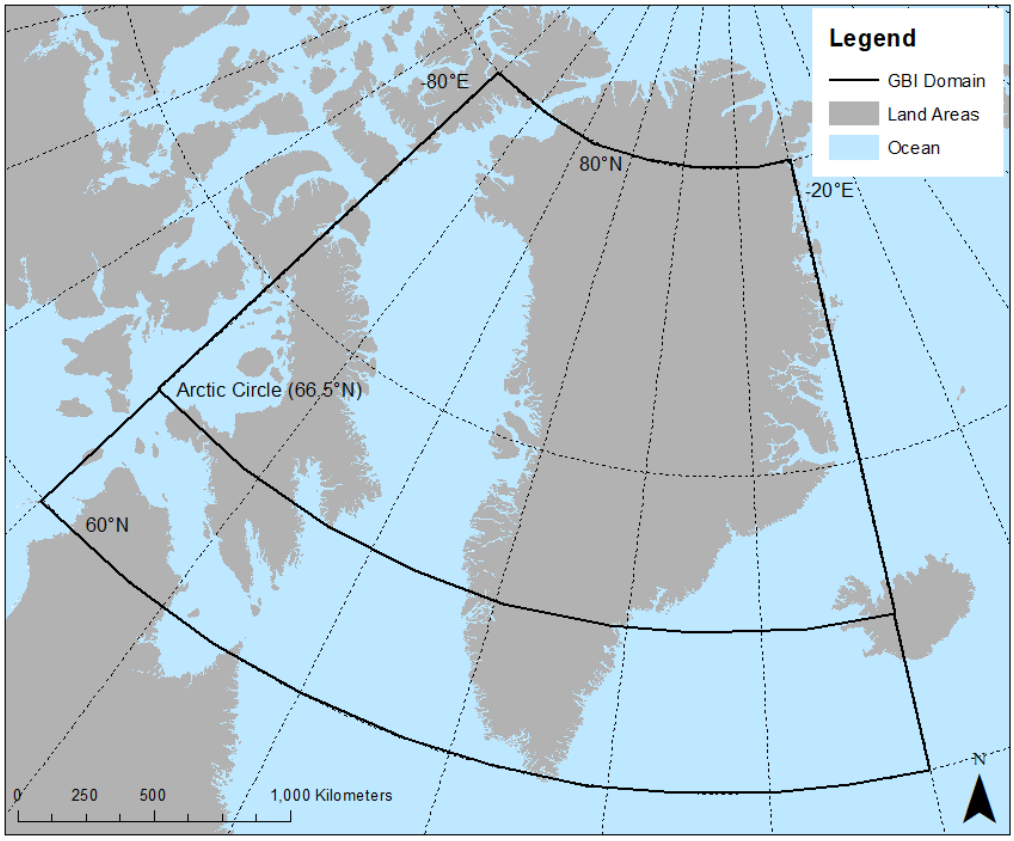

Figure 2. The Greenland Blocking Index (GBI) domain is shown by the solid black line, with the latitude for the Arctic Circle given for reference.

3. RESEARCH OBJECTIVES

Using a statistical framework, the goals of this thesis research are:

1) to assess the strength of multidecadal (n=40 years, 1979–2018) relationships between regional Arctic sea ice variability and GB at monthly and seasonal time scales, and

2) to evaluate GB teleconnections with weather patterns across NA, focusing on periods of strong associations between marginal sea ice conditions and the GBI.

The first objective is addressed through a correlative approach that examined time series associations for monthly sea ice metrics (e.g. SIE and SIA) for each of the 14 Arctic marginal seas (**Figure 1**) and their relationships with monthly and seasonal GBI values. The second objective is carried out primarily by applying a composite approach to assess NA weather and climate conditions linked with years of anomalously high and low sea ice conditions and GBI values.

4. DATA AND METHODS

4.1. DATA

4.1.1. SEA ICE

Arctic sea ice data were collected from the National Snow and Ice Data Center (NSIDC) for each of the fourteen marginal seas (ftp://sidads.colorado.edu/DATASETS /NOAA/G02135/seaice_analysis/). SIE and SIA data are derived from passive microwave sensors aboard satellites from the Defense Meteorological Satellite Program (DMSP); sensors include the Scanning Multichannel Microwave Radiometer (SMMR), the Special Sensor Microwave/Imager (SSM/I), and the Special Sensor Microwave Imager/Sounder (SSMIS). For SIE, each satellite data cell is calculated to be ice-covered or ice-free based on a 15% sea ice concentration (SIC) threshold, meaning that if the data cell has ≥15% SIC, the cell is considered ice-covered, otherwise it is ice-free. The same 15% threshold is used for SIA, except that the area of each grid cell ≥15% threshold is multiplied by the percent ice coverage of that cell and summed for all similar grid cells to report how much of the Arctic is ice covered, accounting for any holes in the ice. Temporal coverage for sea ice began October 26, 1978 and covers 30.98–90°N and the spatial resolution of a grid cell in this domain is 25 km x 25 km. Alternating daily imagery from October 1978 through August 1987, then continuous daily imagery beginning August 1987, is averaged to create a monthly temporal resolution (Fetterer et al. 2017). **Figure 1** shows the 14 marginal seas that comprise the

whole of the Arctic and reflects the regional sea ice data aggregations from NSIDC and Meier et al (2007). Temporal resolution of interest for SIE and SIA is January 1979 to December 2018 (n=40); however, some monthly data (December 1987–January 1988) is missing due to lack of satellite coverage (total number of months=588, though this may vary by correlation test because of months without ice values).

4.1.2. GREENLAND BLOCKING INDEX

Greenland Blocking Index (GBI) data were collected from the National Oceanic and Atmospheric Administration's Earth System Research Laboratory (NOAA ESRL; http://www.esrl.noaa.gov/psd/data/timeseries/daily/GBI/). GBI is the mean 500 mb geopotential height (GPH in meters above sea level) for the 60–80°N, 20–80°W region. Daily data are available for 1948 to present, though the temporal coverage of interest for this study is from January 1979 to December 2018 at the monthly scale, therefore, daily values are aggregated to the monthly scale for all months of the year. The climatology, or climate normal period, used for standardization when necessary is 1981–2010, which is consistent with the modern record that is commonly used by the National Centers for Environmental Information (NCEI).

4.1.3. WEB-BASED REANALYSIS INTERCOMPARISON TOOL

Several European Center for Medium Range Forecast (ECMWF) ERA5 (Copernicus Climate Change Service (C3S), 2017; Hersbach et al. 2020) climate variables were examined and visualized using the Web-based Reanalysis Intercomparison Tool (WRIT) from NOAA ESRL PSD, which can be found at: https://www.esrl.noaa.gov /psd/data/writ/. These variables include: 500 mb geopotential height (GPH), mean sea-

level pressure (MSLP), surface air temperature (two-meter air temperature; T2m), and precipitation data (precipitable water; PW) for NA. ERA5 reanalysis was used for its fine spatial resolution, and has performed well in capturing the climate of the Arctic (including Greenland) and North America (e.g. Tarek et al. 2019; Wang et al. 2019; Delhasse et al. 2020). The reanalysis incorporates data from various sources such as ships, rawinsonde, satellites, and buoys to compile a comprehensive, global 0.25° x 0.25° grid of atmospheric phenomena for retrospective weather and climate analysis. Temporal resolution includes monthly and seasonal means extending from January 1979 to December 2018 following the sea ice period of analysis.

4.2. METHODS

4.2.1. PART 1: MULTIDECADAL CORRELATION ANALYSIS

Descriptive statistics, including long-term (1981–2010) means and standard deviations, were used to explore the time series of SIE, SIA, and GBI. An initial assessment of each dataset's distribution was conducted using a Shapiro-Wilk test for monthly SIE and SIA of the 14 marginal Arctic seas as well as monthly GBI values to determine the best statistical approach for further analysis.

Natural trends in a time series may be present for variables used in analysis, which may affect correlation statistics. Therefore, to avoid this, detrending needs to be done to remove the trend throughout the time series before correlations are run. Trend analysis was conducted on the raw datasets using linear and polynomial fits to assess changes in the monthly-averaged data series with time, allowing for the assessment of the best-fit trend line, which was then used to determine the slope-intercept equation for the detrending process. The optimal fit, as determined by the explained variance (r^2) and root

mean squared error (RMSE), was used to evaluate the robustness of the regression models. The r^2 value is the total percent of variation in a dependent variable explained by one (or more) independent variable(s). The RMSE value indicates the proximity of data points with respect to a regression line, where larger deviations result in greater error values and vice versa. An approach similar to that of Walsh et al. (2019) was followed to test linear, and 3rd and 4th degree polynomial fits of the monthly sea ice. After running the three line-fits, monthly r^2 and RMSE values were averaged across all marginal seas, then averaged values were averaged across the entire year to give a final value for each metric and to determine the best line-fit for detrending. No higher order polynomial fit was tested, in part, to avoid over-fitting the data.

The aforementioned missing data from the sea ice satellite record (months of December 1987–January 1988 for all regions of both SIE and SIA, and August 1987 for Central Arctic SIA) were filled using the initial 4th degree polynomial function equation, to get the best estimated value for the month in question. Some marginal seas, such as St. Lawrence, have very little to no ice during certain months of the year, therefore, those months with zero values for SIE and SIA were left at zero and not correlated against GBI, resulting in omitted or "no data" labels in certain figures provided in the next section. After filling in data, a second 4th degree polynomial fit was used to detrend the entire data series. An example of the 4th degree polynomial fit equation used to detrend the data is as follows: Baffin SIE January $=51660838-25296.53*\text{Year}+1198.71*(\text{Year}-1998.77)^2 + 71.34*(\text{Year}-1998.77)^3-3.19*(\text{Year}-1998.77)^4$. Each of the years in the time series (1979–2018) were plugged iteratively into the monthly equation and solved. The solution was then subtracted from initial monthly values to provide a new time series that represents

40 years of detrended (DT) sea ice data.

After detrending was conducted, correlation tests could be run for both raw and DT datasets to obtain correlation coefficients. Based on previous assessments of the sea ice and GBI data, the bivariate, non-parametric Kendall's tau (τ) test was selected for these analyses. Both SIE and SIA were correlated against GBI values and tested for significance (i.e. two-tailed t-test) in time varying scenarios (contemporary, lags, and leads). For contemporary correlations, n=40 and the significance threshold is 0.223 (using n-2) for Kendall's Tau coefficient. An n-2 degrees of freedom adjustment was chosen to produce a more stringent threshold for the correlation analyses.

Seven iterations of correlations were run for each month, marginal sea, sea ice metric (SIA and SIE) and raw and DT combination including 1, 2, and 3 month lag, contemporary, and 1, 2, and 3 month lead correlations, holding GBI constant. Lag and lead analysis required the offsetting of months and years for sea ice for the appropriate correlation to be run. For example, when conducting the lag correlations, the first year of GBI data and the last year of sea ice data were removed to stay within the bounds of the study period; the GBI dataset consisted of monthly values for 1980 to 2018 while the sea ice datasets included 1979 to 2017. Expanding on this example, January GBI 1980 was compared to the preceding 3 months of sea ice for lag 1, 2, and 3 correlation analysis (October, November, December of 1979, respectively) and the following 3 months of sea ice for lead 1, 2, and 3 (February, March, and April of 1980, respectively) to examine the potential for persistent influence of Arctic sea ice with the GB pattern.

Using a synoptic approach to study the Pan-Arctic region can reveal broad changes; however, to simplify classification, the regions were partitioned into two

sectors. Similar to Park and Lee (2015), the marginal seas were grouped into an Atlantic and a Pacific sector in this study, each containing seven marginal seas. The Atlantic sector consists of Baffin Bay, Barents Sea, Canadian Archipelago, Greenland Sea, Hudson Bay, Kara Sea, and Gulf of St. Lawrence, while the Pacific sector consists of the Beaufort Sea, Bering Sea, Chukchi Sea, Central Arctic Ocean, East Siberian Sea, Laptev Sea, and Sea of Okhotsk.

4.2.2. PART 2: MONTHLY COMPOSITE ANALYSIS

Significant monthly sea ice and GBI analyses from Part 1 were focused upon in Part 2 to assess the potential for Arctic-mid-latitude teleconnections via GB anomalies. Each of the correlation tests highlighted those months that produced statistically significant raw and detrended data, then from those results lists of the top 10 years of maximum (minimum) sea ice and minimum (maximum) GBI from January 1979 to December 2018 were used to determine years of overlap for each month. Those years of overlap were then used to create composites of ERA5 NA atmospheric variables using the WRIT visualization tool. The variables of interest include 500 mb geopotential height (500GPH), mean sea-level pressure (MSLP), 2m air temperature (hereafter T2m), and precipitable water (PW), and they allow us to observe the state of the NA atmosphere for potential spatial teleconnection patterns through time during extreme sea ice and GBI years. Additionally, monthly data allow for the assessment of lead-lag intraseasonal relationships.

For the composite maps, a cylindrical equidistant Robinson map projection was used as this option provided the best visibility of high and mid-latitude areas relative to other options available with the WRIT and the continent appear relatively correct in size

and location (Ipbuker 2004). The map area constraints were formatted to include 20°N as the lowest latitude and 85°N as the highest latitude, and 160°E as the westernmost longitude and 40°E as the easternmost longitude. These latitude and longitude constraints were chosen to best show the NA continent as well as Greenland.

4.3. CONCEPTUAL FRAMEWORK

Relating surface environmental conditions to atmospheric patterns and vice versa is the basis of synoptic climatology (e.g. Yarnal et al. 2001; Sheridan and Lee 2012). Synoptic climatological approaches attempt to explain local or regional weather by atmospheric states and variability. Synoptic climatologists use an empirical and deductive approach to attempt to model complex climatic systems; this strategy relies on statistics to assess the linkage between atmospheric circulation (i.e. Greenland blocking) and the surface environment (**Figure 3**). Four factors that contribute to this assessment include: a classification of the atmosphere, a linkage of large-scale atmosphere to small-scale environment, the study of the effects of climate variability on the surface environment, and a focus on the region as the spatial entity of concern (Yarnal et al. 2001). Statistical methods employed here include correlative and composite approaches inspired by the synoptic climatology framework.

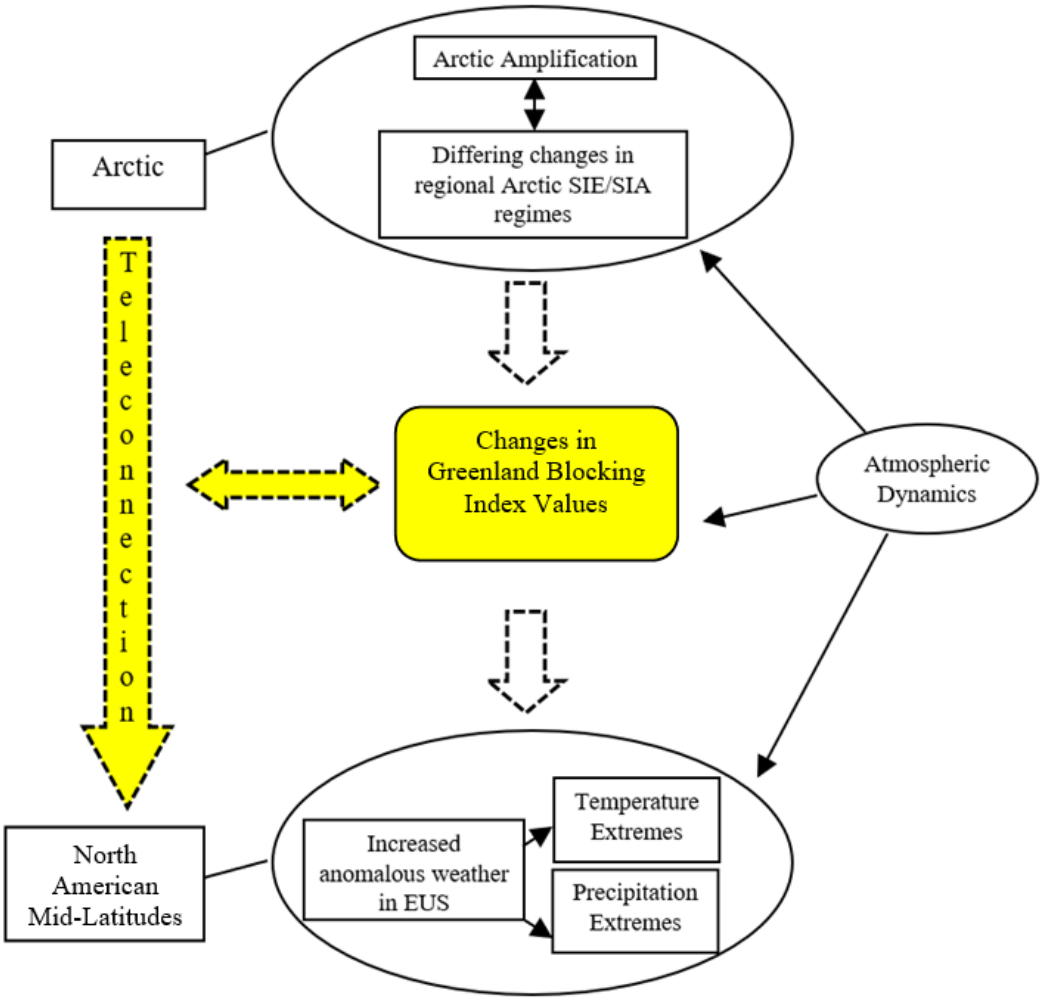

Figure 3. Conceptual model for Arctic-North American mid-latitude teleconnection with the GBI pattern. Solid arrows represent known relationships, while dashed arrows show relationships explored in this research, and the yellow color emphasizes the variable and bi-directional relationships of interest.

5. RESULTS PART 1: MULTIDECADAL CORRELATION ANALYSIS

5.1 VARIABLE ASSESSMENTS

Using the Shapiro-Wilk test, it was found that of the 165 monthly marginal sea ice time series (excluding August, September, and October for the Gulf of St. Lawrence region when sea ice is close to if not completely melted), 114 SIE and 100 SIA values were non-normal, suggesting that a non-parametric correlation technique should be used for subsequent analyses. Two correlation tests, Spearman's Rho and Kendall's Tau (τ), were run on a subset of data (using the months of January and February from the contemporary raw datasets of both SIE versus GBI and SIA versus GBI) to determine which test was the optimal choice for the remainder of correlation analyses based on their correlation coefficients. Due to the similarity in the resulting correlation coefficients, other traits of the tests were considered and the Kendall's Tau test was deemed to be more robust, specifically because the test is less sensitive to errors and discrepancies in the data (including extreme outliers), the p-values are more accurate for smaller sample sizes (n=40), and the results are more easily interpreted (Bulygina et al. 2015). The correlation test was chosen prior to detrending in order to determine the applicability of the test to the raw data, which was readily available for initial testing.

After the correlation test was selected, the removal of trend from the raw data was necessary to assess detrended (DT) correlation analyses. To determine the best detrending method, different functions were used to assess best fit, including linear, cubic, and quadratic forms. An averaging of all line-fit analyses for all months and marginal seas showed the most optimal fit using a quadratic function (r^2=0.37; RMSE=5.7x10^4 km^2), followed by cubic (r^2=0.34; RMSE=5.8x10^4 km^2) and linear (r^2=0.25; RMSE=6.1 x10^4

km^2). The highest r^2 and lowest RMSE values indicate that the quadratic polynomial function was the best fit, possessing the smallest global residuals. Therefore, the quadratic function was used to detrend sea ice and GBI data prior to conducting correlation analyses.

Additionally, monthly averages were calculated to create time series graphs for each dataset (raw and DT) of both sea ice variables, which were discussed later in their individual sections. For the Atlantic and Pacific sectors this included calculating monthly averages for seven marginal seas. After the raw sea ice and raw GBI data were averaged for each sector to obtain monthly averages, the values were again averaged for all 12 months to obtain an annual average for each year of the time series. Linear trends were subsequently fit to the data to assess multidecadal changes. The linear fits of the SIE for the Atlantic sector (**Figure S1**) and Pacific sector (**Figure S2**) show very clear downward trends from 1979 to 2018. The Atlantic sector SIE regression line (**Figure S1**) starts off around $6.8x10^5$ km^2 at the beginning of the time series and drops down to around $5x10^5$ km^2 at the end of the series. The SIE regression line for the Pacific sector (**Figure S2**) shows a much smaller decrease from $1.1x10^5$ km^2 around the start of the time series (1979) to $1x10^5$ km^2 at the end (2018), though looking at the individual years there appears to be more variability for the Pacific sector compared to the Atlantic sector. The linear fits for SIA do not show similar trends to that of the SIE for the Atlantic sector (**Figure S3**) but do for the Pacific sector (**Figure S4**). Within the Atlantic sector SIA graph (**Figure S3**), there are some notable changes in the SIA trend. For the first nine years of the time series (1979–1987), there appears to be an upward slope with relatively low SIA values, but then there is a large increase around 1988, after which a downward

trend starts to show. Focusing on second part of the trend (1988–2018), some of the highest values are around 8.6 $x10^5$ km^2 but the time series ends at about 7.8 $x10^5$ km^2. This graph again shows greater variability than that of the Pacific sector. The Pacific sector graph for SIA (**Figure S4**) again shows a decrease from $6x10^5$ km^2 at the start of the time series (1979) to $4.6x10^5$ km^2 toward the end (2018). Finally, the linear fit for the GBI (**Figure S5**) reveals slight increases for this variable from 1979 to 2018, with the start of the time series showing an average of 5280 meters above sea level (m ASL) and the end of the series showing an average of 5320 m ASL. Though linear fits for each of the variables revealed slight differences in the overall trends, there was a clear decrease for SIE, a slight increase or decrease, depending on the sector and the time period, for SIA, and an increase for the GBI.

To assess the decadal values, the 12-month averages were first calculated for years 1980, 1990, 2000, and 2010 using raw data. Then the decadal changes were calculated by subtracting the average of the previous decade from the more recent decade. For example, for Atlantic SIE, the average for the year 2000 is $5.6x10^5$ km^2 and the average for 2010 is $5.0x10^5$ km^2 and subtracting the 2000 value from the 2010 value gives us a decadal change of $-0.6x10^5$ km^2. The SIE decadal changes can be seen for the Atlantic in **Table 1** and Pacific in **Table 2**, and decadal changes for SIA in the Atlantic are given in **Table 3** and Pacific in **Table 4**. The decadal analysis for SIE shows the Atlantic with negative values for every decade (**Table 1**), but the greatest decrease is for 2000–1990 at $-0.7x10^5$ km^2, though the 2010–2000 decrease is also fairly large at $-0.6x10^5$ km^2. The Pacific (**Table 2**), however, shows its greatest decrease for 1990–1980 ($-0.7x10^5$ km^2), then an increase for 2000–1990 (0.4 $x10^5$ km^2), and finally, another

decrease for 2010–2000 ($-0.6x10^5$ km^2). For the Atlantic sector SIA (**Table 3**), the greatest decrease is shown for 2000–1990 ($-0.3x10^5$ km^2), though the 2010–2000 period also shows a decrease ($-0.2x10^5$ km^2), and 1990–1980 shows a large increase of $1.0x10^5$ km^2. Pacific SIA (**Table 4**) again shows the greatest decrease for 1990–1980 ($-0.7x10^5$ km^2), then a small increase for 2000–1990 ($0.1x10^5$ km^2) and another decrease for 2010–2000 ($-0.6x10^5$ km^2). The same decadal analysis was done for the GBI (**Table 5**) but for this variable there are increases in values for 2000–1990 (48.4 m) and 2010–2000 (88.3 m), with the 1990–1980 producing the only decrease (-66.0 m).

Upon removing trends from all of the time series, correlation tests were completed for both the raw and DT data. Tests included monthly correlations for all regions including lag (by 1, 2, and 3 months), contemporary (lead/lag=0), and lead (by 1, 2, and 3 months) with a total of 1143 tests for the raw data and 1155 tests for the DT data; however, due to zero values present in the datasets for the Gulf of St. Lawrence region, there are missing correlations as Kendall's Tau test cannot be run with zero values. These instances will either be left blank or labeled "no data" in the figures to follow. Kendall's Tau correlation tests ($p \leq 0.05$) returned 196 statistically significant values (SSV) for raw correlations between SIE and GBI out of a total of 1143 tests, and 99 SSV out of 1155 tests for DT SIE versus GBI. In addition, 185 SSV out of 1143 tests were found for raw SIA versus GBI, and 134 SSV out of 1155 tests were found for DT SIA versus GBI.

Initial assessments of GBI and sea ice were done to assess the overall monthly trends across the time series. Each monthly GBI value was averaged (for a total of 40 values for each month) and plotted. Monthly sea ice times series were partitioned by

Atlantic and Pacific sectors, where each sector contains the average monthly values for seven marginal seas. All of the time series graphs (**Figure 4-13**) include individual line graphs for each season and interval markers in grey dashed lines.

The raw GBI data (**Figure 4a-d**) generally show the highest geopotential heights (GPH in m ASL) for the summer months (**Figure 4c**) with lower GPH for spring (**Figure 4b**) and autumn (**Figure 4d**), and the lowest GPH for winter months (**Figure 4a**). The DT GBI time series graphs are given in **Figure 5a-d**. The removal of the trend allows for the interannual fluctuations to be better observed within individual months, specifically anomalies that may be present in the data. The summer months (**Figure 5c**) show relatively stable GPH values, within +/- 100 m; while those for spring (**Figure 5b**) and autumn (**Figure 5d**) show greater interannual variability, with at least one month exceeding the +/- 100 m mark; and finally, the winter months (**Figure 5a**) show the most interannual variability and all three months having at least one year exceeding the +/- 100 m mark. Some larger deviations are noticeable for winter months between the 1980–1990 and from 2009–2012 within the raw time series (**Figure 4a**), and they become even more obvious when looking at the DT time series (**Figure 5a**). The DT data show some of the largest positive deviations for the months of winter (**Figure 5a**) especially around the 1985 and 2010 periods, with the largest positive deviation, upwards of 200 m above average, seen in December of 2010. Several spring (**Figure 5b**) months appear to show large deviations in either direction between years 2005–2018, with an increase in the interannual variability, and the most highly negative deviation in April of 2011 and the most highly positive deviation in March of 2013.

As with the GBI, monthly SIE and SIA data were averaged for each month for

seven marginal seas and organized into Atlantic and Pacific time series graphs. The raw data time series graphs for SIE, **Figure 6a-d** shows plots for the Atlantic sector, with a clear downward trend across the study period for all seasons. The DT data time series for Atlantic sector SIE (**Figure 7a-d**) shows some general areas where slightly more negative or more positive monthly deviations can be seen, such as around 1985 (negative deviation) for summer (**Figure 7c**) and autumn (**Figure 7d**), and 2013–2015 (positive deviation) for autumn (**Figure 7d**) and winter (**Figure 7a**). The month of November (**Figure 7d**) in particular shows several instances of greater deviation compared to other months in the same year for four years from the last decade including 2008 (positive), 2012 (negative), 2014 (positive), and 2016 (negative), with 2016 approaching $-1x10^5$ km^2.

The Pacific sector time series graphs for raw (**Figure 8a-d**) and DT (**Figure 9a-d**) SIE show some similarities to those of the Atlantic in terms of seasonal ice coverage, though the combined marginal seas that make up the Pacific sector appear to show greater SIE values overall. It appears the raw SIE for summer (**Figure 8c**) and autumn (**Figure 8d**) months show a more pronounced downward trend of sea ice compared to the other seasons within this time series. The months of July, August, September, and October in particular reveal a much more obvious decline in SIE, while other months only show a very slight downward trend. Looking at the DT SIE time series for the Pacific (**Figure 9a-d**), highly negative and positive deviations are much more apparent for individual months. One summer month (August; **Figure 9c**) and two autumn months (September and October; **Figure 9d**) each appear to have comparatively greater variability to the other month(s) of the same season. Each of these months shows some of

the most highly negative deviations for years of 1990, 2007, and 2012, surpassing the -$1x10^5$ km^2 mark, though it appears only the month of September shows any years that exceed the +$1x10^5$ km^2 mark (around 1996 and 2001).

Figure 10a-d shows the raw time series for SIA for the Atlantic sector. This series does not show a clear downward trend as with SIE; however, looking at the DT SIA time series for the Atlantic sector (**Figure 11a-d**), the interannual variability becomes much more obvious. Although monthly SIA values tend to stay within the +/-$0.5x10^5$ km^2 boundary, a few years have shown some greater deviation in either direction. Some of the most highly positive SIA deviations ($\geq$+$0.5x10^5$ km^2) can be seen during the winter (**Figure 11a**) and the autumn (**Figure 11d**), around the 2013–2015 period. One of the most notable years is 2016 for the months of November, February, and May, with each month showing a negative deviation $\leq$-$0.5x10^5$ km^2.

The time series for raw SIA for the Pacific (**Figure 12a-d**) shows a downward trend in all months, though the trend is more apparent for summer (**Figure 12c**) and autumn (**Figure 12d**) months. The DT SIA time series for the Pacific sector (**Figure 13a-d**) shows more similarities in SIA deviations within winter (**Figure 13a**), spring (**Figure 13b**), and summer (**Figure 13c**), in other words the monthly deviations track closely to one another and almost all of the months produced deviations within the +/-$1x10^5$ km^2 boundary. The autumn season (**Figure 13d**), however, shows much more interannual variability and month-to-month variability. The year 2007 in particular shows relatively large negative deviations for all summer months (**Figure 13c**), which preceded the greatest negative deviations (<-$1x10^5$ km^2) for the entire time series shown in the months of September and October (**Figure 13d**).

Overall, there appears to be a generally consistent downward trend for both SIE and SIA in both sectors with months of summer and autumn experiencing greater losses. Also of note are the consistent interannual fluctuations across all DT graphs, with some years seeing highly positive deviations only to see large negative deviations the following years; this interannual variation appears for both SIE and SIA, and for GBI.

Further analysis of the two sectors was accomplished by creating bar graphs for individual correlation tests (lag-3, lag-2, lag-1, contemporary, lead-1, lead-2, lead-3), which detail the raw and DT Kendall's Tau (τ) correlation coefficient values of each marginal sea for each month of the year (**Figures 14-17**, **20**, **23**, **26-30**, **33**, **36** and **39**). Within each graph are pairs of bars depicting the intensity and direction of monthly correlations (left bar is for raw data, and right bar is for DT data). Letters a-g show individual graphs for those seven marginal seas that make up the Atlantic sector, and letters h-n show marginal seas within the Pacific sector. For lag and lead analyses, the SIE and SIA variables are those lagging and leading the GBI variable. For example, when running the lag 3 analysis, monthly GBI values for June were correlated with those monthly sea ice values from the previous March; and at lead-3, monthly GBI values for June were correlated with monthly sea ice values for September. The contemporary graphs do not list either lead or lag, and for these, monthly values for a given month of GBI were correlated with those for sea ice of the same month.

The bar graphs reveal how the removal of trend can at times drastically change both the strength and direction of the correlation coefficient. Among the seven tests, none of the correlation tests returned a coefficient greater than +0.5 or less than -0.5; however, a coefficient of $\tau \geq +0.35/\leq -0.35$ is considered to be a strong association. The dash-dot line

within these bar graphs represents the significance threshold, +/-0.223, (at a 95% confidence level; $p \leq 0.05$) for the Kendall's Tau test using n-2 degrees of freedom (n=40).

Heatmaps (**Figures 18-19**, **21-22**, **24-25**, **31-32**, **34-35**, **37-38**, **S6-S21**) were also created to show all correlation coefficients values within a given correlation test (lag-3, lag-2, lag-1, contemporary, lead-1, lead-2, and lead-3), where an asterisk denotes a value greater than or equal to the significance threshold. Within these heatmaps, there is a partition separating Atlantic and Pacific sectors given by a dashed white line. From these heatmaps, persistent SSV are observable both across marginal seas (within the same month, e.g. SSV present in Baffin Bay, Barents Sea, and Canadian Archipelago) and across seasons or across the year (from month-to-month, e.g. SSV present from September to November).

Though there is an obvious concentration of SSV across lag (lag-3, lag-2, lag-1), contemporary, and lead (lead-1, lead-2, lead-3) correlations for raw values of both SIE (**Figures 18**, **21, 24, S6**, **S8**, **S10, S12**) and SIA (**Figures 31**, **34**, **37**, **S14**, **S16**, **S18, S20**) during the summer months for almost all marginal seas, these do not hold up for DT data (DT SIE shown in **Figures 19**, **22**, **25**, **S9**, **S11 S13**; DT SIA shown in **Figure**s **32**, **35**, **38, S15, S17**, **S19, S21**), which give far fewer instances of SSV overall. This indicates that the trend for each of the variables has an influence on the correlation and removing the trend from the data results in far fewer instances of significant correlation coefficients, and often weaker associations for those months that produced SSV. Generally, both sea ice extent and area have been on a downward trend, and will likely continue in this way, while the GBI pattern has recently seen an increase in the frequency and strength of extreme values with some seasons seeing more pronounced changes.

Although the strength of the correlations varies across regions, a majority of SSV are negative, indicating the sea ice and GBI variability are moving in opposite directions. For the Atlantic sector, 114 of 119 SSV in SIE versus GBI correlations and 108 of 110 SSV in SIA versus GBI correlations are negative, while for the Pacific sector, 64 of 77 SSV in SIE versus GBI correlations and 58 of 75 SSV in SIA versus GBI correlations are negative.

5.2 REGIONAL ASSESSMENTS OF ATLANTIC AND PACIFIC

5.2.1 SIE VERSUS GBI

The lag-3 (SIE lagging GBI) results for the Atlantic sector are shown in **Figure 14a-g**. Although most graphs do not show any consistencies in intensity or direction of correlation coefficient values, there does appear to be some consistent month-to-month associations present for the Gulf of St. Lawrence (**Figure 14c**) and the Baffin Bay (**Figure 14d**). The Gulf of St. Lawrence (**Figure 14c**) shows consistent negative associations for both the raw and DT data from March to September, but only the coefficients for the month of August exceed the significance threshold. This persistent negative association indicates SIE and GBI are anticorrelated (one variable decreases (e.g. sea ice) while the other increases (e.g. GBI)). Baffin Bay (**Figure 14d**) also shows several negative associations but includes some slight positive associations as well, and both May and August show both raw and DT values at or beyond the significance threshold. The remaining graphs reveal more variability in both the intensity and direction between the raw and DT data and no months where both the raw and DT data exceed the significance threshold. Overall, there are very few instances of significant

values for both the raw and DT data within the lag 3 graphs.

The Pacific sector bar graphs allowed for a comparison with those of the Atlantic sector to help determine which sector's sea ice regimes may have a greater potential for association with the GBI. The Pacific sector graphs are referenced in **Figure 14h-n** (SIE lagging GBI). The results reveal very few consistencies in the coefficient values. A somewhat consistent positive raw and DT coefficient association shows up in the Central Arctic (**Figure 14h**; January to May), the Laptev Sea (**Figure 14i**; March to July), and the East Siberian Sea (**Figure 14j**; April to August), though none of these graphs produced any month of statistically significant coefficient values for both raw and DT data. Most notable is the Chukchi Sea (**Figure 14k**), which shows a negative raw and DT coefficient association for about ten months, with the other two months, June and July, showing a shift to positive coefficient values for both raw and DT data. In the Pacific sector, only the Sea of Okhotsk (**Figure 14n**) produced both raw and DT coefficient values that meet or exceed significance, but only for the month of May. All other graphs show very little consistencies in the direction and intensity of the monthly coefficients.

At lag-2 for the Atlantic sector (**Figure 15a-g**; SIE lagging GBI), only the Baffin Bay (**Figure 15d**) and the Greenland Sea (**Figure 15e**) show any months with both raw and DT values reaching the significance threshold; these include the months of May in **Figure 15d** and December in **Figure 15e**. Throughout many of the graphs, there appear to be inconsistencies in the direction and intensity of the coefficients when comparing the raw to the DT values, though the Gulf of St. Lawrence (**Figure 15c**) and Baffin Bay (**Figure 15d**) show some consistency in negative values as well as the months in which negative values are found, from around February to about August.

At lag-2 for the Pacific sector (**Figure 15h-n**; SIE lagging GBI), some graphs show consistent month-to-month associations, though these vary in direction (negative/positive). In the Central Arctic (**Figure 15h**), there is a general positive association from January to May, then a shift to a general negative association for June to November. Almost all months for the Laptev Sea (**Figure 15i**) shows positive associations. The Chukchi Sea (**Figure 15k**) shows eight months of mostly negative coefficient associations, though they are not very strong. Lastly, the Bering Sea (**Figure 15m**) and the Sea of Okhotsk (**Figure 15n**) both produced some negative associations for raw and DT coefficient values, but they show up in opposite times of the year. The Bering Sea (**Figure 15m**) shows a negative association from August to December and the Sea of Okhotsk (**Figure 15n**) shows a negative association from January to May. None of the graphs indicate a single month of significant raw and DT coefficient values.

The Atlantic sector graphs for lag-1 (**Figure 16a-g**; SIE lagging GBI) reveal sporadic instances of values meeting or exceeding the significance threshold, and none of the graphs showing any months where both raw and DT values meet the threshold in the same month. Baffin Bay (**Figure 16d**) comes closest to having both significant raw and DT values for the month of February, but only the DT value reaches significance. As in lag-2, the Gulf of St. Lawrence (**Figure 16c**) and Baffin Bay (**Figure 16d**) show some consistency in negative values from January to around August. The months of SON in Baffin Bay (**Figure 16d**) all show positive values, only to turn negative again in December. The Gulf of St. Lawrence (**Figure 16c**) shows August values turn positive and might continue to show the same for SON if values were available for correlation.

At lag-1 for the Pacific sector (**Figure 16h-n**; SIE lagging GBI), the graphs with

the most consistent negative monthly associations include Chukchi Sea (**Figure 16k**) and Sea of Okhotsk (**Figure 16n**). The Chukchi Sea (**Figure 16k**) shows almost all months with negative associations, with a few exceptions; however, none of months in this graph produced significant values for both raw and DT coefficients. The Sea of Okhotsk (**Figure 16n**) shows a general negative association for January through May, then mostly positive values for June through October, and slightly negative again in November and December. Of all the graphs, only the Laptev Sea (**Figure 16i**) shows raw and DT coefficients reaching significance, for one month, February.

Atlantic sector contemporary correlations (**Figure 17a-g**; same month correlations for SIE and GBI) show some more consistent negative associations in the Canadian Archipelago, Hudson Bay, Gulf of St. Lawrence, and Baffin Bay (**Figure 17a**, **b**, **c**, and **d**), but the months in which these associations occur is not the same across the graphs. Hudson Bay (**Figure 17b**) and Baffin Bay (**Figure 17d**) show almost all months with negative associations, although some very slight positive values for either raw or DT do show up as well. In the Hudson Bay (**Figure 17b**), only the month of October shows both raw and DT values exceeding the significance threshold, though November and December also come close. Baffin Bay (**Figure 17d**) by far has the greatest number of months where both raw and DT values meet or exceed significance; with four months showing strong raw and DT coefficients including January (raw τ=-0.37; DT τ=-0.41), March (raw τ=-0.42; DT τ=-0.35), October (raw τ=-0.45; DT τ=-0.32), and December (raw τ=-0.41; DT τ=-0.41).

The contemporary correlation test for the Pacific sector (**Figure 17h-n**; same month correlations for SIE and GBI) produced some of the most consistent associations

in East Siberian, Beaufort Sea, and the Sea of Okhotsk (**Figure 17j**, **l**, and **n**). Within the East Siberian Sea (**Figure 17j**), raw and DT coefficients for May through August are negative, then positive in September, and negative again for November and December; none of the coefficients reached significance. The Beaufort Sea (**Figure 17l**) shows some strong negative values for the raw data, though these values are still significant for the DT data, they are much weaker; the significant months include May (raw τ=-0.31; DT τ=-0.22), June (raw τ=-0.38; DT τ=-0.28), and August (raw τ=-0.39; DT τ=-0.24). These associations are among the most highly negative in any of the graphs for this sector and correlation tests. Lastly, the Sea of Okhotsk (**Figure 17n**) shows some slight positive associations from January to May, then a switch to negative associations from June to December. Although this graph indicates the most month-to-month consistency, the coefficients are not highly positive or negative.

Heatmaps were also produced as summary figures for those SIE versus GBI correlation tests which produced the greatest number of months with consistent and significant raw and DT monthly values, in particular, contemporary (**Figure 18-19**), lead-1 (**Figure 21-22**), and lead-2 (**Figure 24-25**) tests. Additional SIE versus GBI heatmaps are shown in **Figure S6-S13**. These figures list monthly numerical correlation coefficients for both sectors (separated by the dashed white line) and each of the marginal seas within. The contemporary SIE versus GBI correlation test is summarized in **Figure 18** (raw) and **Figure 19** (DT). For the Atlantic sector (top portion), Baffin Bay produced the greatest number of statistically significant values (SSV) for the months of January, March, October, and December across both the raw and DT data. Aside from the two winter months, January and December, it does not appear a persistent seasonal pattern.

The only marginal sea to produce significant coefficient values for both raw (**Figure 18**) and DT (**Figure 19**) data for the Pacific sector (bottom portion) was the Beaufort Sea, including the months of May, June, and August.

At lead-1 for the Atlantic sector (**Figure 20a-g**; SIE leading GBI), the Canadian Archipelago, Hudson Bay, and Baffin Bay (**Figure 20a**, **b**, and **d**) show consistent negative associations for many of the same months. Baffin Bay (**Figure 20d**) again shows the greatest number of months with significant raw and DT coefficients, though almost all of the raw coefficient values returned more stronger negative associations than those of the DT values. Those significant months include January (raw τ=-0.38; DT τ=-0.25), February (raw τ=-0.32; DT τ=-0.36), March (raw τ=-0.40; DT τ=-0.31), April (raw τ=-0.34; DT τ=-0.27), August (raw τ=-0.43; DT τ=-0.27), October (raw τ=-0.39; DT τ=-0.38), and November (raw τ=-0.27; DT τ=-0.40). The Canadian Archipelago (**Figure 20a**) and the Hudson Bay (**Figure 20b**) show negative associations for both raw and DT from March to October (with some very slight positives appearing for a few months in graph b), which overlap with negative associations seen in the Baffin Bay (**Figure 20d**), while the Kara Sea (**Figure 20g**) overlaps only for months of May, June, July, and somewhat for December. The Gulf of St. Lawrence (**Figure 20c**) shows DJF and March with negative associations, though March is the only month with both raw and DT meeting the significance threshold. The Greenland Sea (**Figure 20e**) and the Barents Sea (**Figure 20f**) again both show inconsistencies in almost every month in the strength and direction of the correlation coefficient when comparing raw and DT data.

At lead-1 for the Pacific sector (**Figure 20h-n**; SIE leading GBI), a few graphs such as the East Siberian (**Figure 20j**) and the Sea of Okhotsk (**Figure 20n**) show several

months with consistently positive or negative associations, but do not show any months where both raw and DT coefficient values meet the significance threshold. The Beaufort Sea (**Figure 20l**) once again shows consistent negative association for several months, this time April to August, though only May (raw τ=-0.29; DT τ=-0.36) and June (raw τ=-0.46; DT τ=-0.42) produced mostly strong coefficients that exceed significance.

The lead-1 correlation heatmaps for raw (**Figure 21**) and DT (**Figure 22**) SIE versus GBI show the greatest number of months with consistent SSV for raw and DT data of any of the correlation tests for the Baffin Bay. These consistencies are produced for two winter months (January and February), two spring months (March and April), one summer month (August), and two autumn months (October and November), suggesting partial relationships (the consistencies are for some months within a season, but never for all three months) for sea ice extent and the GBI in all seasons for this marginal sea. In the Beaufort Sea, only the months of May and June show raw (**Figure 21**) and DT (**Figure 22**) SSV consistencies.

At lead-2 for the Atlantic sector (**Figure 23a-g**; SIE leading GBI), some similar patterns can be observed as with previous correlations. The Canadian Archipelago, Hudson Bay, and Baffin Bay (**Figure 23a**, **b**, and **d**) each show some months of consistent negative associations from about February to October. In the Canadian Archipelago (**Figure 23a**), the months of June (raw τ=-0.23; DT τ=-0.23), August (raw τ=-0.31; DT τ=-0.22), and September (raw τ=-0.25; DT τ=-0.28), produced coefficients that barely meet or slightly exceed the significance threshold for both raw and DT data, so the associations are not strong for this marginal sea. In Hudson Bay (**Figure 23b**), May is the only month to meet the significance standard. Baffin Bay (**Figure 23d**) has

returned the most consistently negative coefficients for all months except November. Only January (raw τ=-0.34; DT τ=-0.26), February (raw τ=-0.28; DT τ=-0.31), and June (raw τ=-0.34; DT τ=-0.24) have raw and DT coefficients that surpass the significance threshold, though very few of these associations are very strong.

The lead-2 for the Pacific sector (**Figure 23h-n**; SIE leading GBI) produced several graphs with consistent, albeit fairly weak associations, such as in the Central Artic, Laptev Sea, East Siberian Sea, and Chukchi (**Figure 23h**, **i**, **j**, and **k**). Within these graphs, consistencies of about five months can be observed, though the direction of the association varies. In the Central Arctic (**Figure 23h**), raw and DT coefficients mostly lean negative for January to July. A similar negative association is found in the Laptev Sea (**Figure 23i**) for July through December. The East Siberian Sea (**Figure 23j**) and the Chukchi Sea (**Figure 23k**), however, show mostly positive raw and DT coefficients for January to May, followed by a negative association from June to August. The graph for the East Siberian Sea (**Figure 23j**) shows two months of statistically significant raw and DT coefficients for April (raw τ=0.30; DT τ=0.22) and July (raw τ=-0.38; DT τ=-0.22); this is the first and last instance of more than one month of significant values for this marginal sea. Lastly, the Beaufort Sea (**Figure 23l**) produced the greatest number of months with consistently negative trends, from April to October, though among these, only May (raw τ=-0.24; DT τ=-0.35), June (raw τ=-0.40; DT τ=-0.32), and August (raw τ=-0.43; DT τ=-0.23) produced significant raw and DT coefficients.

The lead-2 correlations are the last to show SSV consistencies for more than one month for either marginal sea. The heatmaps for the raw (**Figure 24**) and DT (**Figure 25**) data show these consistencies for January, February, and June in the Baffin Bay, showing

a slight seasonal relationship for winter. The Beaufort Sea shows May, June, and August months are significant, possibly hinting at a late spring and summer relationship.

At lead-3 for the Atlantic sector (**Figure 26a-g**; SIE leading GBI), negative associations similar to previous correlations can be seen for the Canadian Archipelago, Hudson Bay, Baffin Bay, and Kara Sea (**Figure 26a**, **b**, **d**, and **g**). It appears most instances of monthly values reaching or exceeding the significance threshold for raw and DT values have disappeared at lead-3, with only the month of September in the Hudson Bay (**Figure 26**b) and January in the Baffin Bay (**Figure 26d**) showing significance.

Lead-3 for the Pacific sector (**Figure 26h-n**; SIE leading GBI) shows graphs for the Chukchi Sea, Beaufort Sea, and Bering Sea (**Figure 26k**, **l**, and **m**) with at most four to five months each of consistently negative month to month associations, though of these graphs, the Chukchi (**Figure 26k**) and the Beaufort Sea (**Figure 26l**) are the only to produce any months with significant raw and DT coefficients. Many of these graphs also show summer (JJA) months with mostly negative associations, though the strength varies by marginal sea.

Overall, the results of the correlation tests represented by the bar graphs and heatmaps suggest some consistencies in significant coefficient values for a few months across the tests with different time leads or lags. Within Baffin Bay, these include the month of January for contemporary, lead-1, and lead-2 tests, and the month of March for contemporary and lead-1 tests, hinting at a slight relationship for the winter and spring seasons. For the Beaufort Sea, the month of June was the most consistently significant across the three tests, but the month of August also showed some consistency in the contemporary and lead-2 tests, possibly indicating a slight relationship for summer. The

lead tests indicate a lasting association between the sea ice extent and the GBI for those months within these marginal seas. The tests suggest that the GBI variable may affect the sea ice immediately through poleward warm air advection and radiative feedbacks, for instance, but also some weeks later, depending on the background state of the atmosphere and ocean and other variables not accounted for within this study.

5.2.2 SIA VERSUS GBI

The following correlation bar graphs for the Atlantic sector (**Figure 27a-g**) show SIA versus GBI. Comparing the SIA to the SIE correlations can show whether the change in the ice variable affected the consistency of significant monthly correlations. Starting with the lag-3 (SIA lagging GBI), there are some instances of consistent negative associations across these graphs. The Hudson Bay (**Figure 27b**) overall has the greatest number of months with both raw and DT data leaning negative, yet the month of April produced a slight positive result for the DT data. Other than the Hudson Bay, the Gulf of St. Lawrence (**Figure 27c**) and the Greenland Sea (**Figure 27e**) are the only other graphs to produce somewhat consistent negative coefficients for both raw and DT data, though the associations are fairly weak. Only the Hudson Bay (**Figure 27b**) and the Baffin Bay (**Figure 27d**) produced a coefficient for both raw and DT data that meets or exceeds the significance threshold (both in the month of August).

At lag-3 for the Pacific sector (**Figure 27h-n**; SIA lagging GBI), few consistencies can be observed throughout any of the graphs. The strength of monthly coefficients appear to change regularly from month to month within many of the graphs. Additionally, none of the graphs show any month where raw and DT coefficients both

exceed significance.

At lag-2 for the Atlantic sector (**Figure 28a-g**; SIA lagging GBI), few graphs produced consistently positive or negative coefficient values for both raw and DT data within the same month. The Hudson Bay (**Figure 28b**) comes closest to revealing an association, with eight of the 12 months showing negative coefficient values for raw and DT data (though raw coefficients for February and September are merely positive), and the month of October almost reaching significance for both values. The only month to meet the significance threshold is August in Baffin Bay (**Figure 28d**). Other than these, few consistencies can be observed for this test.

At lag-2 for the Pacific sector (**Figure 28h-n**; SIA lagging GBI), much of same seemingly sporadic and inconsistent monthly coefficient values can be seen for all graphs. The raw coefficients for the month of August within the Beaufort Sea (**Figure 28l**) reaches significance, while the DT coefficient comes close to but does not reach significance. Other than that, no other graph shows significance for both raw and DT values within the same month.

Lag-1 graphs for the Atlantic sector (**Figure 29a-g**; SIA lagging GBI) show very few consistencies either in direction or strength of correlation coefficients. The Hudson Bay (**Figure 29b**) shows the most consistency in associations with almost all months producing negative coefficients for both raw and DT data, though with some very slight positive values for either raw or DT in February, June and November. None of the graphs produced any month with statistically significant raw and DT values. Baffin Bay (**Figure 29d**) shows the early half of the year with highly negative raw values, yet the DT coefficients are insignificant, and some months (such as May and June) change from

negative values for raw to slightly positive values for DT.

For lag-1 for the Pacific sector (**Figure 29h-n**; SIA lagging GBI), a negative association can be observed in the Beaufort Sea (**Figure 29l**) from June to October, though the intensity of the values is not consistent. The month of August is the only month to produce a significant coefficient for both raw and DT data.

For contemporary correlation for the Atlantic sector (**Figure 30a-g**; same month correlations for SIA and GBI), consistent associations begin to show and can be seen for several graphs including **Figure 30a**, **b**, **c**, **d**, and **g**. In the Canadian Archipelago (**Figure 30a**), all months except for February and March have produced negative raw and DT coefficient values at varying intensity. March raw and DT values are significant in the positive direction while the same is true for May in the negative direction, a complete reversal of associations within the same season. Hudson Bay (**Figure 30b**) reveals negative raw and DT coefficient values for almost all months except for September with a very slight positive raw value. The months of January, October, November, and December show strongly negative raw and DT coefficient values, but only January and October produced raw and DT values surpassing the significance threshold. The Gulf of St. Lawrence (**Figure 30c**) shows consistent negative associations for January, February, March, and April, but only March coefficients exceed significance for raw and DT data. In Baffin Bay (**Figure 30d**), some of the most highly negative coefficients appear from October to about April, with five months exceeding significance for both raw and DT data. These months include January (raw τ=-0.41; DT τ=-0.42), February (raw τ=-0.32; DT τ=-0.27), March (raw τ=-0.36; DT τ=-0.28), October (raw τ=-0.44; DT τ=-0.32), and December (raw τ=-0.39; DT τ=-0.43), with January and December showing some of the

strongest associations. Lastly, the Kara Sea (**Figure 30g**) appears to show some persistent negative associations from April to August, then again in November and December, though none of these months produced significant coefficients for both raw and DT values.

The contemporary correlation graphs for the Pacific (**Figure 30h-n**; same month correlations for SIA and GBI) exhibit month to month consistencies for raw and DT data for several graphs including for the Chukchi Sea, Beaufort Sea, Bering Sea, and Sea of Okhotsk (**Figure 30k**, **l**, **m**, and **n**). In the Chukchi Sea (**Figure 30k**), the months of May through August reveal negative coefficient values, though none are significant. For the Beaufort Sea (**Figure 30l**), every month except March and September produced negative coefficients for both raw and DT data. The summer months, June (raw τ=-0.45; DT τ=-0.37) and July (raw τ=-0.38; DT τ=-0.26) were the only two months to reach significance and the coefficient values are fairly strong for both raw and DT data. The Bering Sea (**Figure 30m**) produced consistent negative values for June through December, but none of these months show significant raw and DT coefficient values. Lastly, the Sea of Okhotsk (**Figure 30n**) shows the greatest number of months with negative associations from June to December, but overall, the coefficients are not very strong, and no months produced significant raw or DT coefficients.

Similar to the analysis of SIE versus GBI, heatmap summary graphs were created to display the numerical coefficient values for all SIA versus GBI correlation tests (**Figures 31-32**, **34-35**, **37-38**, **S14-S21**); however, only those tests which produced the greatest number of consistently significant monthly coefficients are considered here (**Figure 31-32**, **34-35**, **37-38**). The contemporary SIA versus GBI raw (**Figure 31**) and

DT (**Figure 32**) heatmaps show Baffin Bay with the greatest number of month-to-month consistencies in both raw and DT data including the months of January, February, March, August, October, and December. The winter (DJF) appears to be the only season to show consistent significant associations. No other marginal sea produced concurrent significant raw and DT values for more than two months. For the Pacific sector, the Beaufort Sea and Laptev Sea each produced two months of concurrent significant raw (**Figure 31**) and DT (**Figure 32**) coefficients; specifically, for the Beaufort Sea, these two months are consecutive, June and July, and for the Laptev Sea they are months apart, March and September. Similar with the SIE, the Beaufort Sea SIA values also seem to show somewhat of a summer relationship with GB.

Lead-1 graphs for the Atlantic sector (**Figure 33a-g**; SIA leading GBI) show some persistence in month-to-month raw and DT coefficients for the Canadian Archipelago, Hudson Bay, Gulf of St. Lawrence, Baffin Bay, and Kara Sea (**Figure 33a**, **b**, **c**, **d**, and **g**). Negative raw and DT associations are present from April to December in the Canadian Archipelago (**Figure 33a**), yet only the month of July produced significant raw and DT values. Within the Hudson Bay (**Figure 33b**) nearly all twelve months produced negative coefficients for both raw and DT values, apart from the DT value for the month of July; however, only May coefficients exceeded significance. A slight persistence can be seen in the Gulf of St. Lawrence (**Figure 33c**) for December through April, with only March producing significant raw and DT coefficients. Baffin Bay (**Figure 33d**) produced some of the strongest negative associations over twelve months, with seven months exceeding the significance threshold for both raw and DT values. These months include January (raw τ=-0.44; DT τ=-0.40), February (raw τ=-0.32; DT τ=-

0.36), March (raw τ=-0.35; DT τ=-0.24), April (raw τ=-0.30; DT τ=-0.24), August (raw τ=-0.45; DT τ=-0.29), October (raw τ=-0.38; DT τ=-0.38), and November (raw τ=-0.26; DT τ=-0.36). After mostly strong negative associations in October and November, the month of December produced only slightly negative coefficient values, then January shows the strongest associations overall. For the Kara Sea (**Figure 33g**) January to April produced positive associations, but May through August show mostly negative associations, then September through November show positive again only to end with a negative association in December. May and December both produced significant raw and DT values, but these appear to be somewhat random and not very strong as they do not reach the +/-0.35 threshold. The remaining graphs for Greenland Sea and the Barents Sea (**Figure 33e** and **f**) appear to have mostly irregular monthly values and did not produce any months where both raw and DT values meet or exceed significance.

At lead-1 for the Pacific sector (**Figure 33h-n**; SIA leading GBI), the strongest and most consistent month-to-month raw and DT coefficients are seen for the Beaufort Sea (**Figure 33l**) for April to August, though February and October also produced negative associations. Of these months, May (raw τ=-0.23; DT τ=-0.31), June (raw τ=-0.49; DT τ=-0.43), July (raw τ=-0.39; DT τ=-0.25), and October (raw τ=-0.28; DT τ=-0.26) produced significant values for both raw and DT data. June appears to have produced the strongest negative association and March (raw τ=0.31; DT τ=0.35) was the only month to produce a positive association for this marginal sea. The Bering Sea (**Figure 33m**) also produced several months of negative associations for both raw and DT data from January, May through August, October, and November. Although both graphs show almost the same months with negative associations, the coefficient values for the

Bering Sea were much weaker than those of the Beaufort Sea.

Heatmaps for the Atlantic sector at lead-1 are given in **Figure 34** (raw) and **Figure 35** (DT). These graphs show significant negative associations for raw and DT coefficient values for January, February, March, April, August, October, and November for the Baffin Bay. It appears there are significant consistencies from part of winter into spring, one month of summer, and again in mid- to late autumn. No other marginal seas within the Atlantic sector produced concurrent significant raw and DT coefficients for more than two months. Within the Pacific sector on the heatmaps, the Beaufort Sea show four months of negative associations, May, June, July, and October, hinting at a possible summer relationship for this marginal sea and the GB. Overall, the lead-1 test produced the greatest number of months with significant raw and DT coefficients (especially for two of the marginal seas, Baffin Bay and the Beaufort Sea) out of all the correlation tests.

At lead-2 for the Atlantic sector (**Figure 36a-g**; SIA leading GBI), graphs for the Canadian Archipelago, Hudson Bay, Gulf of St. Lawrence, Baffin Bay, and Kara Sea (**Figure 36a**, **b**, **c**, **d**, and **g**) all show persistent negative month-to-month associations. In the Canadian Archipelago (**Figure 36a**), these negative associations can be seen for both raw and DT values from April through September, with both April and September producing significant values for both raw and DT data. Other months only produced slightly positive or negative associations for either raw or DT data. Within the Hudson Bay graph (**Figure 36b**), an eight-month persistence of negative associations can be seen from February through September, but only the month of May produced a raw and DT coefficient value exceeding significance. The Gulf of St. Lawrence (**Figure 36c**) shows only some slight persistence in associations from January to March, then from September

through December (note: data for June–August are missing), but no month produced raw and DT coefficients that exceeded the significance threshold. As in previous tests, Baffin Bay (**Figure 36d**) produced the most consistent month-to-month negative associations for both the raw and DT data as November was the only month within this graph to produce positive raw and DT coefficients. The months of January (raw τ=-0.35; DT τ=-0.27), February (raw τ=-0.30; DT τ=-0.28), June (raw τ=-0.33; DT τ=-0.23), and October (raw τ=-0.35; DT τ=-0.23) produced both raw and DT coefficients that just met or slightly exceeded the significance threshold, with few coefficients showing strong associations. Finally, the Kara Sea (**Figure 36g**) also shows some negative raw and DT values for the months of April through August, then again in November and December; however, none of these produced significant values for both raw and DT coefficients.

Lead-2 graphs for the Pacific sector (**Figure 36h-n**; SIA leading GBI) show persistence in negative summer month (JJA) associations within the East Siberian, Chukchi Sea, and Beaufort Sea (**Figure 36j**, **k**, and **l**), though only the Beaufort Sea produced a few significant raw and DT coefficients. The Beaufort Sea (**Figure 36l**) has the greatest number of negative month-to-month consistencies from April to October for both raw and DT data, but only June produced significant values (raw τ=-0.34; DT τ=-0.29).

Lead-2 heatmaps for the Atlantic sector, **Figure 37** (raw) and **Figure 38** (DT), show the Baffin Bay with the greatest number of months of significant raw and DT coefficients including January, February, June, and October, with the strongest relationship shown for two of the three winter months. For the Pacific sector, the heatmaps reveal at most one month of statistically significant values for the Beaufort Sea

for raw (**Figure 37**) and DT (**Figure 38**). The lead-2 test produced the least number of months with significant values of the three tests discussed, including contemporary, lead-1, and lead-2, though as with previous correlation tests, the month of June is significant, indicating a potentially persistent summer relationship for the Beaufort Sea ice and the GB.

Lead-3 graphs for the Atlantic (**Figure 39a-g**; SIA leading GBI) show much of the same patterns in negative associations as compared to lead-2 and lead-1, though there are far fewer instances of significant associations within the lead-3 test. The Canadian Archipelago (**Figure 39a**) produced seven months of persistent negative coefficients for both raw and DT data, but only September values reached significance. Except for a very slightly positive DT coefficient for December, the Hudson Bay (**Figure 39b**) shows negative coefficient values for all months for both raw and DT data, though only September produced significant values for both raw and DT coefficients. In the Gulf of St. Lawrence (**Figure 39c**), as shown in previous tests, despite of missing data, out of the nine months with data, seven produced negative coefficients for both raw and DT data, or in the case of the DT coefficient for October, a very slight positive (nearly zero) value. Aside from the Hudson Bay (**Figure 39b**), the Baffin Bay (**Figure 39d**) shows some of the most persistent associations. Almost all months returned a negative correlation coefficient for both raw and DT data, with a few exceptions for DT values in the months of March, April, and October. January is the only month that produced significant values for both raw and DT data. The Greenland Sea (**Figure 39e**) and the Barents Sea (**Figure 39f**) show some slight month-to-month consistency in sea ice-GBI associations for four and three months, respectively. These include February, March, April, and May for the

Greenland Sea (**Figure 39e**) and March, April, and May for the Barents Sea (**Figure 39f**). Lastly, some month-to-month associations can be seen for the Kara Sea (**Figure 39g**). The months of January through June produced mostly negative associations, except for the raw value for January. The DT coefficients seem to be much more highly negative for many of these months compared to the raw value.

Lastly, lead-3 graphs for the Pacific (**Figure 39h-n**; SIA leading GBI) show a negative association in summer (JJA) for the Central Arctic, East Siberian Sea, Chukchi Sea, Beaufort Sea, and the Bering Sea (**Figure 39h**, **j**, **k**, **l**, and **m**). The raw coefficient values for these trends are highly negative, but reduced in intensity for the DT coefficients, and only the Chukchi Sea (**Figure 39k**) and the Beaufort Sea (**Figure 39l**) produced at least one month (June in both graphs) with both raw and DT coefficients exceeding the significance threshold.

In summary, the bar graphs and heatmaps produced for SIA versus GBI were able to show several correlation tests produced consistently significant raw and DT coefficients for months of January (contemporary, lead-1, lead-2, and lead-3), February (contemporary, lead-1, and lead-2), and October (contemporary, lead-1, and lead-2) for Baffin Bay. A strong relationship for winter and a weaker relationship in autumn seem to exist in this region. For the Beaufort Sea, the month of June (contemporary, lead-1, lead-2, and lead-3) and July (contemporary, lead-1) showed the strongest relationships, which suggests a strong summer association within this marginal sea. These two marginal seas were the only seas within their respective sectors to consistently show significant coefficients across the various correlations tests. Also, it appears as though the change in which sea ice variable (SIE or SIA) was used for correlation against the GBI did not

greatly affect the monthly correlations. Both SIE and SIA correlation tests showed that the Atlantic sector, specifically the Baffin Bay, appears to have produced a greater number of monthly SSV for both raw and DT values than that of the Beaufort Sea from the Pacific sector. The total number of SSV for the DT data from the Atlantic sector is 62 out of a total of 567 values calculated (not including those three months for which the Gulf of St. Lawrence had zero values), and the total number of SSV for the DT data for the Pacific sector is 38 out of a total of 588, which suggests at a more substantial association for Atlantic sector sea ice with GBI than that of the Pacific sector.

Table 1. Decadal averages and differences for SIE for the Atlantic sector.

SIE - Atlantic Decadal Changes (in x10^5 km^2)	
Year	**Average**
2010	5.0
2000	5.6
1990	6.3
1980	6.4
Year	**Difference**
2010–2000	-0.6
2000–1990	-0.7
1990–1980	-0.1

Table 2. Decadal averages and differences for SIE for the Pacific sector.

SIE - Pacific Decadal Changes (in x10^5 km^2)	
Year	**Average**
2010	10.2
2000	10.8
1990	10.4
1980	11.1
Year	**Difference**
2010–2000	-0.6
2000–1990	0.4
1990–1980	-0.7

Table 3. Decadal averages and differences for SIA for the Atlantic sector.

SIA - Atlantic Decadal Changes (in x10^5 km^2)	
Year	**Average**
2010	8.0
2000	8.2
1990	8.5
1980	7.5
Year	**Difference**
2010–2000	-0.2
2000–1990	-0.3
1990–1980	1.0

Table 4. Decadal averages and differences for SIA for the Pacific sector.

SIA - Pacific Decadal Changes (in x10^5 km^2)	
Year	**Average**
2010	4.7
2000	5.3
1990	5.2
1980	5.9
Year	**Difference**
2010–2000	-0.6
2000–1990	0.1
1990–1980	-0.7

Table 5. Decadal averages and differences for GBI.

GBI Decadal Changes (in m ASL)	
Year	Average
2010	5392.05
2000	5303.70
1990	5255.26
1980	5320.78
Year	Difference
2010–2000	88.35
2000–1990	48.44
1990–1980	-65.52

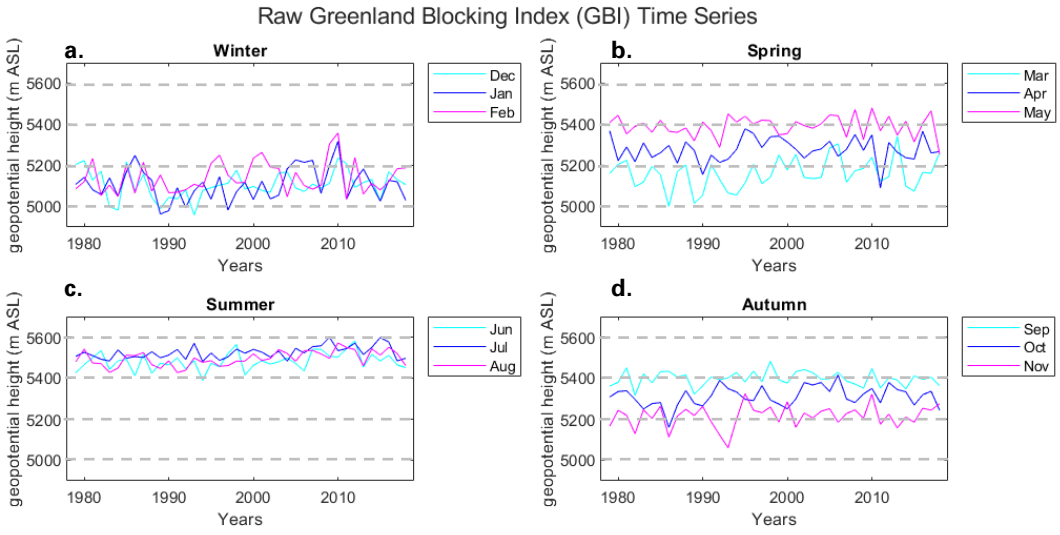

Figure 4. Raw GBI time series plots are shown for months comprising a) winter (DJF), b) spring (MAM), c) summer (JJA), and d) autumn (SON).

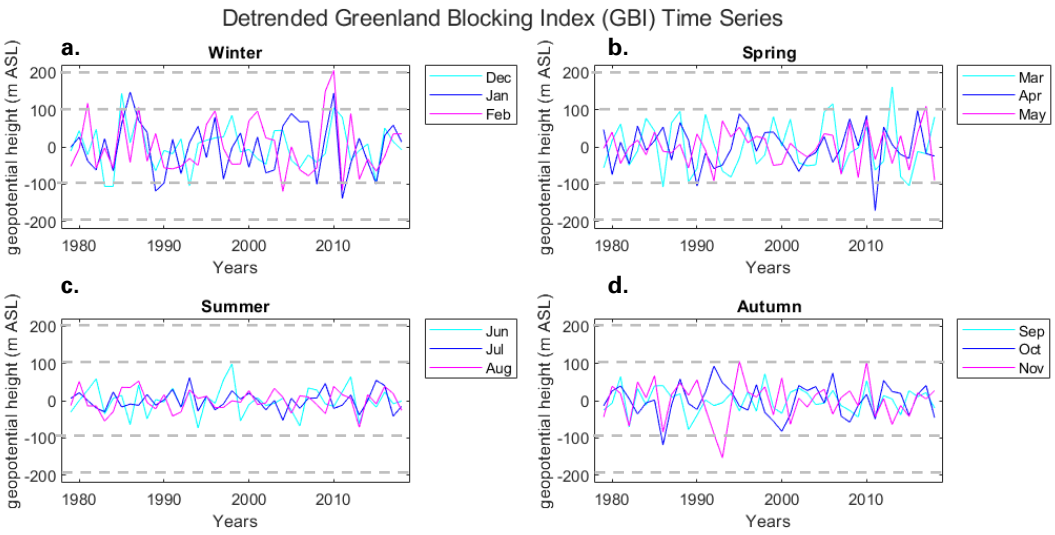

Figure 5. Detrended GBI time series plots are shown for months comprising a) winter (DJF), b) spring (MAM), c) summer (JJA), and d) autumn (SON).

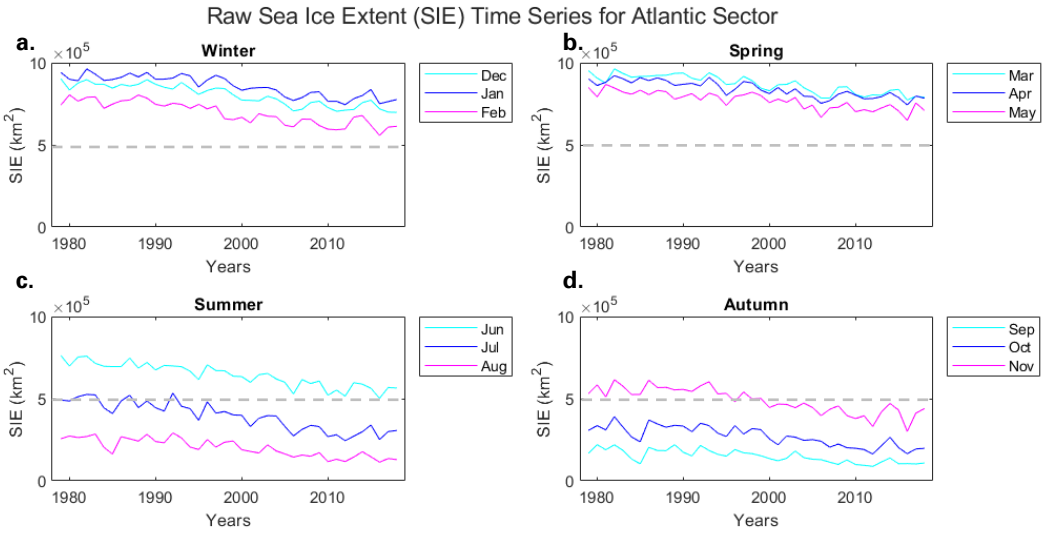

Figure 6. Raw SIE time series plots are shown for the Atlantic sector for a) winter (DJF), b) spring (MAM), c) summer (JJA), and d) autumn (SON). Monthly values were averaged across all 7 marginal seas (Baffin Bay, Barents Sea, Canadian Archipelago, Greenland Sea, Hudson Bay, Kara Sea, and Gulf of St. Lawrence).

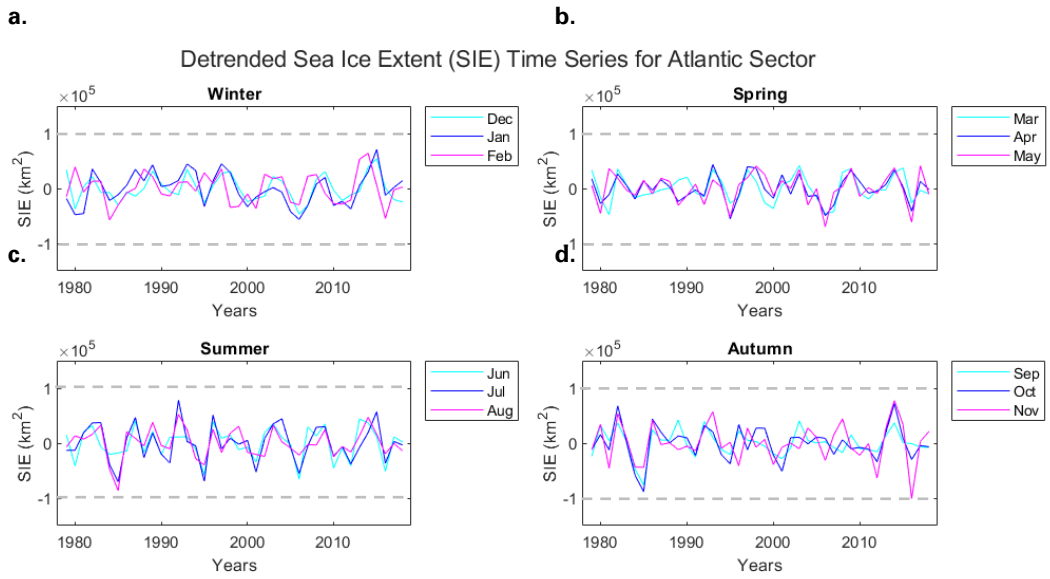

Figure 7. Detrended SIE time series plots are shown for the Atlantic sector for a) winter (DJF), b) spring (MAM), c) summer (JJA), and d) autumn (SON). Monthly values were averaged across all 7 marginal seas (Baffin Bay, Barents Sea, Canadian Archipelago, Greenland Sea, Hudson Bay, Kara Sea, and Gulf of St. Lawrence).

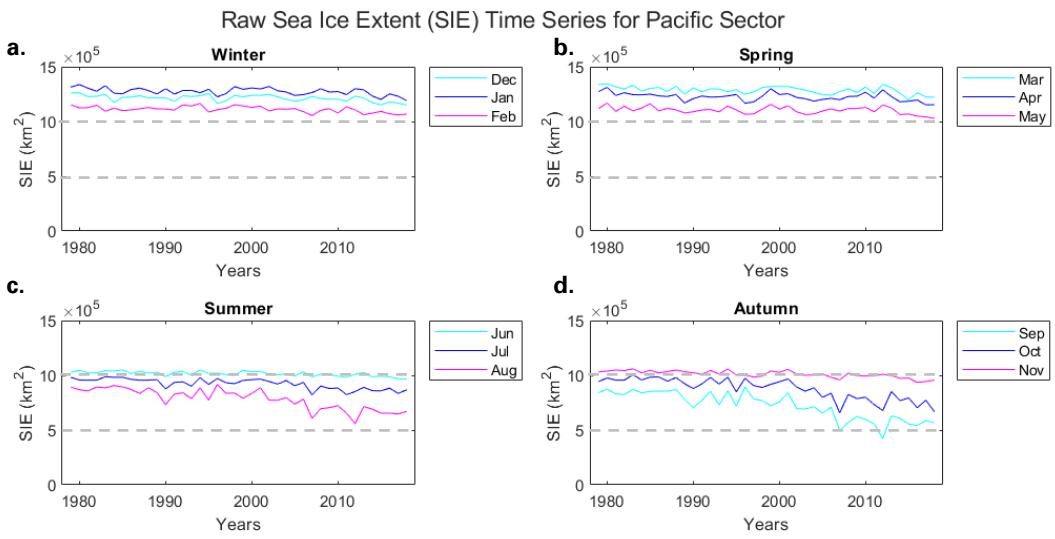

Figure 8. Raw SIE time series plots are shown for the Pacific sector for a) winter (DJF), b) spring (MAM), c) summer (JJA), and d) autumn (SON). Monthly values were averaged across all 7 marginal seas (Beaufort Sea, Bering Sea, Central Arctic, Chukchi Sea, East Siberian Sea, Laptev Sea, and Sea of Okhotsk).

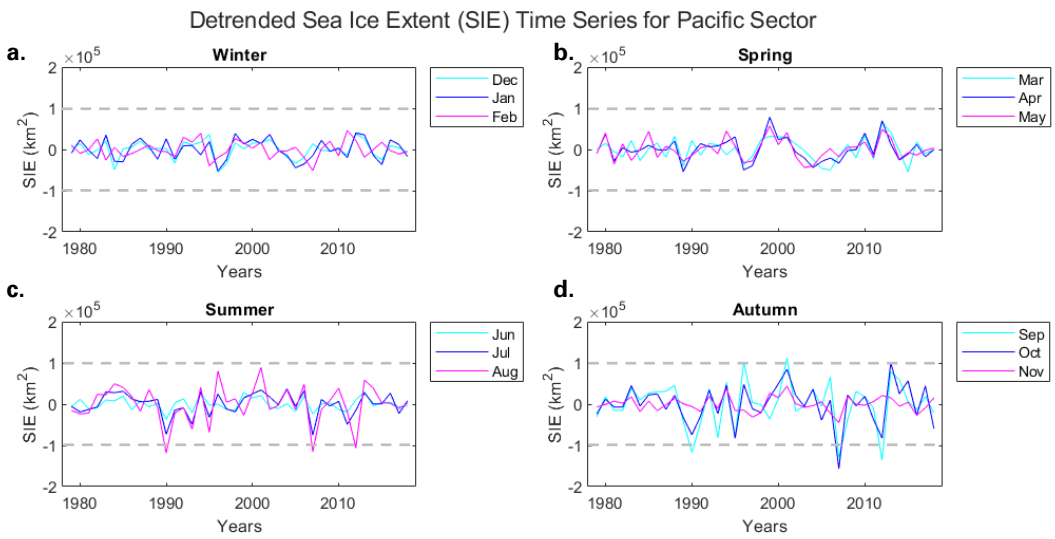

Figure 9. Detrended SIE time series plots are shown for the Pacific sector for a) winter (DJF), b) spring (MAM), c) summer (JJA), and d) autumn (SON). Monthly values were averaged across all 7 marginal seas (Beaufort Sea, Bering Sea, Central Arctic, Chukchi Sea, East Siberian Sea, Laptev Sea, and Sea of Okhotsk).

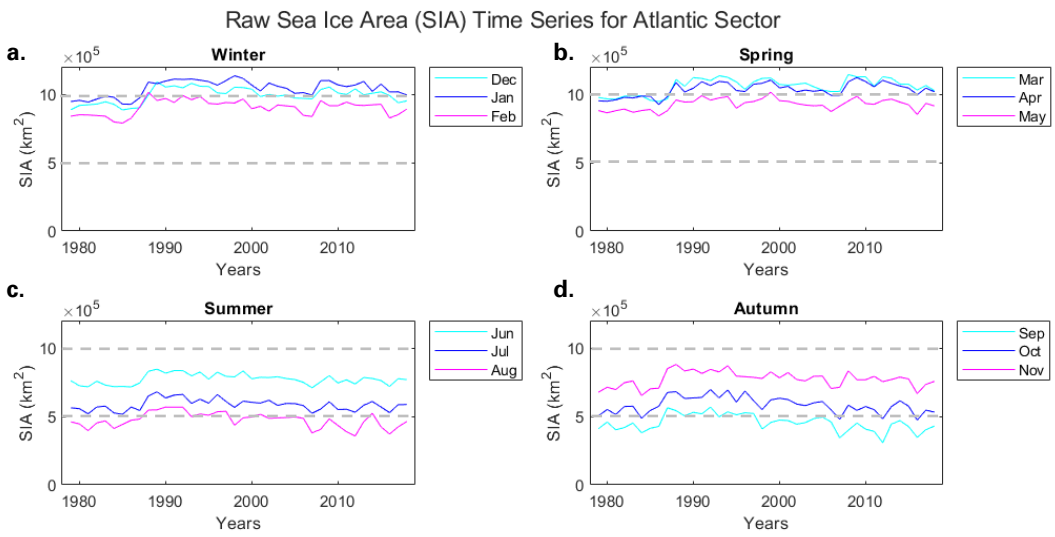

Figure 10. Raw SIA time series plots are shown for the Atlantic sector for a) winter (DJF), b) spring (MAM), c) summer (JJA), and d) autumn (SON). Monthly values were averaged across all 7 marginal seas (Baffin Bay, Barents Sea, Canadian Archipelago, Greenland Sea, Hudson Bay, Kara Sea, and Gulf of St. Lawrence).

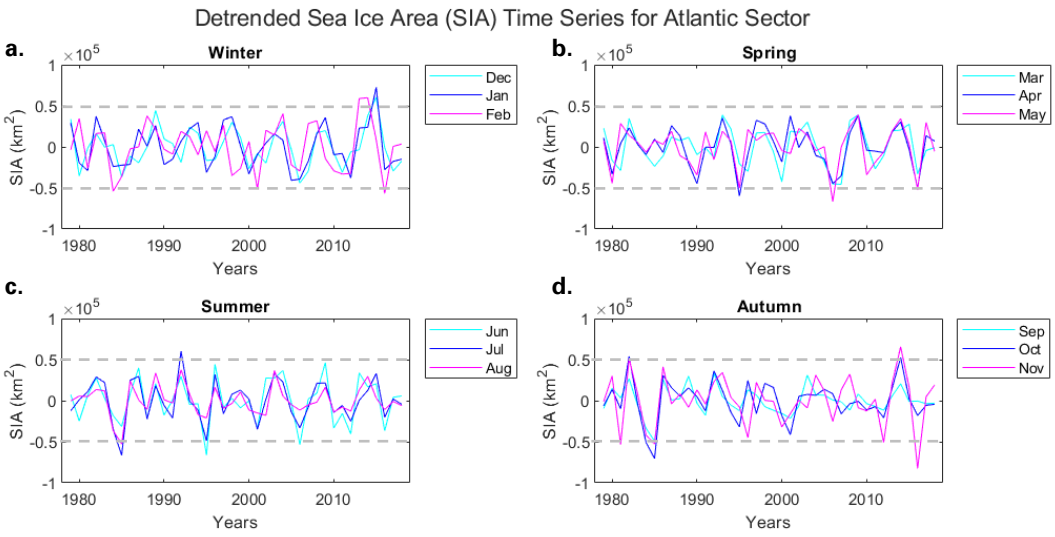

Figure 11. Detrended SIA time series plots are shown for the Atlantic sector for a) winter (DJF), b) spring (MAM), c) summer (JJA), and d) autumn (SON). Monthly values were averaged across all 7 marginal seas (Baffin Bay, Barents Sea, Canadian Archipelago, Greenland Sea, Hudson Bay, Kara Sea, and Gulf of St. Lawrence).

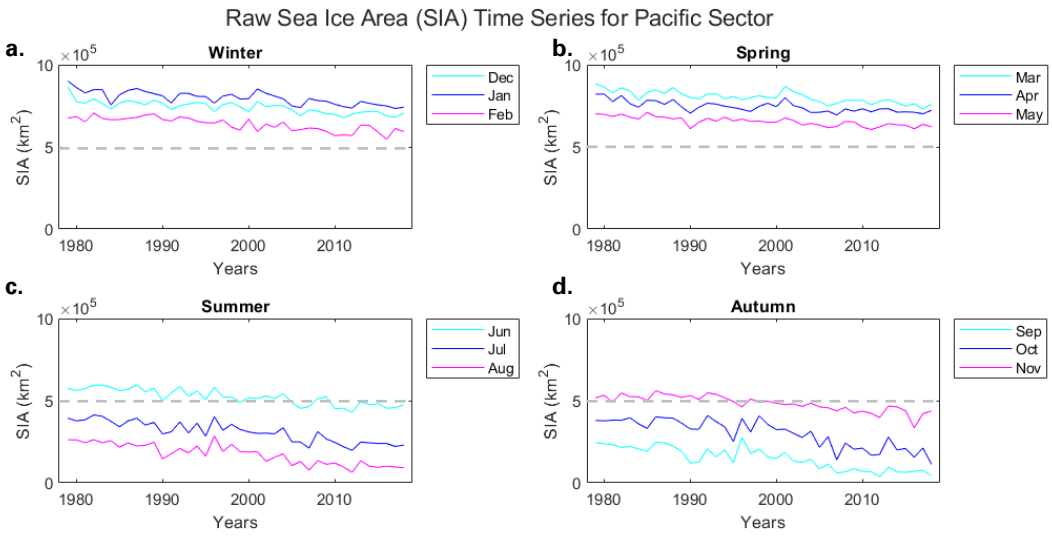

Figure 12. Raw SIA time series plots are shown for the Pacific sector for a) winter (DJF), b) spring (MAM), c) summer (JJA), and d) autumn (SON). Monthly values were averaged across all 7 marginal seas (Beaufort Sea, Bering Sea, Central Arctic, Chukchi Sea, East Siberian Sea, Laptev Sea, and Sea of Okhotsk).

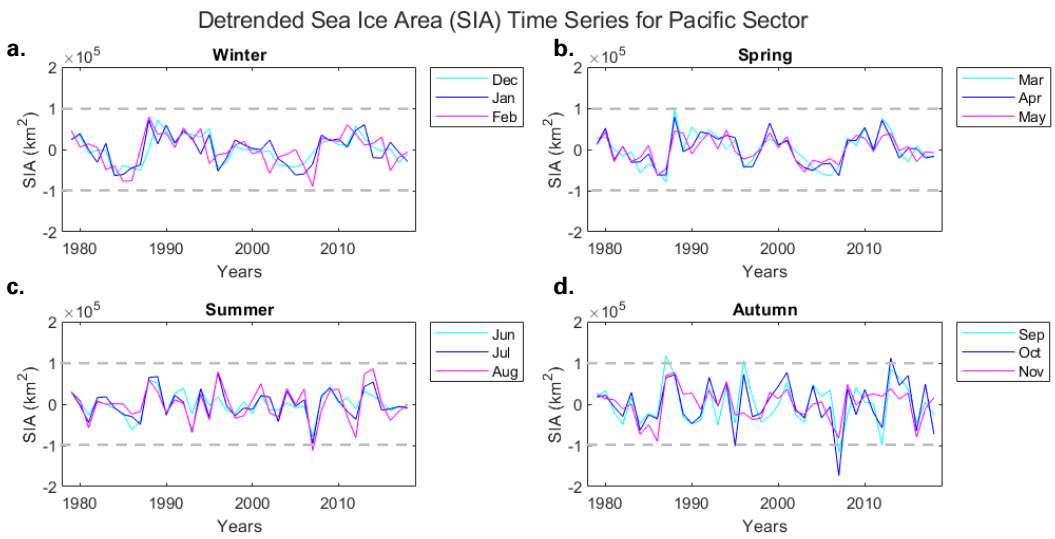

Figure 13. Detrended SIA time series plots are shown for the Pacific sector for a) winter (DJF), b) spring (MAM), c) summer (JJA), and d) autumn (SON). Monthly values were averaged across all 7 marginal seas (Beaufort Sea, Bering Sea, Central Arctic, Chukchi Sea, East Siberian Sea, Laptev Sea, and Sea of Okhotsk).

Figure 14. Correlation results for SIE against GBI at 3 month lag (a-n). The dash-dot lines represent the significance threshold, +/-0.223, (at a 95% confidence level; $p \leq 0.05$) for the Kendall's Tau test using n-2 degrees of freedom (n=40).

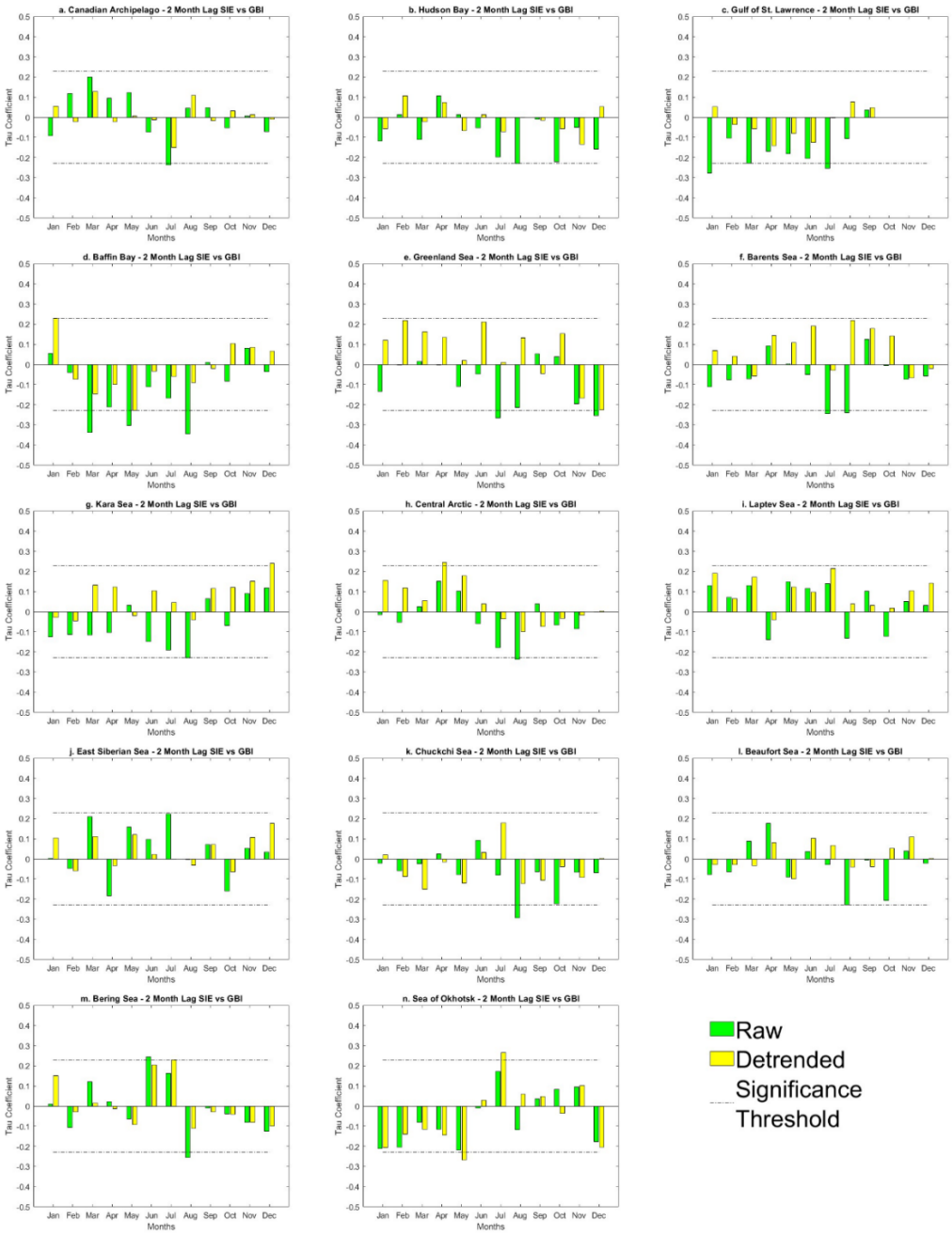

Figure 15. Correlation results for SIE against GBI at 2 month lag (a-n). The dash-dot lines represent the significance threshold, +/-0.223, (at a 95% confidence level; $p \leq 0.05$) for the Kendall's Tau test using n-2 degrees of freedom (n=40).

Figure 16. Correlation results for SIE against GBI at 1 month lag (a-n). The dash-dot lines represent the significance threshold, +/-0.223, (at a 95% confidence level; $p \leq 0.05$) for the Kendall's Tau test using n-2 degrees of freedom (n=40).

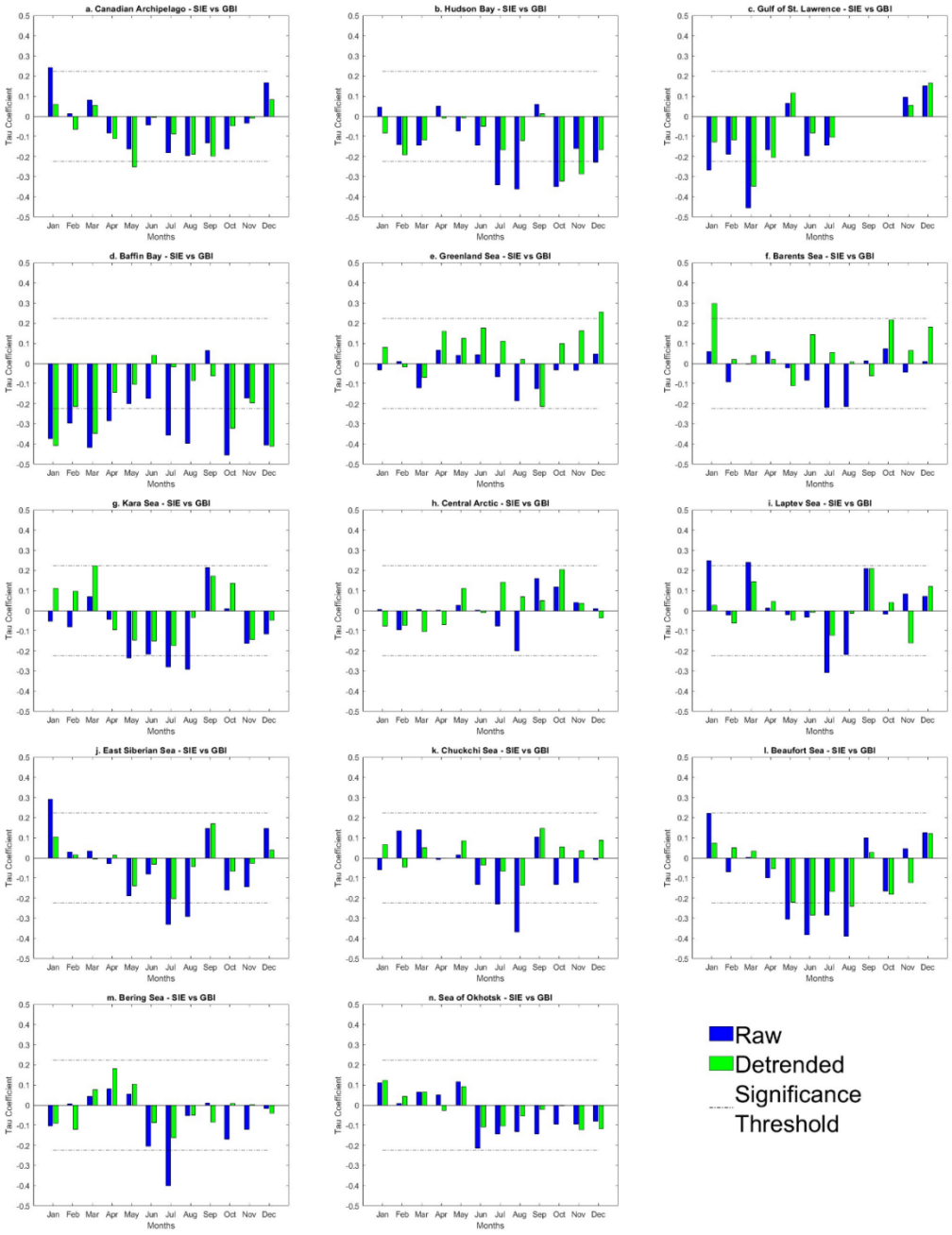

Figure 17. Correlation results for contemporary SIE against GBI (a-n). The dash-dot lines represent the significance threshold, +/-0.223, (at a 95% confidence level; $p \leq 0.05$) for the Kendall's Tau test using n-2 degrees of freedom (n=40).

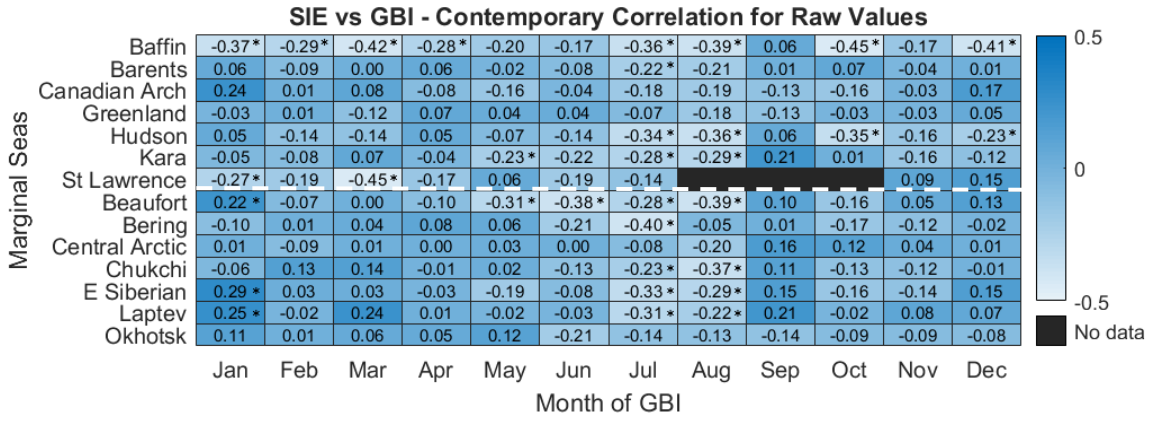

Figure 18. Heatmap showing contemporary monthly correlation coefficients for raw SIE versus GBI. SSV are denoted with an asterisk where p≤0.05. The dashed white line divides Atlantic (top) and Pacific (bottom) sectors.

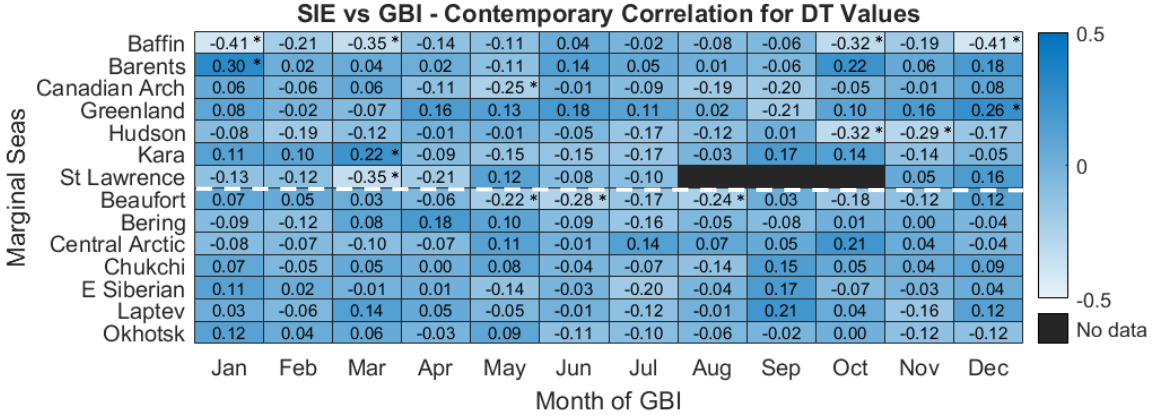

Figure 19. Heatmap showing contemporary monthly correlation coefficients for detrended SIE versus GBI. SSV are denoted with an asterisk where p≤0.05. The dashed white line divides Atlantic (top) and Pacific (bottom) sectors.

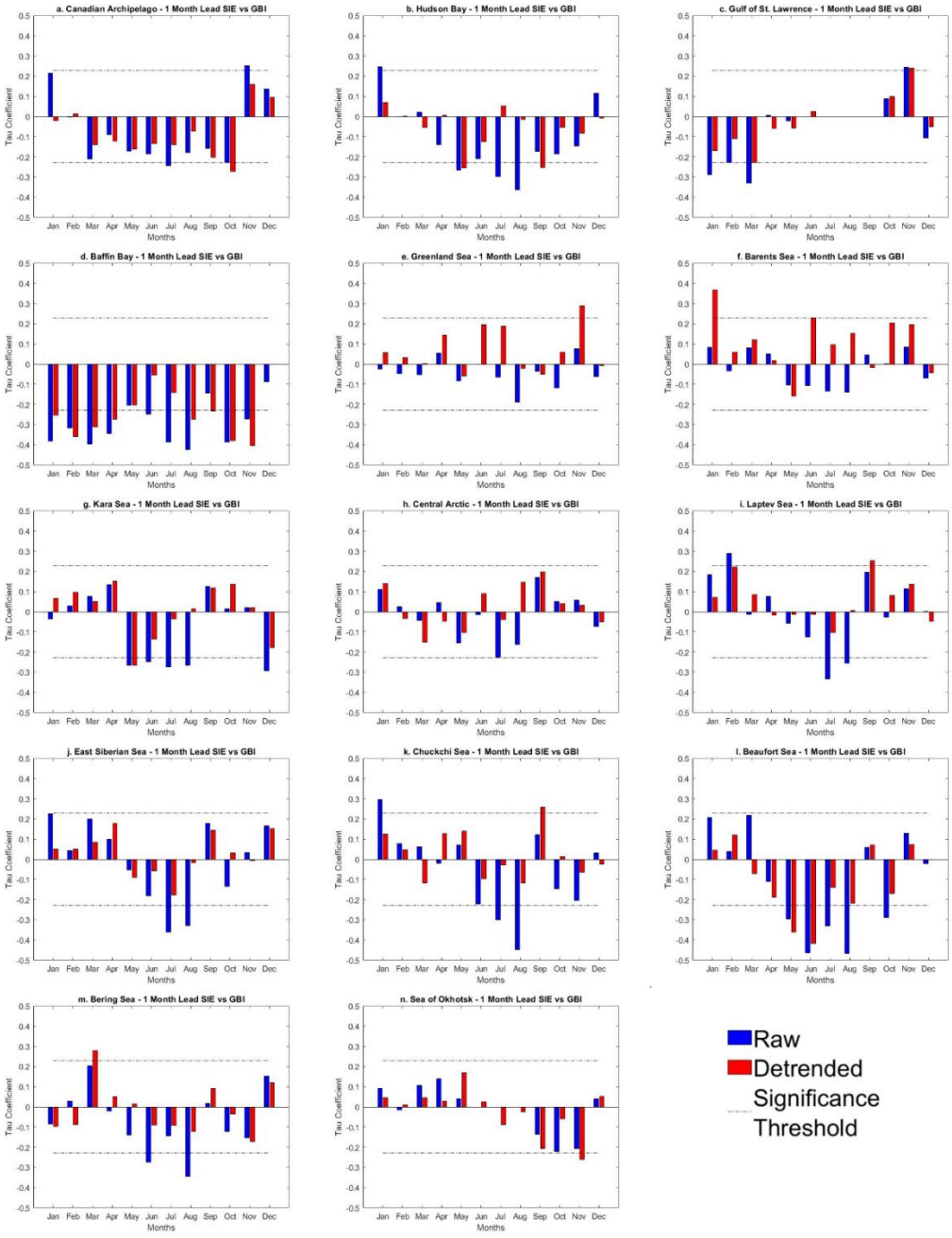

Figure 20. Correlation results for SIE against GBI at 1 month lead (a-n). The dash-dot lines represent the significance threshold, +/-0.223, (at a 95% confidence level; $p \leq 0.05$) for the Kendall's Tau test using n-2 degrees of freedom (n=40).

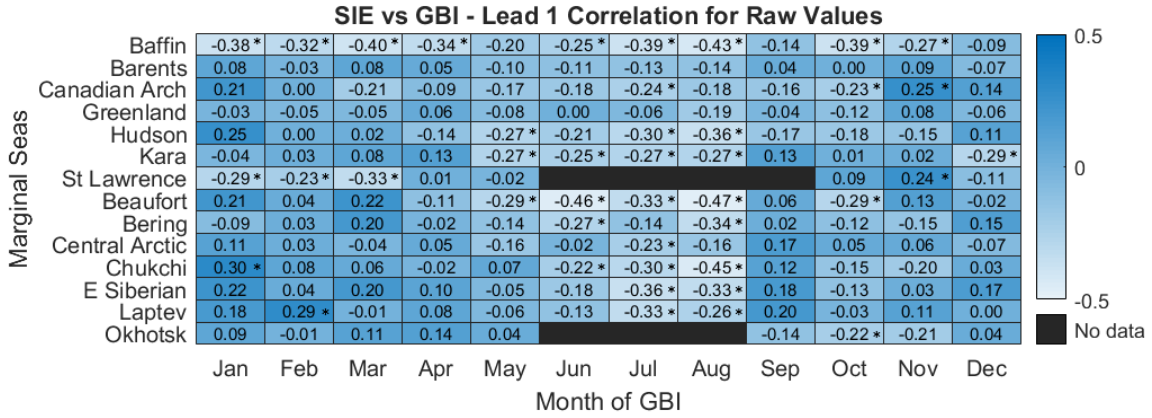

Figure 21. Heatmap showing all correlation coefficients for SIE versus GBI at lead-1 for raw values. SSV are denoted with an asterisk where p≤0.05. The dashed white line divides Atlantic (top) and Pacific (bottom) sectors.

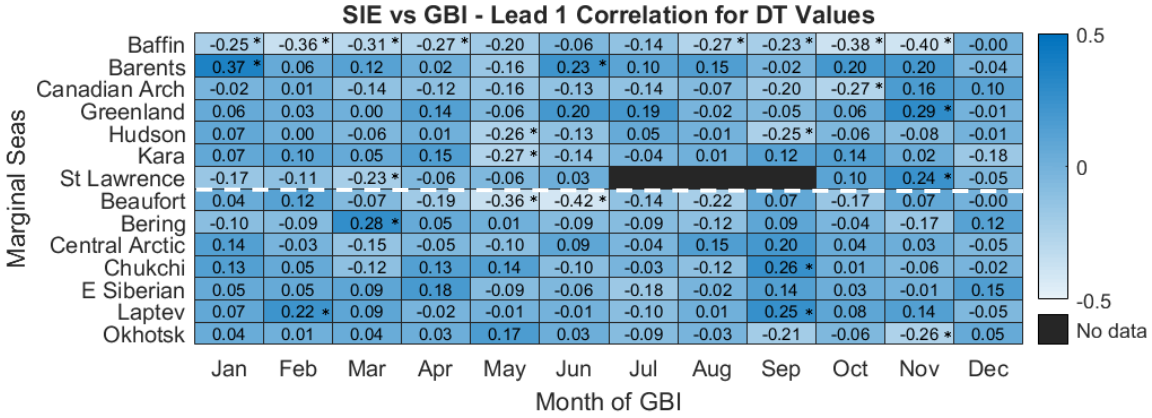

Figure 22. Heatmap showing all correlation coefficients for SIE versus GBI at lead-1 for detrended values. SSV are denoted with an asterisk where p≤0.05. The dashed white line divides Atlantic (top) and Pacific (bottom) sectors.

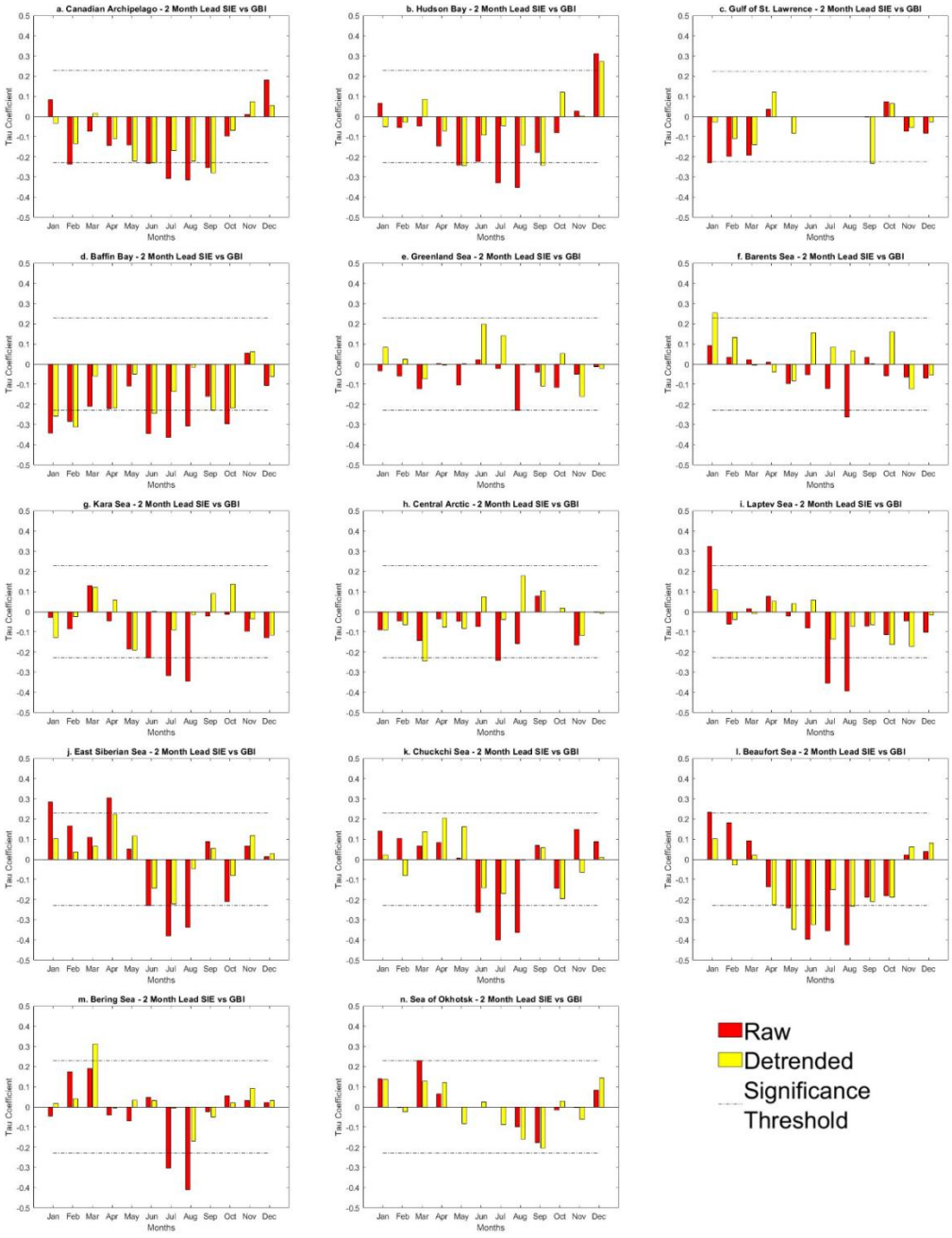

Figure 23. Correlation results for SIE against GBI at 2 month lead (a-n). The dash-dot lines represent the significance threshold, +/-0.223, (at a 95% confidence level; $p \leq 0.05$) for the Kendall's Tau test using n-2 degrees of freedom (n=40).

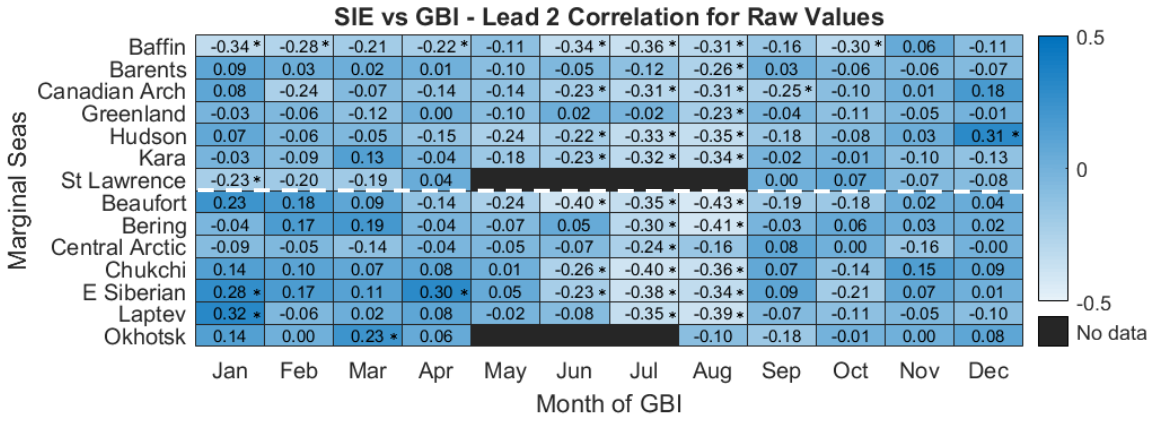

Figure 24. Heatmap showing all correlation coefficients for SIE versus GBI at lead-2 for raw values. SSV are denoted with an asterisk where p≤0.05. The dashed white line divides Atlantic (top) and Pacific (bottom) sectors.

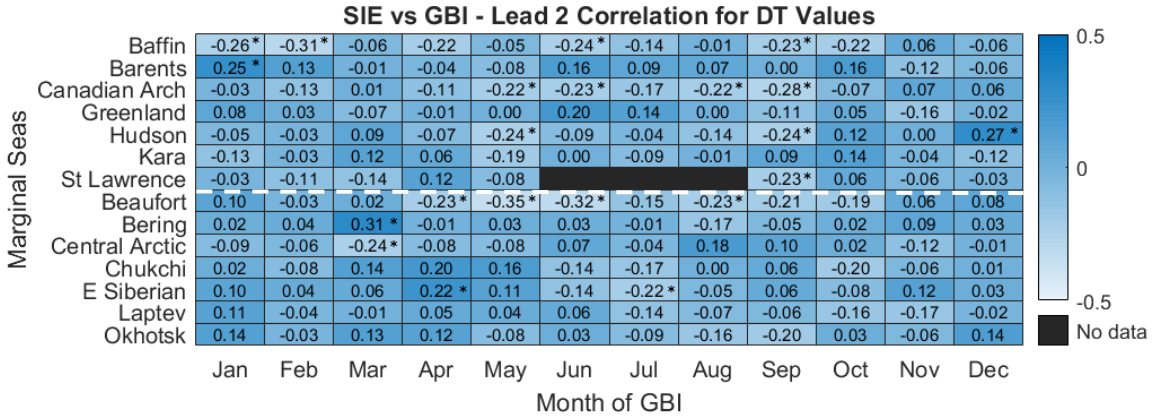

Figure 25. Heatmap showing all correlation coefficients for SIE versus GBI at lead-2 for detrended values. SSV are denoted with an asterisk where p≤0.05. The dashed white line divides Atlantic (top) and Pacific (bottom) sectors.

Figure 26. Correlation results for SIE against GBI at 3 month lead (a-n). The dash-dot lines represent the significance threshold, +/-0.223, (at a 95% confidence level; $p \leq 0.05$) for the Kendall's Tau test using n-2 degrees of freedom (n=40).

Figure 27. Correlation results for SIA against GBI at 3 month lag (a-n). The dash-dot lines represent the significance threshold, +/-0.223, (at a 95% confidence level; $p \leq 0.05$) for the Kendall's Tau test using n-2 degrees of freedom (n=40).

Figure 28. Correlation results for SIA against GBI at 2 month lag (a-n). The dash-dot lines represent the significance threshold, +/-0.223, (at a 95% confidence level; $p \leq 0.05$) for the Kendall's Tau test using n-2 degrees of freedom (n=40).

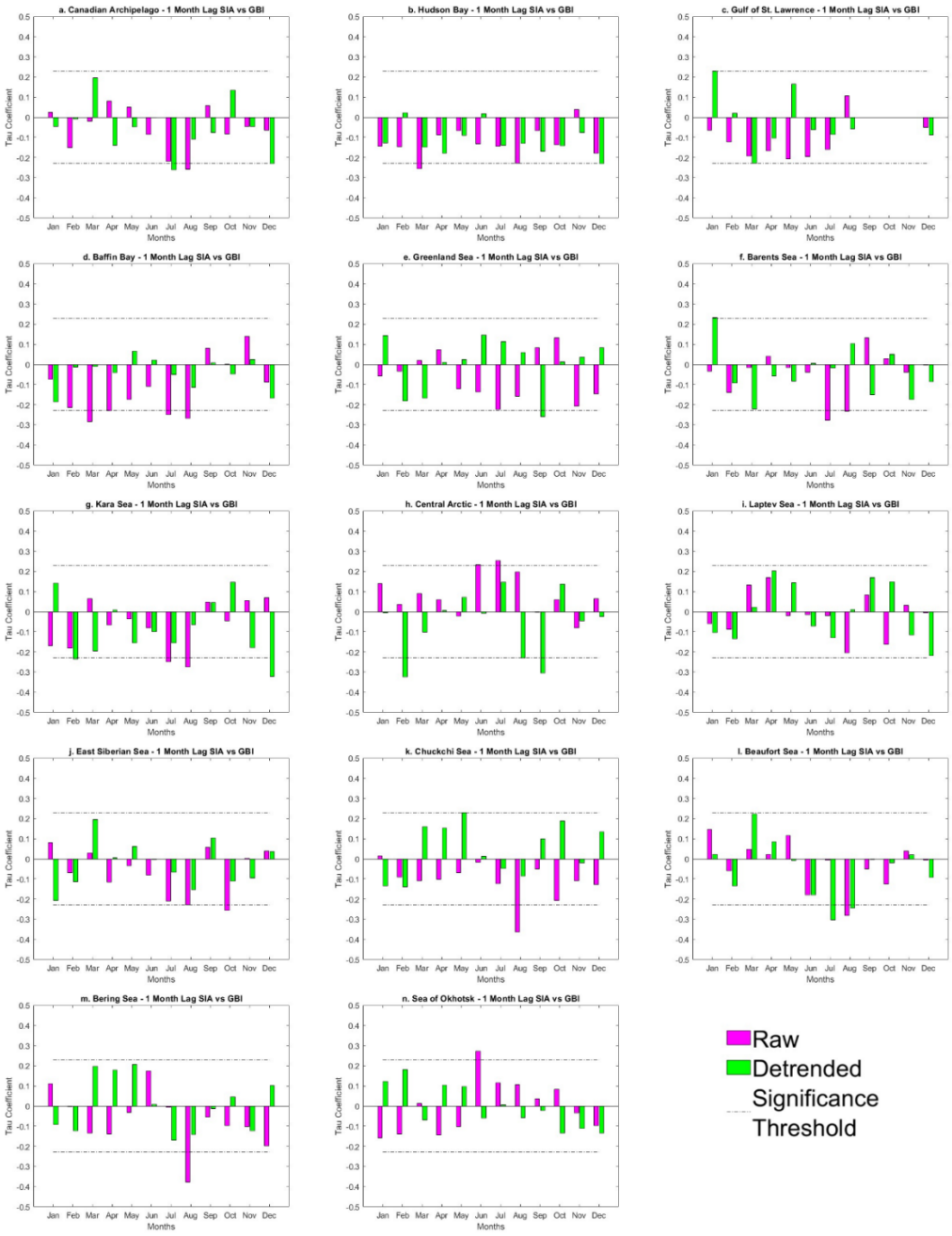

Figure 29. Correlation results for SIA against GBI at 1 month lag (a-n). The dash-dot lines represent the significance threshold, +/-0.223, (at a 95% confidence level; $p \leq 0.05$) for the Kendall's Tau test using n-2 degrees of freedom (n=40).

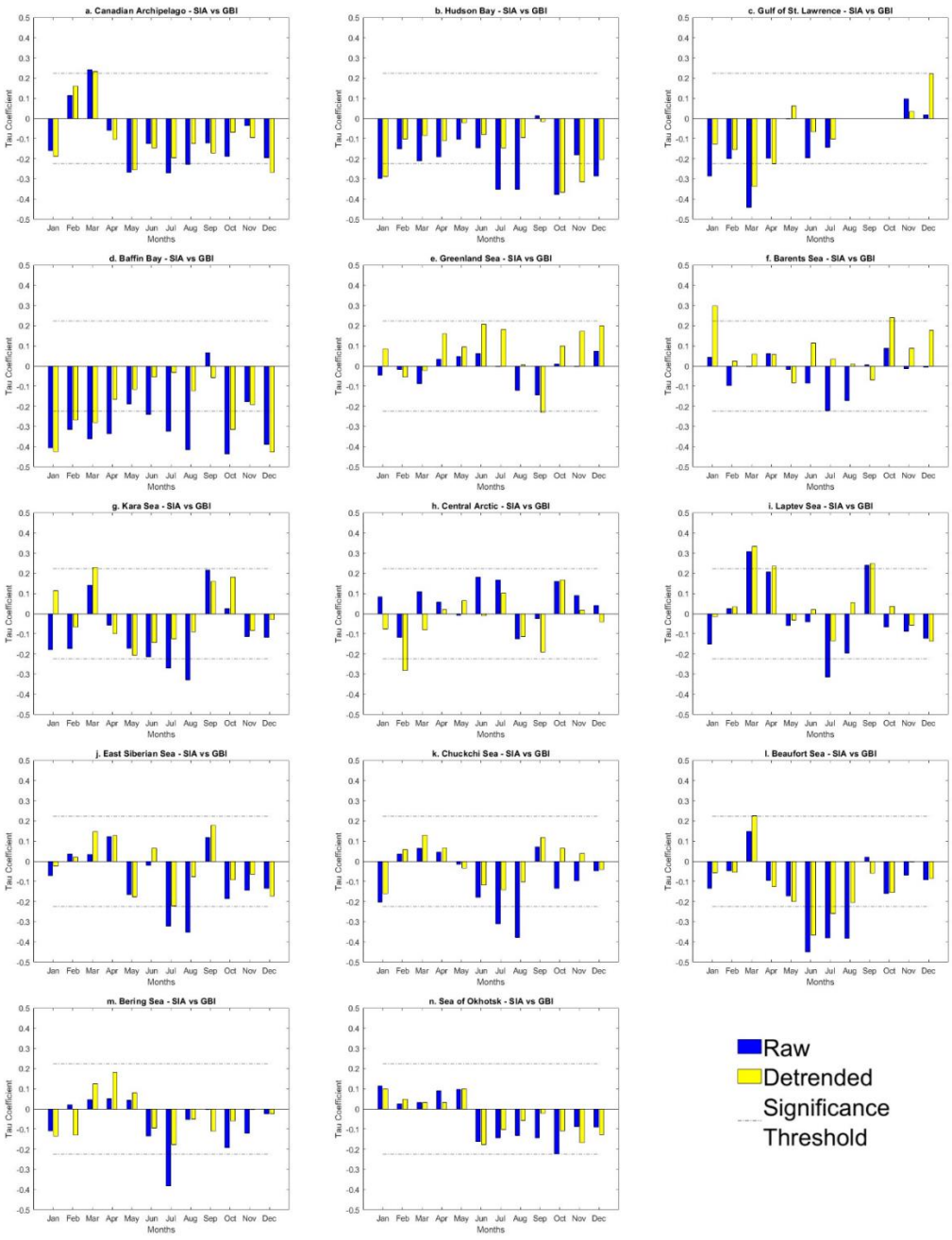

Figure 30. Correlation results for contemporary SIA against GBI (a-n). The dash-dot lines represent the significance threshold, +/-0.223, (at a 95% confidence level; $p \leq 0.05$) for the Kendall's Tau test using n-2 degrees of freedom (n=40).

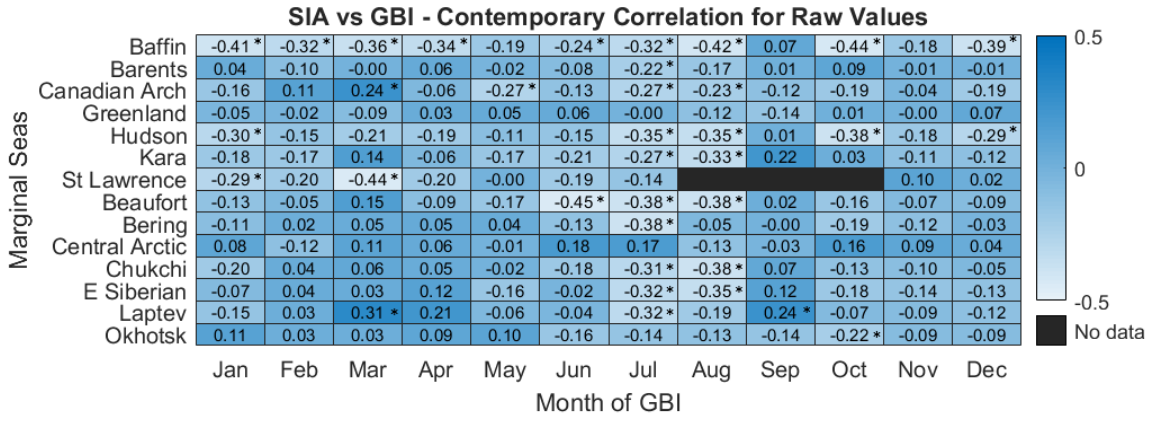

Figure 31. Heatmap showing contemporary monthly correlation coefficients for raw SIA versus GBI. SSV are denoted with an asterisk where p≤0.05. The dashed white line divides Atlantic (top) and Pacific (bottom) sectors.

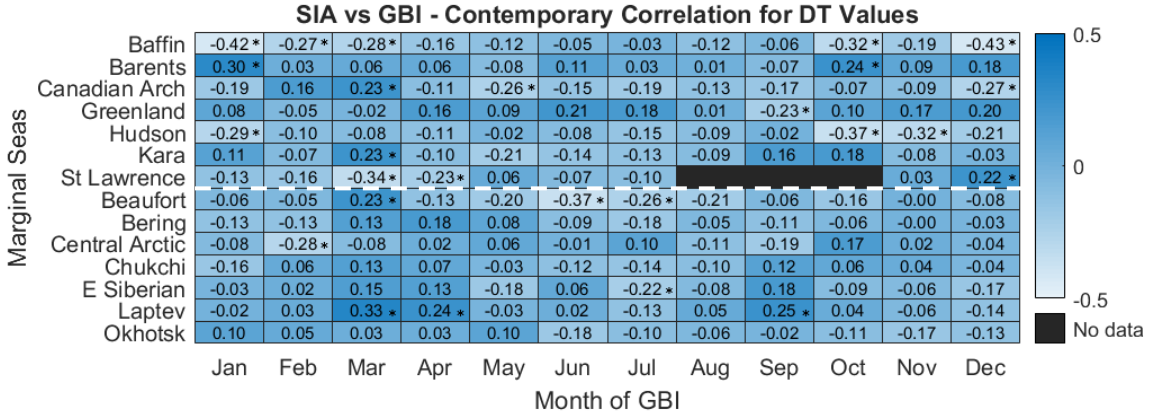

Figure 32. Heatmap showing contemporary monthly correlation coefficients for detrended SIA versus GBI. SSV are denoted with an asterisk where p≤0.05. The dashed white line divides Atlantic (top) and Pacific (bottom) sectors.

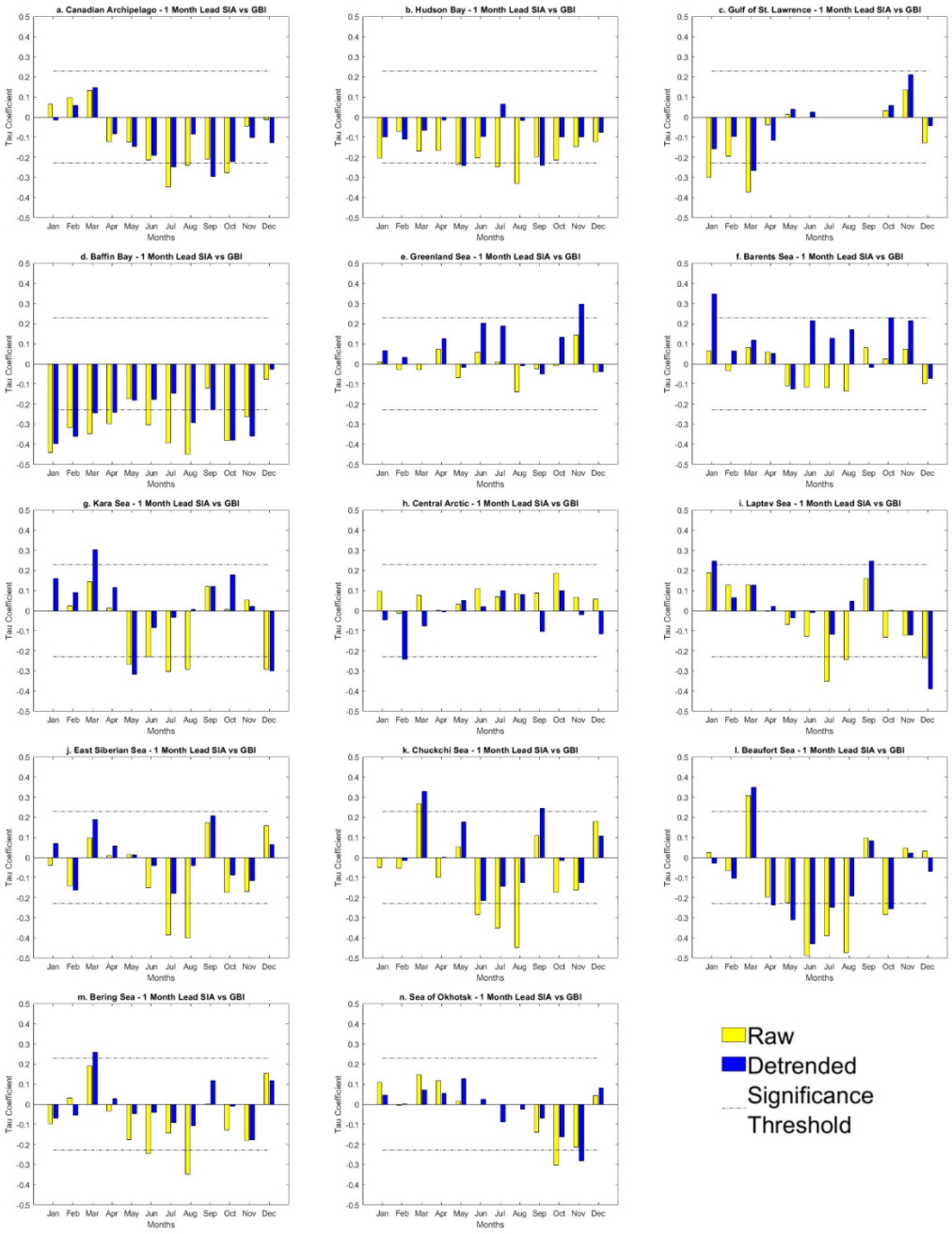

Figure 33. Correlation results for SIA against GBI at 1 month lead (a-n). The dash-dot lines represent the significance threshold, +/-0.223, (at a 95% confidence level; $p \leq 0.05$) for the Kendall's Tau test using n-2 degrees of freedom (n=40).

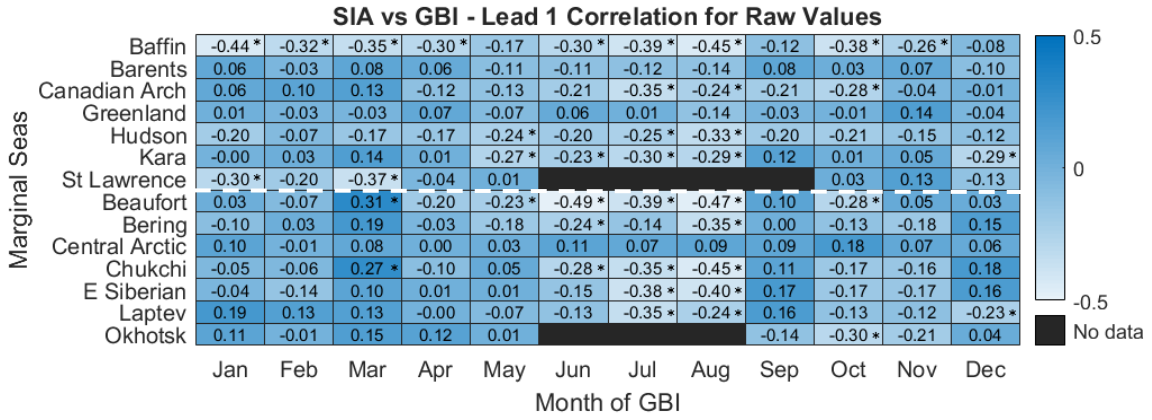

Figure 34. Heatmap showing all correlation coefficients for SIA versus GBI at lead-1 for raw values. SSV are denoted with an asterisk where p≤0.05. The dashed white line divides Atlantic (top) and Pacific (bottom) sectors.

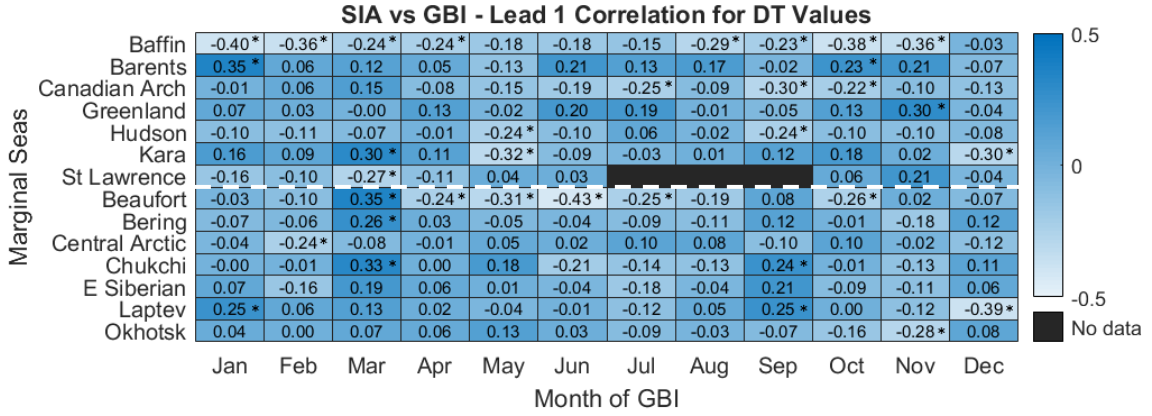

Figure 35. Heatmap showing all correlation coefficients for SIA versus GBI at lead-1 for detrended values. SSV are denoted with an asterisk where p≤0.05. The dashed white line divides Atlantic (top) and Pacific (bottom) sectors.

Figure 36. Correlation results for SIA against GBI at 2 month lead (a-n). The dash-dot lines represent the significance threshold, +/-0.223, (at a 95% confidence level; $p \leq 0.05$) for the Kendall's Tau test using n-2 degrees of freedom (n=40).

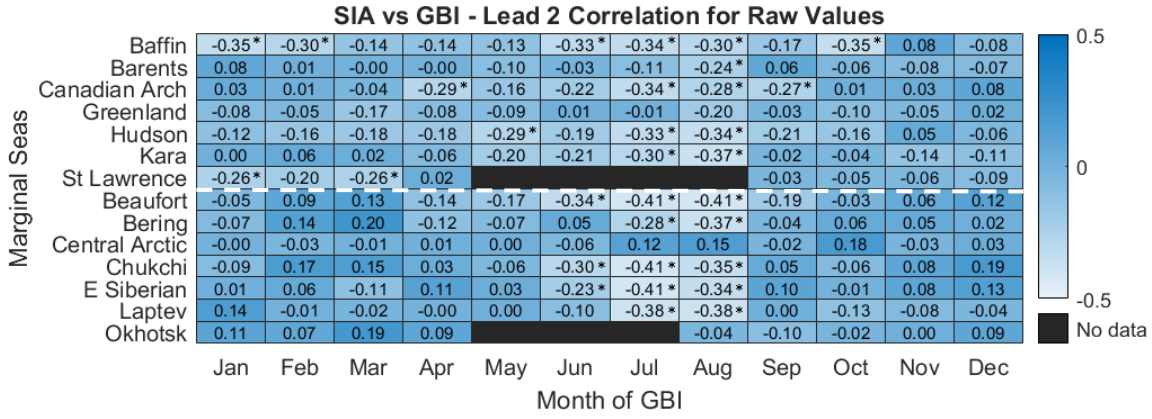

Figure 37. Heatmap showing all correlation coefficients for SIA versus GBI at lead-2 for raw values. SSV are denoted with an asterisk where p≤0.05. The dashed white line divides Atlantic (top) and Pacific (bottom) sectors.

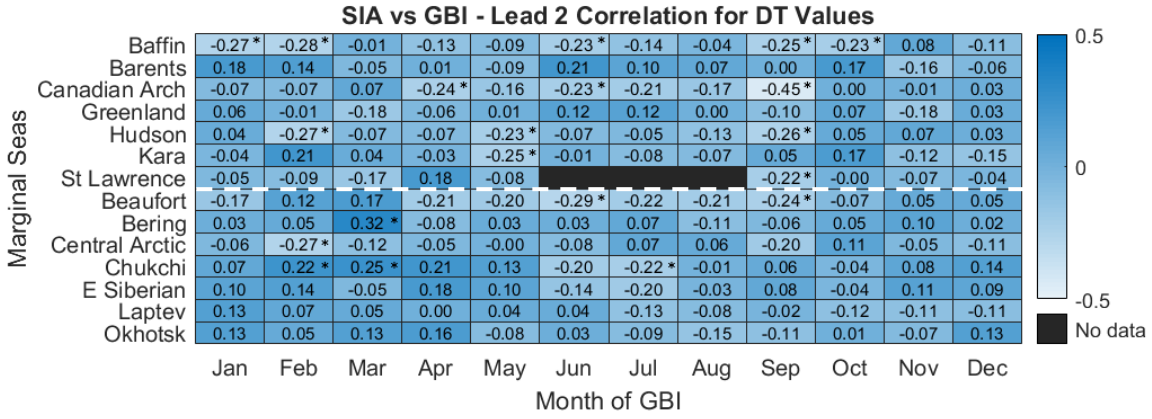

Figure 38. Heatmap showing all correlation coefficients for SIA versus GBI at lead-2 for detrended values. SSV are denoted with an asterisk where p≤0.05. The dashed white line divides Atlantic (top) and Pacific (bottom) sectors.

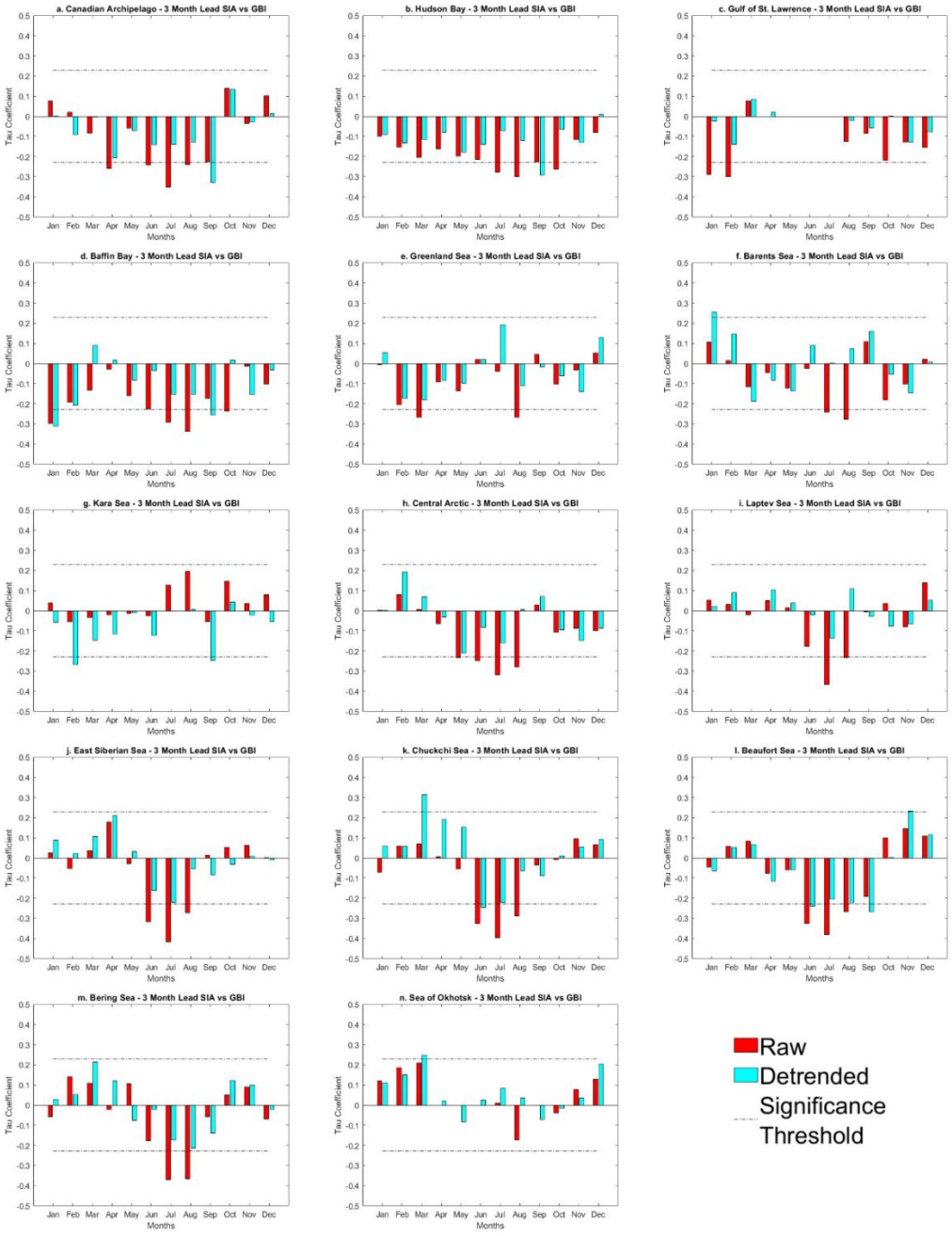

Figure 39. Correlation results for SIA against GBI at 3 month lead (a-n). The dash-dot lines represent the significance threshold, +/-0.223, (at a 95% confidence level; $p \leq 0.05$) for the Kendall's Tau test using n-2 degrees of freedom (n=40)

6. RESULTS PART 2: MONTHLY COMPOSITE ANALYSIS

6.1 INITIAL PROCESSING

As shown in the results of Chapter 5, there are a few marginal seas wherein ice conditions are significantly correlated (in raw and detrended analyses) with GBI across multiple months. To extend results in Chapter 6, focus is placed on the raw sea ice data for Baffin Bay and the Beaufort Sea where the strongest monthly, correlative relationships with GBI were found. These associations were further investigated to reveal the atmospheric response to extreme sea ice and GBI conditions over NA. The ten highest (lowest) and lowest Baffin and Beaufort monthly SIE and GBI lowest (highest) values (and their associated years) were ranked and compared since these variables tend to be anti-correlated, as evident from the consistent negative correlation coefficients produced. From these, common years are identified to create contemporary composite maps, then lead-1 and lead-2 composite maps for each marginal sea of interest (using the same years or jumping forward to the following year if the lead composites require). The month of May for the Beaufort Sea for the maximum SIE and minimum GBI produced a total of ten years of overlap, the most among all combinations, simply because many years reached the maximum SIE value for this marginal sea (~9.4×10^5 km^2).

Mean composite maps were created for each month using the 1981-2010 climatology for comparison with anomaly composite maps. The four atmospheric variables shown in the composite maps include 500mb geopotential height (GPH; hereafter 500GPH), mean sea level pressure (MSLP), 2m air temperature (T2m), and precipitable water (PW). Both the climatology and anomaly composite maps for each of these four atmospheric variables reveal a snapshot of the North American (NA)

atmospheric circulation, air temperature, and moisture response to regional sea ice-atmosphere anomalies. Each monthly figure included climatology composites and anomaly composites side by side for each of the variables of interest. For example, for the contemporary analyses, **Figure 40** shows Baffin Bay's January maximum SIE composites for 500GPH with climatology (**Figure 40a**) and anomaly (**Figure 40b**) on the first row, the composites for MSLP with climatology (**Figure 40c**) and anomaly (**Figure 40d**) on the second row, the composites for January T2m climatology (**Figure 40**e) and anomaly (**Figure 40f**) on the third row, and PW climatology (**Figure 40g**) and anomaly (**Figure 40h**) on the fourth row. For lead-1 and lead-2 composites, the same method was employed using the same years from the contemporary composites, only these account for one and two months ahead of the contemporary month.

Further exploration of SIE and SIA correlation analyses indicated that there was substantial overlap of statistically significant monthly correlations produced between the raw SIE and raw SIA data. For example, it was found that in comparing all raw correlation analyses for SIE against those correlations for SIA, 79% of the monthly SSV matched. In this case a match does not indicate that the values are an exact numerical match, but rather that each variable produced a correlation coefficient for the same month that meets or exceeds the significance threshold. In other words, SIE and SIA extremes tend to overlap in time. As a result, only the raw SIE data were analyzed in the composite analyses in tandem with the GBI values.

6.2 BAFFIN BAY

6.2.1 MAXIMUM SIE VERSUS MINIMUM GBI

6.2.1.1 CONTEMPORARY ANALYSIS

The contemporary analysis focuses on the months of January, March, October, and December for the Baffin Bay based on strong associations between GBI and SIE in those months. **Table 6** shows the top 10 maximum SIE and minimum GBI years (both ranked highest to lowest) for each month, with years of overlap highlighted. This maximum SIE-minimum GBI combination yielded six years of overlap for January, four common years for March, five common years for October, and six overlapping years for December. It is acknowledged that more total overlapping years, and therefore larger sample sizes, are ideal in creating representative and robust atmospheric composites, though analyses were still performed even with relatively few overlapping cases.

In January composites (**Figure 40a-h**), the mean composite for 500GPH (**Figure 40a**) shows a strong gradient of atmospheric heights with lower heights toward the pole and higher heights toward the equator with a ridge over northwestern North America, trough over central Canada, and ridge over Greenland. The anomaly composite for 500GPH, **Figure 40b**, shows a large, negative height anomaly stretching from the southeast coast of Greenland into northeast Alaska (-100 m), with a slightly positive anomaly over the northeast US, and another very small positive anomaly off the southern coast of Alaska. Similar spatial patterns can be seen for MSLP in **Figure 40c** and **Figure 40d**. The mean composite in **Figure 40c** shows low MSLP centers off the southeast and southwest coasts of Greenland and Alaska, respectively. The anomaly composite in **Figure 40d** shows an extensive area of low MSLP throughout the Arctic region, dipping

into central Canada with the most anomalously negative area off the southeast coast of Greenland at -6 mb. This is accompanied with slightly positive and somewhat large areas of positive MSLP anomalies shown for eastern Canada and the northeast United States (US), as well as another area off southern Alaska. The T2m mean composites in **Figure 40e** again show a steep temperature gradient over the GrIS and between the snow-covered land in Nunavut and adjacent landfast ice, for instance, and open water in southern Baffin Bay and northern Labrador Sea. **Figure 40f** shows a large negative T2m anomaly, -9°C at its strongest, emanating from the west coast of Greenland outward, with only a few very weak and small positive anomalies in NA. Other much smaller and weaker negative anomalies are spread across central and western US and western Canada. **Figure 40g** shows the mean composite for PW, with very large areas of very low PW shown for much of the Arctic as well as Canada. The PW anomalies are shown in **Figure 40h** and most anomalies are found over bodies of water. The largest negative anomaly is shown around south Greenland (in the Atlantic Ocean), though some smaller negative anomalies appear off the western coast of the US. The largest positive anomalies are shown for the south Atlantic Ocean and Gulf of Mexico, reaching into parts of the southeastern US and into the mid-Atlantic Ocean.

Figure 41a-h shows contemporary composite maps for March. **Figure 41a** shows mean 500GPH with a weaker gradient, as compared to that of January, but still with negative GPH anomalies toward the northern pole and positive GPH anomalies toward the equator. In the anomaly 500GPH composite (**Figure 41b**), a large, closed negative anomaly is centered over south Greenland, indicating a low pressure cyclone. These low pressure cyclones are an important part of weather for this region because the

counterclockwise rotation acts to steer warm and moist air masses into the Arctic, which help to offset heat and moisture deficits produced by radiative and freshwater imbalances (Serreze 1988; Zhang et al 2004). At the surface level, low pressure centers are associated with rising air that contributes to the formation of clouds. Negative anomalies can be seen across much of the Arctic region with the 500GPH revealing a trough over Alaska, a ridge over the CAA indicating zonal atmospheric flow, and a trough over Greenland. Two very slightly positive GPH anomalies can be seen off the coast of the northeast US and off western Canada. **Figure 41c** shows the mean composite for MSLP, with the lowest MSLP areas found around southern Alaska and southeastern Greenland. The MSLP anomalies, in **Figure 41d**, closely match the configuration of the GPH anomalies. The strongest negative MSLP anomaly is found in southeast Greenland at -9 mb, but also in the high Arctic latitudes, and the largest positive anomaly is found south of the negative anomaly in the Atlantic Ocean, but only reaches +4 mb. In **Figure 41e**, a gradual T2m gradient can be seen in the mean composite, while **Figure 41f** shows its strongest negative anomaly center off the west coast of Greenland. The negative T2m anomaly encompasses much of Greenland and reaches into northern Canada and a small part of the Atlantic Ocean. Another weaker negative anomaly is shown off the northwestern coast of Alaska. A slightly positive T2m anomaly can be seen over northeast Canada, reaching into Alaska. The mean composite for PW is shown in **Figure 41g**, which again shows small amounts of moisture (<4 kg/m^2) north of the 60°N, but especially for the Canadian Archipelago (CAA). The anomaly map for PW (**Figure 41h**) shows a very slight negative anomaly area from the western coast of Greenland into the Atlantic Ocean. Several slightly positive anomaly areas are shown for a small portion of

northwest Canada into central Alaska, and another off the southern coast of Alaska, though the largest areas of positive PW anomalies are seen extending equatorward of 30°N. The positive anomaly reaches from the southern Atlantic Ocean and Gulf of Mexico into much of the southern and eastern US.

Within **Figure 42a-h**, are the contemporary composites for the month of October. Beginning with the mean 500GPH composite **(Figure 42a**), the lowest line of GPH (5200 m) is above the 80°N latitude line, and the highest GPH line (5800 m), is up well past the 30°N latitude line. The 500GPH anomaly composite map in **Figure 42b** shows a substantial area of negative GPH with a local minima of -70 m around western Greenland. The closed, negative anomaly in the 500GPH field is indicative of a low pressure system, which is surrounded by closely spaced isohypses indicative of strong winds. Two positive anomaly areas can be seen south of the extensive negative anomaly field, one off the eastern coast of Canada and the other over western Canada and a portion of the western US. Another slightly negative 500GPH anomaly can be seen off the western coast of the US, in the Pacific Ocean. The 500GPH anomaly reveals a ridge over northwestern NA and a trough over northeastern Canada. The anomaly appears to transition from meridional to more zonal atmospheric flow. **Figure 42c** shows the mean composite for MSLP, again with two low MSLP regions located around southern Alaska and southeast of Greenland. The MSLP anomaly map in **Figure 42d** produced a large area of slightly negative anomaly which covers all of Greenland with the most intensely negative portion covering western portion of the island at -5 mb, but also extends north and eastward. The negative anomaly covers much of the Arctic north of 80°N as well. There are also several positive though mostly weak MSLP anomalies on the map. Three

large areas can be seen, including one over northern Canada, one on the western coast of Canada, and the other stretching across much of the central NA continent. The largest positive anomaly, however, is situated far out into the Atlantic Ocean south of the large negative anomaly, but it is not very strong. **Figure 42e** gives the mean composite map for T2m, showing overall warmer temperatures for the NA continent. **Figure 42f** shows T2m anomalies, with a substantial negative anomaly covering much of the Arctic, with the strongest area (-4°C) situated over the CAA. The negative anomaly also extends southward across a slim portion of the NA continent. Some very slight positive T2m anomalies also appear covering small areas throughout western NA continent. The PW climatology map in **Figure 42g** shows slightly positive PW gradients south of 30°N. The PW anomaly map in **Figure 42h** shows a large area of negative anomaly reaching from northern Canada into the southern US, where the most intensely negative anomaly can be found at -3.5 kg/m^2. Positive anomalies are found on either side of the negative anomaly, one in the Atlantic Ocean and the other in the western US into the Pacific Ocean (+4 kg/m^2 at its strongest), and another slight negative anomaly can be seen far off into the Pacific Ocean.

The contemporary composite maps for December can be seen in **Figure 43a-h**. The mean 500GPH composite is shown in **Figure 43a**. The 500GPH anomaly composite (**Figure 43b**) shows an extensive negative anomaly across much of the Arctic with the strongest area (-80 m) centered over a portion of southwest Greenland and the CAA. There is also a large positive anomaly situated over the eastern portions of Canada and the US with the strongest center (+80 m) over the northeastern US. Two other very slight anomalies are present, one negative over a portion of the southwestern US and the other

positive out in the Pacific Ocean, off the southern coast of Alaska. The 500GPH anomalies reveal only slight ridges and troughs over NA with zonal flow over much of the continent. The climatology composite for MSLP (**Figure 43c**) once again shows low MSLP centers for southern Alaska and Greenland. The anomaly map (**Figure 43d**) closely resembles the anomaly 500GPH map with negative anomaly areas reaching across the Arctic. The strongest negative MSLP anomalies are shown off southeastern Greenland and southwestern Alaska at -6 m. The strongest positive anomaly is shown south of the negative anomaly center at the very tip of eastern Canada coast (at +5 mb), but extends across much of eastern Canada and US, and eastward across the Atlantic Ocean. Another positive anomaly appears in the Pacific Ocean, also south of a negative anomaly. The T2m composite map (**Figure 43e**) shows a strong temperature gradient with the lowest temperatures over Greenland and parts of the CAA. The T2m anomaly composite (**Figure 43f**) once again shows widespread negative anomalies over much of northern Canada (-4°C) and parts of Alaska. The strongest positive anomaly (+4°C) can be seen over eastern US, but the anomaly also reaches into the central US and Canada. Other slightly positive anomalies appear over southern Alaska and off the eastern coast of Greenland. **Figure 43g** shows the climatology for PW, with much of the Arctic and northern Canada with very low PW at 4 kg/m^2. The PW anomaly map (**Figure 43h**) shows a large though only slightly negative anomaly for the south and west coasts of Greenland and parts of northern Canada. The positive anomaly (+3.5 kg/m^2) is much larger and reaches well across the southern, eastern and central parts of the US into parts of eastern and central Canada.

6.2.1.2 LEAD-1 ANALYSIS

Regarding lead-1 composites, **Figure 44a-h** shows composite maps for February (one month ahead of the contemporary month of January). **Figure 44a** shows 500GPH climatology and **Figure 44b** shows the anomalies. Several areas of negative anomalies appear off the southwestern coast of Alaska and western coast of Greenland. Both anomalies appear to have a closed low pressure system at their center. They, along with a few smaller negative anomalies, surround a positive anomaly reaching from western Canada into the Atlantic Ocean, where the strongest positive anomaly is situated. The 500GPH reveals a very low trough over southern Alaska, then a very slight ridge over western Canada, and another slight ridge over eastern Canada; the atmospheric flow appears more meridional over western NA and more zonal over eastern NA. The MSLP composite map (**Figure 44c**) shows two repeated areas of the lowest regions of MSLP off the southwestern coast of Alaska and the southeastern coast of Greenland, similar to the results of the contemporary analysis. The anomaly MSLP map (**Figure 44d**) shows a large negative anomaly covering much of the Arctic and parts of northern Canada. The strongest negative anomaly, however, resides off the coast of southwestern Alaska at -6 m, and part of the largest positive anomaly (+3 m) reaches from the Atlantic Ocean into eastern Canada. The T2m climatology (**Figure 44e**) shows the coldest temperatures for Greenland and parts of the CAA, though mild temperatures are shown for all of NA. The anomaly T2m map (**Figure 44f**) shows the strongest negative anomaly off the western coast of Greenland, which reaches across Canada and into Alaska. Small spots of positive anomalies are shown off the coast of northeast Greenland, north of the CAA, and for central and western Canada. **Figure 44g** shows the climatology for PW and **Figure 44h**

shows the PW anomalies. There are several PW anomalies, mostly over coastal areas. Negative PW anomalies appear over off the southwestern coast of Greenland, reaching into northeastern Canada; over much of the southern US and a small portion of southwestern US; over western Alaska, reaching into the Pacific Ocean; and lastly, the strongest negative appears in the Pacific Ocean over Hawai'i (-1.6 kg/m^2). Two positive anomalies are shown off of both the eastern and western coasts of Canada, though they extend on to small portions of Canada as well, but the strongest positive anomaly is shown off the southern coast of the US (+2.4 kg/m^2), which extends out into the Atlantic Ocean.

The composites for April are shown in **Figure 45a-h** (one month ahead of the contemporary month of March). Within the 500GPH climatology composite (**Figure 45a**), the highest GPH heights are located north of 70°N. The anomaly map (**Figure 45b**) reveals a large negative anomaly with its center just northeast of the Hudson Bay (-80 m), which extends further north into the high Arctic and south into central Canada and a small portion of the northern US, but also eastward across Greenland into the Atlantic Ocean. Two positive anomaly areas are shown, one off the eastern coast of the US and Canada, and the other reaching from the Bering Sea and encompassing nearly all of Alaska. Another slight negative anomaly appears in the Pacific Ocean, south of the positive Alaska anomaly. This 50GPH anomaly map reveals an atmospheric ridge over Alaska, which transitioned into a deep trough over much of Canada with meridional flow, and another slight ridge over the Atlantic Ocean with more zonal flow. The MSLP climatology (**Figure 45c**) reveals a similar pattern to previous composite maps, with two areas of relatively low pressure around southern Alaska and southern Greenland. The

MSLP anomaly map (**Figure 45d**) shows a very large negative anomaly covering much of the Arctic. The two strongest negative anomaly areas (-5 mb) cover Baffin Bay and the eastern coast of Greenland, but the anomaly also reaches out into the Atlantic Ocean. South of the negative anomaly area is a positive anomaly that reaches from the Atlantic Ocean into a portion of the eastern and central US. Another positive anomaly area is shown over the Bering Sea, which extends on to the western coast of Alaska, and south of that in the Pacific Ocean is another negative anomaly area that just reaches the western coast of Canada. The T2m composite (**Figure 45e**) shows a very gradual change in temperature gradients. The anomaly T2m map (**Figure 45f**) shows a large negative anomaly area covering much of Greenland and Canada and reaches into the central US (-4°C at its strongest). Smaller and weaker positive T2m anomalies appear over Alaska and parts of the western US. The PW climatology (**Figure 45g**) shows a shifting northward of the lowest PW value, north of 70°N, but otherwise a steep gradient remains. The PW anomaly map (**Figure 45h**) once again shows positive anomalies for the southern US and the bordering bodies of water, but the strongest positive anomaly is shown southeast of the US in the Pacific Ocean (+3.2 kg/m^2). A much weaker positive anomaly reaches across almost all of the western coast of NA and covers much of Alaska.

The composite maps for November (one month ahead of the contemporary month of October) are shown in **Figure 46a-h**. The climatology composite map for 500GPH (**Figure 46a**) shows a steep gradient in the middle latitudes, but more uniform GPH fields north of 60°N and south of 30°N, which reflects the transition season period when the pressure and temperature gradients strengthen over the NH. The anomaly 500GPH map (**Figure 46b**) shows a large negative anomaly across much of the Arctic, though the

strongest negative anomalies are shown around the Hudson Bay and along the eastern coast of Canada (-32 m). Several positive anomalies are shown both north and south of those strong negative anomalies in the Atlantic Ocean. The strongest positive anomaly (+36 m) reaches from the Atlantic Ocean across much of the eastern coast of Greenland and almost touches the west coast. The other slightly positive anomaly is shown far off the eastern coast of the US but reaches into a portion of the northern US. Another strong, closed positive anomaly is situated off the northwestern coast of the US. The 500GPH anomalies appear more variable for this month, with a large trough over much of CA and ridges over western and eastern US as well as another ridge over southeastern Greenland. The atmospheric flow appears mixed as well with areas of both zonal flow (across the US) and meridional flow (over Greenland). The composite MSLP map (**Figure 46c**) shows similar low pressure areas to previous climatology maps. These low pressure areas are situated off the southwestern coast of Alaska and southeastern coast of Greenland. Anomaly MSLP is shown in **Figure 46d**, with both a large positive and negative area. The positive MSLP anomaly area reaches across much of the Arctica and down to both the western coast of Alaska and eastern coast of Greenland, but only reaches +2.8 mb at its maximum value. The negative MSLP anomaly area encompasses much of NA, though the strongest negative anomaly centers touch the east coast of Canada and a small portion of the northwestern US. At its lowest value, the negative anomaly is around -2.4 mb. The T2m climatology (**Figure 46e**) again shows steep changes in T2m across NA, with Greenland showing the lowest temperature values. The T2m anomaly map (**Figure 46f**), however, shows a slight positive anomaly for Greenland, a small portion of the southeastern US, and for an area of central to western Canada. Much of the remainder of

Canada and the Arctic shows a negative anomaly. The strongest negative anomalies can be seen over Baffin Bay and part of the Arctic Ocean just north of Alaska. Lastly, the climatology for PW is shown in **Figure 46g** and the anomaly in **Figure 46h**. The anomaly map shows a positive anomaly for parts of central and western Canada that reaches out into the Pacific Ocean, as well as another for the southern US, which is the largest and most intensely positive anomaly area, reaching +3.6 kg/m^2. The very small negative anomaly areas are interspersed between the positive areas, but mostly appear over bodies of water. The largest negative anomaly is shown far off the eastern coast of the US in the Atlantic Ocean.

The last month of the lead-1 composites is January of the following year (one month ahead of the contemporary month of December). For example, years of overlap highlighted in **Table 6** for December include 1982, 1984, 1986, etc., so these then became 1983, 1985, 1987, and so on. **Figure 47a** shows the 500GPH climatology map with steep changes in GPH across much of NA. The 500GPH anomaly map (**Figure 47b**) shows large areas of positive anomalies for both northwest Canada, a portion of Alaska, and much of Greenland. Large negative anomalies are also shown south of those areas of positive anomalies. The strongest negative anomaly is shown far off the southeast coast of Alaska in the Pacific Ocean (-90 m), but another much larger and weaker negative anomaly stretches from the southwestern US into northeast Canada and the Atlantic Ocean. These 500GPH anomalies reveal a ridge over Alaska, a trough over the western US, and another ridge over eastern US. The flow appears to be meridional for the most part. The climatology map for MSLP (**Figure 47c**) shows two low pressure centers, one off the southwest coast of Alaska and the other off the southeast coast of Greenland. The

MSLP anomaly map (**Figure 47d**) shows a very large negative anomaly area that spans from the Pacific Ocean, across NA, and into the Atlantic Ocean. The strongest negative anomaly area is shown off the southeast coast of Alaska, similar to the negative 500GPH anomaly. Additionally, a positive MSLP anomaly is shown reaching the eastern coast of Greenland, but few other positive anomalies are shown. The T2m climatology is shown in **Figure 47e** and once again shows the strongest negative regions for Greenland and the Arctic. The T2m anomaly map (**Figure 47f**) shows two large positive anomaly areas; one positive area is shown over much of Greenland extending upward into the Arctic and eastward into the Atlantic and the other is shown reaching from the Bering Sea across Alaska and into central Canada. Two fairly weak negative anomalies areas are shown over the Baffin Bay and over a portion of south central and western US. The climatology map for PW (**Figure 47g**) shows a more gradual gradient as compared to previous months, with the lowest value band reaching down into northern Canada and parts of Alaska. The PW anomaly map (**Figure 47h**) shows large positive anomaly areas across all of Alaska and northwest Canada, along the eastern coast of Greenland, and along the south and southeastern coasts of the US. A large negative anomaly region can also be seen extending from the central US into a portion of northeastern Canada.

6.2.1.3 LEAD-2 ANALYSIS

The lead-2 analysis (**Figure 48a-h)** shows composites for the month of March (two months ahead of the contemporary month of January). **Figure 48a** is the 500GPH climatology, which shows a smaller region for the lowest heights, though a steep GPH gradient is still shown for NA. The anomaly 500GPH map (**Figure 48b**) shows a large and strong negative anomaly (-45 m at its strongest) reaching from the Arctic down into

mid-latitude region of the Pacific Ocean, and another weaker, closed negative anomaly is sprawled across much of the US. The positive anomaly that reaches from Alaska far out into the Atlantic Ocean seemed to be contained between those areas of negative anomalies. There is a deep trough over the Pacific Ocean, which transitions into a ridge over Alaska, with meridional flow. There is another slight ridge over the CAA, but this has more zonal flow. The additional negative 500GPH anomaly over the US indicates another ridge, although the flow is more zonal. The MSLP climatology (**Figure 48c**) shows two areas of relatively lower MSLP around southwest Alaska and southeast Greenland. The MSLP anomaly map (**Figure 48d**) reveals an expansive negative anomaly for the western Arctic which joins another large negative anomaly that extends south of the southwestern coast of Alaska. Another much weaker negative anomaly is shown to cover much of the central and eastern parts of the US. A few small and weak positive anomalies appear over the Baffin Bay region. The largest positive anomaly area reaches from the Atlantic into the southern portion of the Baffin Bay region, though again it is not a strong anomaly. The composite for T2m climatology (**Figure 48e**) shows a gradual change in T2M over much of NA. The T2m anomaly map (**Figure 48f**) reveals several areas of positive and negative anomalies, though the largest anomaly areas are north of 50°N. The largest negative anomaly area appears to cover almost all of Greenland and the Baffin Bay, as well as a small portion of the CAA. Another slight negative anomaly appears over the northeastern coast of Alaska. Two positive anomaly areas are shown as well. The largest appears over Alaska, which extends on to a portion of northwestern Canada. The other positive anomaly is situated north of the CAA in the Arctic Ocean. A few other very small and weak negative anomalies appear over parts of

the central and western US. The PW climatology map (**Figure 48g**) shows the lowest values of PW north of 50°N, including almost all of Canada and Greenland. The anomaly map for PW (**Figure 48h**) reveals two large positive anomaly areas on either side of NA and another in the Gulf of Mexico region. One such spot is an expansive positive anomaly covering much of Alaska and a portion of Pacific Ocean that borders the western coast of NA, as well as parts of western Canada and the US. The other primary positive anomaly area is shown off the southeastern coast of the US. The last positive anomaly appears over portions of the northeastern US and western Canada, extending into the Atlantic Ocean. Negative anomalies appear around several areas of the Greenland coast, though these anomalies are fairly weak. Most of the negative anomaly areas are shown south of 30°N, the strongest of which appears over Hawai'i and extends northward. Another negative anomaly is shown for much of the southern US, and the last is shown off the eastern coast of Florida in the Atlantic Ocean.

Composite maps for the month of May (two months ahead of the contemporary month of March) are shown in **Figure 49a-h**. The 500GPH climatology map (**Figure 49a**) shows a gradual change in GPH across NA indicative of gradual weakening of the pressure gradient in the warm season. The 500GPH anomaly map (**Figure 49b**) shows a large positive anomaly area extending over much of the CAA, across much of Greenland, a portion of western Canada, and off the northern coast of Alaska. The strongest positive area is a closed upper-air anticyclone over the CAA, upwards of +45 m. Several areas of negative anomalies surround the large positive anomaly areas as well. The strongest of which (around -45 m) is situated over the Bering Sea and reaches on to the southwestern part of Alaska. Several other weaker negative anomaly areas connect and reach from the

Pacific Ocean to the Atlantic Ocean, which includes two closed low-pressure centers. These mixed anomaly patterns produced very wavy atmospheric flow with many ridges and trough over NA. The MSLP climatology (**Figure 49c**) shows a similar low MSLP area for southwest Alaska, but the other found near Greenland does not show up for this month. Instead, there is a high MSLP area over the central Greenland region. The anomaly MSLP map (**Figure 49d**) shows an extensive positive anomaly area covering all of Greenland and much of the CAA, which also extends further into the Arctic region. Several negative anomaly areas appear as well, over much of the eastern and southern coasts of the US, but the strongest negative area reaches from a portion of the Bering Sea into Alaska and further down the western coast of NA. The climatology for T2m is given in **Figure 49e** with the only a low region covering part of central Greenland. The T2m anomaly in **Figure 49f** reveals extensive positive anomaly areas from Alaska and parts of western Canada into the CAA and further into the upper Arctic region. Several large negative T2m anomalies are also shown. One negative region encompasses a large area of western and central US and the other extends from eastern US and Canada into Baffin Bay and the Atlantic Ocean. **Figure 49g** shows the PW climatology composite with relatively higher PW values shown across NA compared to previous months. The PW anomaly map (**Figure 49h**) shows several areas of slightly positive anomalies over the CAA, Alaska, and western and central parts of both Canada and the US, but the strongest positive PW anomaly appears in the Gulf of Mexico and off of the southern Florida coast; at its strongest, the anomaly is +2.8 kg/m^2. A large negative anomaly is shown over a large portion of the Pacific Ocean, and another negative area is situated over eastern Canada and the US, though it is weaker than the Pacific anomaly.

The following composite maps (**Figure 50a-h**) are for December (two months ahead of the contemporary month of October). The 500GPH climatology map is given in **Figure 50a**, which shows steep changes in GPH across NA. The 500GPH anomaly map (**Figure 50b**) shows a very large negative anomaly covering much of NA and all of Greenland, as well as a portion of the Atlantic Ocean. A negative anomaly area at -40 m is seen over the Atlantic Ocean, off the eastern most tip of Canada. A large, closed positive anomaly area is shown over the southern coast of Alaska, which covers the entire state and extends over a portion of northwestern Canada as well as the Bering Sea and Arctic Ocean. At its most highly positive, the anomaly reaches +60 m. The two large anomalies within the 500GPH anomaly map produced a large trough over Alaska and a large ridge over much of the rest of NA, and with a meridional flow pattern. The MSLP climatology (**Figure 50c**) again shows two low MSLP areas off southwestern Alaska and southeastern Greenland. The MSLP anomaly map (**Figure 50d**) shows very similar patterns to the 500GPH anomalies. The largest negative anomaly covers parts of the CAA, Greenland and the Atlantic Ocean, where the anomaly is strongest. The negative MSLP in the Atlantic Ocean reaches -3.5 mb. Another smaller negative anomaly sits over a portion of the western US. One very large positive anomaly reaches from its highest center off the southern coast of Alaska into the Arctic Ocean and across much of Canada and a part of the central US. The T2m climatology map (**Figure 50e**) shows a steep temperature gradient for much of NA, while the anomaly map (**Figure 50f**) reveals a very large negative T2m anomaly that covers much of NA and parts of the Arctic. The most negative anomalies are found over Baffin Bay and Hudson Bay. Two positive anomalies are shown, the largest of which covers much of Alaska and the surrounding waters, and

the smaller weaker positive anomaly is shown over central Greenland. The PW climatology is shown in **Figure 50g**. The anomaly map (**Figure 50h**) shows a negative anomalies over a part of the western US and much of central and northeastern Canada, while positive anomalies cover parts of Alaska and a portion of the southeastern US.

The composite maps for February (two months ahead of the contemporary month of December) are shown in **Figure 51a-h**. The 500GPH climatology map is shown in **Figure 51a**. The 500GPH anomaly map (**Figure 51b**) shows several negative anomaly areas surrounding a large positive anomaly situated over the central and western parts of Canada and the US. At its highest the positive anomaly is +30 m. The surrounding negative anomalies are found over the CAA, over the Pacific Ocean and a part of Alaska, and over a portion of the southern and eastern US. The strongest negative anomaly area for this composite, at -70 m, is situated over the Pacific Ocean south of Alaska. The 500GPH anomalies reveal a large trough over Alaska and the Pacific Ocean transitioning into a ridge over much of NA. This pattern shows meridional flow over northern Canada and more zonal flow over the US. The MSLP climatology map (**Figure 51c**) shows low MSLP regions off southwestern Alaska and southeastern Greenland. The MSLP anomaly map (**Figure 51d**) shows a positive anomaly for a large portion of the Arctic, covering the CAA and on both the eastern and western coasts of Greenland. The closed negative MSLP anomaly over the Pacific Ocean closely matches the shape of the 500GPH anomaly, but unlike the GPH anomaly, the MSLP anomaly reaches from the Pacific Ocean northward into Alaska and northwestern Canada, then diagonally into the southeastern US, and north again along the eastern coast of NA into the Atlantic Ocean. The T2m climatology (**Figure 51e**) shows a steep temperature gradient over much of NA.

The T2m anomaly composite (**Figure 51f**) shows an extensive negative anomaly covering much of Alaska, the CAA, and a portion of Greenland. A large positive anomaly is found over central Canada (+4°C at its strongest), extending to cover much of the western NA coast, and some parts of the central and eastern US. Lastly, a small positive anomaly can be seen over some parts of central and eastern Greenland. The PW climatology (**Figure 51g**) shows low PW averages for much of NA. The PW anomaly map (**Figure 51h**) shows an extensive positive anomaly over a portion of the western coast of NA, which reaches into the central US and Canada. Another large positive PW anomaly (2.8 kg/m^2 at its strongest) is shown off the southeastern coast of the US and reaches across the Atlantic Ocean to the eastern coast of Greenland.

Generally, within the maximum SIE and minimum GBI climatology composite maps, there tend to be lower values north of the 60°N for GPH, MSLP, T2m, and PW; however, a few positive anomalies north of the 60°N start to show up in the lead-1 and lead-2 anomaly composites. The presence of negative anomalies are common over Greenland and the surrounding regions, the Canadian Archipelago, and Alaska while positive anomalies appear over eastern and western NA, including the Atlantic and Pacific oceans.

6.2.2 MINIMUM SIE VS. MAXIMUM GBI

6.2.2.1 CONTEMPORARY ANALYSIS

The years for minimum SIE versus maximum GBI composites for the Baffin Bay can be found in **Table 7.** This minimum SIE-maximum GBI combination yielded four years of overlap for January, seven common years for March, six common years for October, and four common years for December.

The contemporary composite maps for January are shown in **Figure 52a-h**. The 500GPH climatology (**Figure 52a**) shows low GPH for much of Canada, Alaska, and Greenland. The anomaly map (**Figure 52b**), however, shows extensive positive anomalies north of 60°N. The strongest positive anomaly area (+120 m) is found over the Baffin Bay and reaches across all of Greenland, much of northern Canada, a part of western US, and into Alaska, where another high GPH center (+80 m) can be found. The two large, closed negative anomaly areas are situated south of the large, closed positive anomaly areas. One is shown off the northeastern coast of the US (at -80 m) and reaches into the eastern US, and the other far off the southern coast of Alaska in the Pacific Ocean. Except for a slight ridge over the western US, the 500GPH anomalies have created mostly zonal flow across NA. The MSLP climatology (**Figure 52c**) again shows two areas on either side of the map with lower MSLP, including southwestern Alaska and southeastern Greenland. The MSLP anomaly map (**Figure 52d**) shows an expansive positive MSLP anomaly reaching from the Arctic into much of Canada and the US. The highest positive anomalies of +6 mb are located over northwestern Canada and eastern Greenland. The two large negative anomaly areas, +6 mb at their strongest, are located on either side of NA in the Pacific and Atlantic Oceans, though both anomalies reach the coast lines of the US and Canada on both sides. The T2m climatology map (**Figure 52e**) shows a steep gradient across NA. The T2m anomaly map (**Figure 52f**) shows a large positive anomaly for much of the Arctic region, including the strongest positive anomaly over the Baffin Bay. There is also a negative T2m anomaly reaching from northwestern Canada to the eastern US. The PW composite map (**Figure 52g**) shows a large swath of northern Canada with very little PW, yet the anomaly map (**Figure 52h**) shows large

positive PW anomaly areas covering parts of western and northeastern Canada. A large negative anomaly area is also shown covering parts of central and eastern Canada and US.

Contemporary March composite maps are shown in **Figure 53a-h**. The 500GPH climatology map is shown in **Figure 53a**. The anomaly 500GPH map (**Figure 53b**) again shows low GPH climatology replaced with a large positive anomaly, with the strongest positive area shown over the Baffin Bay upwards of +140 m. This positive anomaly extends to cover all of Greenland and further into the Arctic. The strongest negative anomaly is seen south of the positive anomaly in the Atlantic Ocean and reaches the eastern US. Another slightly negative anomaly is shown over southwestern Alaska and the Bering Sea. The anomaly 500GPH patterns have created a slight trough over the Alaska area with meridional atmospheric flow, and a very large ridge over the eastern US and Atlantic Ocean with a trough southward, which created more zonal flow. **Figure 53c** shows the MSLP climatology and **Figure 53d** shows the MSLP anomalies, which closely match that of the 500GPH anomalies. The two strongest areas of MSLP anomaly are shown over eastern Greenland (+10 mb) and south of that spot a strong negative anomaly is shown in the Atlantic Ocean (at -10 mb). Another large negative anomaly area is shown over Alaska, though only at -2 mb at its strongest. The T2m climatology composite (**Figure 53e**) shows a gradual temperature gradient over NA. The T2m anomaly map (**Figure 53f**) shows a very large positive anomaly over much of Canada and Greenland with the strongest areas reaching +6°C A comparatively smaller negative anomaly area is shown for much of the eastern US at just -1°C. The climatology for PW is shown in **Figure 53g**, and the anomaly map is presented in **Figure 53h**. A large

positive anomaly can be seen over much of northeastern Canada into the Baffin Bay. Additionally, a larger negative anomaly covers much of the eastern and central US, but also extends further into the Atlantic Ocean and is connected to a negative anomaly in the Pacific Ocean.

Composite maps for the month of October are shown in **Figure 54a-h**. The climatology for 500GPH is shown in **Figure 54a** with the highest GPH reaching into parts of the southern US and lower GPH receding further north. The 500GPH anomaly map (**Figure 54b**) reveals an expansive positive anomaly covering all of Alaska, almost all of the CAA, and all of Greenland. The anomaly area with highest positive deviation is shown for a small portion of northeastern Greenland at +80 m. Two large negative anomaly areas are also shown, one over the northeastern US and central Canada, and over a region in the Pacific Ocean, far off the southern coast of Alaska. There are atmospheric ridges over Alaska and Greenland, while a trough is situated over central and eastern NA, and together these 500GPH anomalies created meridional atmospheric flow. The MSLP climatology map (**Figure 54c**) shows a similar low MSLP area for southwestern Alaska, but the low for southeastern Greenland has migrated slightly further eastward. The MSLP anomaly map (**Figure 54d**) shows a very large positive anomaly that covers all of Greenland and reaches into the Arctic. At its highest, the positive MSLP anomaly reaches +5 mb over parts of Greenland and the Atlantic Ocean. Another positive anomaly is shown over a portion of northwestern Canada and eastern Alaska. Two negative anomaly areas are also shown; one covers much of the eastern half of NA and reaches into the Atlantic Ocean, and the other is over a part of the Pacific Ocean and reaches north into the Bering Sea. The T2m climatology map (**Figure 54e**) shows a gradual temperature

gradient, with the lowest temperatures around 70°N. The T2m anomaly map (**Figure 54f**) shows an extensive positive anomaly area covering much of the Arctic region and reaching southward into parts of NA, though the strongest positive anomalies, upwards of +4.5°C are found from 70°N northward. The PW climatology composite map (**Figure 54g**) shows a migration of higher PW areas further northward across NA. The anomaly composite (**Figure 54h**) shows a large positive anomaly surrounding much of NA. The anomaly extends from the Pacific Ocean northward over much of the Arctic and over much of the eastern coast of NA, as well as the entire coastline of Greenland. Several smaller areas of negative anomalies appear over small areas of central NA, though they are much weaker. The strongest negative anomaly appears over southeastern US.

The last contemporary monthly composites are for the month of December in **Figure 55a-h**. The 500GPH climatology composite (**Figure 55a**) shows a very steep GPH gradient for NA. The anomaly map (**Figure 55b**) shows a large, closed positive anomaly over the Baffin Bay and southwestern Greenland, but also extends to cover the Hudson Bay and reaches over parts of northern Canada and all of Alaska. At its strongest, this positive anomaly reaches +160 m. Two smaller and weaker negative anomalies are found over parts of NA; one is situated over the Pacific Ocean and reaches into northwestern US, and the other is over parts of the central and eastern US and extends into the Atlantic Ocean. The large atmospheric ridge over Baffin Bay and weaker trough southward show mostly zonal flow. The MSLP climatology (**Figure 55c**) again shows two low MSLP areas, while the anomaly map (**Figure 55d**) shows a large positive anomaly. At its strongest the positive MSLP anomaly reaches +12 mb and is situated over central and eastern Greenland. The positive anomaly reaches far beyond Greenland,

however, across much of Canada and all of Alaska and into the northern Arctic. The T2m climatology is given in **Figure 55e**. The T2m anomaly (**Figure 55f**) reveals a drastic deviations from the climatology, with a large positive anomaly covering much of northeastern Canada and almost all of Greenland at +7°C. Another positive anomaly appears over the Bering Sea and touches the western coast of Alaska. A negative anomaly cuts diagonally across NA, starting at Alaska and extending into the eastern US. The PW climatology is shown in **Figure 55g**. The anomaly PW composite map (**Figure 55h**) reveals a positive anomaly covering much of northeastern Canada, including Baffin Bay, Hudson Bay, and parts of the CAA, and reaching the western and eastern coasts of Greenland. Another positive anomaly covers the Bering Sea, and yet another appears over several areas of the Pacific Ocean. A large negative anomaly connects from the Pacific Ocean into NA to cover much of the eastern US and parts of the Atlantic Ocean.

6.2.2.2 LEAD-1 ANALYSIS

Lead-1 analysis accounts for a one-month jump forward from the contemporary months, or in the case of December, it becomes January of the next year. **Figure 56a-h** shows climatology and anomaly composite maps for February (one month ahead of the contemporary month of January). The climatology 500GPH map (**Figure 56a**) shows the lowest GPH values north of the 50°N latitude line. The anomaly map for 500GPH (**Figure 56b**), however, shows several positive anomaly areas of +20–40 m, covering almost all of Greenland and the Baffin Bay as well as a portion of northwestern Canada and Alaska. One large negative anomaly area also appears, which extends from the western US into the Atlantic Ocean with its lowest value at -100 m. The largest negative 500GPH anomaly over the Atlantic Ocean along with the weaker positive anomaly

northward over Greenland reveal a mostly zonal atmospheric flow. The MSLP climatology map (**Figure 56c**) shows a shift of the low MSLP centers in both the Alaska and Greenland areas. The low MSLP area found in southwestern Alaska appears to have migrated westward and similarly, the low MSLP area typically found in the southeastern Greenland area appears to have migrated slightly further eastward. The MSLP anomaly map (**Figure 56d**) shows only a few anomalies over NA, though there is a very large and strong negative anomaly (-7 mb at its strongest) off the eastern coast of Canada, which reaches on to eastern Canada and the US as well as northward into the Baffin Bay region. Several positive anomalies are shown, one over central and eastern Greenland, and another much stronger positive anomaly appears to emanate from the East Siberian Sea, reaching northern Alaska. The T2m climatology map is shown in **Figure 56e** and the anomaly map is shown in **Figure 56f**. The T2m anomaly reveals two large positive anomaly areas. The strongest covers the Baffin Bay, Hudson Bay, and much of Greenland (+8°C). The other positive anomaly resides over almost all of Alaska and parts of northwestern Canada (+4°C). A slight negative anomaly covers much of the US and parts of central Canada, though it is a fairly weak anomaly. The PW climatology map is shown in **Figure 56g**. The PW anomaly map (**Figure 56h**) again reveals a positive anomaly bordering much of the Greenland coastline as well as a portion of the northeastern Canada coast. Another positive anomaly is shown over much of Alaska and parts of northwestern Canada. There is also a large negative anomaly covering much of the US, which extends outward into both the Atlantic and Pacific Oceans.

April monthly composites (one month ahead of the contemporary month of March), are shown in **Figure 57a-h**. The 500GPH climatology (**Figure 57**a) shows high

GPH for much of NA, but some lower GPHs for northern Canada. The 500GPH anomaly map (**Figure 57b**) reveals two large positive anomaly areas: the first of which contains two large, closed anomaly areas (+30 m), which connect and span much of central and eastern NA and southern Greenland, and the other strong positive anomaly area is situated over the Pacific Ocean (+50 m), far off the southern coast of Alaska. Several smaller negative anomalies are also shown over Alaska, a part of the western US, and a part of eastern Canada. The 500GPH anomalies reveal a ridge in the Pacific Ocean, a trough over Alaska, and another ridge over much of eastern NA, which created meridional atmospheric flow patterns. The MSLP climatology is shown in **Figure 57c** and shows the low MSLP area found in southeastern Greenland has become slightly higher for this month. The MSLP anomaly map (**Figure 57d**) shows several areas of positive anomalies. The first and strongest is situated over the Pacific Ocean (+2.8 mb), which reaches up into the Arctic Ocean, touching much of the western coast of Alaska. Another positive anomaly is shown over the eastern US, which reaches out into the Atlantic Ocean. The last positive anomaly is shown over much of southern Greenland and reaches into the Atlantic Ocean. A strong negative MSLP anomaly (-2.4 mb) appears over the western part of the CAA but also reaches into parts of the central US and eastern Canada. The T2m climatology composite is shown in **Figure 57e** and the anomaly composite is shown in **Figure 57f**. A very large positive T2m anomaly appears over much of NA (+2.8°C at its strongest) though it does not reach the western coastline. Western Greenland is also affected by the positive anomaly, with some of the strongest positive anomaly values found in the Baffin Bay region. Negative T2m anomalies cover much of Alaska, parts of the western US, and small portion of eastern Greenland. The

PW climatology composite is shown in **Figure 57g** and the PW anomaly composite in **Figure 57h**. The anomaly composite shows a large positive anomaly spanning much of the eastern half of the US into central Canada and into the Baffin Bay area. Another positive anomaly appears in the Pacific Ocean and just reaches the furthest southern tip of Alaska. Most of Alaska is covered by a negative anomaly area, and two other large negative anomaly areas are found on either side of the US, though the anomaly in the Atlantic Ocean is stronger than that in the Pacific Ocean.

Composites for the month of November (one month ahead of the contemporary month of October) are shown in **Figure 58a-h**. The 500GPH climatology map is shown in **Figure 58a**, and **Figure 58b** shows the anomaly composite for 500 GPH with a substantial area of positive anomaly reaching across much of the NA continent. By far, the strongest positive anomaly area of +45 m appears over the Bering Sea and the western coast of Alaska. This anomaly is not a distinct feature, however, it reaches from Alaska into southern Canada and much of the US, then northward again over the Baffin Bay and almost all of Greenland, as well as a portion of the Atlantic Ocean. Several negative 500GPH anomalies are also shown, which appear interspersed between the larger positive anomaly area. The strongest negative anomaly is situated over northern Canada near the CAA, and at its strongest is around -25 m. The 500GPH anomalies reveal a ridge over western Alaska, a trough over parts of the CAA, another ridge over Baffin Bay, and another trough eastward over the Atlantic Ocean; these are indicative of meridional atmospheric flow for much of NA. The MSLP climatology is shown in **Figure 58c** and the anomaly is shown in **Figure 58d**. The MSLP anomaly map closely matches that of the 500GPH anomaly map, with a very large positive anomaly (+3.2 mb

at its strongest) over the Bering Sea and Alaska region, which stretches over much of the US and Canada. Another positive MSLP anomaly is shown over Greenland and parts of northern Canada. Several negative anomalies are shown, one over the CAA region, another far off the eastern coast of the US, and the last in the Atlantic, eastward of Greenland. The T2m climatology map (**Figure 58e**) shows lower temperatures north of 60°N, which are largely replaced with a positive anomaly, as shown in the T2m anomaly map (**Figure 58f**). The strongest positive anomaly area (+5°C) is over the Baffin Bay region; however, the anomaly stretches across the CAA into the Atlantic and Bering Seas as well as Alaska. The PW climatology composite is shown in **Figure 58g** and the anomaly PW in **Figure 58h**. The PW anomaly map reveals several positive anomaly areas, including over the Bering Sea, Alaska, parts of Baffin Bay and Hudson Bay, and off the eastern coast of the US. The strongest negative anomaly is shown over southeastern US and the Gulf of Mexico (-2.8 kg/m^2).

Composites for the month of January (one month ahead of the contemporary month of December) are shown in **Figure 59a-h**. The 500GPH climatology composite is given in **Figure 59a** and shows the lowest heights for much of northern NA. The anomaly composite map (**Figure 59b**), however, shows an extensive positive anomaly area, reaching from the East Siberian Sea, across Alaska, Canada, and Greenland, and into the Atlantic Ocean, though it appears strongest over Greenland and the northern Atlantic Ocean (+80 m). South of this positive anomaly area is a negative anomaly, which stretches across the US into the Pacific Ocean, reaching -60 m at its strongest. The 500GPH anomaly map shows a slight trough over the Pacific Ocean, southwest of Alaska, a ridge over much of NA and Greenland, and another trough over the Atlantic

Ocean, east of the US. The anomalies show both meridional flow over the Pacific Ocean and zonal atmospheric flow over much of NA. The MSLP climatology is shown in **Figure 59c** and the MSLP anomaly composite is shown in **Figure 59d**. The MSLP anomaly composite closely matches that of the 500GPH anomaly map. One large positive anomaly area is situated over much of the Arctic including Greenland and the CAA, and another is over parts of western Canada and western and central US. The T2m climatology is shown in **Figure 59e** and the anomaly is shown in **Figure 59f**. The low temperatures of the climatology map are replaced with a positive anomaly area, which covers almost all of Alaska, Canada, and Greenland. The strongest positive T2m at +6°C appears over the Baffin Bay region. Small and weak negative anomaly areas are shown over portions of the central and western US. The PW climatology map is shown in **Figure 59g** and the PW anomaly map is shown in **Figure 59h**. The PW anomaly map shows a large area of above average values for much of the Pacific Ocean, Alaska, Canada, and the bodies of water surrounding Greenland. A large negative anomaly (-2.4 kg/m^2 at its strongest) also appears far off the southwestern coast of the US and stretches across the southern US into the Atlantic Ocean.

6.2.2.3 LEAD-2 ANALYSIS

As with lead-1, composites for lead-2 analyses used the same years but jump forward two months from the contemporary months (except for December, which jumps to February of the following year). The composites for the month of March (two months ahead of the contemporary month of January) are shown in **Figure 60a-h**. The 500GPH climatology composite is shown in **Figure 60a** and the anomaly 500GPH is shown in **Figure 60b**. The strongest negative anomaly appears off the southern coast of Alaska and

reaches across much of Alaska, onto the CAA, and out to the Baffin Bay region. This closed negative anomaly reaches -60 m at its strongest. Most of the other anomalies shown are positive. The largest of these positive anomalies covers the Arctic, Bering, and Pacific Oceans before reaching diagonally across NA from western US to eastern Canada. A strong positive anomaly is also shown over the northern Atlantic Ocean, which reaches on to central Greenland (+40 m). The 500GPH anomalies reveal a trough over Alaska and northern CA and ridging over much of the US and eastern Canada. Another ridge is shown eastward of Greenland. The atmospheric flow around these anomalies is mostly meridional. The MSLP climatology map (**Figure 60c**) shows two low MSLP anomaly areas over southern Alaska and southeastern Greenland. The anomaly MSLP map (**Figure 60d**) shows an extensive negative anomaly covering much of the Arctic, including Alaska, CAA, and Greenland. As with the 500GPH, the strongest negative anomaly is shown over southern Alaska and reaches -4 mb. There is also a positive anomaly area situated over the Bering and Pacific Seas, which surrounds the negative anomaly and reaches into the northwestern US. Another large positive anomaly is situated over eastern Canada. The T2m climatology is shown in **Figure 60e** and the T2m anomaly is shown in **Figure 60f**. Within the anomaly map there are two large positive anomalies, one off the northern coast of Alaska and the other over Baffin Bay and Greenland (+5°C at its strongest). Although a few other positive anomaly areas appear, they are much smaller and isolated. These cover portions of the western US and eastern Canada. The negative anomalies are also small. The largest negative anomaly appears over southwestern Alaska and few others are shown over small portions of western Canada. Lastly, the PW climatology map is shown in **Figure 60g** and the PW

anomaly map in **Figure 60h**. Several negative PW anomalies are shown over NA, the largest of which is situated over much of Alaska, another is shown over a small portion of the southern US, and the last over eastern Canada. There are also positive anomalies shown over northern Alaska, a small portion of the northwestern US, a portion of the eastern US, and off the southeastern coast of Greenland.

The composites for the month of May (two months ahead of the contemporary month of March) are shown in **Figure 61a-h**. The 500GPH climatology is shown in **Figure 61a** and shows the lowest GPH, around 5400 m, well north of 70°N. The 500GPH anomaly in **Figure 61b** reveals a large positive anomaly over northeastern Canada (+60 m) that extends further northward into parts of the CAA and eastward over southern Greenland and the Atlantic Ocean. Several other positive anomalies appear as well, one that touches the northeastern tip of Greenland, another over the Pacific Ocean that touches a portion of the western US, and the last over the Bering Sea. Several smaller, weaker negative anomaly areas are also shown over a region of the Pacific Ocean, off the southern coast of Alaska; another over a portion of the eastern US; and the last off the eastern coast of NA in the Atlantic Ocean. The strongest anomaly is the positive ridge over eastern Canada, which shows mostly zonal flow with the negative anomalies present southward. The MSLP climatology (**Figure 61c**) shows a low MSLP for southwestern Alaska, though the low for southeastern Greenland does not appear. The MSLP anomaly map (**Figure 61d**) shows an extensive positive anomaly area over much of northeastern Canada, Greenland, and some of Alaska (+2.4 mb at its strongest). Another positive anomaly reaches from the Pacific Ocean on to a portion of the northwestern US. Two negative anomaly areas are shown as well, though they only just

reach the coastline in Alaska and the eastern US. The T2m climatology map is shown in **Figure 61e** and the anomaly in **Figure 61f**. The largest positive anomaly (+2.8°C at its strongest) covers much of Canada and some of Greenland. Several negative anomalies appear as well, though they are very spotty and not very strong. The largest negative anomaly is fairly weak and is found over the Bering Sea and western Alaska. Other smaller negative anomalies are shown over a small area of the CAA and the southeastern US. The PW climatology map is shown in **Figure 61g** and the PW anomaly map in **Figure 61h**. A large positive anomaly is shown over a large region of Canada and reaches into the Atlantic Ocean. Much of the US is covered by a negative anomaly, except for parts of the west. Another very weak negative anomaly is shown over western Alaska. The strongest negative anomaly is shown far off the eastern coast of NA in the Atlantic Ocean (-2.4 kg/m^2) and the strongest positive over the Pacific Ocean (+2.8 kg/m^2).

The composite maps for the month of December (two months ahead of the contemporary month of October) are shown in **Figure 62a-h**. The 500GPH climatology map (**Figure 62a**) features a large region of lower heights for much of Canada and a steep GPH gradient over much of NA. The 500GPH anomaly map (**Figure 62b**) shows two large anomaly areas over the mid-latitudes, including a negative anomaly in the Pacific Ocean that touches much of the western NA coastline and reaches up into the Arctic, and a larger positive anomaly area over much of Canada, reaching eastward to cover all of the Baffin Bay and Greenland. At its strongest, the negative anomaly (in the Gulf of Alaska) reaches -70 m, and the positive anomaly (over eastern Canada) reaches +50 m. A very large atmospheric trough covers much of the Beaufort Sea, Alaska, and a

part of the Pacific Ocean south of Alaska, while a ridge covers much of central and eastern NA; together these have created meridional flow. Another slight trough south of the large ridge, however, created more zonal flow for this portion of NA. The MSLP climatology (**Figure 62c**) again shows two low MSLP areas over parts of southern Alaska and Greenland. The MSLP anomalies (**Figure 62d**) show very similar patterns to the anomaly 500GPH map. The negative anomaly area covers much of the western NA coastline and reaches northward into the Arctic. The positive anomaly covers parts of the CAA, Baffin Bay, and much of Greenland. The T2m climatology is shown in **Figure 62e** and the anomaly in **Figure 62f**. The anomaly map reveals an expansive positive anomaly area covering much of Canada and parts of the US, as well as parts of Greenland. The positive anomaly is strongest over the Baffin Bay region at +5°C. A much smaller and weaker negative anomaly is shown over parts of Alaska as well. The PW climatology is shown in **Figure 62g** and the anomaly in **Figure 62h**. A large positive anomaly area stretches from the Atlantic Ocean to central Canada, and a smaller positive anomaly covers some of the western US. A strong negative anomaly covers much of the southern US, and another negative anomaly appears in the Pacific Ocean, which reaches the southwestern part of Alaska (-3.2 kg/m^2 at its strongest).

The last set of composites for the lead-2 analysis are for the month of February (two months ahead of the contemporary month of December). These composites are shown in **Figure 63a-h**. The 500GPH climatology composite is shown in **Figure 63a** and the anomaly composite in **Figure 63b**. Two very large positive anomalies are shown on either side of NA. The first is shown far off the western coast of NA in the Pacific Ocean. This positive anomaly reaches northward into southern Alaska. The other positive

anomaly covers all of Greenland and reaches into northeastern Canada. A large negative anomaly is also shown. This anomaly covers much of the US and stretches out into the Atlantic Ocean, where the strongest negative anomaly can be seen at -80 m. Mixed anomalies appear in this map creating both extensive ridging and troughing. There is a large ridge over the Pacific Ocean, south of Alaska, then a trough over much of the US and the Atlantic Ocean east of the US, and another ridge is shown over Greenland. The two anomalies over the Pacific and western US create meridional flow, while the two over central and eastern NA and the Atlantic Ocean show more zonal flow. The MSLP climatology is shown in **Figure 63c** and the MSLP anomaly in **Figure 63d**. Again, the MSLP anomalies closely match those of the 500GPH. The strongest positive anomaly regions are found over the Pacific Ocean and Greenland (+5 mb at their strongest), though another positive anomaly appears over the central US and Canada. Several negative anomalies are shown as well; one over northwestern Canada and northern Alaska, and the strongest over eastern NA and the Atlantic at -7 mb. The T2m composite map is shown in **Figure 63e** and the anomaly map in **Figure 63f**. The anomaly map shows a very large positive anomaly covering much of Alaska, northern Canada, and Baffin Bay. The positive anomaly appears to be strongest over the Baffin Bay region at +7°C. A smaller negative anomaly is shown over parts of the central and western US and Canada. The PW climatology map is shown in **Figure 63g** and the anomaly map in **Figure 63h**. Several negative anomalies cover much of the US, though the strongest negative anomaly area appears over the Pacific Ocean (-3.2 kg/m^2). The largest positive anomaly appears over the Baffin Bay and the Atlantic Ocean.

In summary, almost all of the months shown in the maximum SIE versus

minimum GBI analyses (Section 6.2.1) showed consistently negative anomalies for much of the northern regions of NA, including Alaska, but also for Greenland. Comparing these composites to those of the minimum SIE versus maximum GBI (Section 6.2.2), there is a clear reversal of anomaly patterns; extensive and extreme positive anomalies for all of the variables have become much more common for regions north of 60°N, suggesting warmer temperatures and increased moisture, which have the potential to cause further disruptions to seasonal Arctic changes. Those years of minimum sea ice and maximum GBI produced greater instances of atypical deviations for both the higher latitudes and the mid-latitudes.

6.3 BEAUFORT SEA

6.3.1 MAXIMUM SIE VS. MINIMUM GBI

6.3.1.1 CONTEMPORARY ANALYSIS

The contemporary analysis for the Beaufort Sea region includes the months of May, June, and August. The years used for creating composite maps for maximum SIE versus minimum GBI can be found in **Table 8**. This maximum SIE-minimum GBI combination yielded ten years of overlap for May, four common years for June, and six common years for August.

The composites for the month of May are shown in **Figure 64a-h**. The 500GPH climatology is shown in **Figure 64a** and the anomaly in **Figure 64b**. A large negative 500GPH anomaly can be seen over Greenland and much of the CAA and extends further into the northern Arctic region. The lowest negative anomaly over Greenland at -80 m exhibits closed pattern. The composite map also shows a large positive anomaly, though

it is much weaker than the negative anomaly. The positive anomaly stretches from the Bering Sea across Canada and northern US into the Atlantic Ocean where the greatest anomaly region reaches +40 m. The 500GPH anomalies reveal a trough over much of northern Canada and Greenland, and a ridge over central NA. Together these create mostly zonal atmospheric flow. The MSLP climatology is shown in **Figure 64c** and the MSLP anomaly is shown in **Figure 64d**. The MSLP anomalies closely match those of the 500GPH anomalies, including a large negative MSLP anomaly cover much of Greenland and the CAA (-6 mb at its strongest), and a positive MSLP anomaly over much of the eastern US and parts of eastern Canada. Another positive anomaly appears over the Bering Sea, Alaska, and parts of the western coast of Canada. The T2m climatology (**Figure 64e**) shows a very gradual change in temperature over NA. The T2m anomaly map (**Figure 64f**) shows a large negative anomaly over much of the CAA and Greenland (-2.8°C at its strongest). A smaller negative anomaly is also shown over western Alaska. Additionally, a positive anomaly is shown over northwestern Canada and western US, which extends eastward over the continent into the Atlantic Ocean. The PW climatology map is shown in **Figure 64g** and the anomaly in **Figure 64h**. Much of the Baffin Bay and the CAA are covered with a negative anomaly area, as well as a portion of Alaska. A larger positive anomaly appears over much of the NA continent, which extends outward into the Atlantic Ocean. Another positive anomaly is shown over the Pacific Ocean and just touches a small portion of the western coast of NA.

The composites for the month of June are shown in **Figure 65a-h**. The 500GPH climatology composite is shown in **Figure 65a** and 500GPH anomaly composite in **Figure 65b**. The 500GPH anomaly map shows an extensive negative anomaly over

Greenland (-60 m) and much of the Arctic (-90 m). Several positive anomalies also appear, though they are much weaker than the negative anomaly. The positive anomalies cover much of western NA, including much of Alaska, as well as a small portion of the eastern coast of Canada. Another small negative anomaly is also shown over a part of the eastern US. Atmospheric ridges are shown over Alaska, the CAA, and eastern Canada, while a trough dominates much of the upper CAA and Greenland. Together these create some very slight meridional flow, but mostly zonal. The MSLP climatology map is shown in **Figure 65c** and the MSLP anomaly in **Figure 65d**. Again, the MSLP anomaly map closely matches that of the 500GPH anomaly map. A negative MSLP anomaly appears over Greenland (-5 mb) and part of the northern Arctic (-7 mb), and several positive MSLP anomalies are shown over parts of Alaska, Canada, and the Atlantic Ocean. The T2m climatology map is shown in **Figure 65e** and the T2m anomaly map is shown in **Figure 65f**. Negative anomalies appear to dot parts of the CAA and eastern NA. A negative anomaly covers much of Greenland. A large positive anomaly area is shown over much of western NA and a portion of eastern NA (+2.8°C at its strongest). The PW climatology map is shown in **Figure 65g** and the PW anomaly map in **Figure 65h**. The PW anomalies show a similar distribution to the T2m anomalies. Two large positive anomalies are shown in either side of NA (+3.2 kg/m^2 at its strongest over eastern NA), and a negative anomaly appears to cut through the center of NA.

The composite maps for the month of August are shown in **Figure 66a-h**. The climatology map for 500GPH is shown in **Figure 66a** and the 500GPH anomaly map in **Figure 66b**. A large negative anomaly is shown over much of Alaska, CAA, and Greenland, which extends northward into the upper Arctic region (-60 m at its strongest).

A positive anomaly appears over southern Canada as well. There are some clearly defined areas of troughing over Alaska and Greenland, and a ridge over southern and central Canada. The MSLP climatology map is shown in **Figure 66c** and the MSLP anomaly map in **Figure 66d.** Much of the region north of the 60°N latitude line shows a large negative anomaly (-4.5 mb at its strongest over the Beaufort Sea), while the region south of 60°N shows an extensive but weak positive anomaly. Except for Alaska, the entire US is covered by a positive anomaly, though it is much weaker than the negative anomaly found over Alaska, northern Canada, and Greenland. The T2m climatology map is shown in **Figure 66e** and the T2m anomaly map in **Figure 66f**. There is a large positive anomaly over central and eastern Canada, which is surrounded by various negative anomalies over the southern US, Alaska, and Greenland. The PW climatology map is shown in **Figure 66g** and the PW anomaly map in **Figure 66h.** Positive anomalies appear over the western US as well as northern and eastern Canada. Several negative anomalies are shown over Alaska, the Baffin Bay region, and the Atlantic Ocean.

6.3.1.2 LEAD-1 ANALYSIS

The lead-1 analysis jumps forward by one month from the contemporary months (May, June, and August). The composite maps for the month of June are shown in **Figure 67a-h** (one month ahead of the contemporary month of May). The 500GPH climatology maps are shown in **Figure 67a** and the anomaly map is shown in **Figure 67b.** Several strong positive anomalies areas are shown for this month, including closed anomaly areas over Chukchi Sea, parts of the CAA, and over the western coast of the US (reaching +16 m at their strongest). Another positive anomaly is shown over the eastern coast of Canada, which extends south over the eastern US. A large negative anomaly is shown

over much of the northern Arctic and Greenland (-16 m), which reaches from Baffin Bay and Hudson Bay northward into central Canada and the northern US. Atmospheric ridges appear over Alaska, the CAA, western US, and eastern NA. A large trough is shown over central Canada and Greenland. Together these ridges and troughs create very wavy (meridional) atmospheric flow. The MSLP climatology composite is shown in **Figure 67c** and the MSLP anomaly composite in **Figure 67d.** The anomaly composite reveals negative anomalies much of Greenland and the northern Arctic, as well as for a large area of the Pacific Ocean and much of the US. Positive anomalies are present for eastern Canada and the CAA, western Alaska, and off the southeastern coast of the US. The T2m climatology is shown in **Figure 67e** and the T2m anomaly in **Figure 67f.** The T2m anomaly map reveals a negative anomaly area over central and northern Canada that reaches into Greenland. Most of the other larger anomalies are positive and are found over eastern US and Canada, and almost the entire western coastline of NA. The PW climatology map is shown in **Figure 67g** and the PW anomaly map is shown in **Figure 67h**. Most of the PW anomalies that appear are positive. These positive anomalies cover the southern and eastern US as well as portions of the western US coastline and extend outward into both the Atlantic and Pacific Oceans. A weak negative anomaly is shown over the Hudson Bay region and for a small region of northwestern Greenland.

The composite maps for the month of July (one month ahead of the contemporary month of June) are shown in **Figure 68a-h**. The 500GPH climatology composite is shown in **Figure 68a** and the anomaly 500GPH composite in **Figure 68b**. Similar to the anomaly 500GPH for June, July shows several large, closed positive anomaly areas. Two of these positive anomalies are connected and cover much of the western coastal area of

NA, including much of Alaska (+24 m at their strongest). Another closed positive anomaly area is situated around the northeastern coast of the US and reaches +32 m. One very large negative anomaly appears as well, reaching from the high Arctic over the CAA and down into the central areas of Canada and the US, but also across Greenland and the area of the Atlantic Ocean to the south of Greenland. This extensive negative anomaly produced several closed low areas, including one over the CAA and the other in the Atlantic, both -36 m at their strongest. Like the July anomaly 500GPH composite, the June composite shows many areas of ridges and troughs. Ridges are shown over western and eastern NA, while a ridge dominates the central region, and together these created meridional atmospheric flow. The MSLP climatology map is shown in **Figure 68c** and the MSLP anomaly map in **Figure 68d**. The anomaly map shows a large positive anomaly area stretching from Alaska and northwestern Canada into eastern Canada and the US. The large negative anomaly area covers northeastern Canada, Greenland, and the Atlantic Ocean (-2.8 mb at its strongest). The T2m climatology map is shown in **Figure 68e,** with much of NA showing relatively warm temperatures for this month. The T2m anomaly map (**Figure 68f**) shows an extensive negative anomaly for much of central and eastern NA, while a positive anomaly covers parts of the western coastline of NA including Alaska. Another positive anomaly is shown over a small area of the eastern US and Canada. Although these anomalies are large, they are not very strong. The PW climatology map is shown in **Figure 68g** and the anomaly map is shown in **Figure 68h**. There is a large negative anomaly covering central US, which reaches up into northern Canada, and out into the Atlantic Ocean as well, then to the eastern coast of Greenland. A strong positive anomaly appears over the northeastern US (+4.5 kg/m^2), and another over

a smaller area of the western US. The last positive anomaly spans over the Pacific Ocean and into the western coast of Alaska.

Lastly, the composite maps for the month September (one month ahead of the contemporary month of August) are shown in **Figure 69a-h**. The 500GPH anomaly map is shown in **Figure 69a** and the 500GPH anomaly map in **Figure 69b.** There is a large negative anomaly covering much of Alaska and Canada, which also reaches into the Atlantic Ocean. Three positive anomaly areas are shown as well (+24 m at their strongest), which surround the negative anomaly area (-32 m at its strongest). The first appears over the CAA and extends eastward across Greenland into the Atlantic Ocean; another is situated over the Pacific Ocean and touches the western coast of the US; and the last is over the Chukchi and Bering Seas. A large trough extends from western to eastern NA, with ridges on three sides, the largest of which is situated over the CAA. Together these ridges and trough created somewhat meridional atmospheric flow. The MSLP climatology map (**Figure 69c**) shows two relative low pressure areas, one over southwestern Alaska and the other over southeastern Greenland. The MSLP anomaly map (**Figure 69d**) shows two large positive anomalies. The strongest positive anomaly covers Alaska, the CAA, and much of Greenland (-2.8 mb). Another weaker positive anomaly is shown over much of the eastern US and extends eastward into the Atlantic Ocean. Several smaller negative anomalies appear as well, the largest of which is over the Pacific Ocean. The other negative anomalies cover only small parts of NA and the Atlantic Ocean. The T2m climatology is shown in **Figure 69e** and the T2m anomaly is shown in **Figure 69f**. The anomaly map reveals negative anomaly areas cover much of the NA continent as well as the Baffin Bay region and parts of Greenland. A very small

positive anomaly appears over a portion of the western US coast. The PW climatology map is shown in **Figure 69g** and the PW anomaly in **Figure 69h**. Most of the anomalies that appear over NA are negative, including the largest anomaly area over Alaska and western Canada. Several other smaller negative anomalies appear over eastern Canada and the Baffin Bay. Two small positive anomalies are shown as well, over the western and eastern US.

6.3.1.3 LEAD-2 ANALYSIS

The lead-2 analysis composite maps jumped forward two months from the contemporary months. The first maps are for the month of July (two months ahead of the contemporary month of May), which are shown in **Figure 70a-h**. The 500GPH climatology composite is shown in **Figure 70a** and the 500GPH anomaly composite in **Figure 70b**. Though much of NA shows high GPH heights, the anomaly map reveals several hotspots of positive anomalies. The strongest positive anomaly appears over the Gulf of Alaska, off the southern coast of Alaska, which reaches +40 m. The anomaly extends much further into the Arctic region and beyond to cover all the Baffin Bay and Greenland, though it becomes much weaker. A few small and weak negative anomalies are shown as well, the largest of which is in the Atlantic Ocean, off the eastern coast of Canada. The large positive 500GPH anomaly is indicative of a ridge over the Gulf of Alaska, but overall, there does not appear to be distinct atmospheric flow patterns shown. The MSLP climatology composite is shown in **Figure 70c** and the anomaly in **Figure 70d**. The MSLP anomalies closely resemble those shown in the 500GPH anomaly map. Again, the strongest positive anomaly is shown over the Gulf of Alaska, but also extends across the NA continent and then upward across the Baffin Bay and Greenland into the

Arctic region (+2.5 mb at its strongest). The largest negative anomaly appears out in the Atlantic Ocean, but it is weak. The T2m climatology composite is shown in **Figure 70e** and the T2m anomaly in **Figure 70f**. Both positive and negative anomalies appear over various regions of the CAA and Greenland. The largest positive anomaly for this map appears over the western coastline of NA, which extends westward into parts of the Pacific Ocean as well. Several anomalies appear over Alaska as well, though the largest of these anomalies is positive. A large negative anomaly appears over the northern US. The PW climatology map is shown in **Figure 70g** and the PW anomaly map is presented in **Figure 70h**. There are many PW anomalies over NA, including positive anomalies over parts of Alaska, over the Hudson Bay, and over the southwestern US. Negative anomalies also appear over small regions of the eastern, central, southern, and western US.

The composites for the month of August (two months ahead of the contemporary month of June) are shown in **Figure 71a-h**. The 500 GPH climatology map is shown in **Figure 71a** and the 500GPH anomaly map in **Figure 71b**. A large and extensive negative anomaly is shown for the upper Arctic region where it is strongest at -60 m, but the anomaly also reaches over much of Greenland, and eastern Canada and the US, as well as the western coast of Alaska. A large, close positive anomaly is shown over much of the CAA and eastern Alaska (+50 m at its strongest). Atmospheric troughs are shown over Alaska and parts of Greenland and eastern NA, while a ridge is shown over the CAA. Together these create meridional flow over northern NA. The MSLP climatology map is shown in **Figure 71c** and the anomaly map in **Figure 71d**. The MSLP anomaly patterns follow the 500GPH anomalies closely. Negative anomalies are shown over Alaska, the

northern Arctic, much of Greenland and parts of eastern Canada. The positive anomaly, however, covers much of the rest of NA, from the CAA down into the southeastern US. The T2m climatology map is shown in **Figure 71e** with very gradual changes in temperature across the NA continent. The T2m anomaly map (**Figure 71f**) shows various positive anomalies along the western side of NA, the strongest of which is in the western CAA (+2.4°C). Much of the central and eastern regions of NA show a negative anomaly, as well as some parts of Alaska and Greenland. The PW climatology map is shown in **Figure 71g** with much higher PW values for the southeastern US. The PW anomaly map in **Figure 71h**, shows an extensive negative PW anomaly for much of central and eastern NA, as well as some small areas of the western US. The largest positive anomaly area is shown over Alaska, central Pacific, and the western CAA (+2.4 kg/m^2 at its strongest).

Lastly, the composite maps for the month of October (two months ahead of the contemporary month of August) are shown in **Figure 72a-h**. The 500GPH climatology composite is shown in **Figure 72a** and the anomaly composite in **Figure 72b**. The anomaly map reveals several areas of positive anomalies on either side of NA. The strongest positive anomaly is shown over the western coast of Alaska and reaches parts of the western US; at its strongest this anomaly reaches +32 m. Another large though weaker positive anomaly is shown over eastern Canada, which also reaches the southern tip of Greenland. The last positive anomaly is situated over the northern CAA and reaches northwestern Greenland. The negative anomaly area from the high Arctic reached down into Canada and parts of the southeastern US as well. The strongest negative anomaly (-28 m) in the mid-latitudes is situated south of the strongest positive anomaly area (+32 m) in the Pacific Ocean. An atmospheric ridge is situated over Alaska with

trough directly south of that; another trough appears over northwestern Canada, and two more ridges are shown as well, over the CAA and off the eastern coast of Canada. Altogether, these areas create very wavy and meridional atmospheric flow patterns. The MSLP climatology map is shown in **Figure 72c** and the MSLP anomaly in **Figure 72d**. Two large, positive MSLP anomaly areas appear on either side of NA. The strongest positive anomaly is shown over Alaska and northwestern Canada (+3.6 mb), and the other covers much of eastern Canada and some parts of eastern US, as well as parts of southern Greenland (+2.0 mb). Although this positive anomaly is larger, it is weaker than the one found over Alaska. Negative anomaly areas appear over the CAA, the western US, and out in the Pacific Ocean. The T2m composite map is shown in **Figure 72e** and the anomaly map in **Figure 72f.** Much of the northwestern part of Canada and all of Alaska are covered by a negative anomaly (-4°C); however, other smaller negative anomaly areas appear over central and eastern Canada and over southern Greenland. Positive anomalies are also shown over parts of the western US and northern Greenland. The PW climatology map is shown in **Figure 72g** and the PW anomaly map in **Figure 72h.** Most PW anomalies are confined to the US. The largest negative anomaly is shown over Alaska, though another appears over the southeastern tip of the US. A large positive anomaly is shown reaching eastward from the Pacific Ocean to much of the US (+3.2 kg/m^2 at its strongest).

6.3.2 MINIMUM SIE VS. MAXIMUM GBI

6.3.2.1 CONTEMPORARY ANALYSIS

Composite maps for minimum SIE versus maximum GBI were created for the same contemporary months (May, June, and August), but used different years of overlap

for compositing, which can be found in **Table 9**. This minimum SIE-maximum GBI combination yielded five years of overlap for May, four common years for June, and five common years for August.

The composite maps for the month of May are shown in **Figure 73a-h**. The 500GPH climatology is shown in **Figure 73a** and the 500GPH anomaly is shown in **Figure 73b**. A large positive anomaly covers Greenland, the CAA, and parts of northwestern NA (+80 m). Two negative anomalies are also shown in either side of NA. The strongest negative anomaly is shown over southwestern Alaska (-60 m), though another negative anomaly covers much of the US and extends into the Atlantic Ocean. Atmospheric troughs are shown over Alaska, and parts of the US and the Atlantic Ocean. A large ridge appears to cover much of northern NA. The atmospheric flow appears mostly meridional. The MSLP climatology map is shown in **Figure 73c** and the MSLP anomaly map is shown in **Figure 73d**. Much of the Arctic region, including Greenland and the CAA are covered in a positive anomaly (+5 mb at its strongest), which closely resembles the 500GPH anomaly. The two negative MSLP anomalies are shown in Alaska and over much of the central eastern US (-4 mb). The anomaly over the eastern US also extends eastward into the Atlantic Ocean where it becomes stronger (-4 mb). The T2m climatology map is shown in **Figure 73e** and the T2m anomaly map in **Figure 73f**. A very large positive anomaly is shown over much of northern Canada, Alaska, and Greenland (+3.5°C at its strongest). The PW climatology map is shown in **Figure 73g** and the PW anomaly map in **Figure 73h**. Like the T2m map, the positive PW anomalies are mostly confined to northern Canada, Alaska, and Greenland. A large negative anomaly is situated over much of central NA.

The composites for the month of June are shown in **Figure 74a-h**. The 500GPH climatology map is shown in **Figure 74a** and the 500GPH anomaly map in **Figure 74b**. Two large and strong closed positive anomalies are shown; the first is situated off the southern coast of Alaska in the Pacific Ocean, and the other covers parts of northeastern Canada and the CAA, as well as Greenland. The strongest positive anomaly region reaches +100 m and is situated over the Baffin Bay. Two small negative anomalies appear as well, though only one touches the eastern coast of NA. There are two atmospheric ridges, one over the Pacific Ocean, south of Alaska, and the other over Baffin Bay. These could be indicative of meridional flow. The MSLP climatology map is shown in **Figure 74c** and the MSLP anomaly map is shown in **Figure 74d**. The largest and strongest positive anomaly covers the CAA, parts of northeastern Canada, and Greenland, though another appears off the southern coast of Alaska in the Pacific Ocean (+5 mb at its strongest). The largest negative anomaly covers central and eastern Canada and the US. Another negative anomaly is shown off the northern coast of Alaska. The T2m climatology map is shown in **Figure 74e** and the T2m anomaly map is shown in **Figure 74f**. Very few negative anomalies appear for this month. The positive anomalies span much of the US, northern and eastern Canada, and Greenland (reaching +4°C at their strongest). The PW climatology map is shown in **Figure 74g** and the PW anomaly in **Figure 74h**. Negative anomalies appear over much of the US (-3 kg/m^2 at their strongest), and positive anomalies cover much of northern and eastern Canada (+3 kg/m^2 at their strongest).

Lastly, the composites for the month of August are shown in **Figure 75a-h**. The 500GPH climatology map is shown in **Figure 75a** and the 500GPH anomaly map in

Figure 75b. A very large positive anomaly is shown over the CAA and Greenland, but also extends further westward (+90 m at its strongest). Another closed positive anomaly area appears over the Gulf of Alaska. A very slight negative anomaly is shown over central Canada. The largest atmospheric ridge shown is situated over the CAA, Baffin Bay, and Greenland, with a slight trough to the south. The flow appears mostly zonal. The MSLP climatology map is shown in **Figure 75c** and the MSLP anomaly in **Figure 75d**. The anomaly map reveals a very large positive anomaly covering much of northern Canada and Greenland (+4 mb at its strongest), and a negative anomaly over almost all of NA (-3 mb at its strongest). The negative anomaly is fairly weak, but strongest over the Hudson Bay. The T2m climatology is shown in **Figure 75e** and the T2m anomaly is shown in **Figure 75f**. Much of NA and Greenland are covered with positive anomalies, though the strongest positive anomalies appear over the CAA (+3.6°C). The PW climatology is shown in **Figure 75g** and the PW anomaly in **Figure 75h**. Many positive anomalies are shown over NA, reaching +3.6 kg/m^2 over the northeastern Canada and southeastern US. The only negative anomaly to appear is shown over a portion of the northwestern US.

6.3.2.2 LEAD-1 ANALYSIS

The lead-1 composites were created by jumping ahead by one month from the contemporary months. The composites for the month of June (one month ahead of the contemporary month of May) are shown in **Figure 76a-h**. The 500GPH climatology map is shown in **Figure 76a** and the 500GPH anomaly map in **Figure 76b**. Two large positive anomalies appear over parts of NA, the largest of which is situated over much of northern and northeastern Canada as well as Greenland. This anomaly is strongest over Greenland,

reaching +40 m. The next largest positive anomaly is shown over both the Bering Sea and the Pacific Ocean. Three negative anomaly areas are also shown: the first over the Gulf of Alaska and parts of the northwestern US, the second over a part of the eastern US, and the last over the Atlantic Ocean, off the western coast of Canada. Atmospheric ridging is shown over the Bering Sea and Pacific Ocean, as well as northeastern NA and Greenland. Several troughs appear over northwestern NA, southeastern US, and in the Atlantic Ocean to the east of NA. Altogether these create very wavy (meridional) atmospheric flow. The MSLP climatology map is shown in **Figure 76c** and the MSLP anomaly map in **Figure 76d**. The anomaly map shows an extensive positive anomaly covering Greenland, northern CAA, and parts of the high Arctic (+2.4 mb at its strongest). Another positive anomaly is shown over the Bering Sea and southwestern Alaska. Much of the rest of the map shows negative anomalies, the largest of which covers much of NA (-1.6 mb at its weakest). This anomaly appears connected to another large negative anomaly over the Atlantic Ocean, though at its strongest only reaches 2 mb below average. The T2m climatology map is shown in **Figure 76e** and the T2m anomaly map is shown in **Figure 76f**. Much of the map shows positive anomalies over NA and Greenland, with the strongest anomalies appearing over northeastern Canada (+3.2°C). Two very small and weak negative anomalies are shown over northwestern US and a small area of the Atlantic Ocean. Lastly, the PW climatology map is shown in **Figure 76g** and the PW anomaly map is shown in **Figure 76h**. The anomaly map shows a very large positive anomaly over parts of central and eastern Canada, as well as the Baffin Bay and the Greenland coastline. The negative PW anomaly covers almost all the US, reaching -4 kg/m^2

The composite maps for the month of July (one month ahead of the contemporary month of June) are shown in **Figure 77a-h**. The 500GPH climatology map is shown in **Figure 77a** and the 500GPH anomaly map in **Figure 77b**. The 500GPH anomaly map shows an expansive positive anomaly over parts of central and western Canada, which reaches across the CAA into the Baffin Bay and Greenland. The strongest anomaly area of +60 m appears over the Baffin Bay. Another positive anomaly appears in the Pacific Ocean off the southwestern coast of Alaska, though much of Alaska is covered by a negative anomaly. Another much smaller and weak negative anomaly appears in eastern Canada. There are several atmospheric troughs over the Chukchi Sea and Alaska, and another very small trough over eastern Canada. The largest ridge is shown over Baffin Bay. These troughs and ridges created meridional atmospheric flow patterns. The MSLP climatology map is shown in **Figure 77c** and the MSLP anomaly map in **Figure 77d**. The anomaly map reveals a large positive anomaly stretching from the upper Arctic into the CAA and across Greenland, where the anomaly is strongest at +3.6 mb. An extensive negative anomaly is also shown reaching from the Chukchi Sea, across Alaska, into central Canada and the US, and finally settling over the eastern side of the NA continent. The T2m climatology is shown in **Figure 77e** and the T2m anomaly in **Figure 77f**. The positive anomaly area shown in the composite map appears to cover almost the entire NA landmass and much of Greenland, though the strongest anomaly areas are shown over the CAA region at +3.6°C. The only negative anomaly covers southern Alaska, though it is a weak anomaly. The PW climatology is shown in **Figure 77g** and the PW anomaly in **Figure 77h**. Similar to the T2m anomaly map, the PW anomaly map shows various positive anomaly areas covering much of NA, and parts of Greenland and the high Arctic,

as well as over the Pacific and Atlantic Oceans, which reach +3.6 kg/m^2 at their strongest. Two of the strongest positive anomaly regions appear over eastern US and a region of the Atlantic Ocean off the eastern coast of Canada. The largest negative anomalies are shown for southwestern Alaska and a small portion of the western US.

Finally, the composites for the month of September (one month ahead of the contemporary month of August) are shown in **Figure 78a-h**. The 500GPH climatology map is shown in **Figure 78a** and the 500GPH anomaly map in **Figure 78b**. The northern Arctic and much of the NA continent are covered by positive anomaly areas, with the strongest areas over the Hudson Bay and eastern Canada reaching +24 m. Two negative anomalies also appear. The first is over the Bering Sea, which extends into the Gulf of Alaska, and the second spans much of the CAA and Greenland. There appears to be a trough, ridge, trough pattern for this month. The first trough is situated over Alaska, then a ridge over much of NA, and troughing over the CAA and Greenland. Atmospheric flow appears to be meridional. The MSLP climatology map is shown in **Figure 78c**, and the MSLP anomaly map is shown in **Figure 78d**. A large negative anomaly is shown over much of the northern NA continent and Greenland, which also extends outward into the surrounding bodies of water and reaches -3.2 mb in the Atlantic Ocean. Another very weak negative anomaly is shown over a small area of the northeastern US. A large positive anomaly area is shown from the Pacific Ocean, across the western US and the Gulf of Mexico, and into the Atlantic Ocean. Another smaller positive anomaly is shown over northeastern Canada. The T2m climatology map is shown in **Figure 78e** and the T2m anomaly map in **Figure 78f**. An extensive positive anomaly is shown reaching from the Beaufort and Chukchi Seas to cover much of NA, as well as over Baffin Bay and

parts of Greenland. The anomaly appears strongest over the Chukchi and Beaufort Seas, and some parts of the CAA (+3.5°C at its strongest). The PW climatology map is shown in **Figure 78g** and the PW anomaly map in **Figure 78h**. There appears to be both positive and negative anomalies over NA, though the positive anomalies are stronger and cover a larger area, reaching +2.8 kg/m^2. Much of the southern and eastern US are covered with positive anomalies, as well as central Canada, and northwestern Alaska.

6.3.2.3 LEAD-2 ANALYSIS

For the lead-2 analysis, the composite maps were produced by jumping forward two months from the contemporary months. First are the composites for the month of July (two months ahead of the contemporary month of May), which are shown in **Figure 79a-h**. The 500GPH climatology map is shown in **Figure 79a** and the 500GPH anomaly map in **Figure 79b**. A large negative anomaly reaches from the Chukchi Sea region through Alaska and into the CAA, where it is strongest at -50 m. A positive anomaly extends southward from the upper Arctic region over Greenland and into eastern Canada. Another slight positive anomaly appears over the northwestern US. An atmospheric trough appears over CAA, while a ridge is situated northward in the high Arctic and eastward over Greenland. There is zonal flow over northern NA and then meridional flow over northeast NA. The MSLP climatology composite is shown in **Figure 79c** and the MSLP anomaly composite in **Figure 79d**. An extensive negative anomaly extends from the Chukchi Sea region across of the NA continent, though it appears to be strongest over northeastern Canada (-2.8 mb). The largest positive anomaly appears over the high Arctic region (at +2.8 mb), but extends southward over parts of Greenland. The T2m climatology map is shown in **Figure 79e** and the T2m anomaly map in **Figure 79f**. A

very large positive anomaly is shown over much of the US, which extends upward into northern Canada and over into Greenland reaching +2.8°C at its strongest. Two smaller though strong positive anomalies appear over the northern coast of Alaska and the Beaufort Sea. A negative anomaly also appears over eastern Alaska and reaches up into the CAA. The PW climatology is shown in **Figure 79g** and the PW anomaly in **Figure 79h**. Large positive anomaly areas appear over much of the southern and eastern areas of NA, though a weaker anomaly area also appears for a portion of central Canada. The Baffin Bay region and Greenland are also covered with a large positive PW anomalies. The only land areas with large negative anomalies include parts of western and central US, southwestern Alaska, and the western CAA.

Composites for the month of August (two months ahead of the contemporary month of June) are shown in **Figure 80a-h**. The 500GPH climatology is shown in **Figure 80a** and the 500GPH anomaly is shown in **Figure 80b**. A very large and strong positive anomaly is shown over northeastern Canada, including the CAA and Hudson Bay. The anomaly also extends over the Baffin Bay, Greenland, and southwest into the western US and Pacific Ocean. At its strongest, the positive anomaly reached +50 m, while two much smaller and weaker negative anomalies also appear. The larger of the two is situated over western Alaska and the surrounding bodies of water, including the Chukchi and Bering seas, and the Gulf of Alaska. A very large atmospheric ridge appears over northeastern NA (+50 m), and a very slight trough over Alaska. The MSLP climatology composite is shown in **Figure 80c** and the MSLP anomaly composite in **Figure 80d**. A very large negative anomaly is shown, which covers much of NA and some of the eastern Greenland coastline. The strongest negative anomalies are shown over the Chukchi and

Beaufort Seas as well as the Atlantic Ocean, reaching -2.3 mb. The smaller though much stronger positive anomaly is situated over northeastern Canada, the Baffin Bay, and much of Greenland reaching +2.5 mb. Another slight positive anomaly appears in the Pacific Ocean. The T2m climatology is shown in **Figure 80e** and the T2m anomaly map in **Figure 80f**. A very large positive anomaly can be seen over parts of the western US, much of Canada, and much of Greenland reaching +3°C at its strongest. Very small and weak negative anomalies appear as well over the central US, parts of Alaska, southern Greenland, and the largest area over a portion of the Pacific Ocean, off the southwestern coast of the US. The PW climatology map is shown in **Figure 80g** and the PW anomaly map in **Figure 80h**. Two large positive anomaly areas are shown, one over much of Canada and parts of Greenland, and another covering parts of the southern US, which also extends eastward over the Atlantic Ocean (3.6 kg/m^2 at their strongest). Negative anomalies are shown over western Alaska, an area of the Pacific Ocean, and the western and central US (-3.2 kg/m^2 at their strongest over the Pacific Ocean).

Lastly, the composite maps for the month of October (two months ahead of the contemporary month of August) are shown in **Figure 81a-h**. The 500GPH climatology map is shown in **Figure 81a** and the 500GPH anomaly map in **Figure 81b**. Two large positive anomalies appear, one over northwestern Alaska (the strongest at +40 m) and the other over northeastern Canada, which extends into the southwestern US. A strong, closed negative anomaly is also shown off the western coast of Canada and the US (-60 m). A large atmospheric trough appears over the Pacific Ocean, west of NA, while ridges appear north, east, and south of the trough. The atmospheric flow appears largely meridional. The MSLP climatology map is shown **Figure 81c** and the MSLP anomaly

map in **Figure 81d**. The anomaly map shows an extensive negative anomaly stretching from the Bering Sea region across the Pacific Ocean and central NA into the Atlantic Ocean. The strongest regions of negative anomaly appear off the northwestern coast of the US and off the southern coast of Greenland (-3.2 mb at their strongest). Some positive anomaly areas appear over the Pacific Ocean and the CAA. The T2m climatology map is shown in **Figure 81e** and the T2m anomaly map in **Figure 81f**. There is an expansive positive anomaly covering much of NA, but the strongest positive anomaly occurs over the Chukchi and Beaufort Seas reaching +6°C. An additional positive anomaly is shown over much of eastern Greenland. The PW climatology map is shown in **Figure 81g** and the PW anomaly map in **Figure 81h**. Several positive anomalies can be seen over NA, Greenland, and the Atlantic Ocean. The strongest positive anomalies appear over the northeastern US and off the southeastern coast of the US (+5 kg/m^2 at its strongest off the Florida coast). There are also several negative anomalies shown with the strongest appearing over the southern US and in the Gulf of Mexico (-5 kg/m^2).

The composite maps showed several consistent anomaly patterns for those years of minimum SIE versus maximum GBI, though there is also some variation included with the lead months. The regions that showed the most persistent positive 500GPH and SLP anomalies include northern Canada and the CAA, Baffin Bay, Greenland, and occasionally, the Gulf of Alaska region. In contrast, there are fewer consistent negative anomalies appear for these variables, but generally, they appear over areas of central and eastern Canada and the US, and sometimes Alaska and western US and Canada. Positive T2m anomalies are more extensive and often cover much of NA, though this is likely due to the summer months observed. Lastly, PW anomalies are more mixed, but many of the

negative anomalies that do appear are over regions of the US.

Table 6. The top 10 values for maximum SIE and minimum GBI for Baffin Bay in January, March, October, and December. Values are listed from highest to lowest. Years of overlap are highlighted, and total counts are shown on the bottom row.

January			
SIE		GBI	
Yr	Max	Yr	Min
1993	1606297.16	2006	5072.61
1984	1603222.08	2002	5068.61
1983	1569060.67	1990	5044.57
1991	1449821.59	1988	5044.32
1985	1390831.72	1991	5037.18
1988	1378271.39	2015	5026.29
1990	1332963.43	1983	4998.55
1992	1300478.69	1989	4989.35
1994	1286078.02	1984	4982.19
1987	1274676.90	1993	4958.44
count: 6			

March			
SIE		GBI	
Yr	Max	Yr	Min
1993	1765671.94	1995	5113.89
1983	1720993.83	1997	5111.68
1984	1658777.57	2014	5099.37
1990	1651612.01	1982	5095.92
1985	1564700.43	2015	5074.75
1994	1554972.99	1993	5065.40
1991	1531833.75	1994	5056.08
1992	1523032.05	1990	5054.74
2008	1515616.76	1989	5014.95
1982	1487905.10	1986	5000.39
count: 4			

October			
SIE		GBI	
Yr	Max	Yr	Min
1986	411209.38	1989	5276.76
1996	395199.82	1984	5275.90
1983	344933.50	1999	5274.08
1982	312541.39	2015	5268.66
1990	299956.85	1987	5268.57
1997	293707.82	1990	5264.27
1987	260648.00	2000	5250.40
1995	260107.66	1983	5249.73
1989	247346.34	2018	5243.24
1994	230311.36	1986	5160.36
count: 5			

December			
SIE		GBI	
Yr	Max	Yr	Min
1982	1160506.11	2015	5080.59
1983	1122201.14	1988	5075.14
1984	1110308.56	1991	5069.25
1986	1091453.08	1990	5066.91
1992	1079252.85	1986	5065.30
1993	1037603.40	2013	5059.77
1987	1029848.89	1982	5053.70
1990	1027208.23	1984	5048.45
1991	965804.30	2004	5047.55
2015	951812.23	2011	5034.71
count: 6			

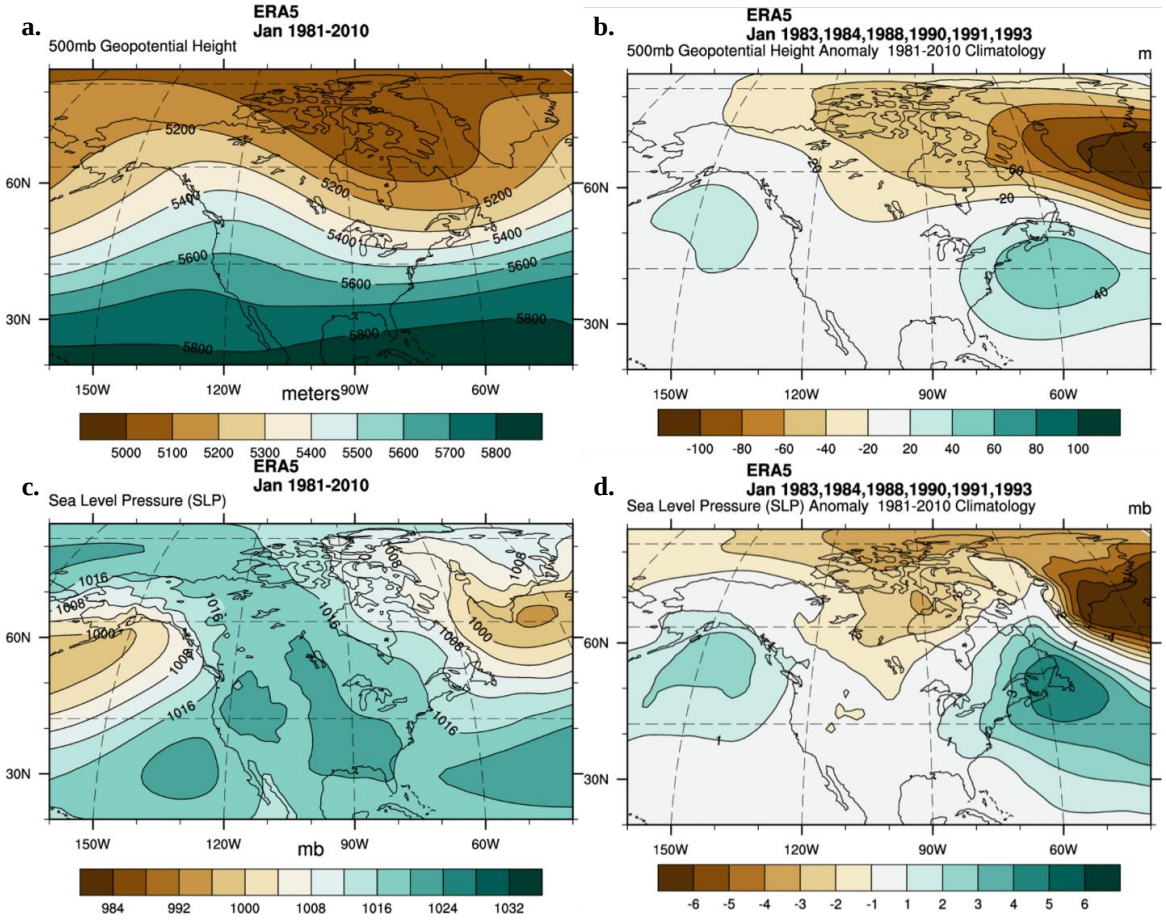

Figure 40. Baffin Bay contemporary January composites for maximum SIE and minimum GBI. The 500GPH composites are on top with the climatology shown in a) and the composite anomaly shown in b). The MSLP composites are on the bottom with the climatology shown in c) and the composite anomaly presented in d).

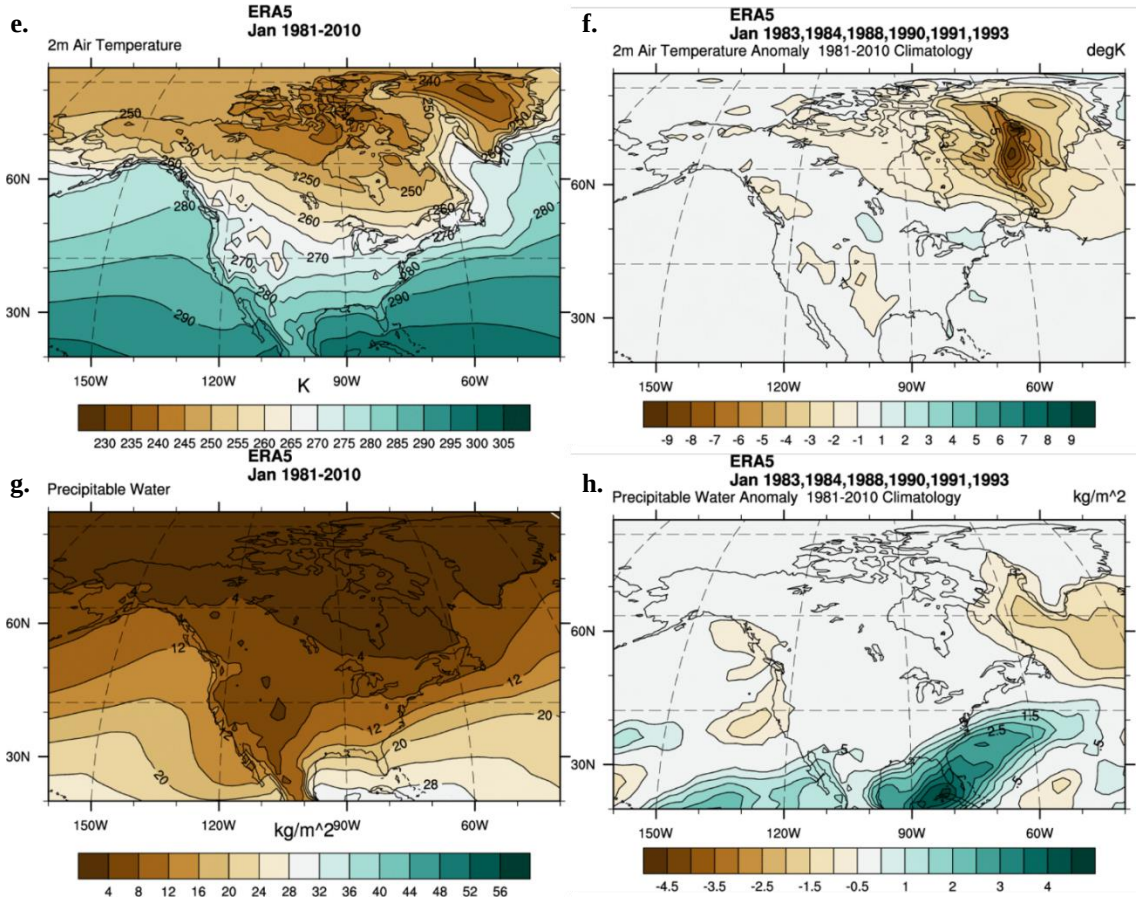

Figure 40. (cont.) Baffin Bay contemporary January composites for maximum SIE and minimum GBI. The T2m composites are on top with the climatology shown in e) and the composite anomaly shown in f). The PW composites are on the bottom with the climatology shown in g) and the composite anomaly presented in h).

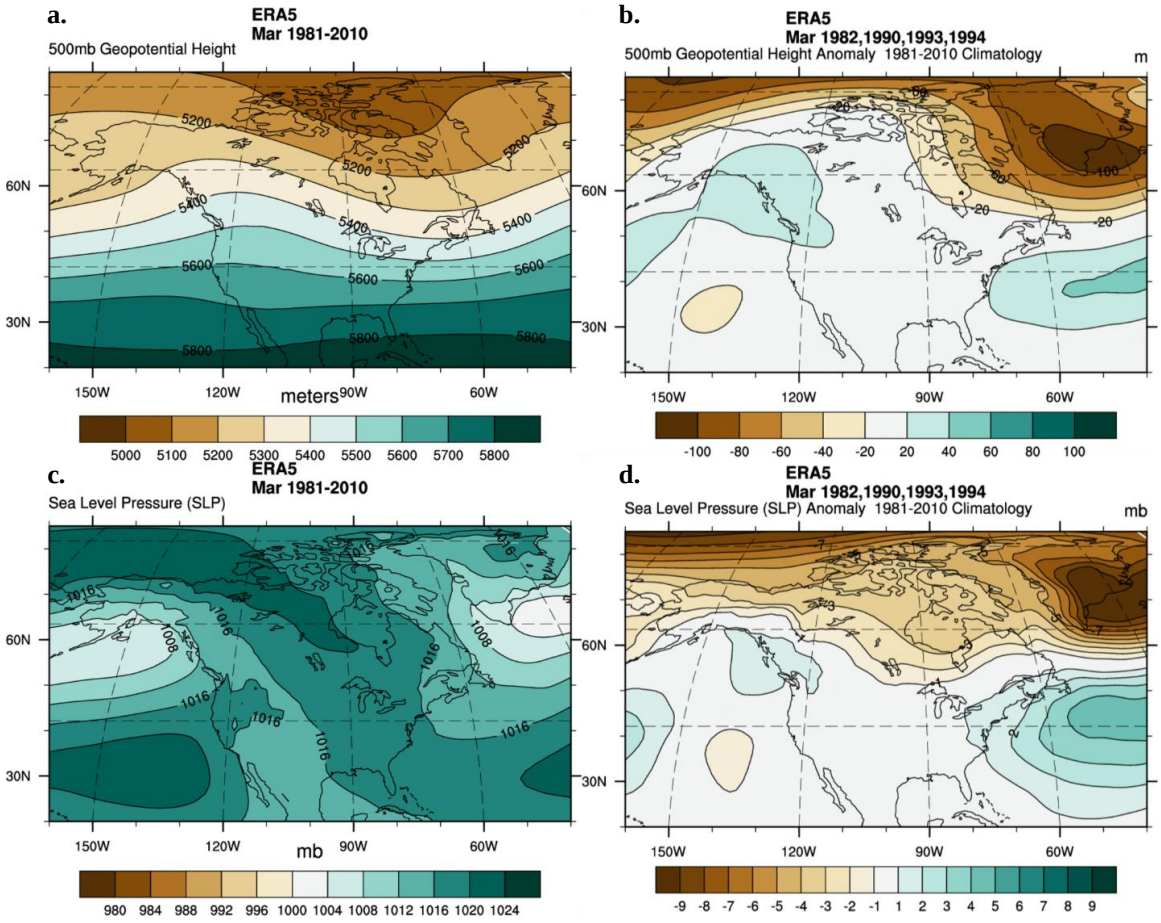

Figure 41. Baffin Bay contemporary March composites for maximum SIE and minimum GBI. The 500GPH composites are on top with the climatology shown in a) and the composite anomaly shown in b). The MSLP composites are on the bottom with the climatology shown in c) and the composite anomaly presented in d).

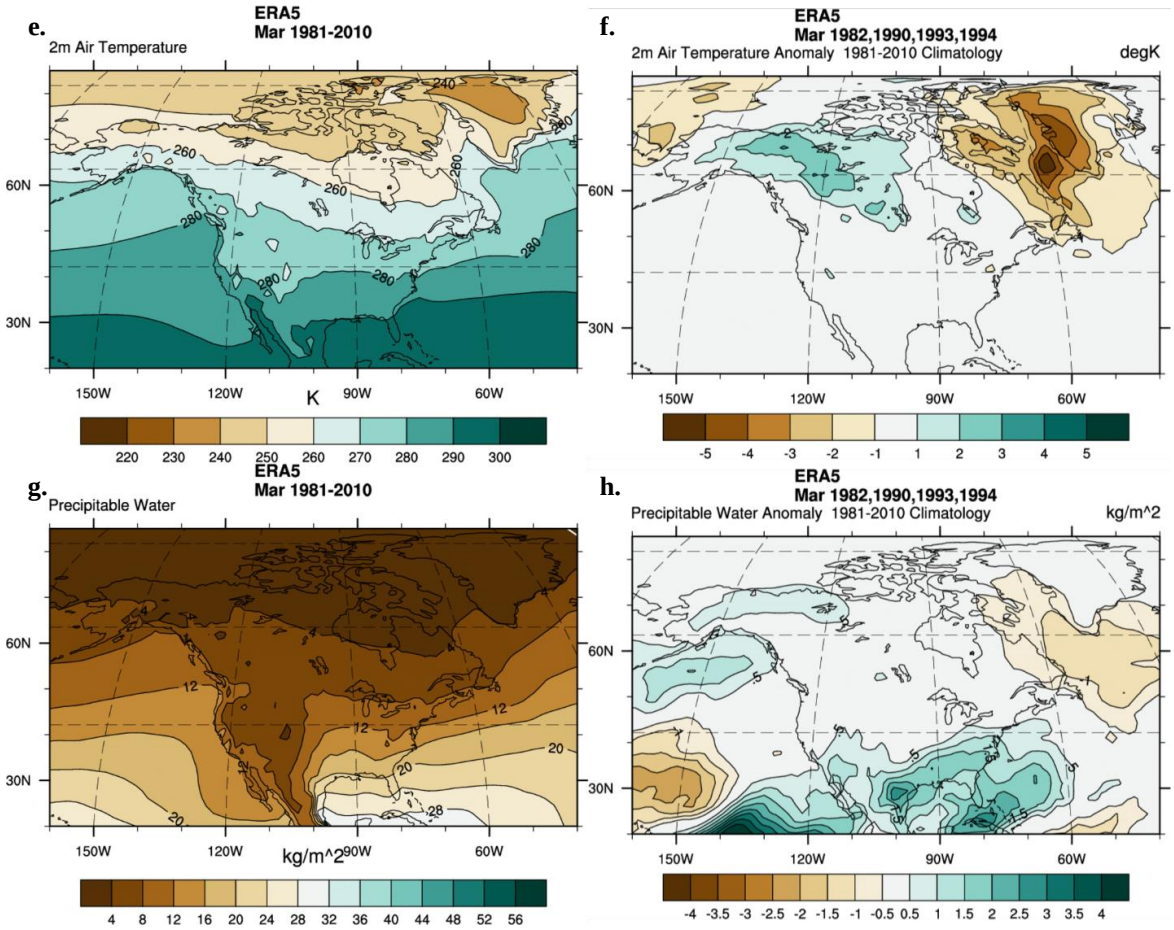

Figure 41. (cont.) Baffin Bay contemporary March composites for maximum SIE and minimum GBI. The T2m composites are on top with the climatology shown in e) and the composite anomaly shown in f). The PW composites are on the bottom with the climatology shown in g) and the composite anomaly presented in h).

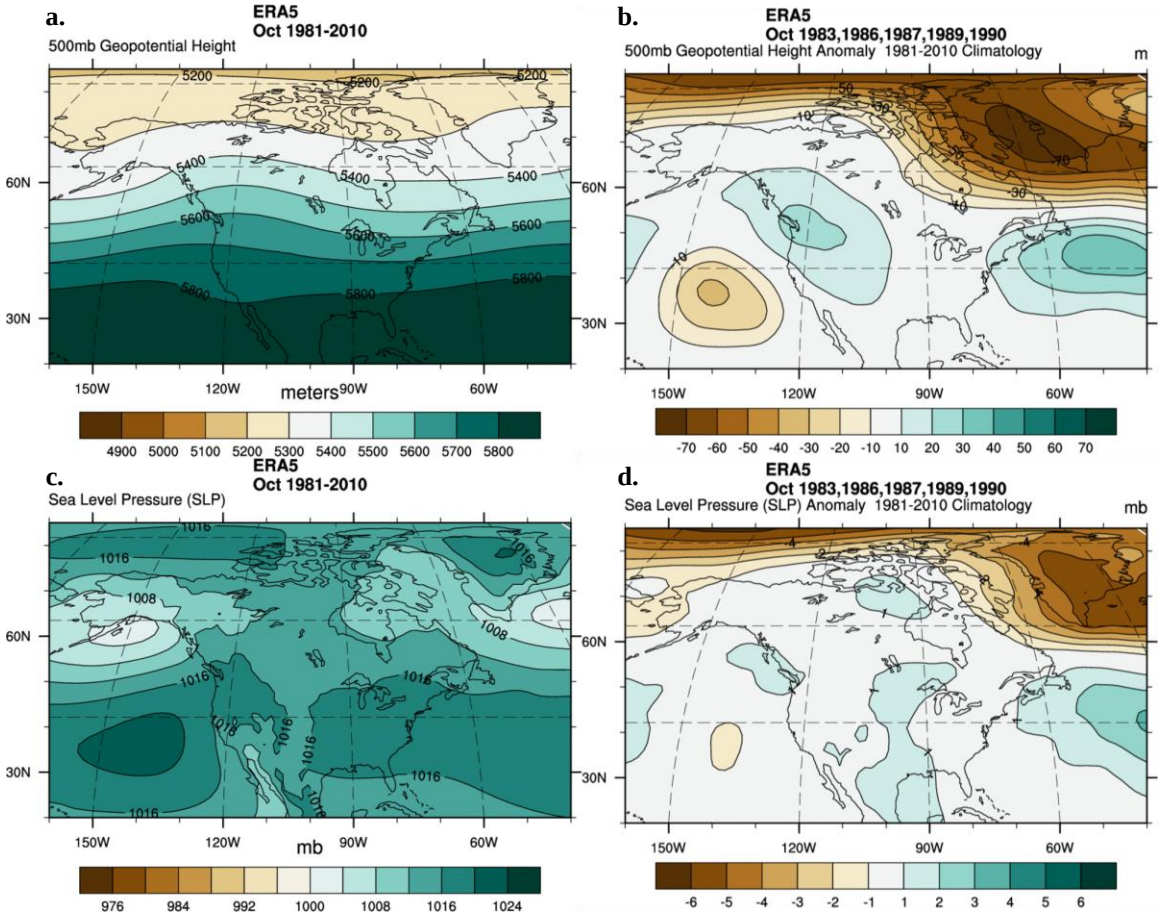

Figure 42. Baffin Bay contemporary October composites for maximum SIE and minimum GBI. The 500GPH composites are on top with the climatology shown in a) and the composite anomaly shown in b). The MSLP composites are on the bottom with the climatology shown in c) and the composite anomaly presented in d).

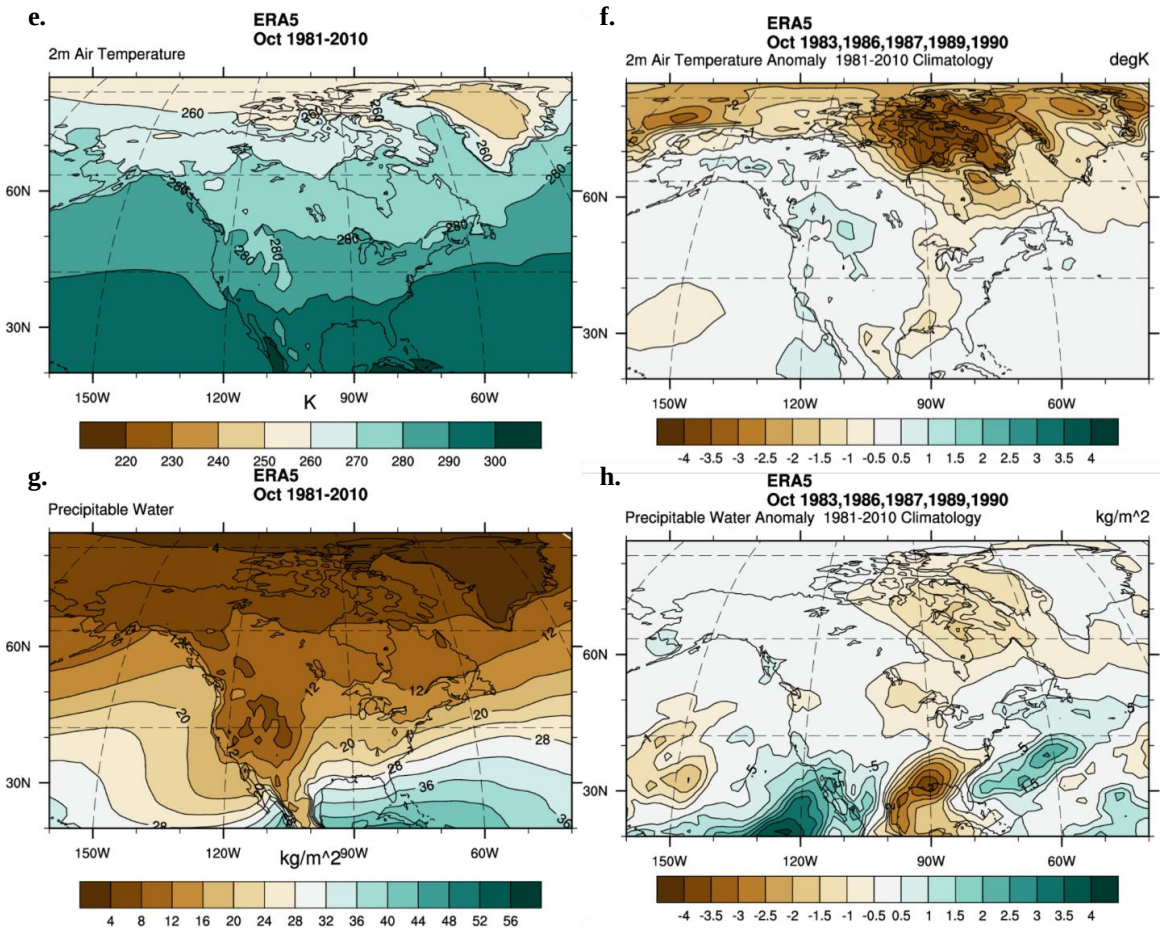

Figure 42. (cont.) Baffin Bay contemporary October composites for maximum SIE and minimum GBI. The T2m composites are on top with the climatology shown in e) and the composite anomaly shown in f). The PW composites are on the bottom with the climatology shown in g) and the composite anomaly presented in h).

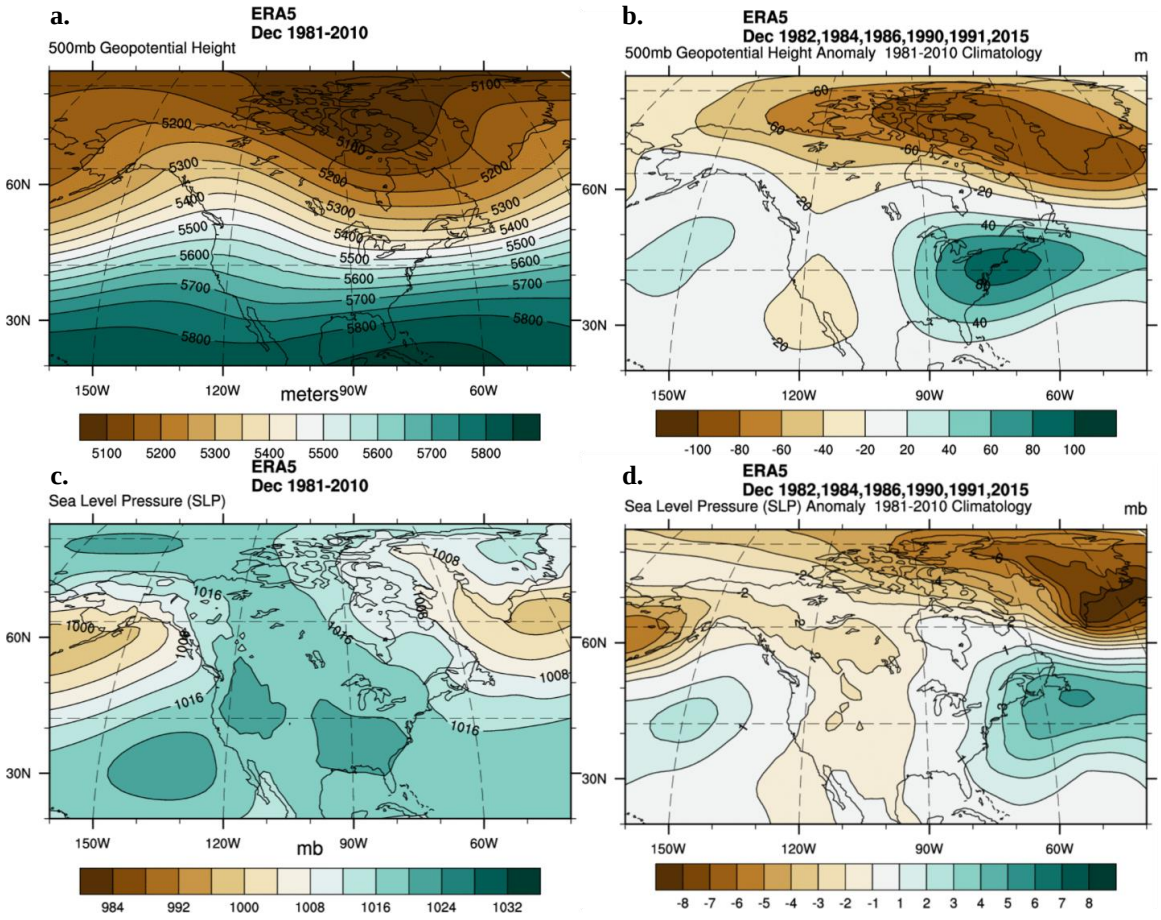

Figure 43. Baffin Bay contemporary December composites for maximum SIE and minimum GBI. The 500GPH composites are on top with the climatology shown in a) and the composite anomaly shown in b). The MSLP composites are on the bottom with the climatology shown in c) and the composite anomaly presented in d).

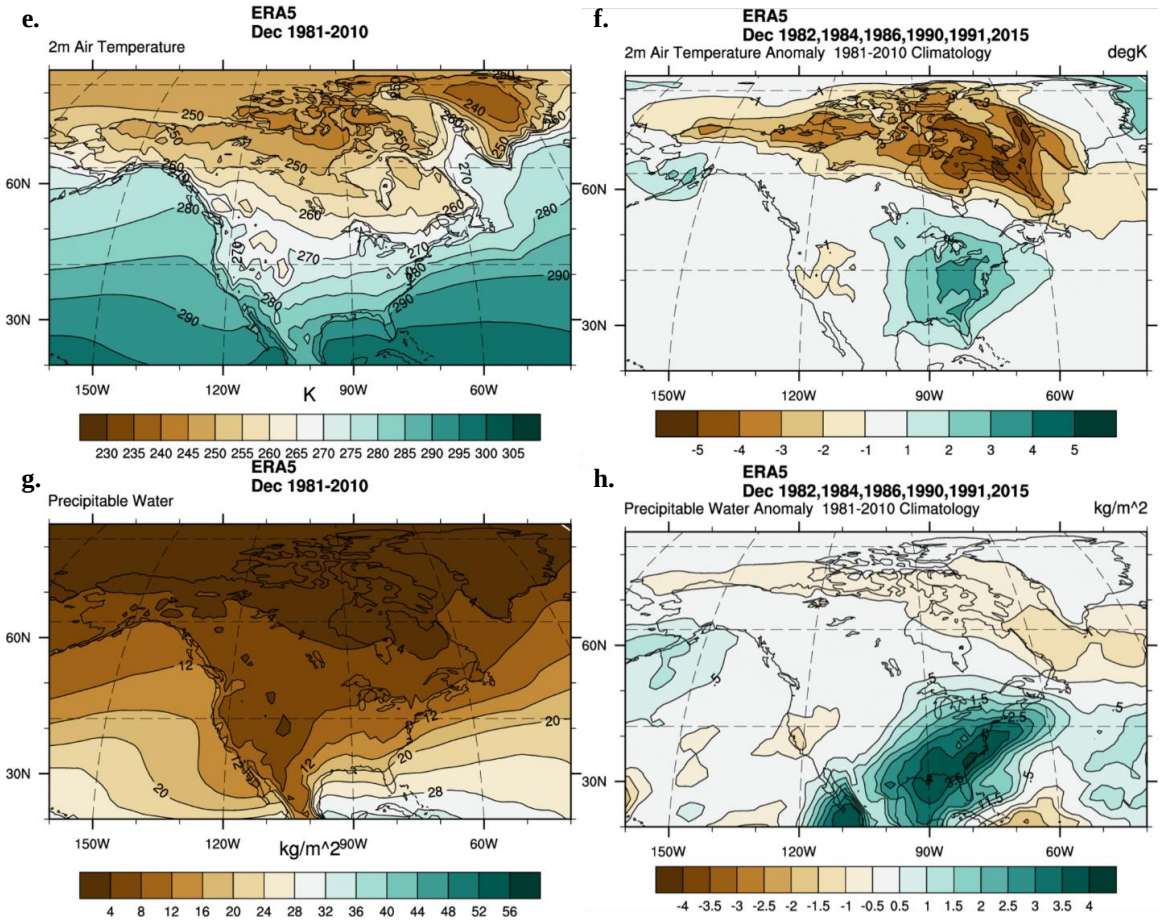

Figure 43. (cont.) Baffin Bay contemporary December composites for maximum SIE and minimum GBI. The T2m composites are on top with the climatology shown in e) and the composite anomaly shown in f). The PW composites are on the bottom with the climatology shown in g) and the composite anomaly presented in h).

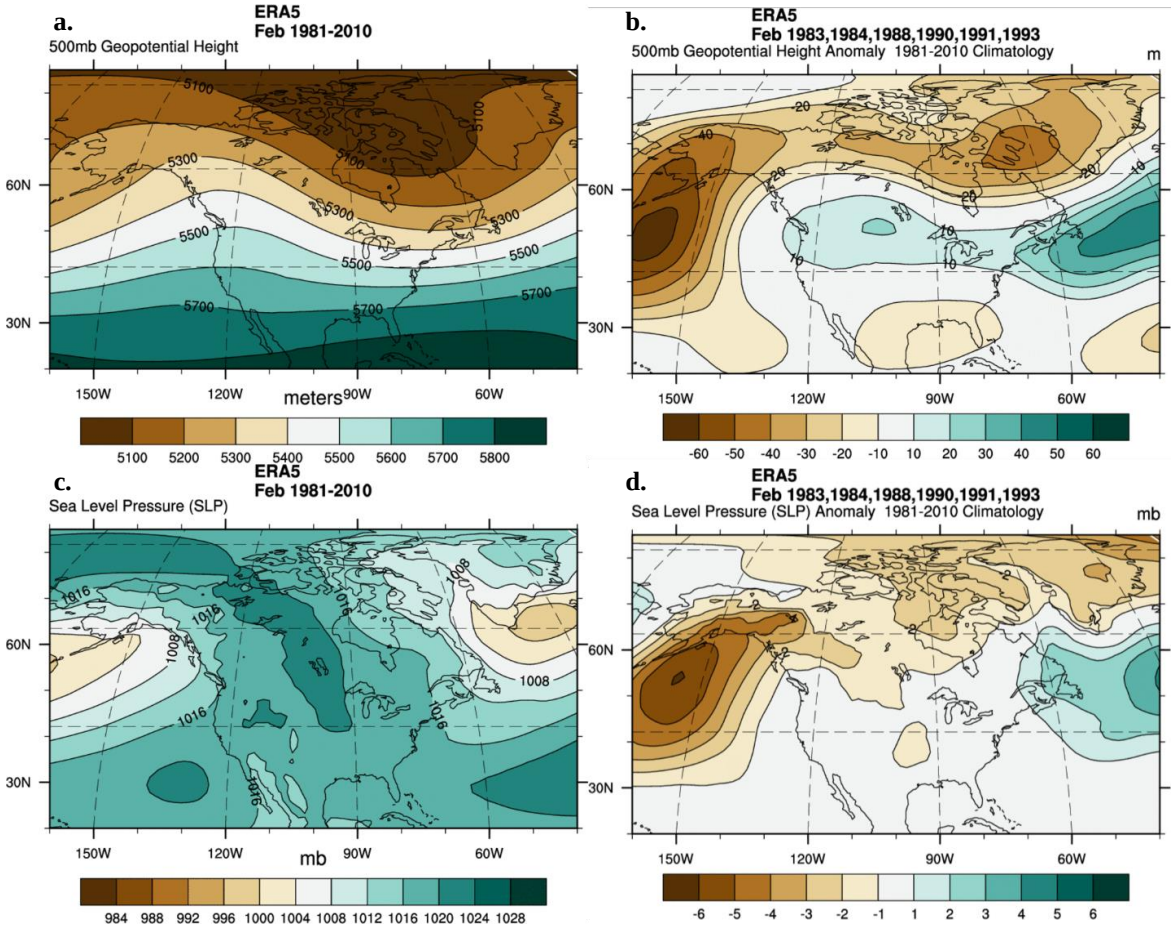

Figure 44. Baffin Bay lead-1 February composites for maximum SIE and minimum GBI. The 500GPH composites are on top with the climatology shown in a) and the composite anomaly shown in b). The MSLP composites are on the bottom with the climatology shown in c) and the composite anomaly presented in d).

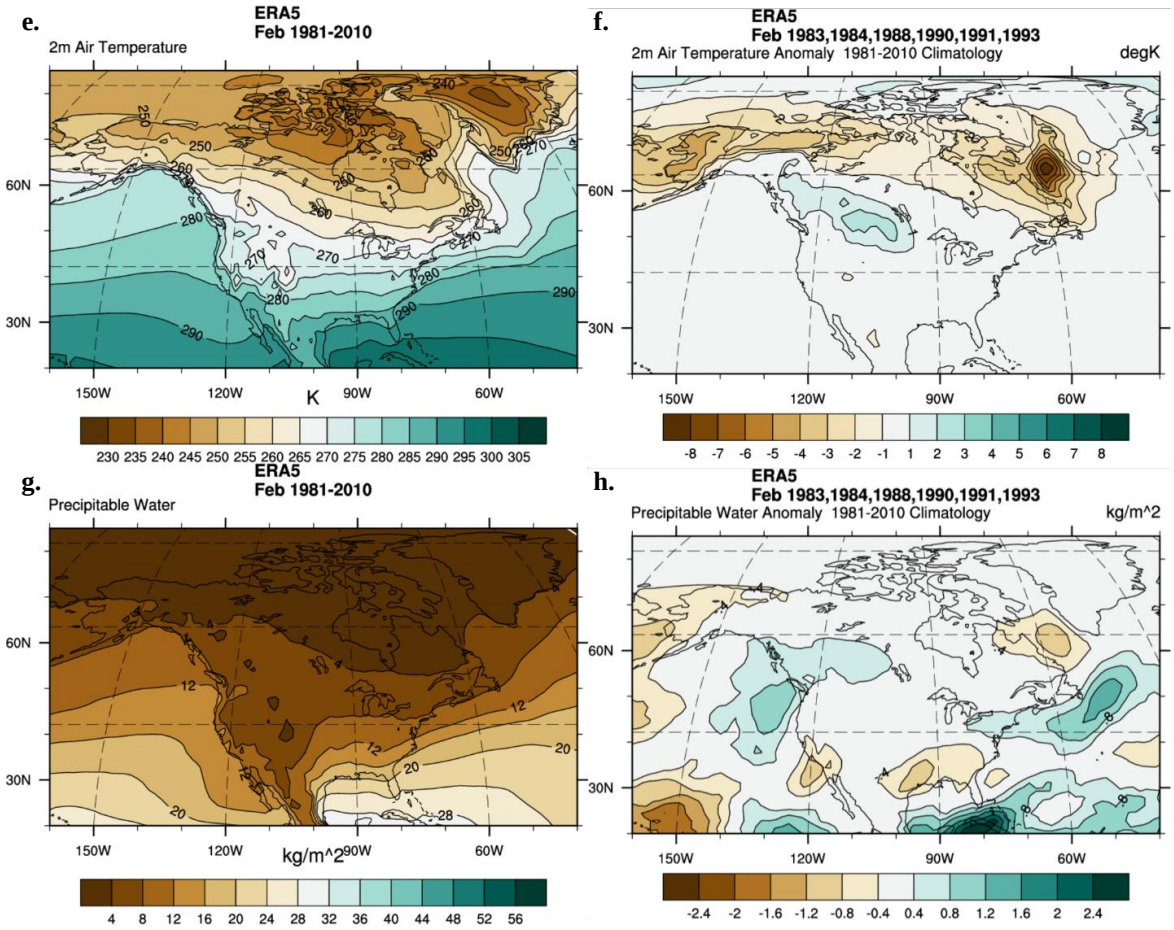

Figure 44. (cont.) Baffin Bay lead-1 February composites for maximum SIE and minimum GBI. The T2m composites are on top with the climatology shown in e) and the composite anomaly shown in f). The PW composites are on the bottom with the climatology shown in g) and the composite anomaly presented in h).

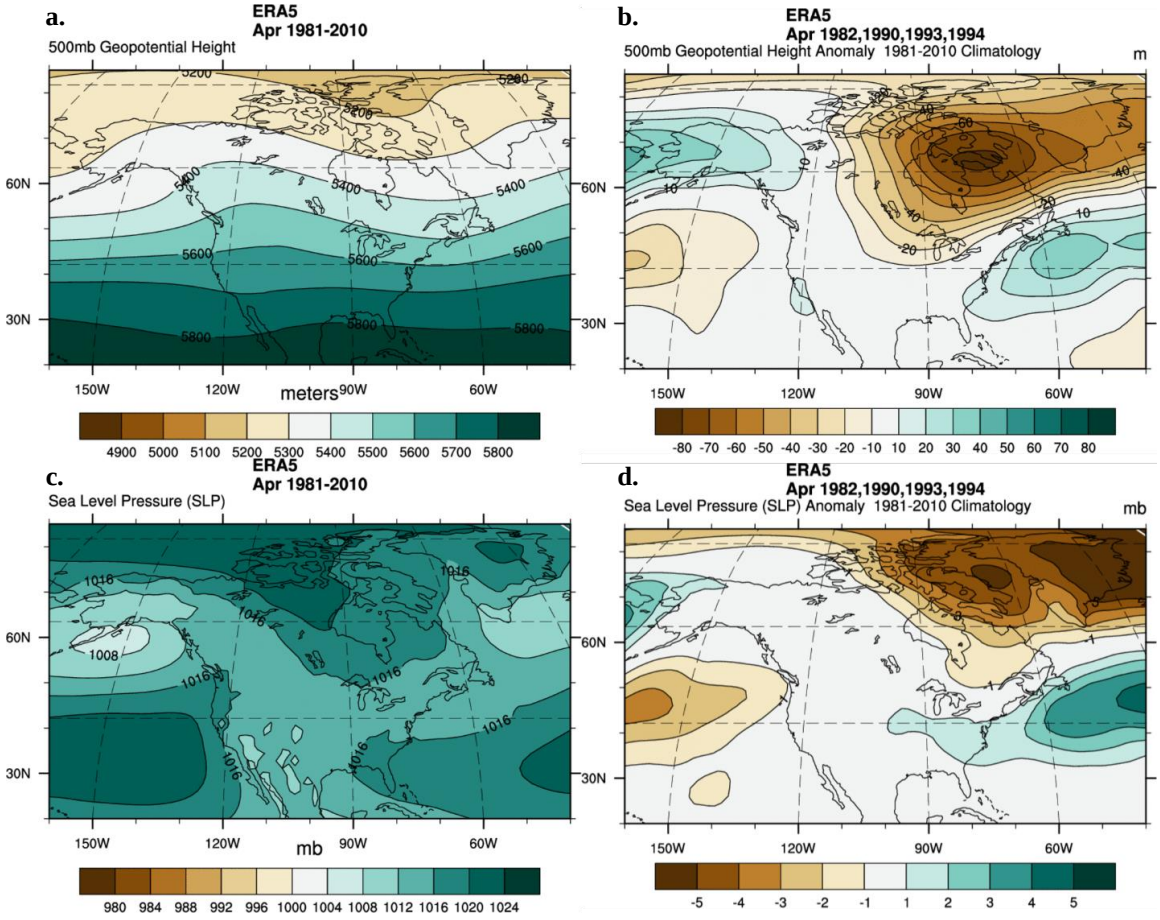

Figure 45. Baffin Bay lead-1 April composites for maximum SIE and minimum GBI. The 500GPH composites are on top with the climatology shown in a) and the composite anomaly shown in b). The MSLP composites are on the bottom with the climatology shown in c) and the composite anomaly presented in d).

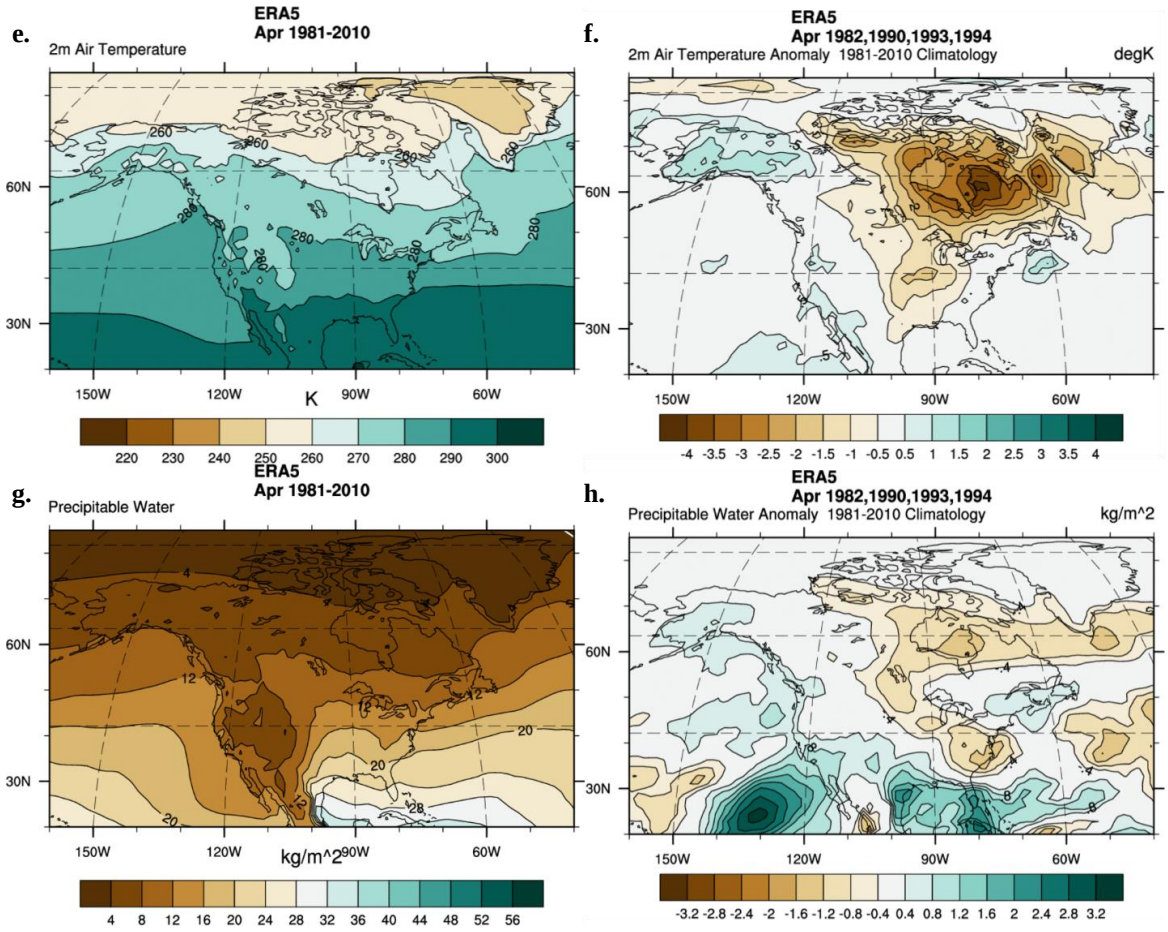

Figure 45. (cont.) Baffin Bay lead-1 April composites for maximum SIE and minimum GBI. The T2m composites are on top with the climatology shown in e) and the composite anomaly shown in f). The PW composites are on the bottom with the climatology shown in g) and the composite anomaly presented in h).

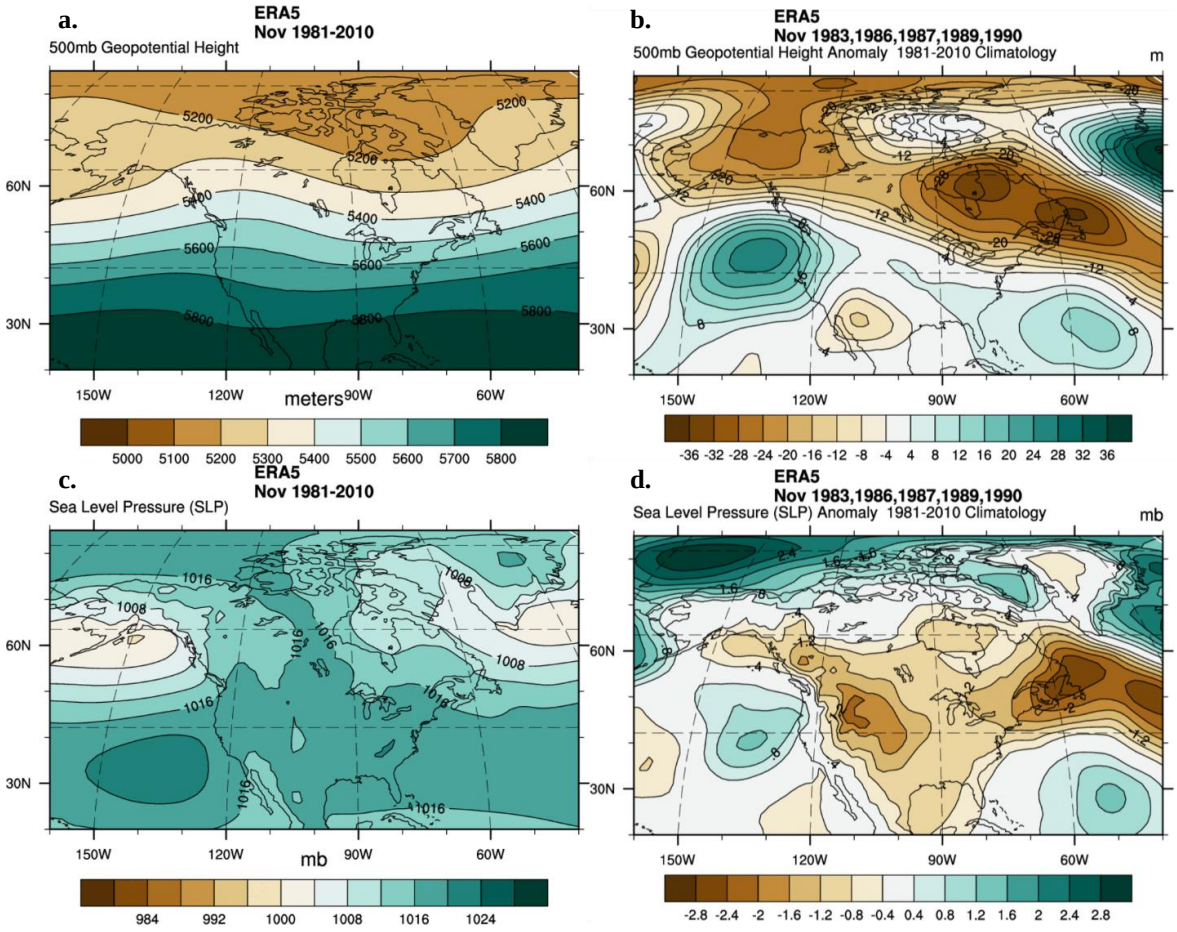

Figure 46. Baffin Bay lead-1 November composites for maximum SIE and minimum GBI. The 500GPH composites are on top with the climatology shown in a) and the composite anomaly shown in b). The MSLP composites are on the bottom with the climatology shown in c) and the composite anomaly presented in d).

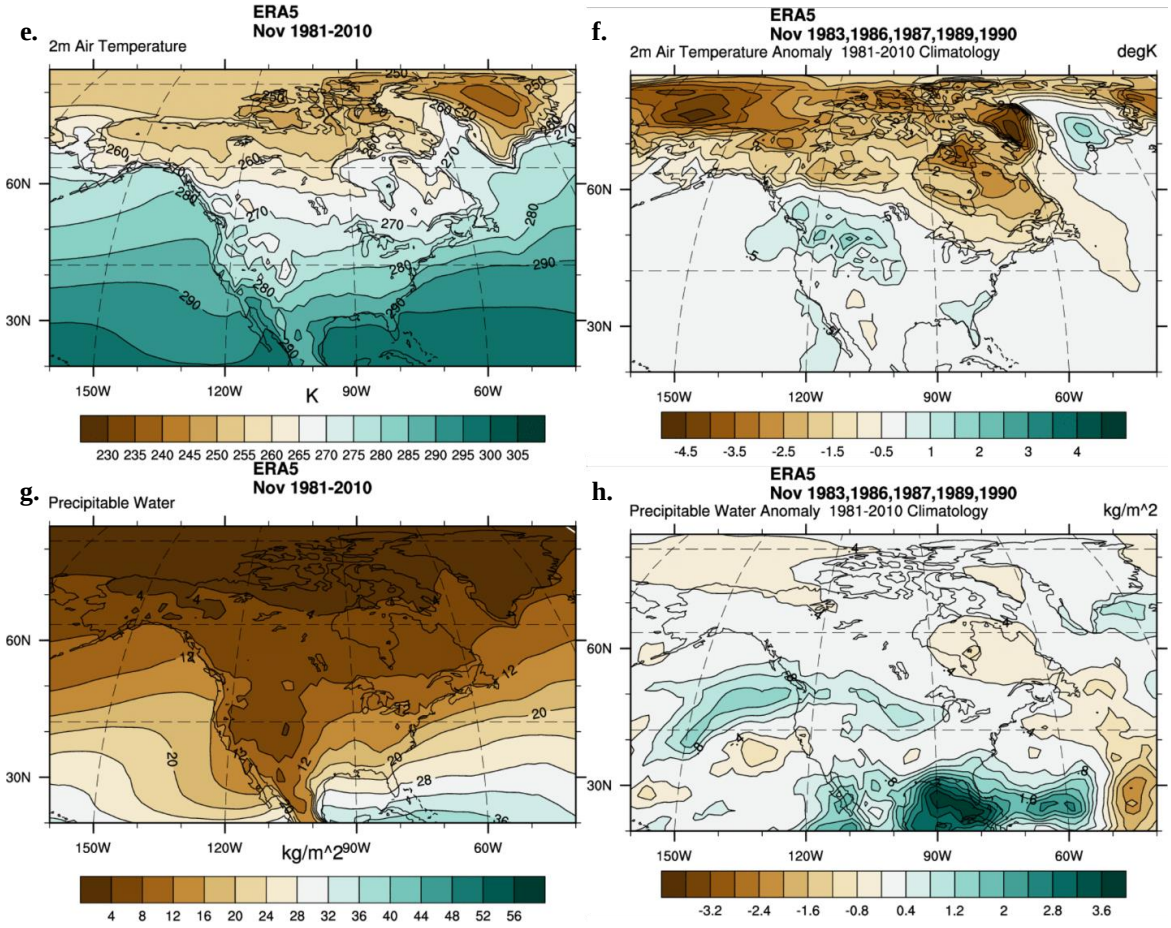

Figure 46. (cont.) Baffin Bay lead-1 November composites for maximum SIE and minimum GBI. The T2m composites are on top with the climatology shown in e) and the composite anomaly shown in f). The PW composites are on the bottom with the climatology shown in g) and the composite anomaly presented in h).

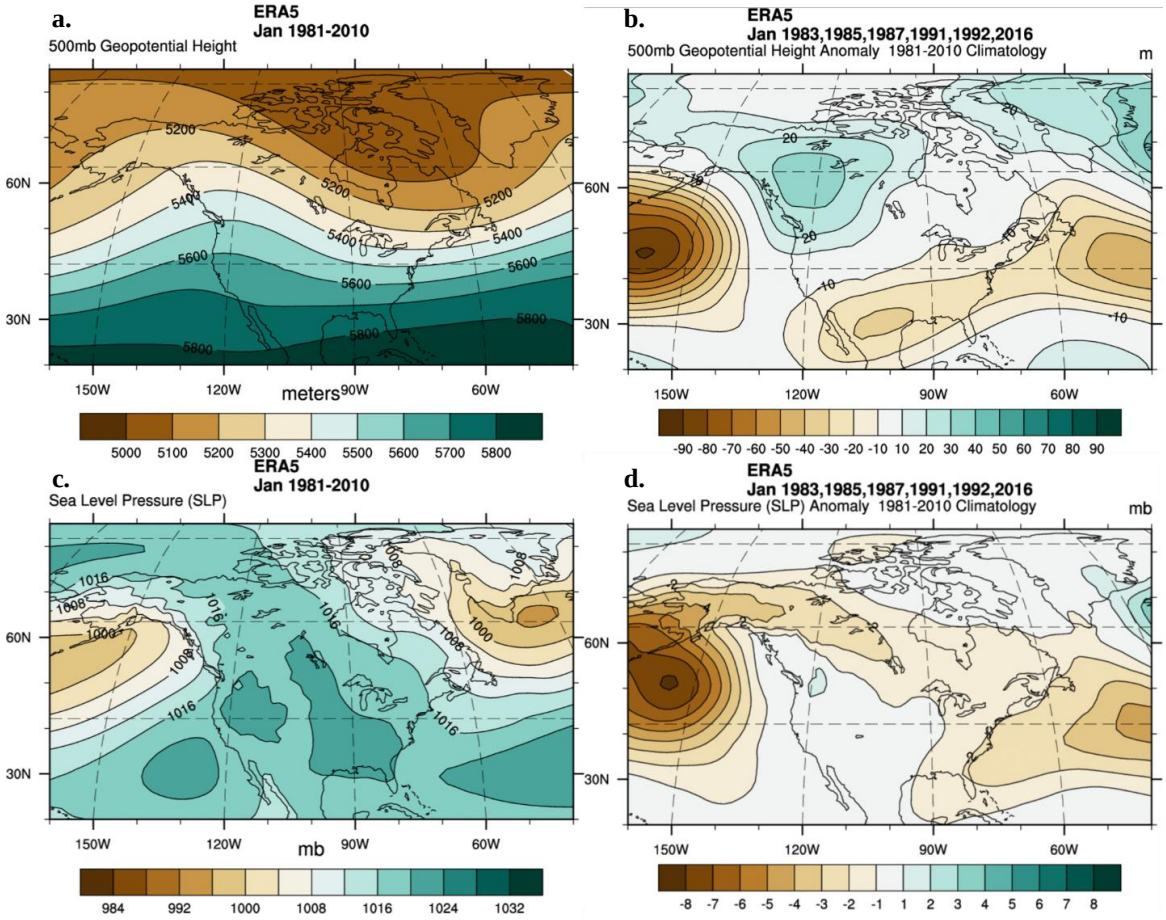

Figure 47. Baffin Bay lead-1 January composites for maximum SIE and minimum GBI. The 500GPH composites are on top with the climatology shown in a) and the composite anomaly shown in b). The MSLP composites are on the bottom with the climatology shown in c) and the composite anomaly presented in d).

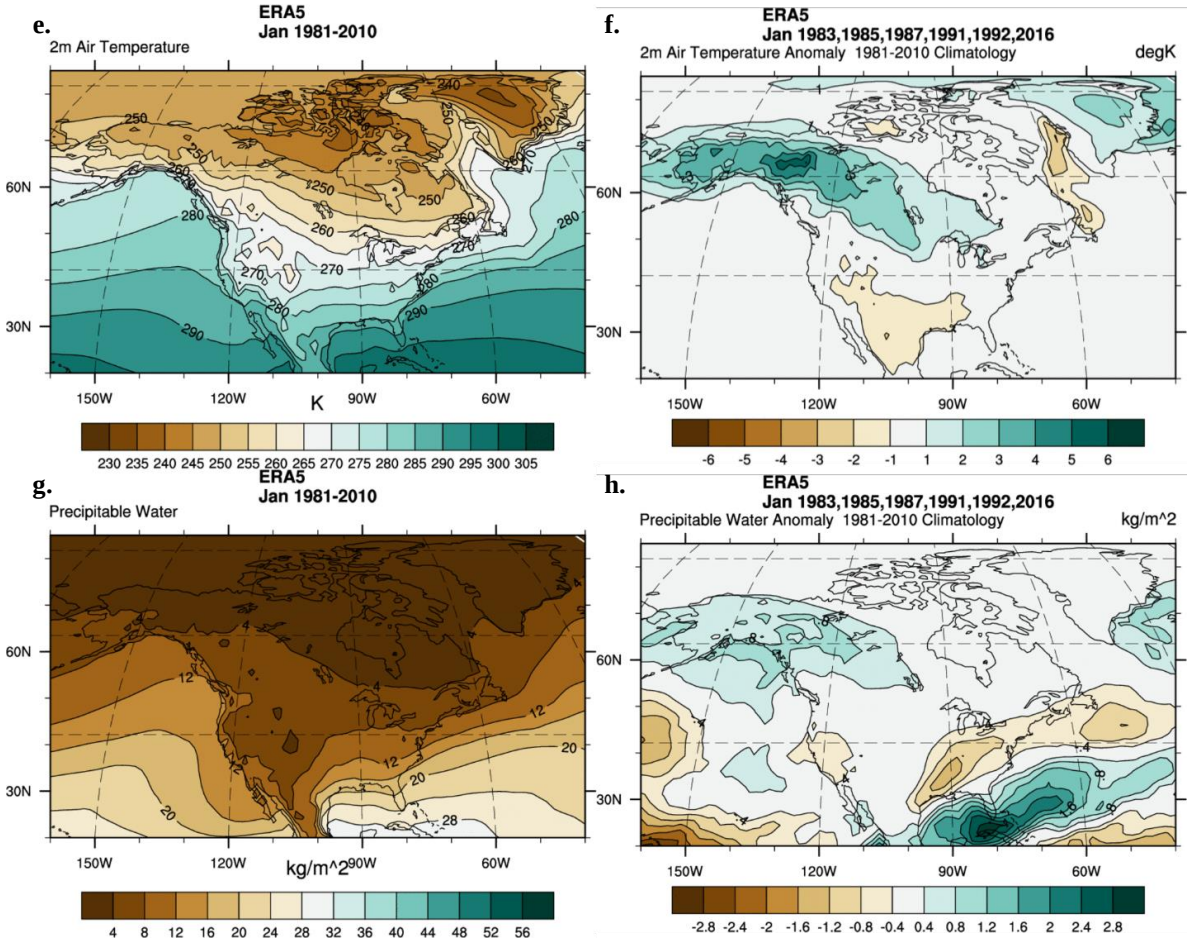

Figure 47. (cont.) Baffin Bay lead-1 January composites for maximum SIE and minimum GBI. The T2m composites are on top with the climatology shown in e) and the composite anomaly shown in f). The PW composites are on the bottom with the climatology shown in g) and the composite anomaly presented in h).

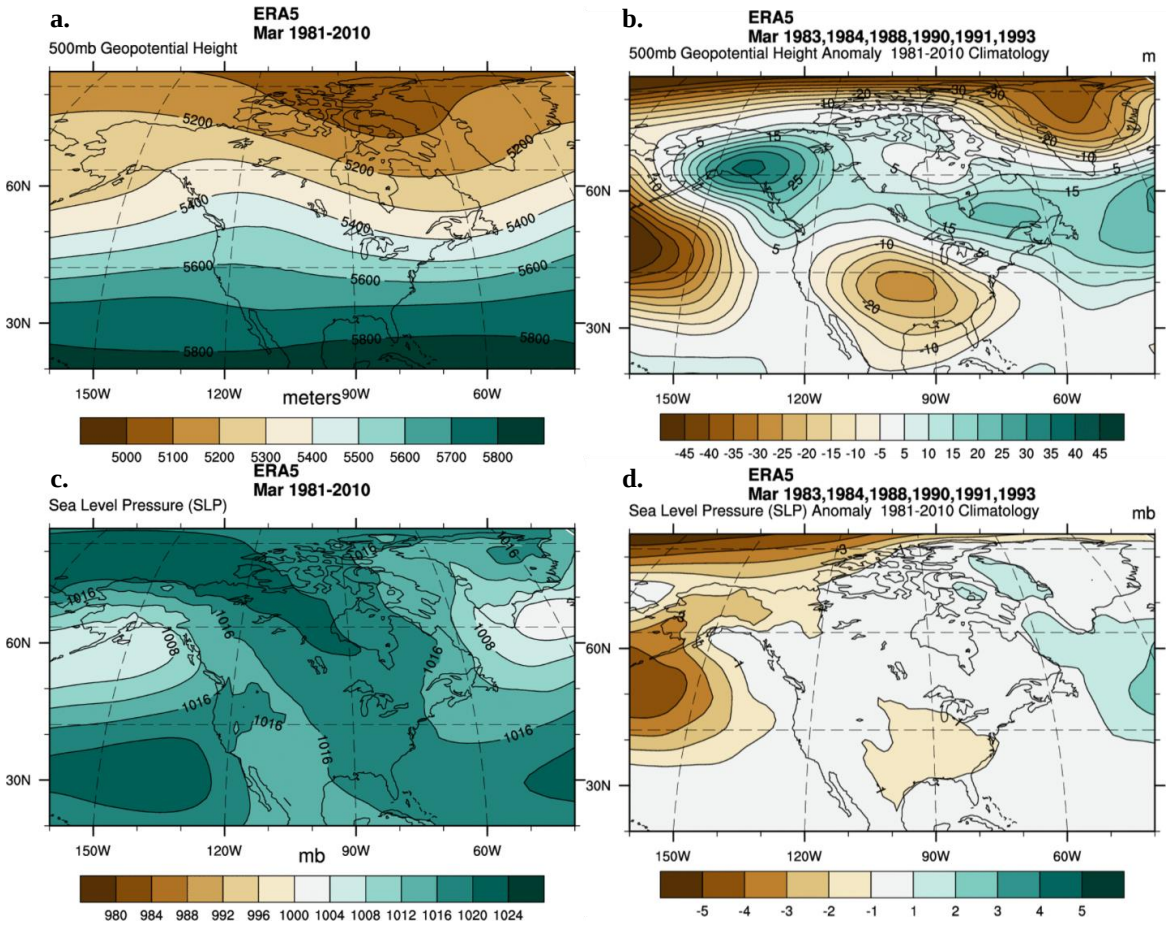

Figure 48. Baffin Bay lead-2 March composites for maximum SIE and minimum GBI. The 500GPH composites are on top with the climatology shown in a) and the composite anomaly shown in b). The MSLP composites are on the bottom with the climatology shown in c) and the composite anomaly presented in d).

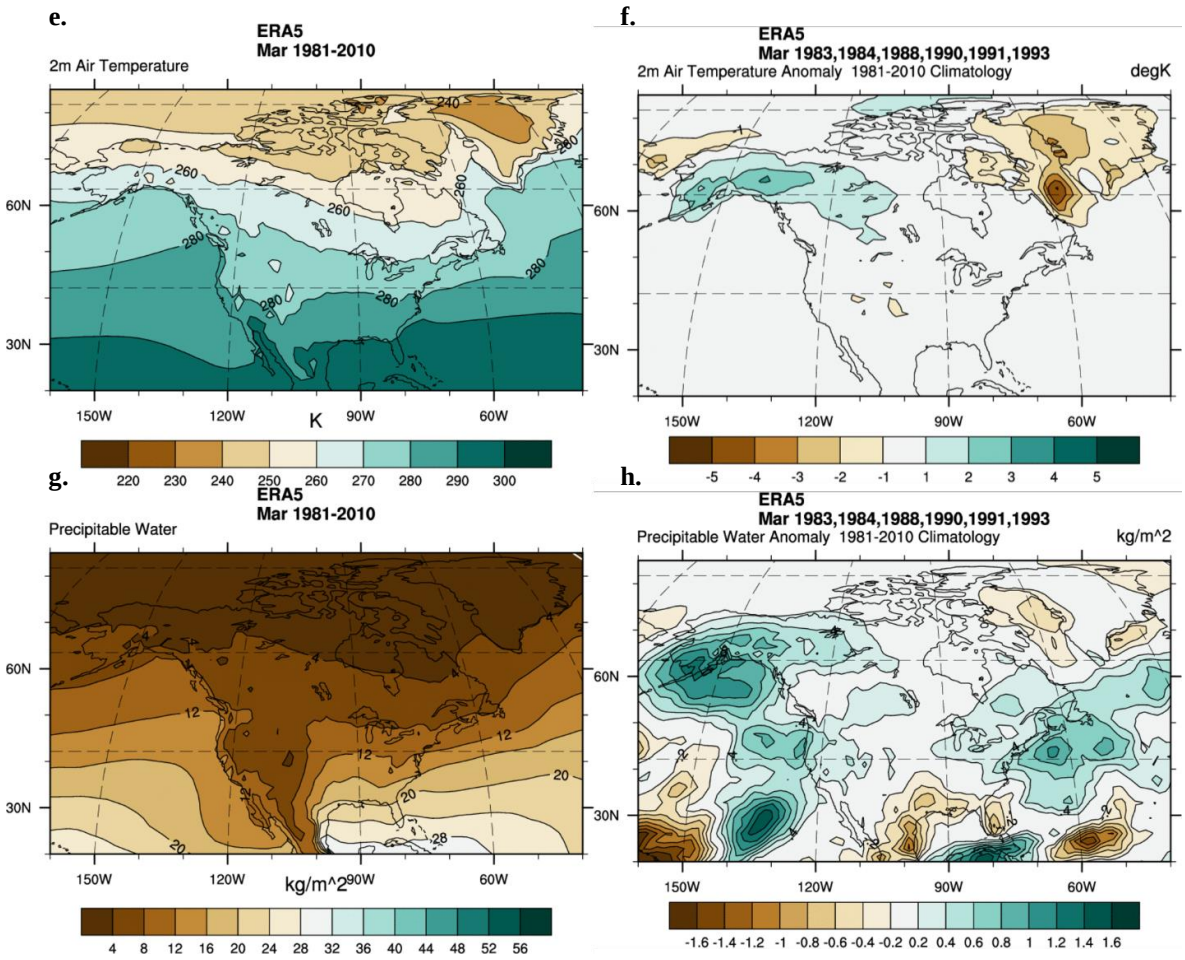

Figure 48. (cont.) Baffin Bay lead-2 March composites for maximum SIE and minimum GBI. The T2m composites are on top with the climatology shown in e) and the composite anomaly shown in f). The PW composites are on the bottom with the climatology shown in g) and the composite anomaly presented in h).

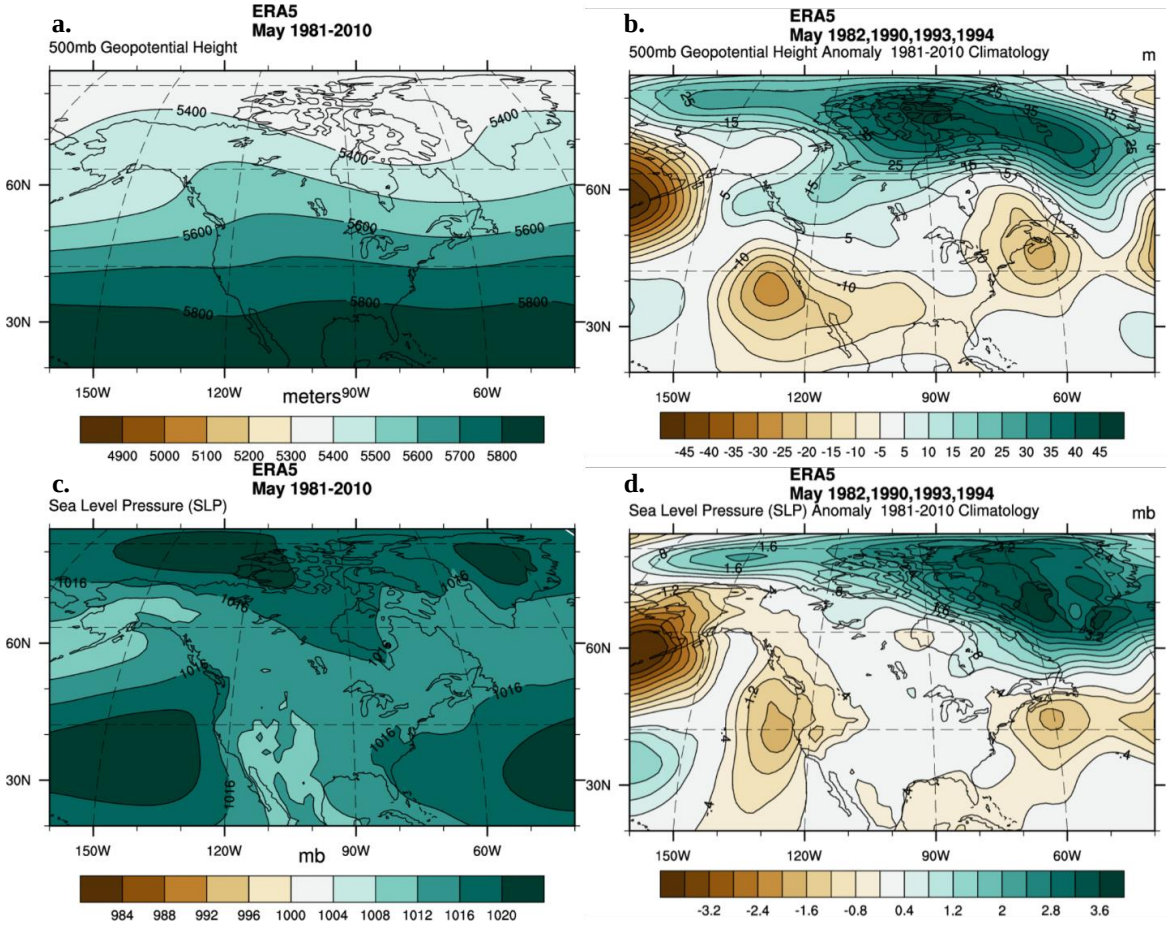

Figure 49. Baffin Bay lead-2 May composites for maximum SIE and minimum GBI. The 500GPH composites are on top with the climatology shown in a) and the composite anomaly shown in b). The MSLP composites are on the bottom with the climatology shown in c) and the composite anomaly presented in d).

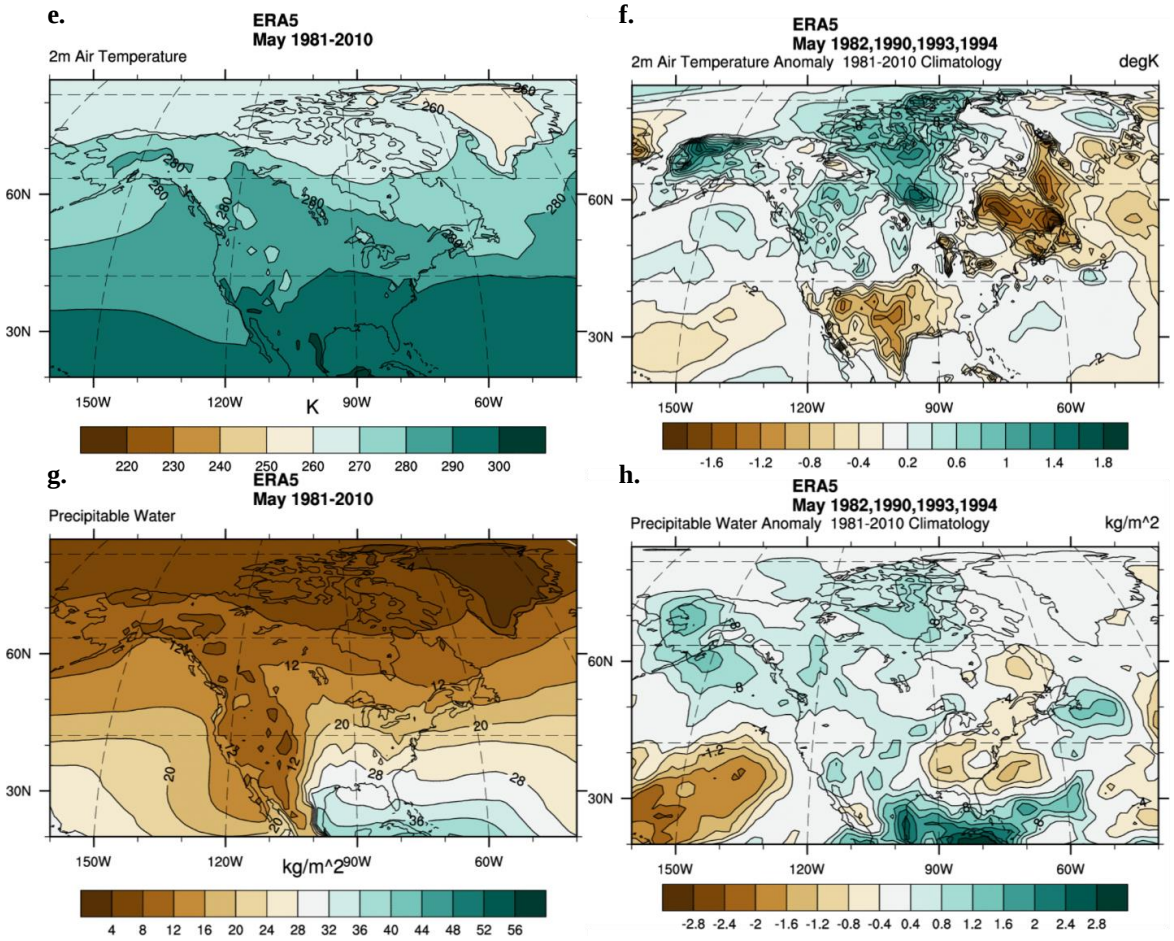

Figure 49. (cont.) Baffin Bay lead-2 May composites for maximum SIE and minimum GBI. The T2m composites are on top with the climatology shown in e) and the composite anomaly shown in f). The PW composites are on the bottom with the climatology shown in g) and the composite anomaly presented in h).

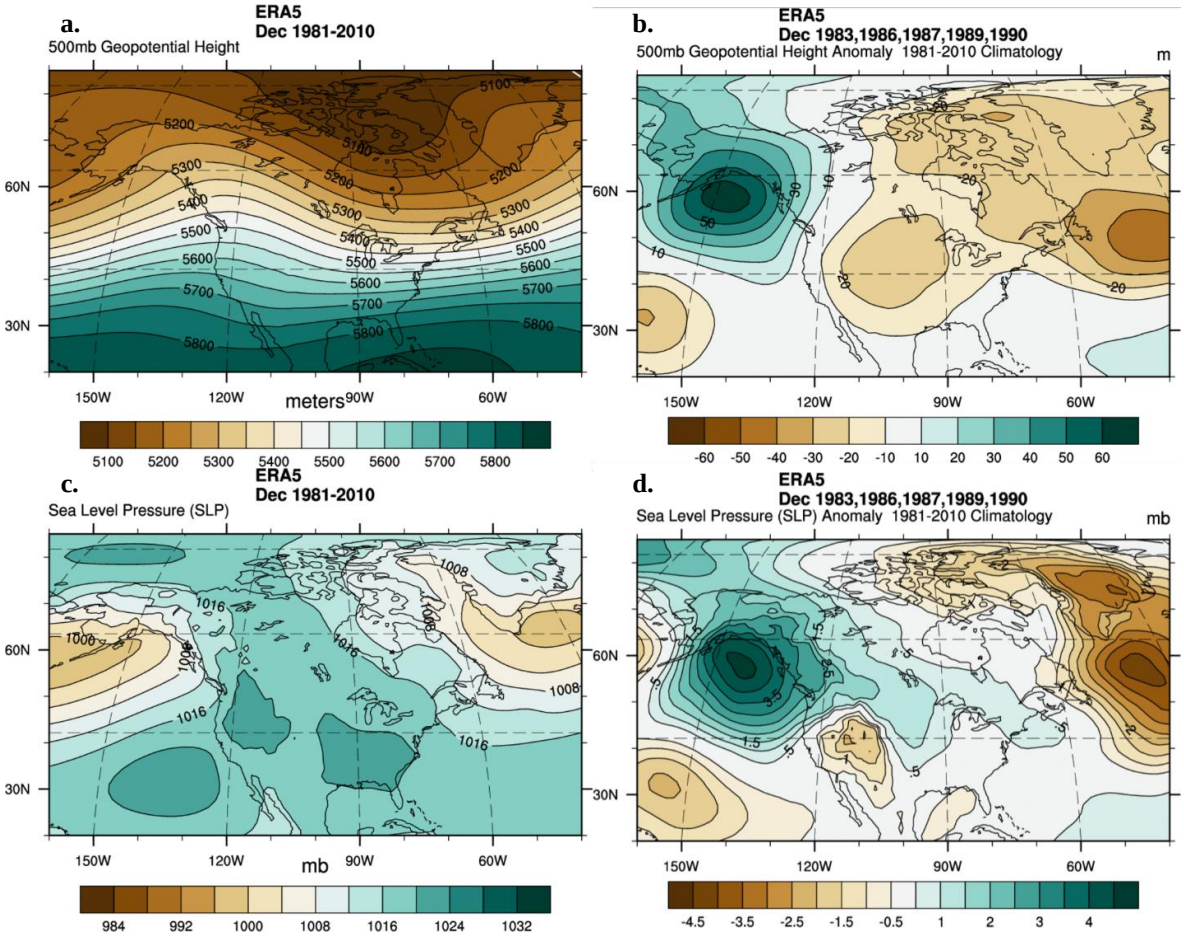

Figure 50. Baffin Bay lead-2 December composites for maximum SIE and minimum GBI. The 500GPH composites are on top with the climatology shown in a) and the composite anomaly shown in b). The MSLP composites are on the bottom with the climatology shown in c) and the composite anomaly presented in d).

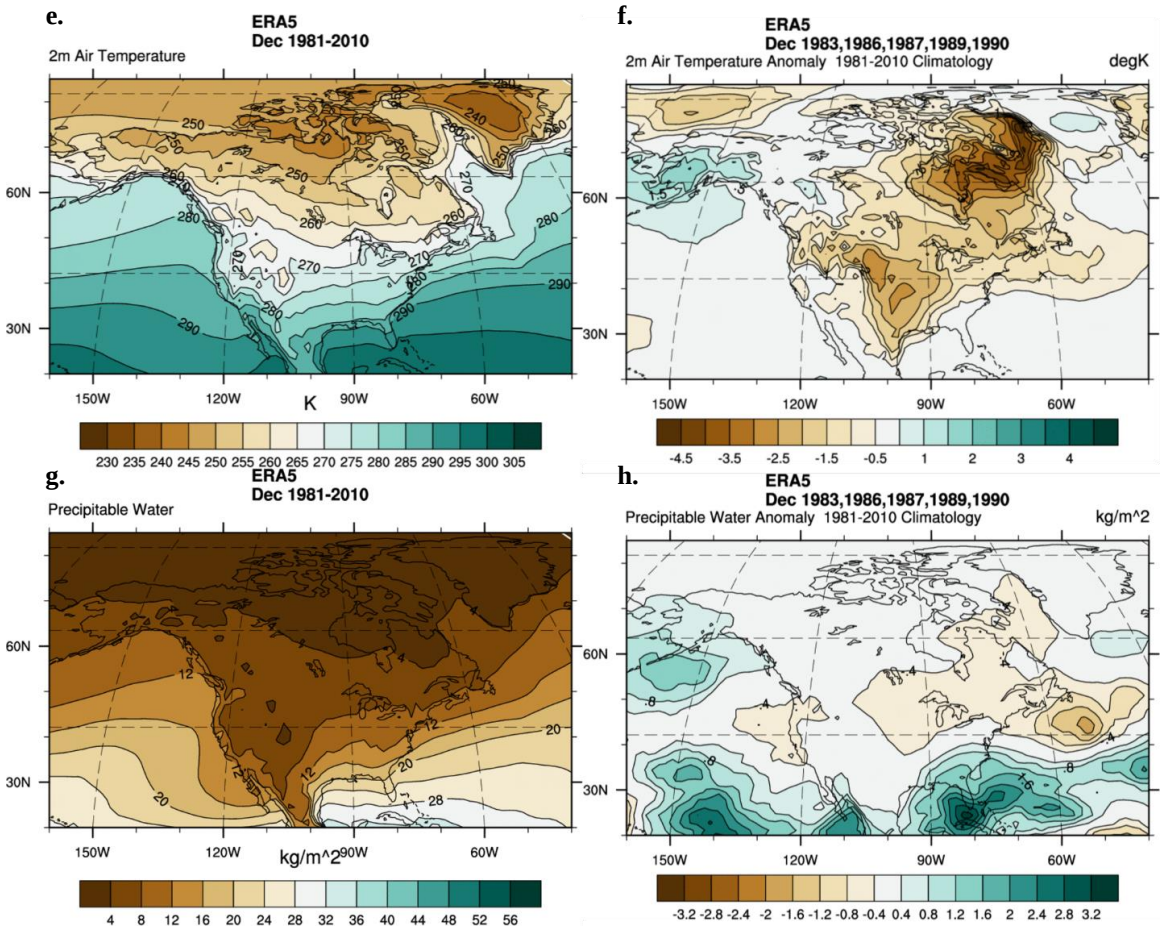

Figure 50. (cont.) Baffin Bay lead-2 December composites for maximum SIE and minimum GBI. The T2m composites are on top with the climatology shown in e) and the composite anomaly shown in f). The PW composites are on the bottom with the climatology shown in g) and the composite anomaly presented in h).

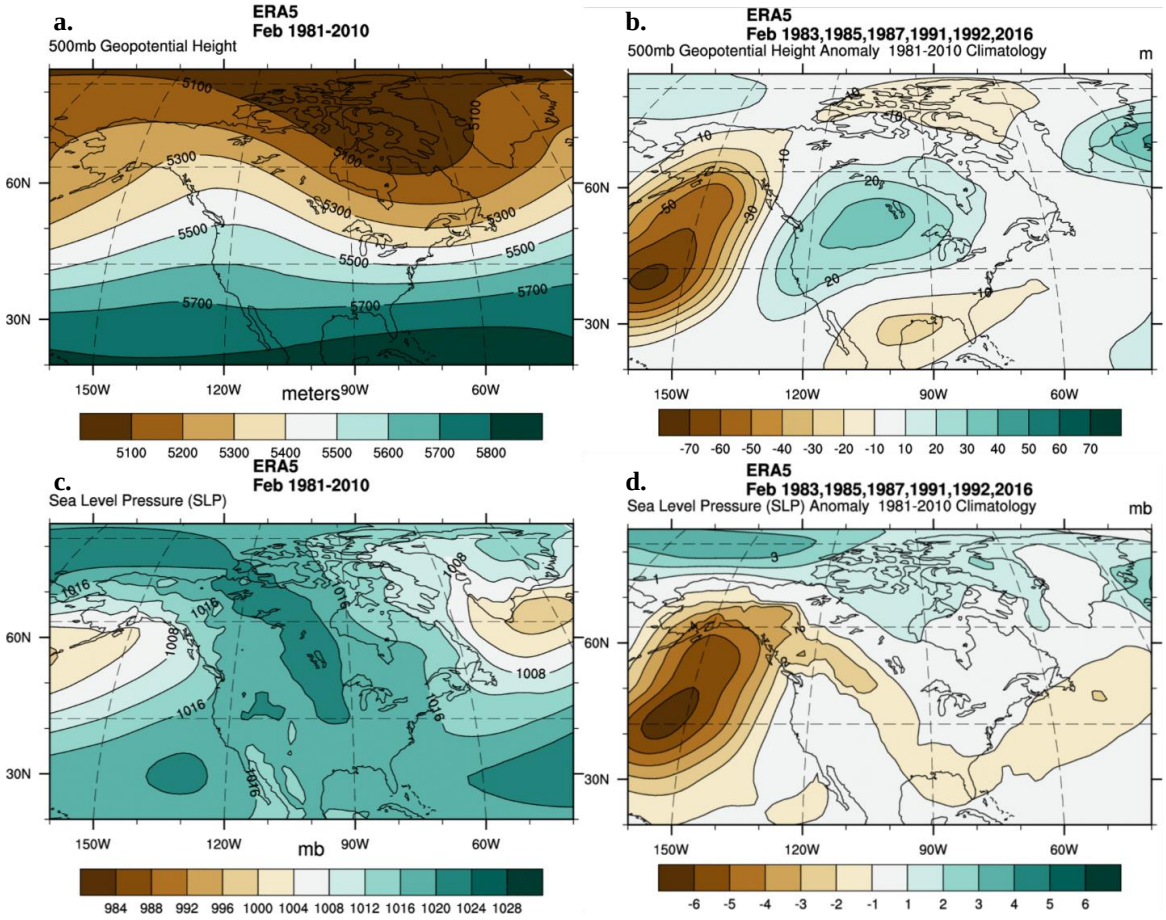

Figure 51. Baffin Bay lead-2 February composites for maximum SIE and minimum GBI. The 500GPH composites are on top with the climatology shown in a) and the composite anomaly shown in b). The MSLP composites are on the bottom with the climatology shown in c) and the composite anomaly presented in d).

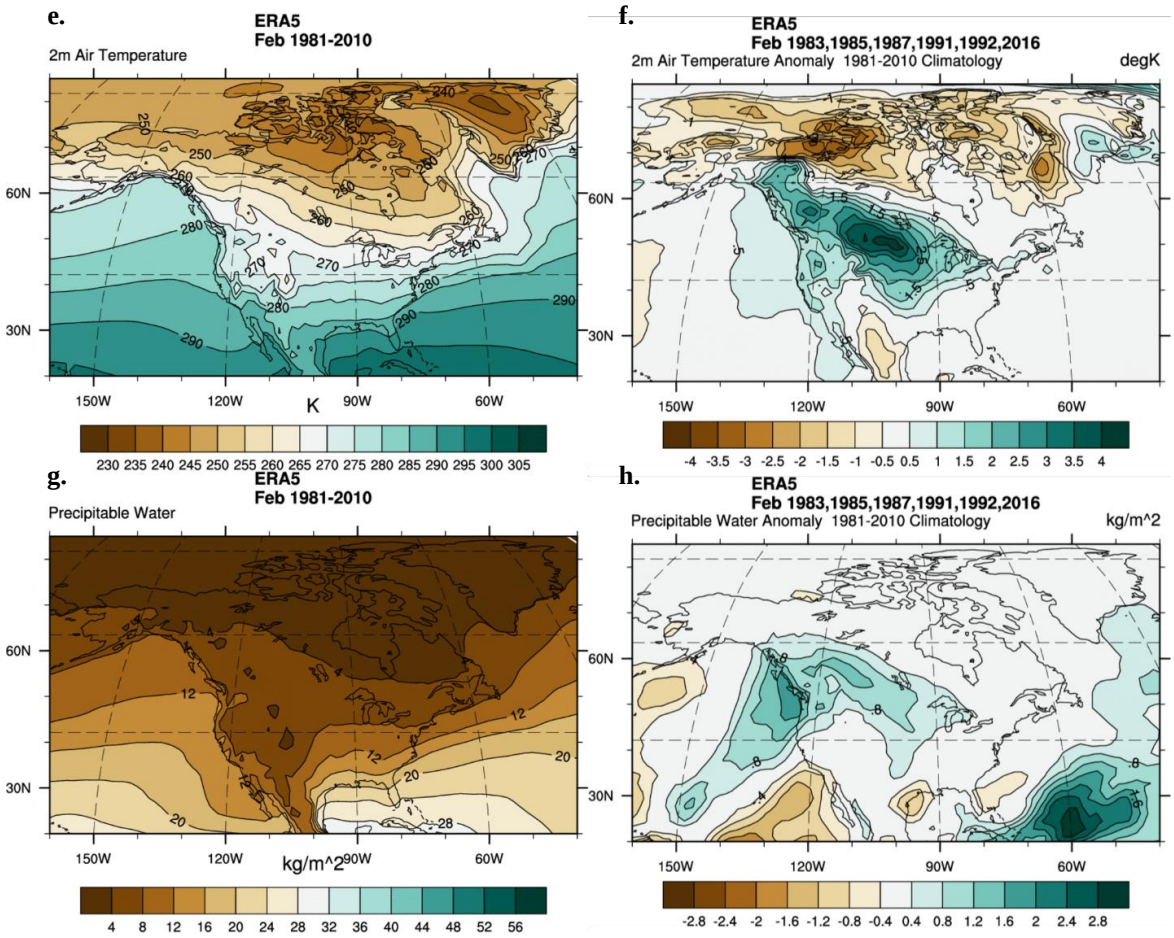

Figure 51. (cont.) Baffin Bay lead-2 February composites for maximum SIE and minimum GBI. The T2m composites are on top with the climatology shown in e) and the composite anomaly shown in f). The PW composites are on the bottom with the climatology shown in g) and the composite anomaly presented in h).

Table 7. The top 10 values for minimum SIE and maximum GBI for Baffin Bay in January, March, October, and December. Values are listed from highest to lowest. Years of overlap are highlighted, and total counts are shown on the bottom row.

January			
SIE		GBI	
Yr	Min	Yr	Max
2013	1036392.79	2010	5235.87
2018	1032532.65	1980	5223.67
2006	1005349.76	1985	5218.56
1997	1000471.59	2011	5209.55
2007	985434.11	1979	5204.19
2002	967592.70	1998	5176.81
2003	940173.51	1982	5172.28
2010	907702.61	2016	5169.48
2004	893490.86	2004	5167.28
2011	714253.78	2003	5163.11
count: 4			

March			
SIE		GBI	
Yr	Min	Yr	Max
1999	1239820.19	2013	5341.77
2001	1186554.07	2006	5305.91
2007	1173655.86	2005	5283.61
2013	1131250.31	2018	5262.40
2004	1130387.35	2001	5253.82
1981	1117472.46	1999	5250.88
2011	1113395.89	2010	5239.57
2005	1094672.27	1981	5225.70
2010	1089005.23	1996	5205.23
2006	1034348.30	1980	5205.21
count: 7			

October			
SIE		GBI	
Yr	Min	Yr	Max
2007	119594.31	2006	5415.27
2014	112340.19	1992	5389.12
2010	112302.62	2004	5378.83
2016	102079.34	2012	5378.80
2002	87035.03	2002	5378.43
2004	84117.08	2003	5366.74
1988	81893.24	1997	5363.73
2006	80806.83	2010	5349.70
2003	77947.65	1993	5348.90
2012	70494.12	2013	5344.08
count: 6			

December			
SIE		GBI	
Yr	Min	Yr	Max
2001	766927.23	2010	5358.11
2009	765507.32	2009	5305.30
1998	756314.76	2001	5263.01
2000	751416.04	1996	5250.33
2012	748516.15	2012	5238.18
2006	731115.28	2000	5235.32
2002	730506.03	1981	5233.86
2003	721858.32	1987	5215.34
2005	712754.72	1995	5209.53
2010	578744.25	1985	5205.04
count: 4			

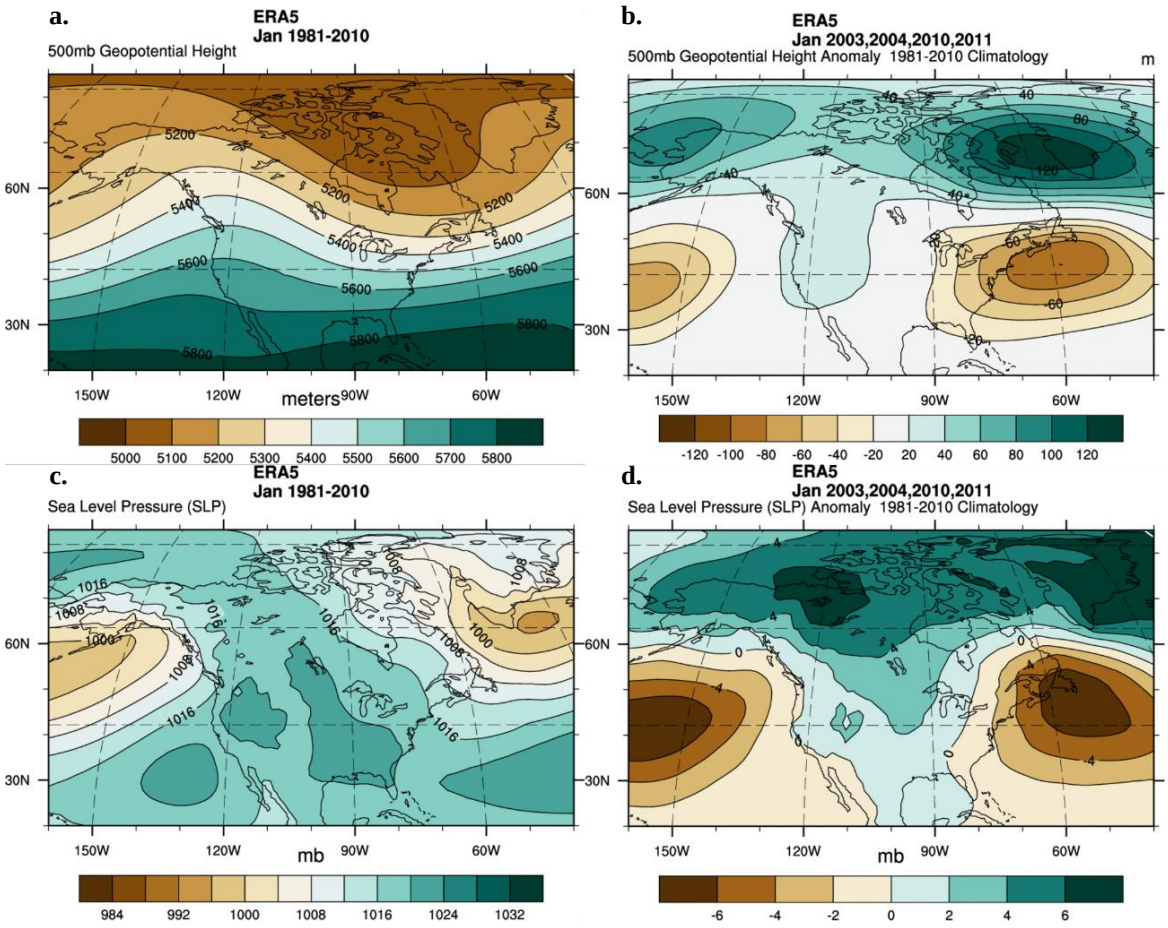

Figure 52. Baffin Bay contemporary January composites for minimum SIE and maximum GBI. The 500GPH composites are on top with the climatology shown in a) and the composite anomaly shown in b). The MSLP composites are on the bottom with the climatology shown in c) and the composite anomaly presented in d).

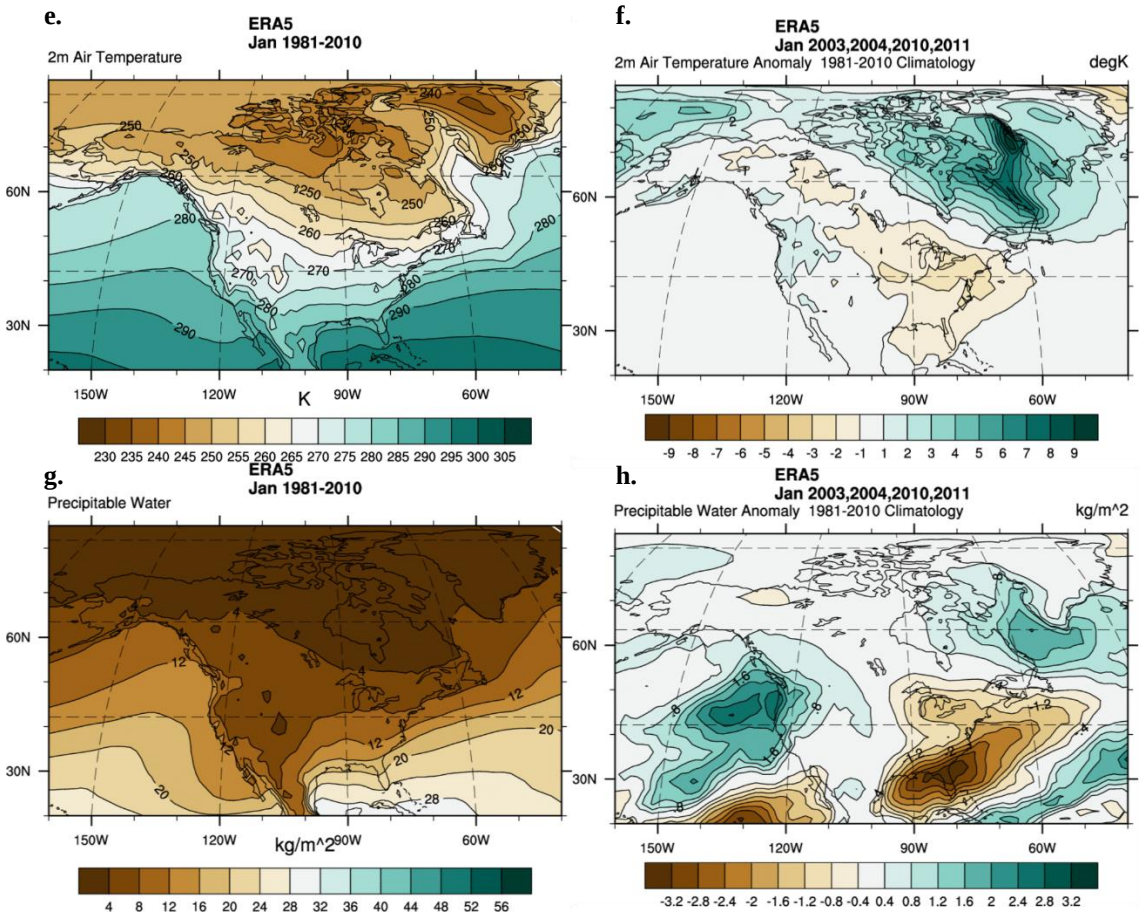

Figure 52. (cont.) Baffin Bay contemporary January composites for minimum SIE and maximum GBI. The T2m composites are on top with the climatology shown in e) and the composite anomaly shown in f). The PW composites are on the bottom with the climatology shown in g) and the composite anomaly presented in h).

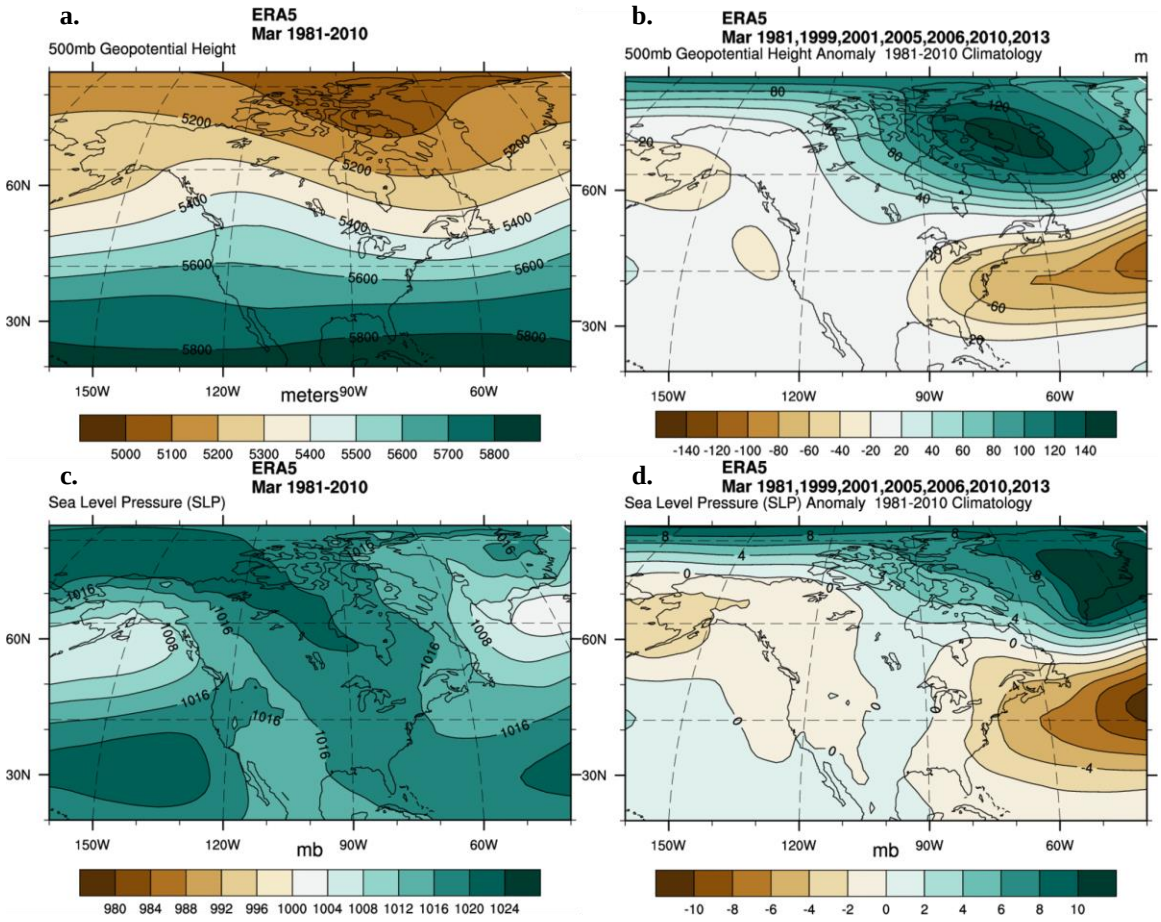

Figure 53. Baffin Bay contemporary March composites for minimum SIE and maximum GBI. The 500GPH composites are on top with the climatology shown in a) and the composite anomaly shown in b). The MSLP composites are on the bottom with the climatology shown in c) and the composite anomaly presented in d).

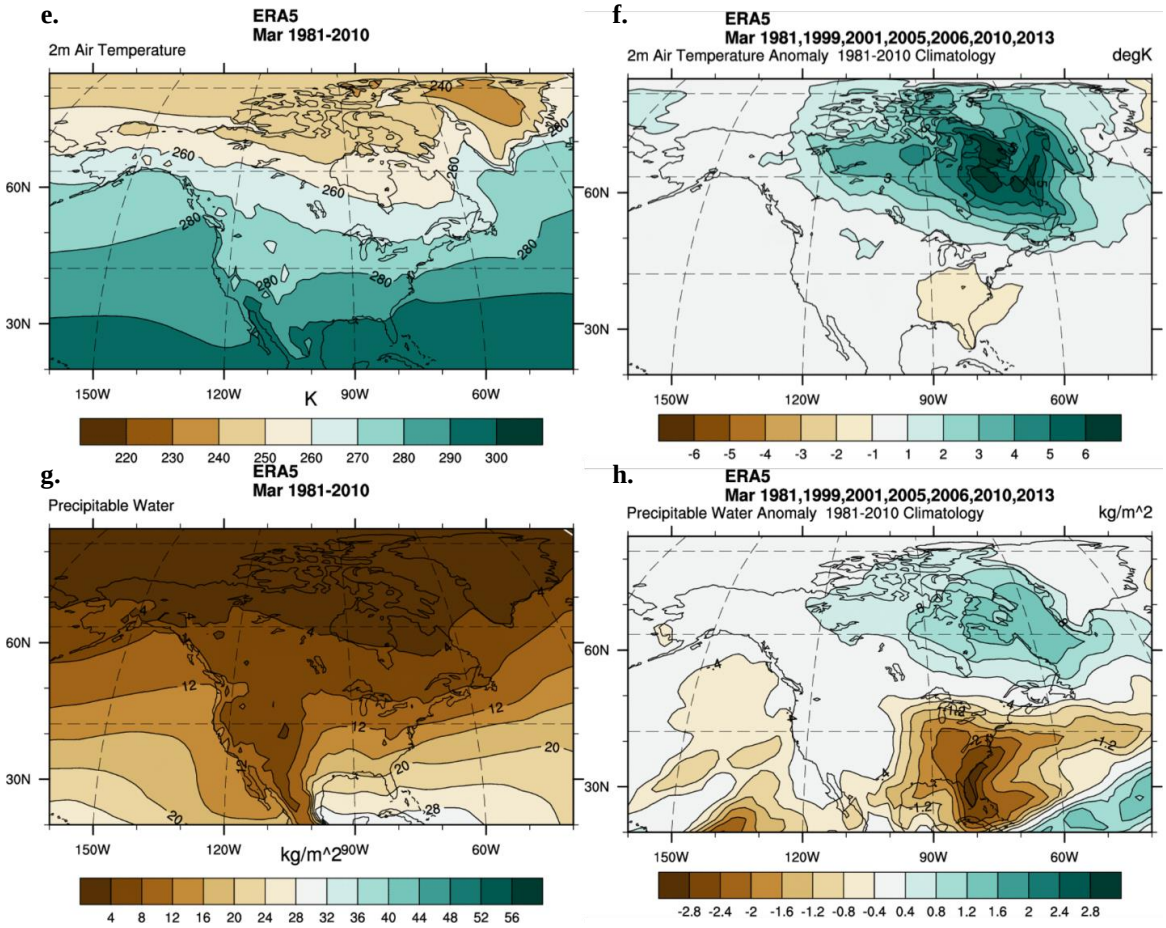

Figure 53. (cont.) Baffin Bay contemporary March composites for minimum SIE and maximum GBI. The T2m composites are on top with the climatology shown in e) and the composite anomaly shown in f). The PW composites are on the bottom with the climatology shown in g) and the composite anomaly presented in h).

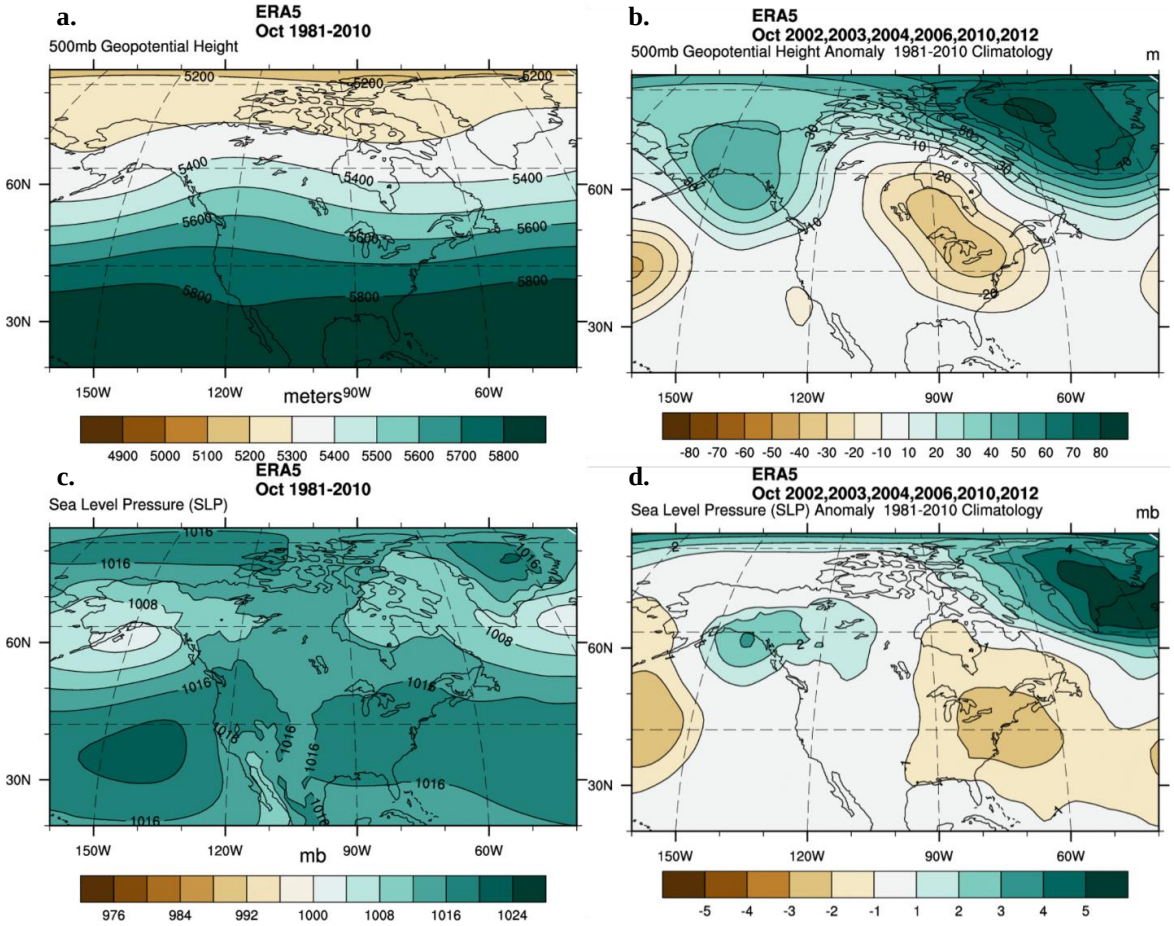

Figure 54. Baffin Bay contemporary October composites for minimum SIE and maximum GBI. The 500GPH composites are on top with the climatology shown in a) and the composite anomaly shown in b). The MSLP composites are on the bottom with the climatology shown in c) and the composite anomaly presented in d).

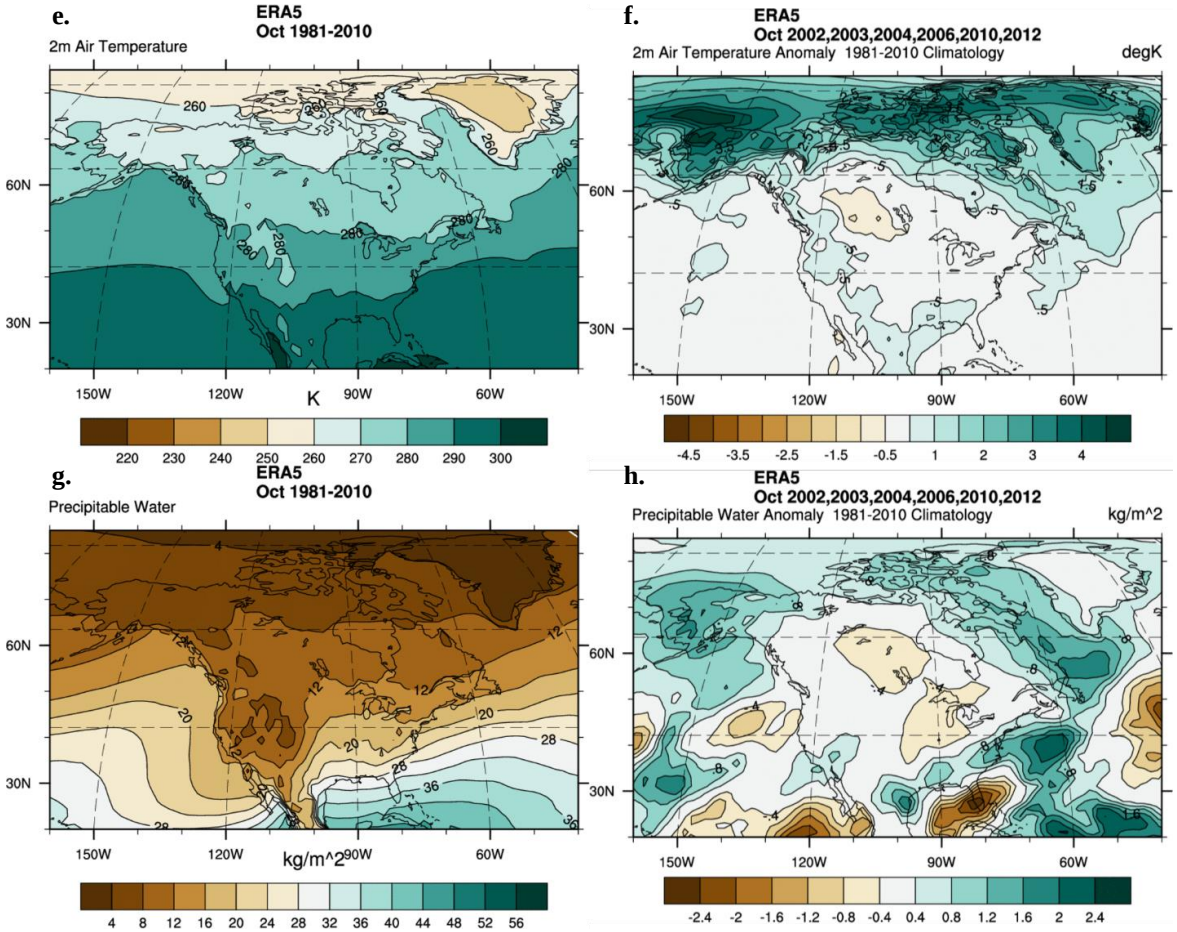

Figure 54. (cont.) Baffin Bay contemporary October composites for minimum SIE and maximum GBI. The T2m composites are on top with the climatology shown in e) and the composite anomaly shown in f). The PW composites are on the bottom with the climatology shown in g) and the composite anomaly presented in h).

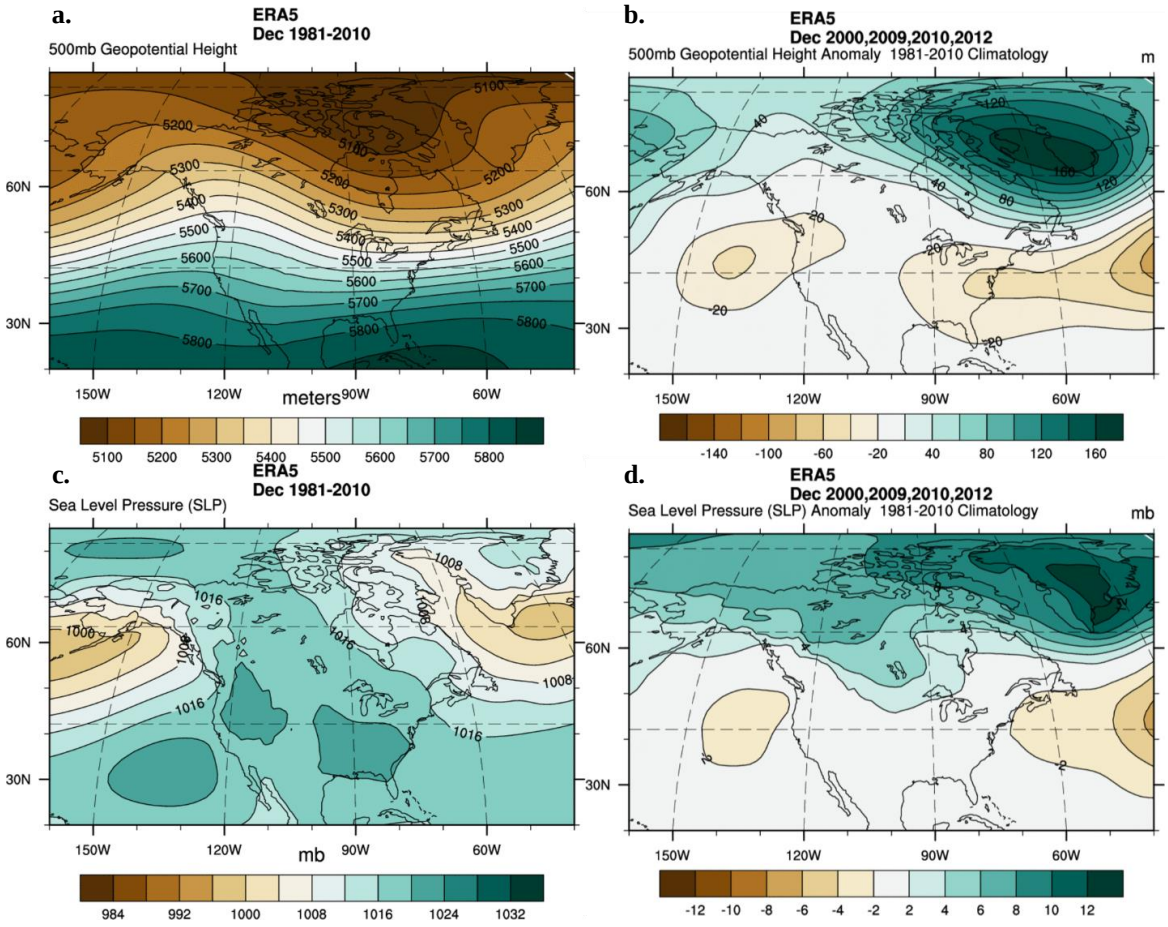

Figure 55. Baffin Bay contemporary December composites for minimum SIE and maximum GBI. The 500GPH composites are on top with the climatology shown in a) and the composite anomaly shown in b). The MSLP composites are on the bottom with the climatology shown in c) and the composite anomaly presented in d).

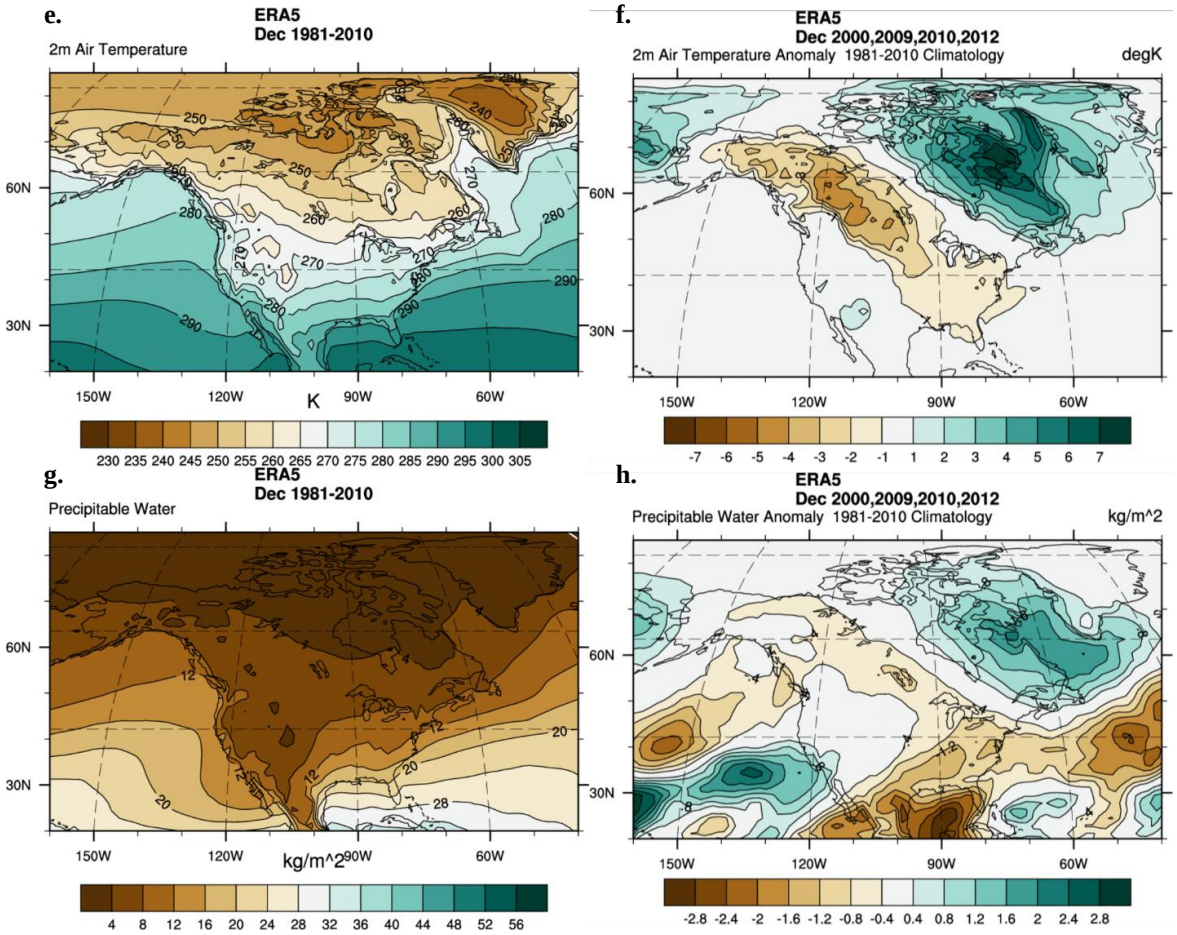

Figure 55. (cont.) Baffin Bay contemporary December composites for minimum SIE and maximum GBI. The T2m composites are on top with the climatology shown in e) and the composite anomaly shown in f). The PW composites are on the bottom with the climatology shown in g) and the composite anomaly presented in h).

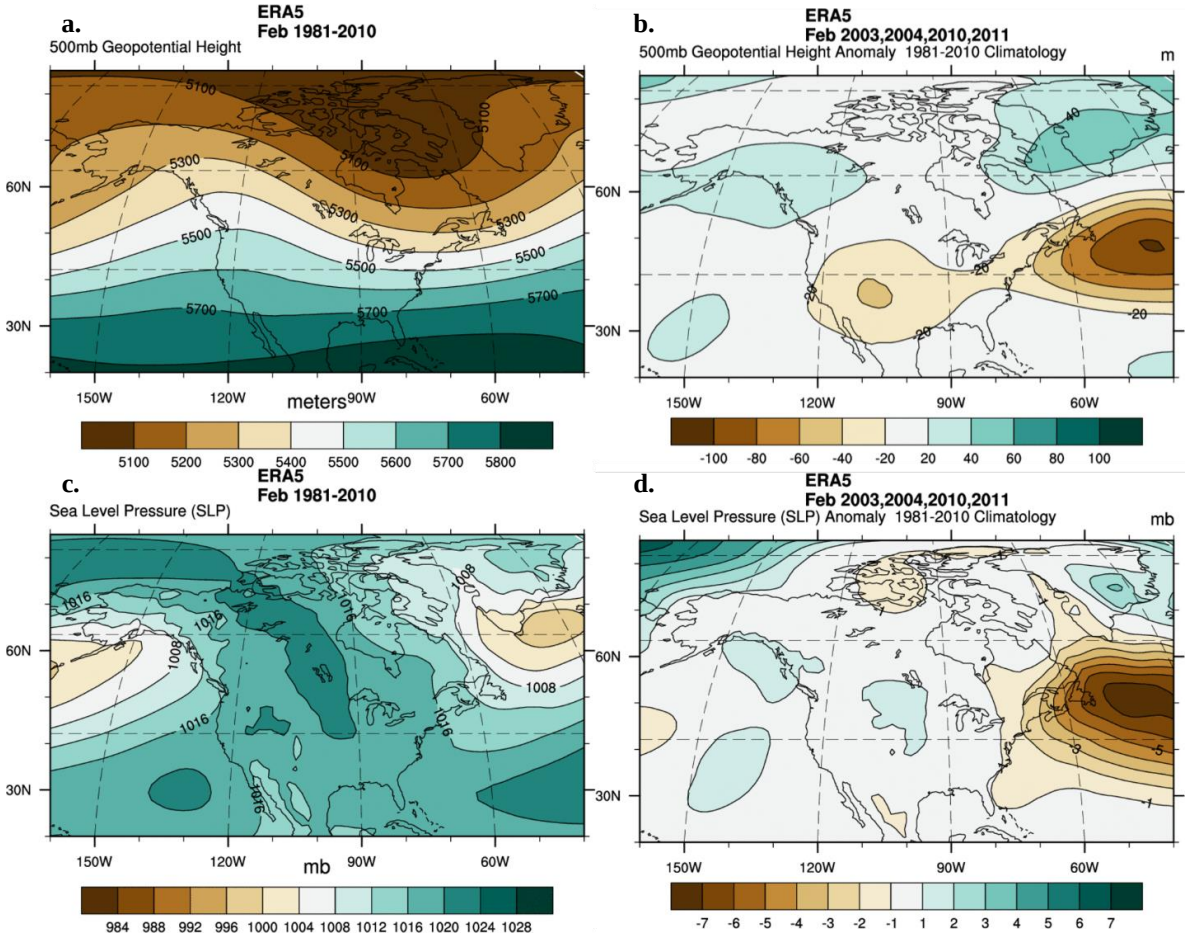

Figure 56. Baffin Bay lead-1 February composites for minimum SIE and maximum GBI. The 500GPH composites are on top with the climatology shown in a) and the composite anomaly shown in b). The MSLP composites are on the bottom with the climatology shown in c) and the composite anomaly presented in d).

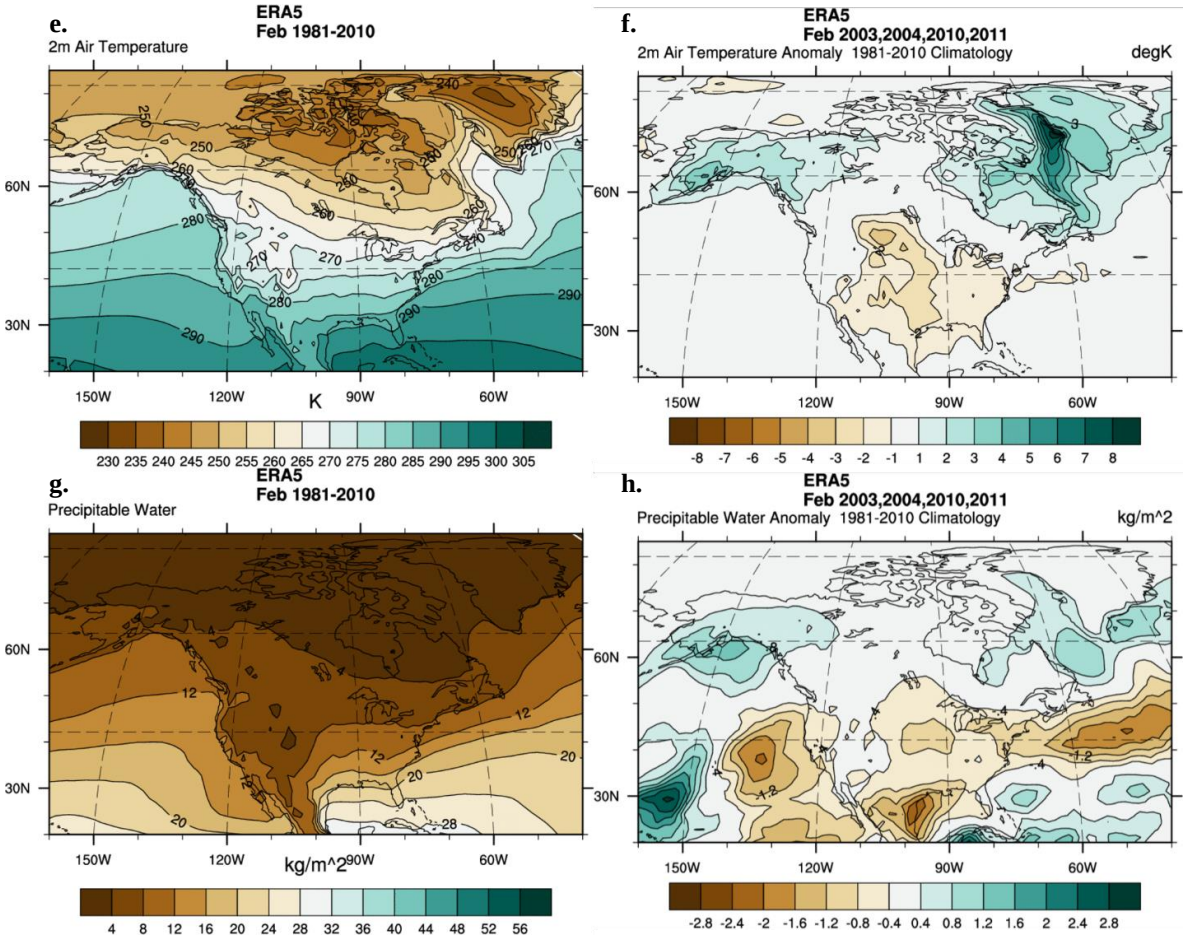

Figure 56. (cont.) Baffin Bay lead-1 February composites for minimum SIE and maximum GBI. The T2m composites are on top with the climatology shown in e) and the composite anomaly shown in f). The PW composites are on the bottom with the climatology shown in g) and the composite anomaly presented in h).

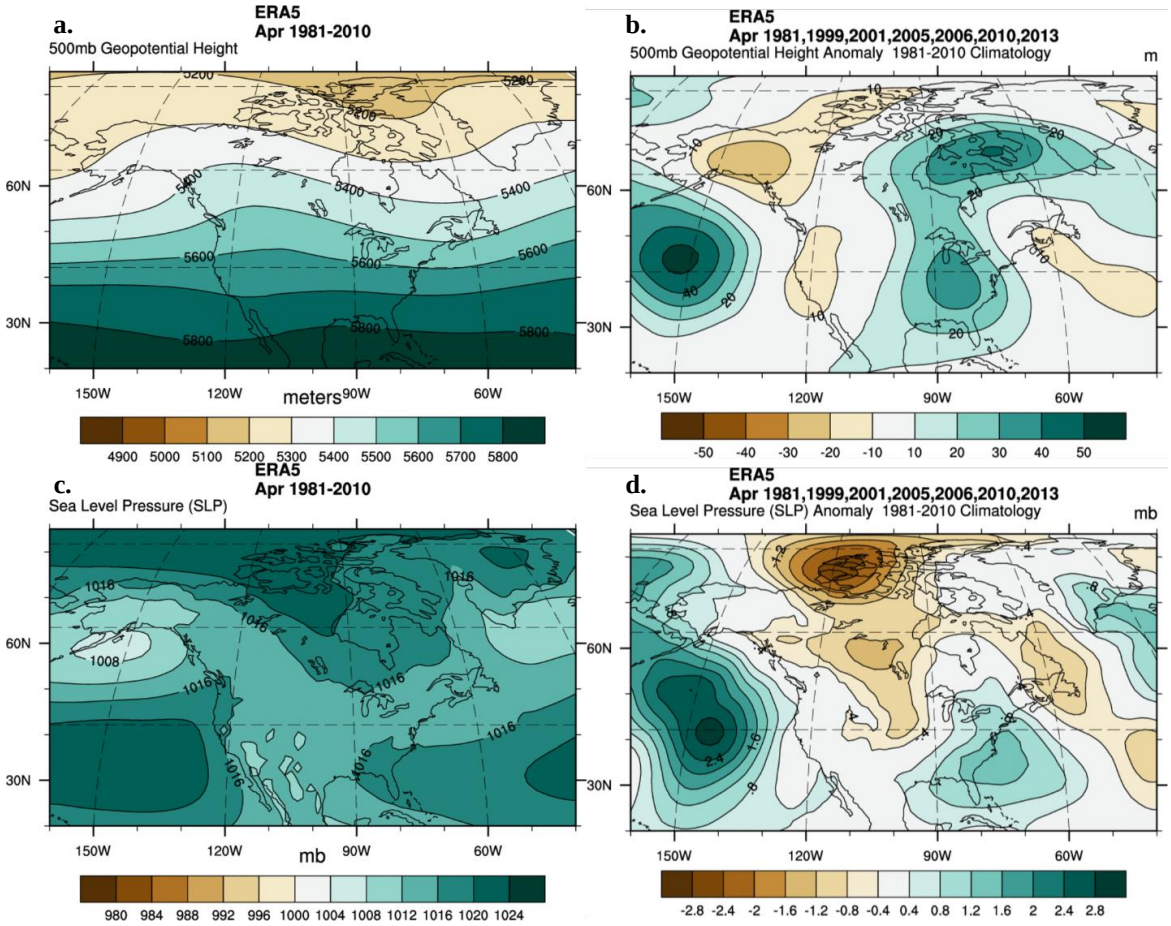

Figure 57. Baffin Bay lead-1 April composites for minimum SIE and maximum GBI. The 500GPH composites are on top with the climatology shown in a) and the composite anomaly shown in b). The MSLP composites are on the bottom with the climatology shown in c) and the composite anomaly presented in d).

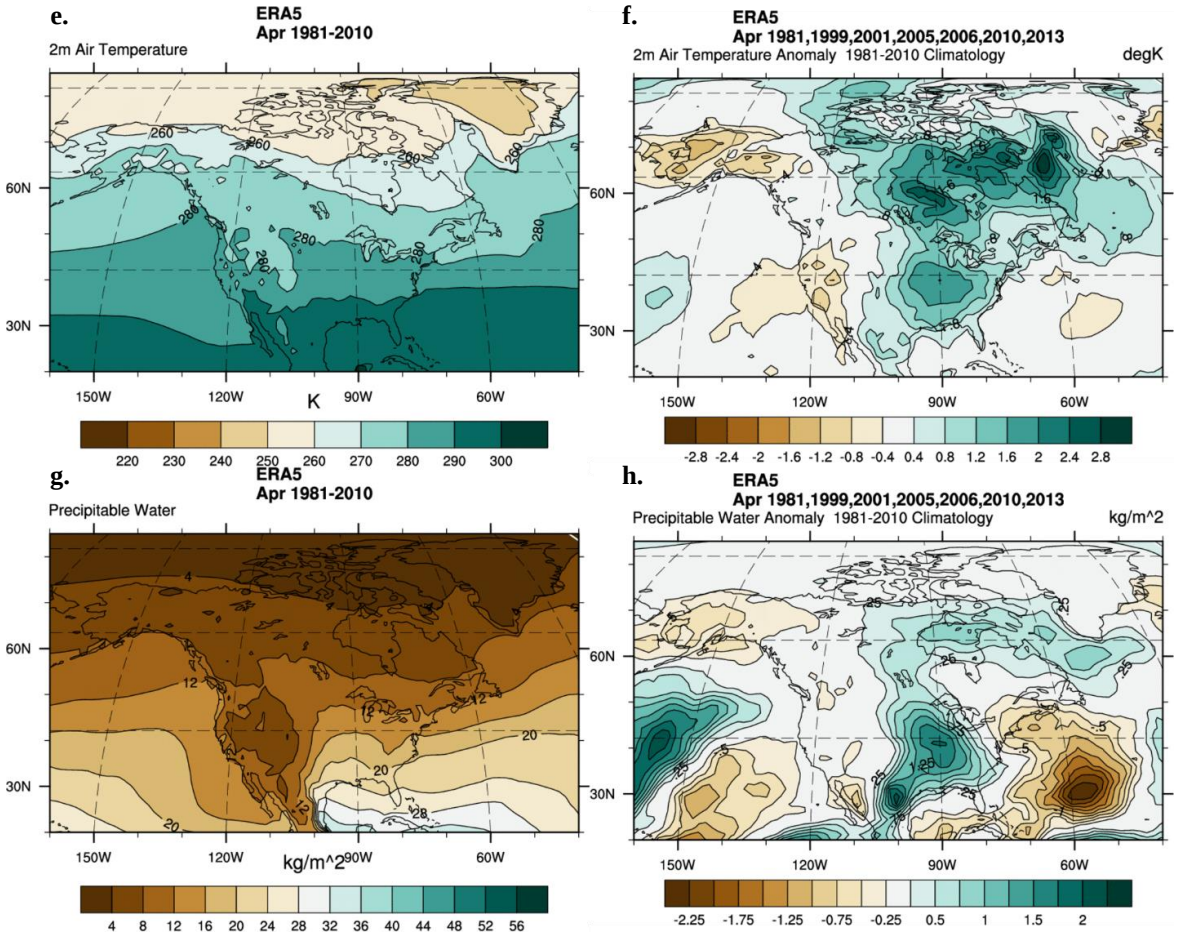

Figure 57. (cont.) Baffin Bay lead-1 April composites for minimum SIE and maximum GBI. The T2m composites are on top with the climatology shown in e) and the composite anomaly shown in f). The PW composites are on the bottom with the climatology shown in g) and the composite anomaly presented in h).

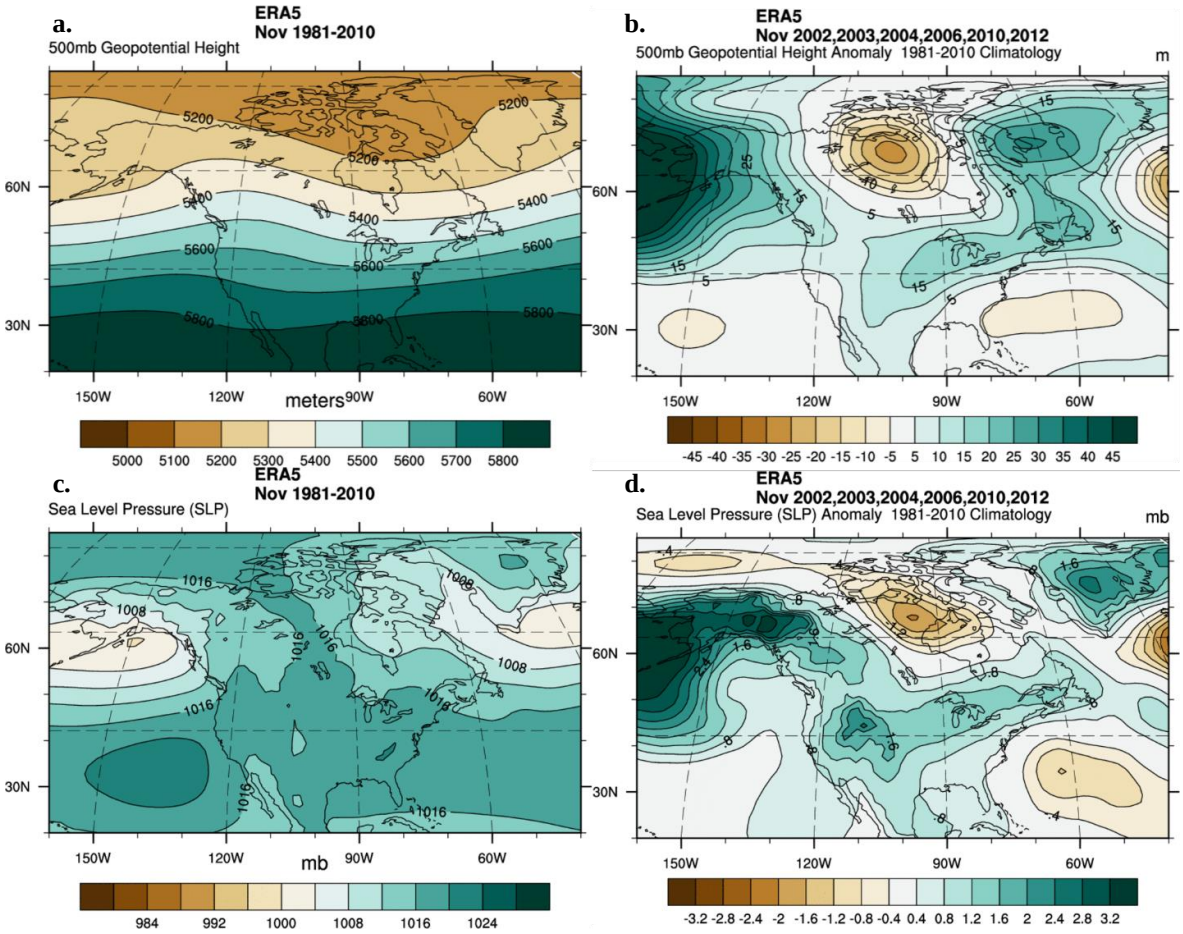

Figure 58. Baffin Bay lead-1 November composites for minimum SIE and maximum GBI. The 500GPH composites are on top with the climatology shown in a) and the composite anomaly shown in b). The MSLP composites are on the bottom with the climatology shown in c) and the composite anomaly presented in d).

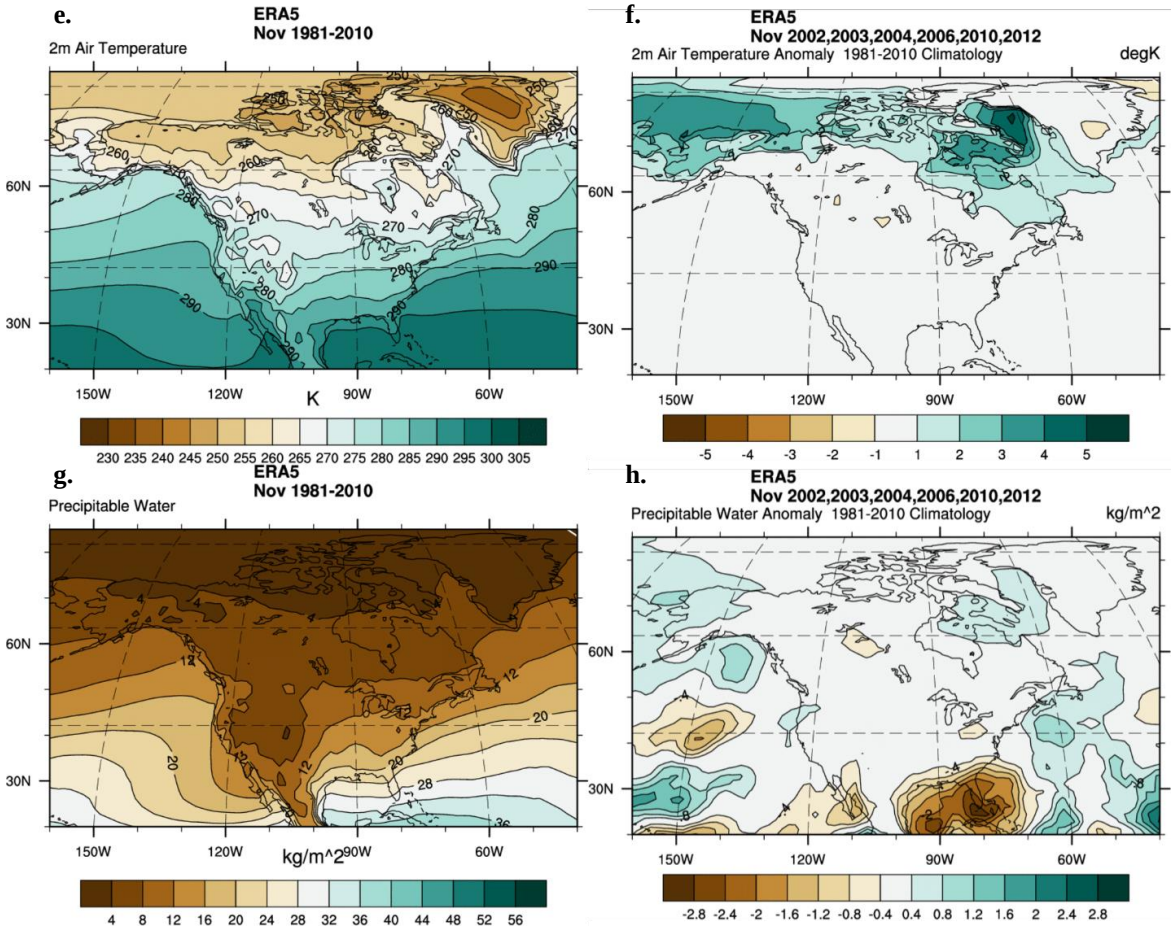

Figure 58. (cont.) Baffin Bay lead-1 November composites for minimum SIE and maximum GBI. The T2m composites are on top with the climatology shown in e) and the composite anomaly shown in f). The PW composites are on the bottom with the climatology shown in g) and the composite anomaly presented in h).

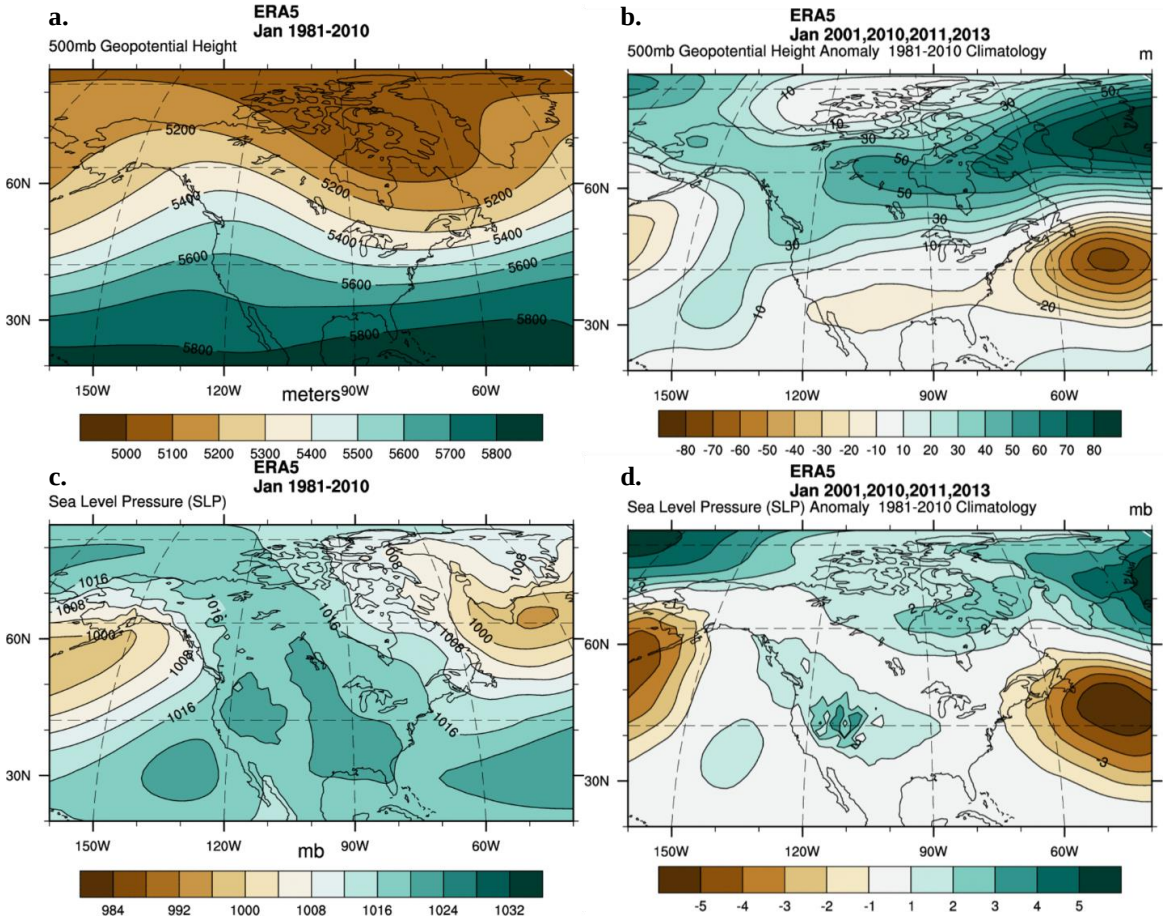

Figure 59. Baffin Bay lead-1 January composites for minimum SIE and maximum GBI. The 500GPH composites are on top with the climatology shown in a) and the composite anomaly shown in b). The MSLP composites are on the bottom with the climatology shown in c) and the composite anomaly presented in d).

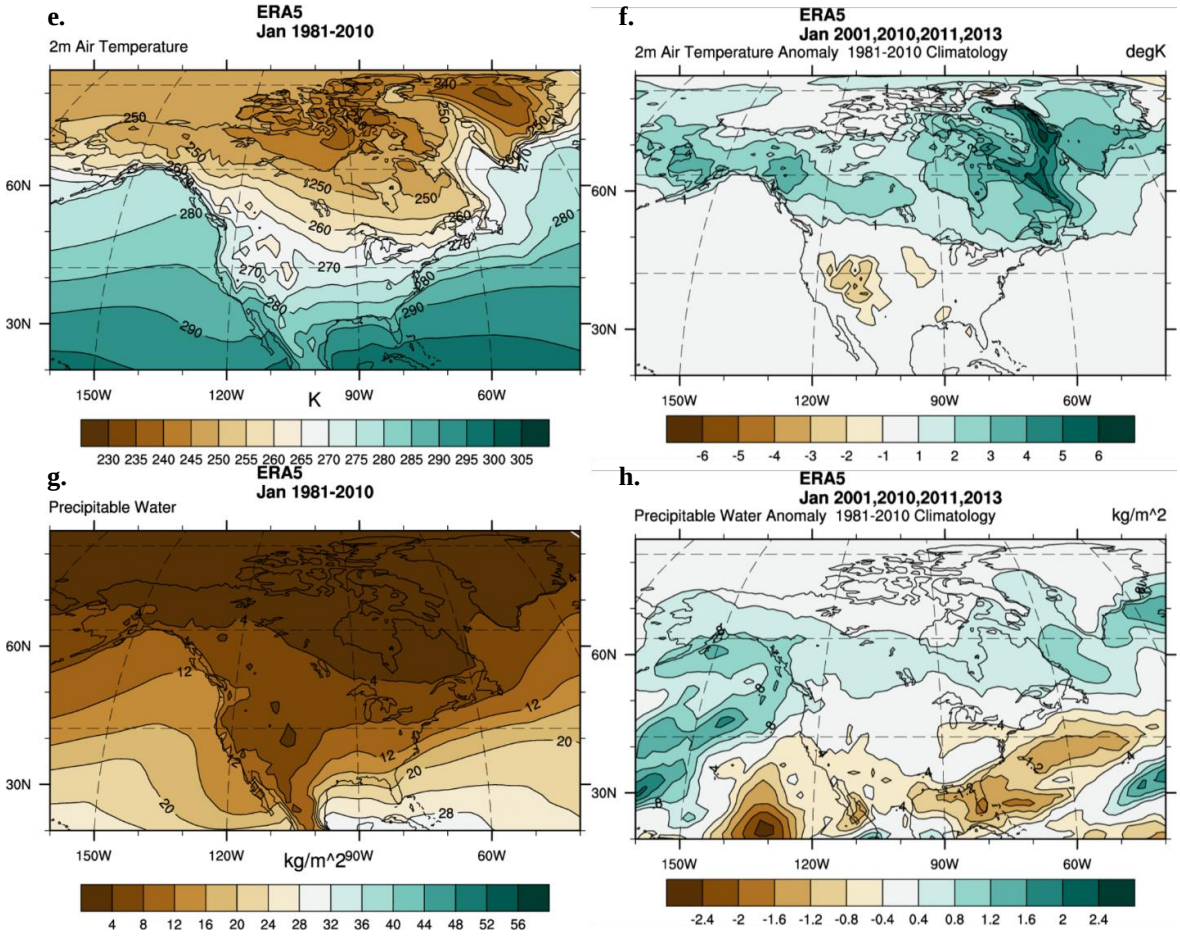

Figure 59. (cont.) Baffin Bay lead-1 January composites for minimum SIE and maximum GBI. The T2m composites are on top with the climatology shown in e) and the composite anomaly shown in f). The PW composites are on the bottom with the climatology shown in g) and the composite anomaly presented in h).

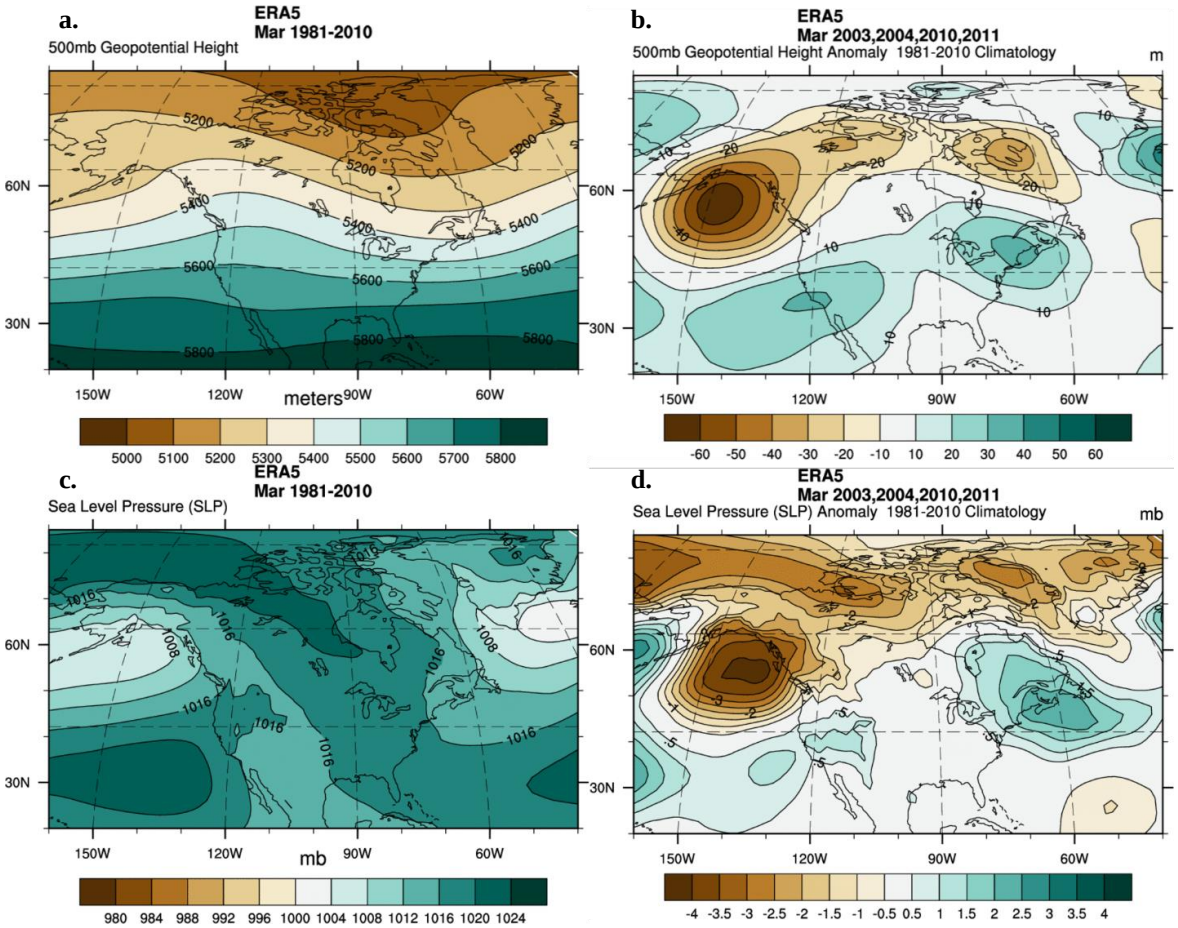

Figure 60. Baffin Bay lead-2 March composites for minimum SIE and maximum GBI. The 500GPH composites are on top with the climatology shown in a) and the composite anomaly shown in b). The MSLP composites are on the bottom with the climatology shown in c) and the composite anomaly presented in d).

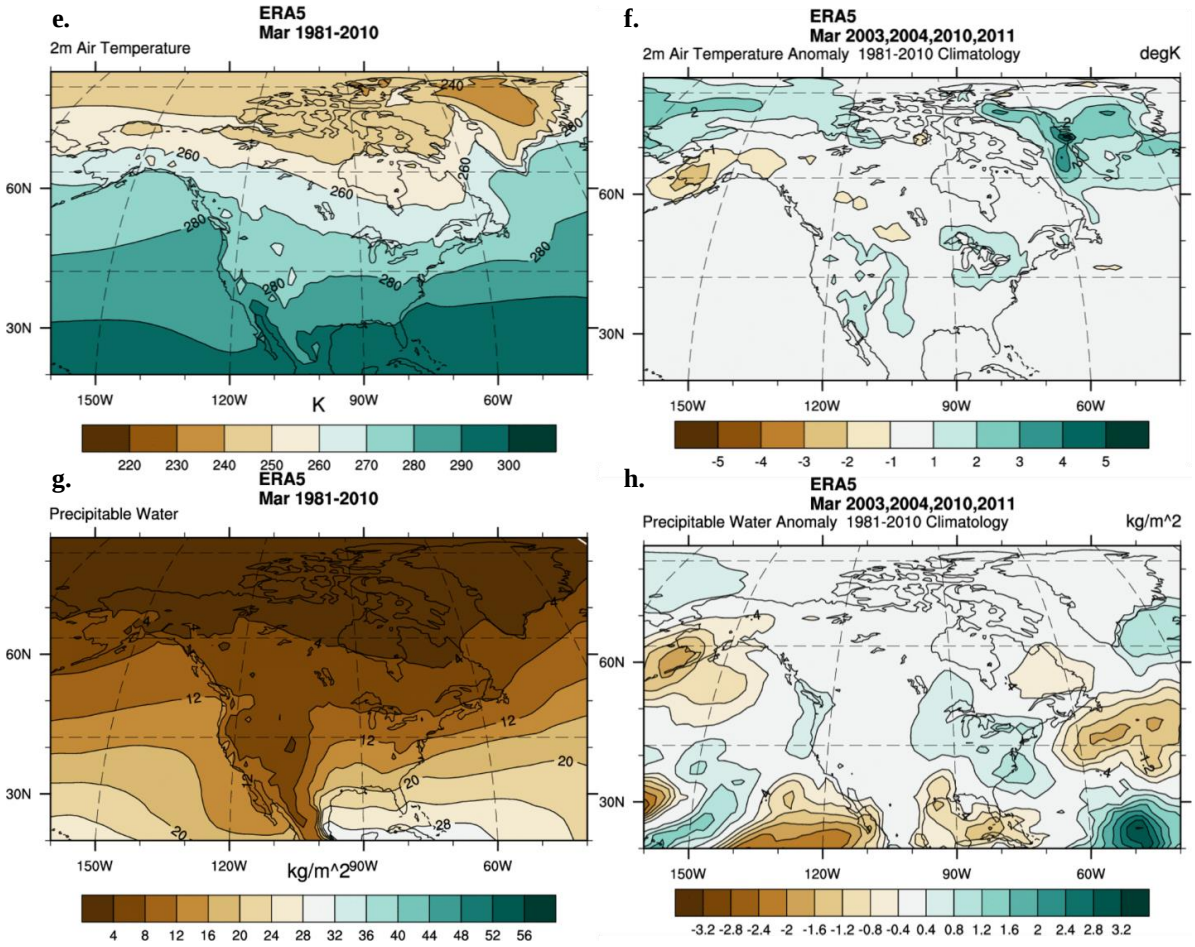

Figure 60. (cont.) Baffin Bay lead-2 March composites for minimum SIE and maximum GBI. The T2m composites are on top with the climatology shown in e) and the composite anomaly shown in f). The PW composites are on the bottom with the climatology shown in g) and the composite anomaly presented in h).

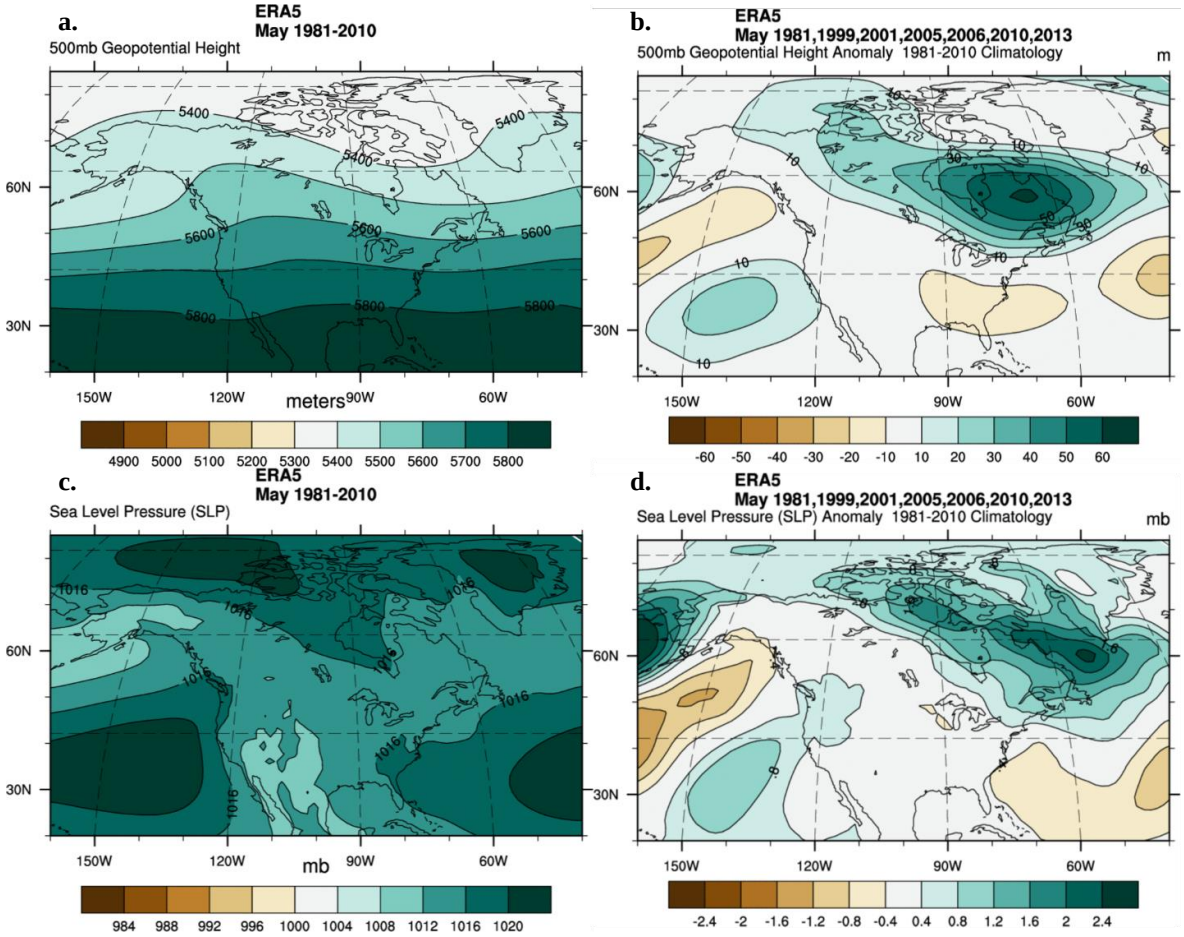

Figure 61. Baffin Bay lead-2 May composites for minimum SIE and maximum GBI. The 500GPH composites are on top with the climatology shown in a) and the composite anomaly shown in b). The MSLP composites are on the bottom with the climatology shown in c) and the composite anomaly presented in d).

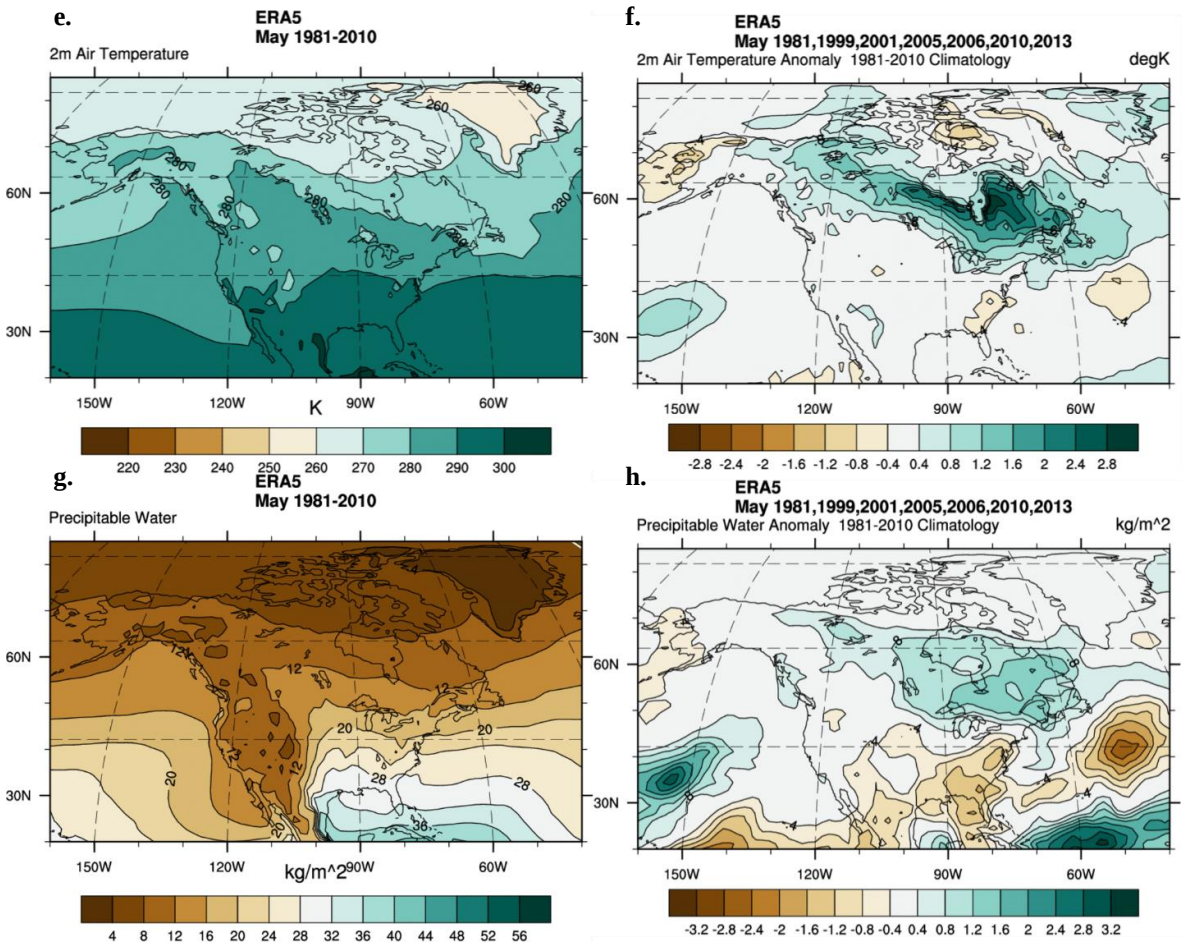

Figure 61. (cont.) Baffin Bay lead-2 May composites for minimum SIE and maximum GBI. The T2m composites are on top with the climatology shown in e) and the composite anomaly shown in f). The PW composites are on the bottom with the climatology shown in g) and the composite anomaly presented in h).

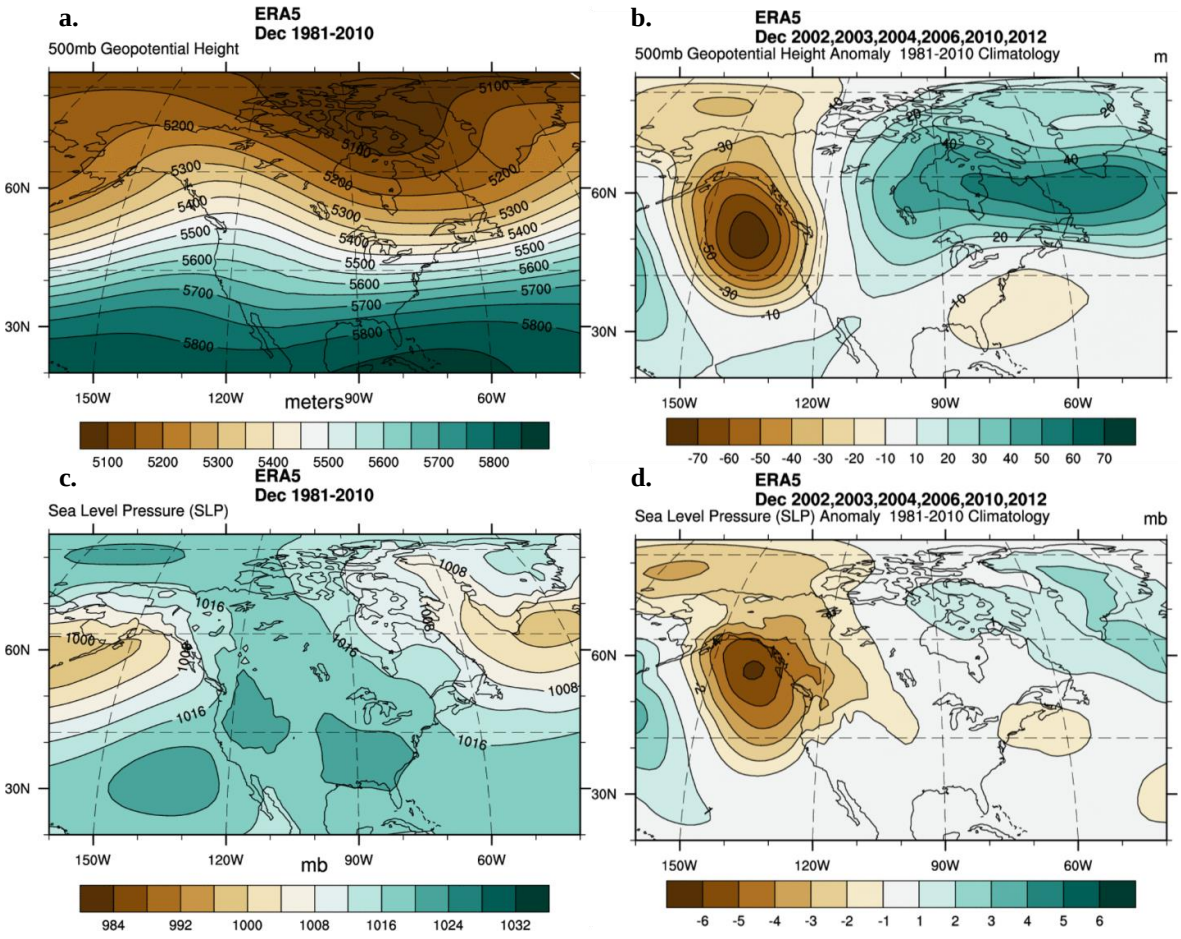

Figure 62. Baffin Bay lead-2 December composites for minimum SIE and maximum GBI. The 500GPH composites are on top with the climatology shown in a) and the composite anomaly shown in b). The MSLP composites are on the bottom with the climatology shown in c) and the composite anomaly presented in d).

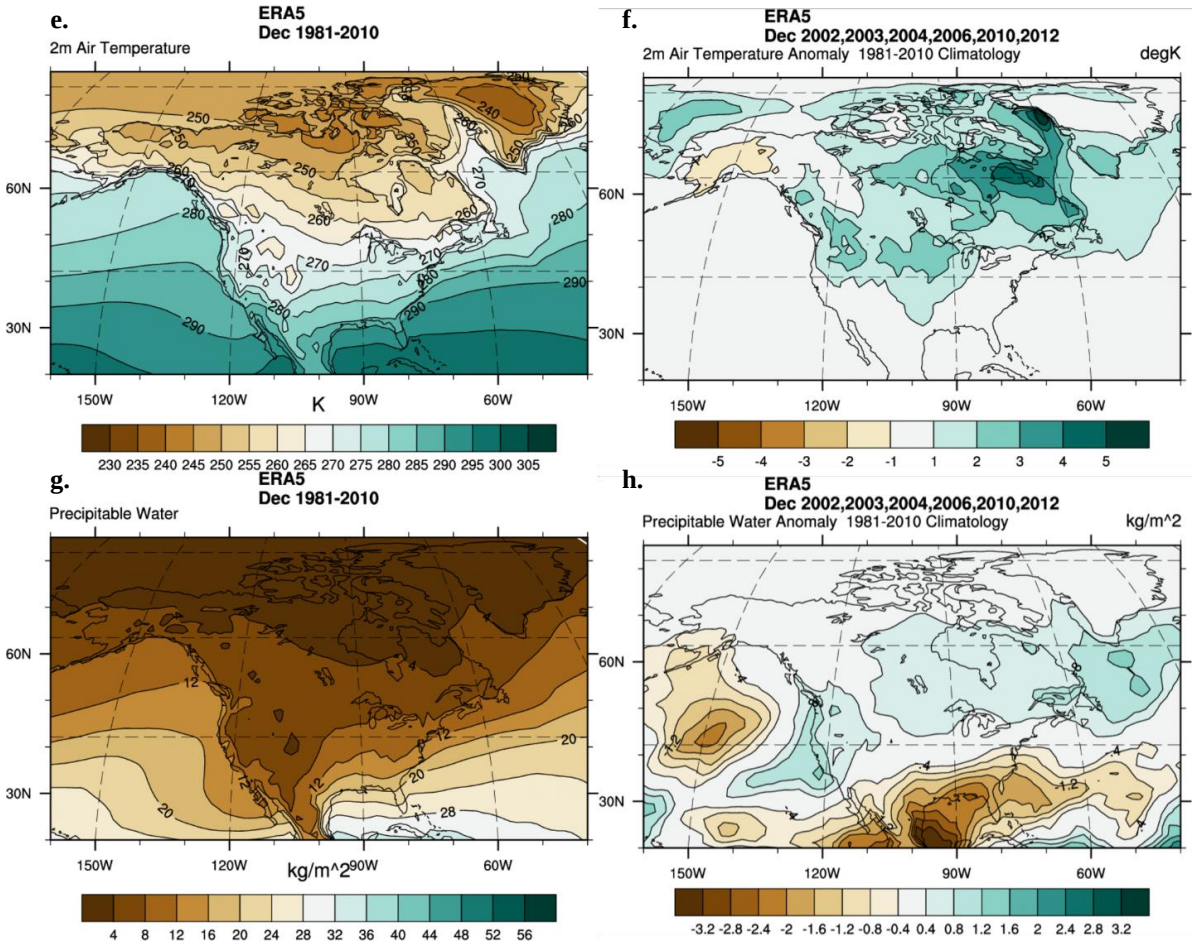

Figure 62. (cont.) Baffin Bay lead-2 December composites for minimum SIE and maximum GBI. The T2m composites are on top with the climatology shown in e) and the composite anomaly shown in f). The PW composites are on the bottom with the climatology shown in g) and the composite anomaly presented in h).

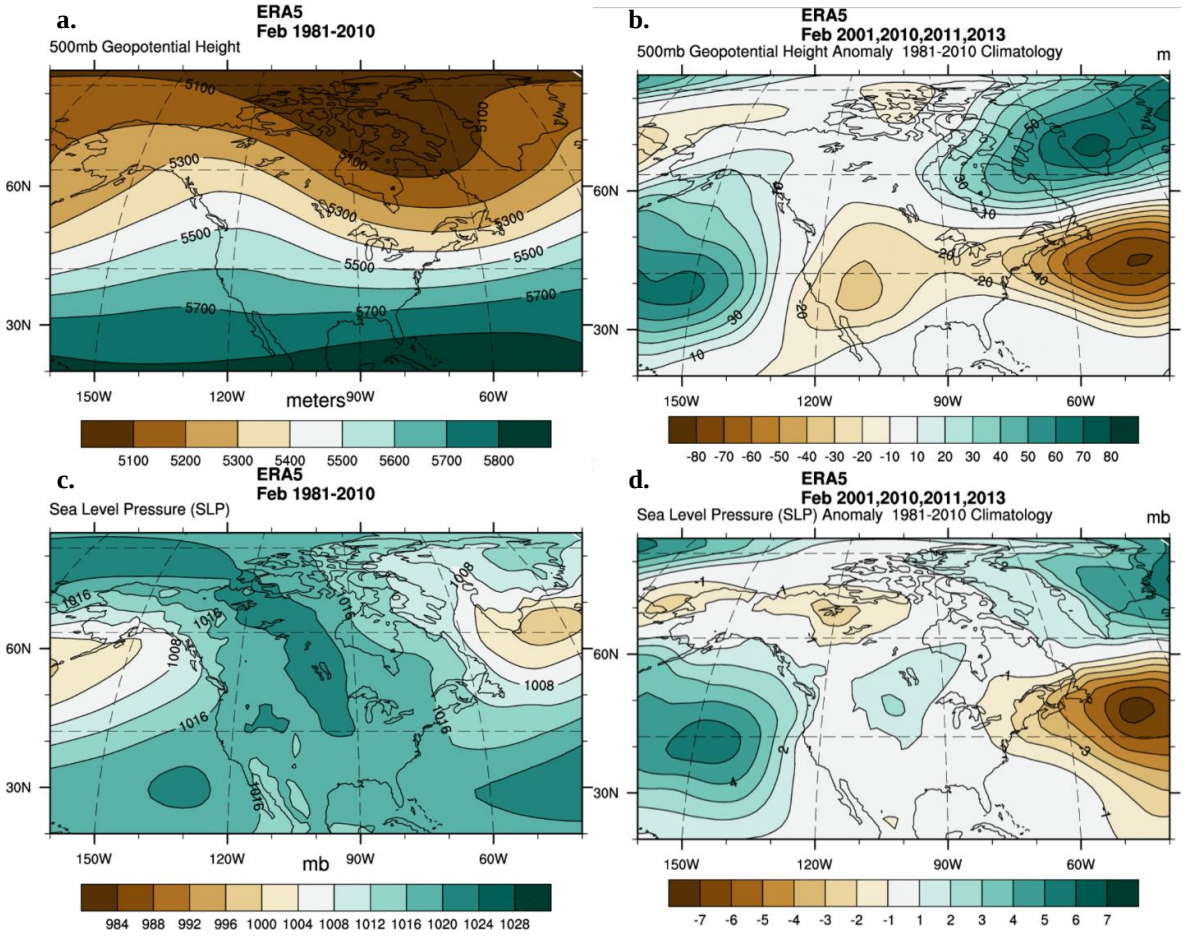

Figure 63. Baffin Bay lead-2 February composites for minimum SIE and maximum GBI. The 500GPH composites are on top with the climatology shown in a) and the composite anomaly shown in b). The MSLP composites are on the bottom with the climatology shown in c) and the composite anomaly presented in d).

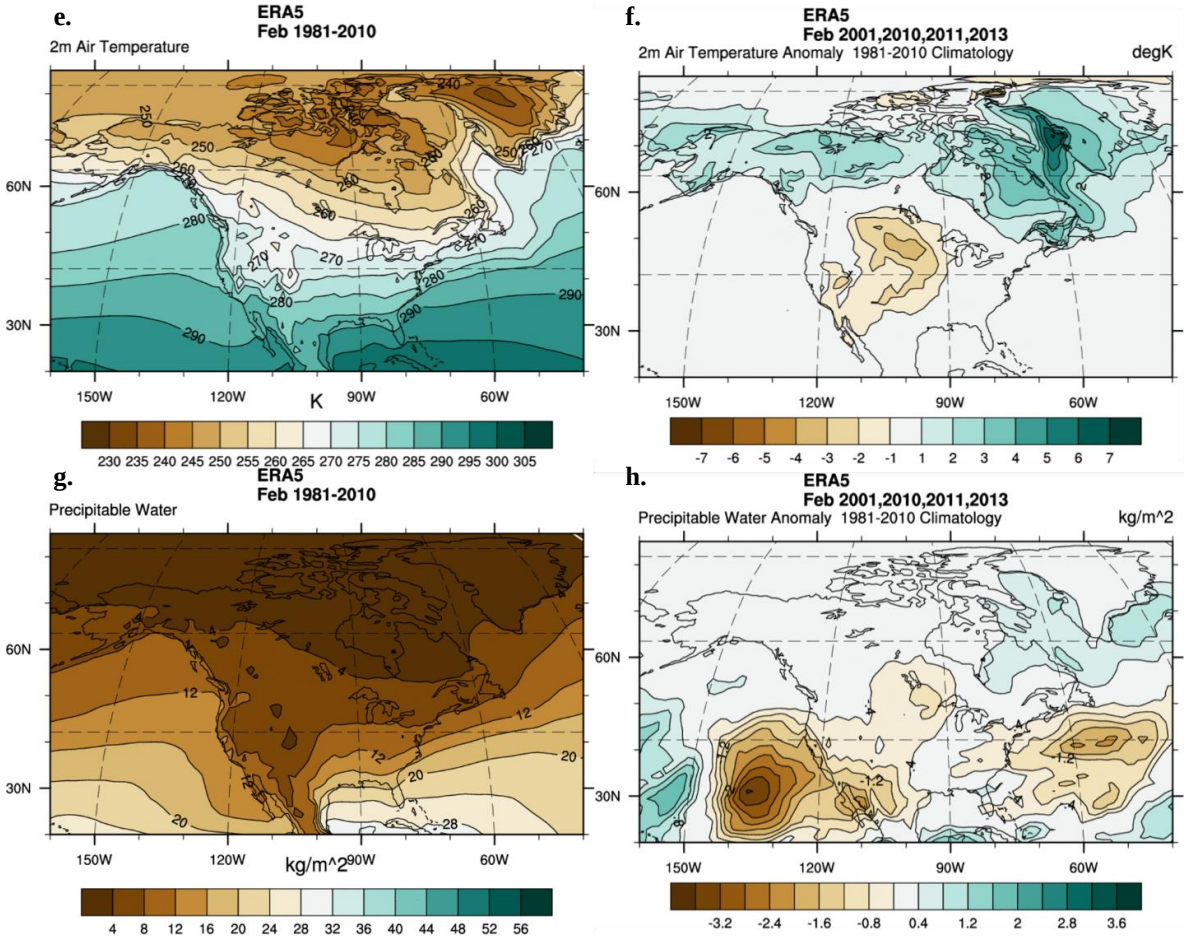

Figure 63. (cont.) Baffin Bay lead-2 February composites for minimum SIE and maximum GBI. The T2m composites are on top with the climatology shown in e) and the composite anomaly shown in f). The PW composites are on the bottom with the climatology shown in g) and the composite anomaly presented in h).

Table 8. The top 10 values for maximum SIE and minimum GBI for the Beaufort Sea in May, June, and August. Values are listed from highest to lowest. Years of overlap are highlighted, and total counts are shown on the bottom row.

May			
SIE		GBI	
Yr	Max	Yr	Min
2000	940219.39	2000	5354.79
1981	940219.39	1981	5353.18
1999	940219.39	1999	5349.03
2013	940219.39	2013	5347.90
2007	940219.39	2007	5337.43
2009	940219.39	2009	5325.90
1989	940219.39	1989	5319.58
2015	940219.39	2015	5315.02
1992	940219.39	1992	5288.23
2018	940219.39	2018	5255.26
count: 10			

June			
SIE		GBI	
Yr	Max	Yr	Min
1992	940219.39	2013	5453.37
2000	940219.39	2018	5451.20
1989	940073.13	1992	5445.97
1996	939969.98	1983	5442.35
2001	939824.85	2006	5434.57
1980	939714.77	1979	5425.67
2006	939659.38	1988	5423.74
2013	939326.59	1999	5414.71
1994	938236.01	1986	5411.90
1984	937489.88	1994	5388.30
count: 4			

August			
SIE		GBI	
Yr	Max	Yr	Min
1991	907297.05	1988	5465.51
1985	886917.08	2018	5461.23
1984	862912.58	1997	5461.06
2001	855409.23	2013	5459.60
1996	837214.88	1996	5457.66
1992	822629.74	1984	5449.66
1983	817714.09	1989	5447.10
1994	805201.25	1992	5438.40
1986	801199.30	1983	5427.38
1988	786583.08	1991	5427.08
count: 6			

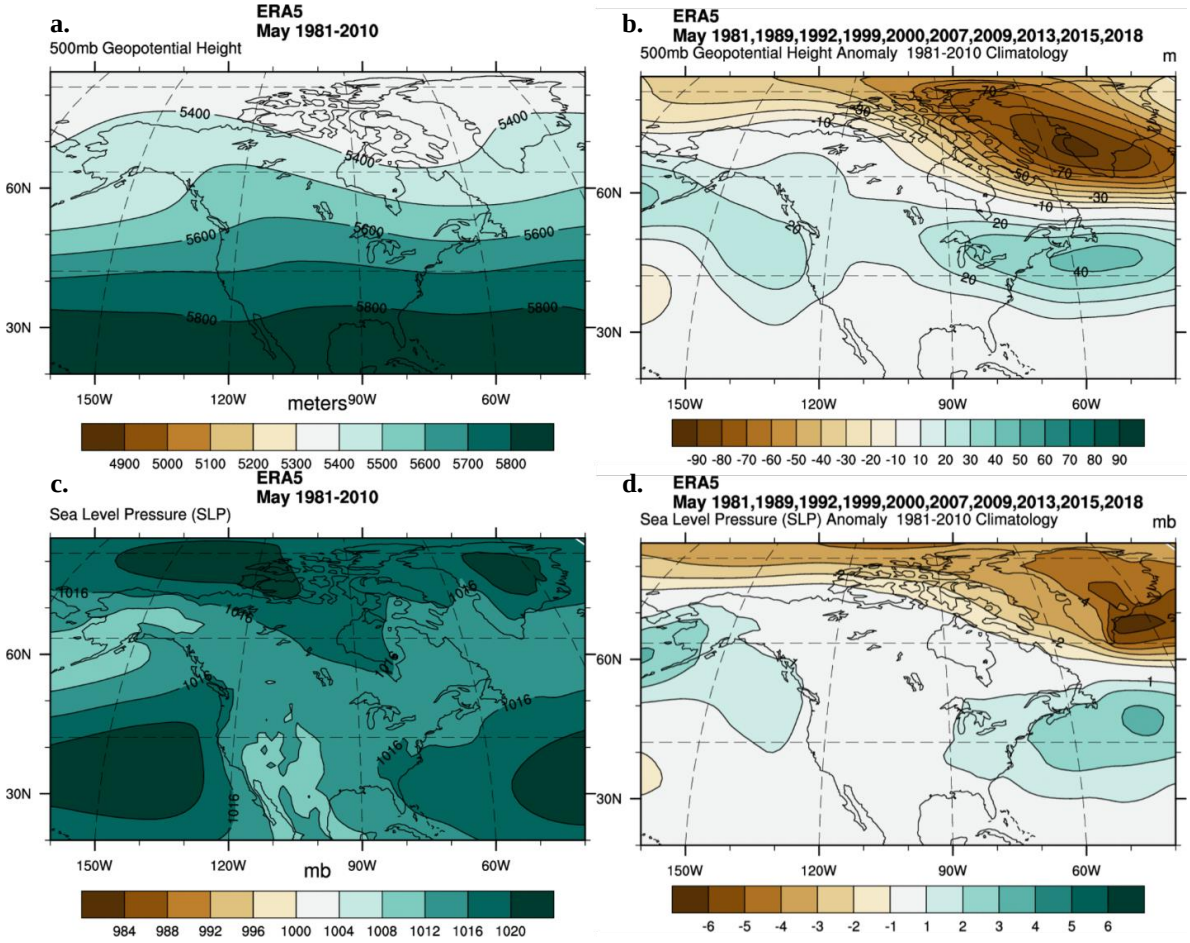

Figure 64. Beaufort Sea contemporary May composites for maximum SIE and minimum GBI. The 500GPH composites are on top with the climatology shown in a) and the composite anomaly shown in b). The MSLP composites are on the bottom with the climatology shown in c) and the composite anomaly presented in d).

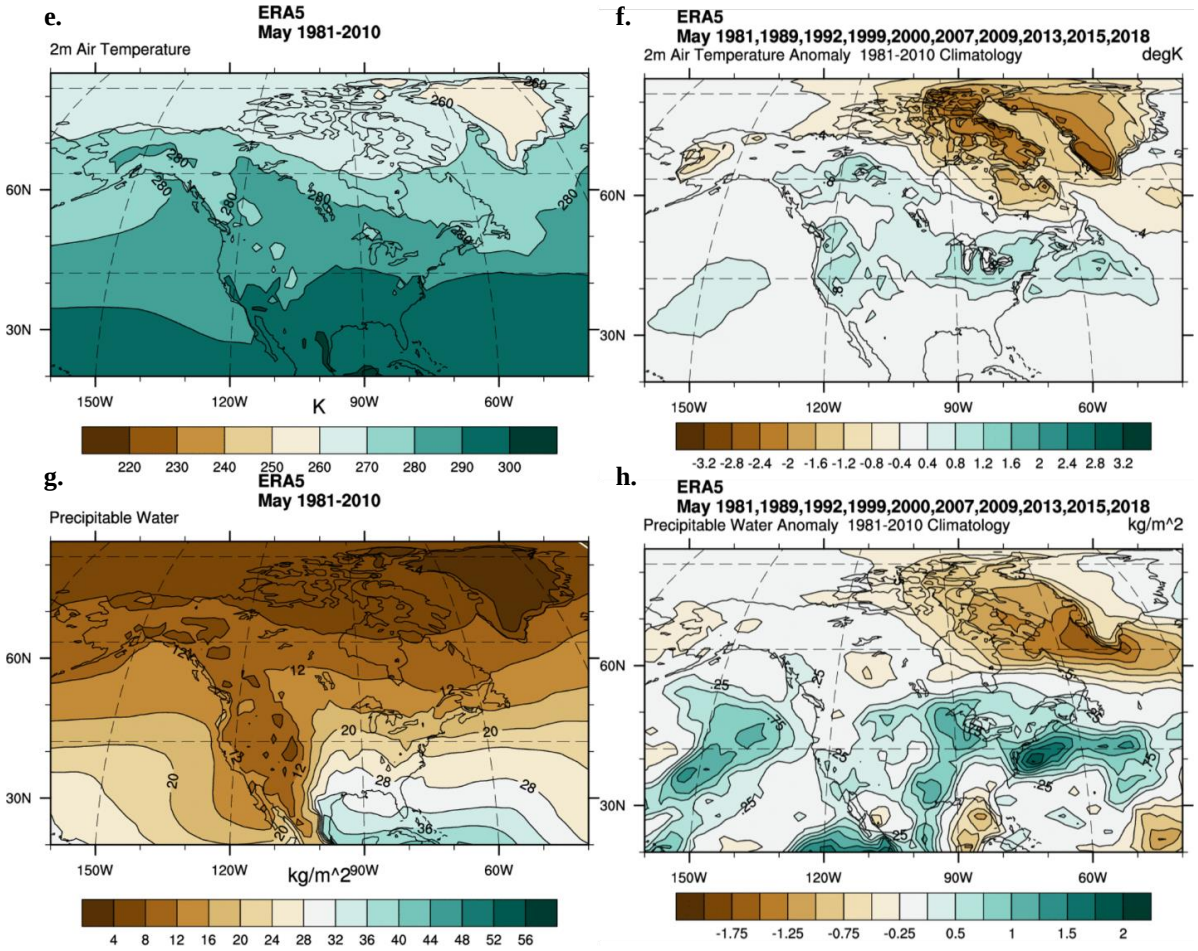

Figure 64. (cont.) Beaufort Sea contemporary May composites for maximum SIE and minimum GBI. The T2m composites are on top with the climatology shown in e) and the composite anomaly shown in f). The PW composites are on the bottom with the climatology shown in g) and the composite anomaly presented in h).

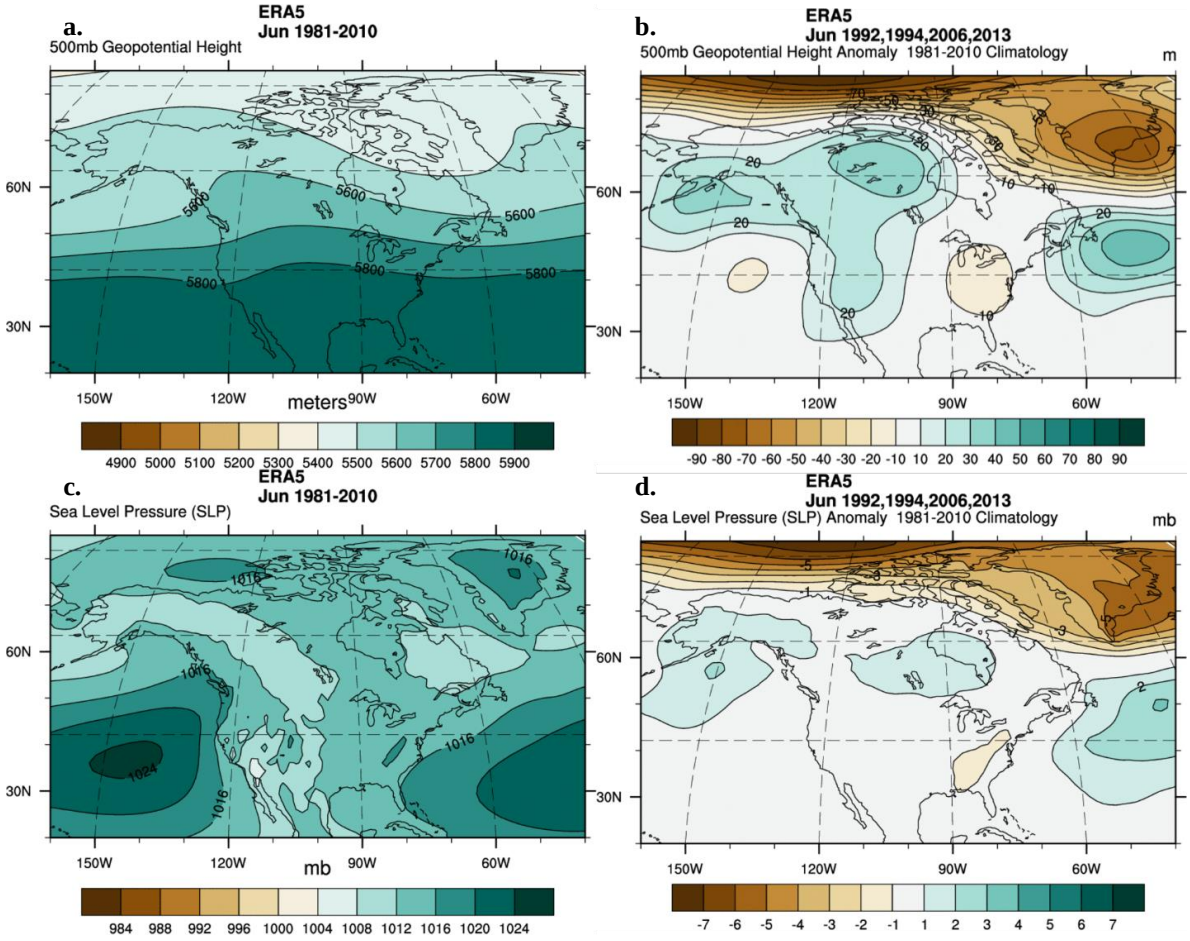

Figure 65. Beaufort Sea contemporary June composites for maximum SIE and minimum GBI. The 500GPH composites are on top with the climatology shown in a) and the composite anomaly shown in b). The MSLP composites are on the bottom with the climatology shown in c) and the composite anomaly presented in d).

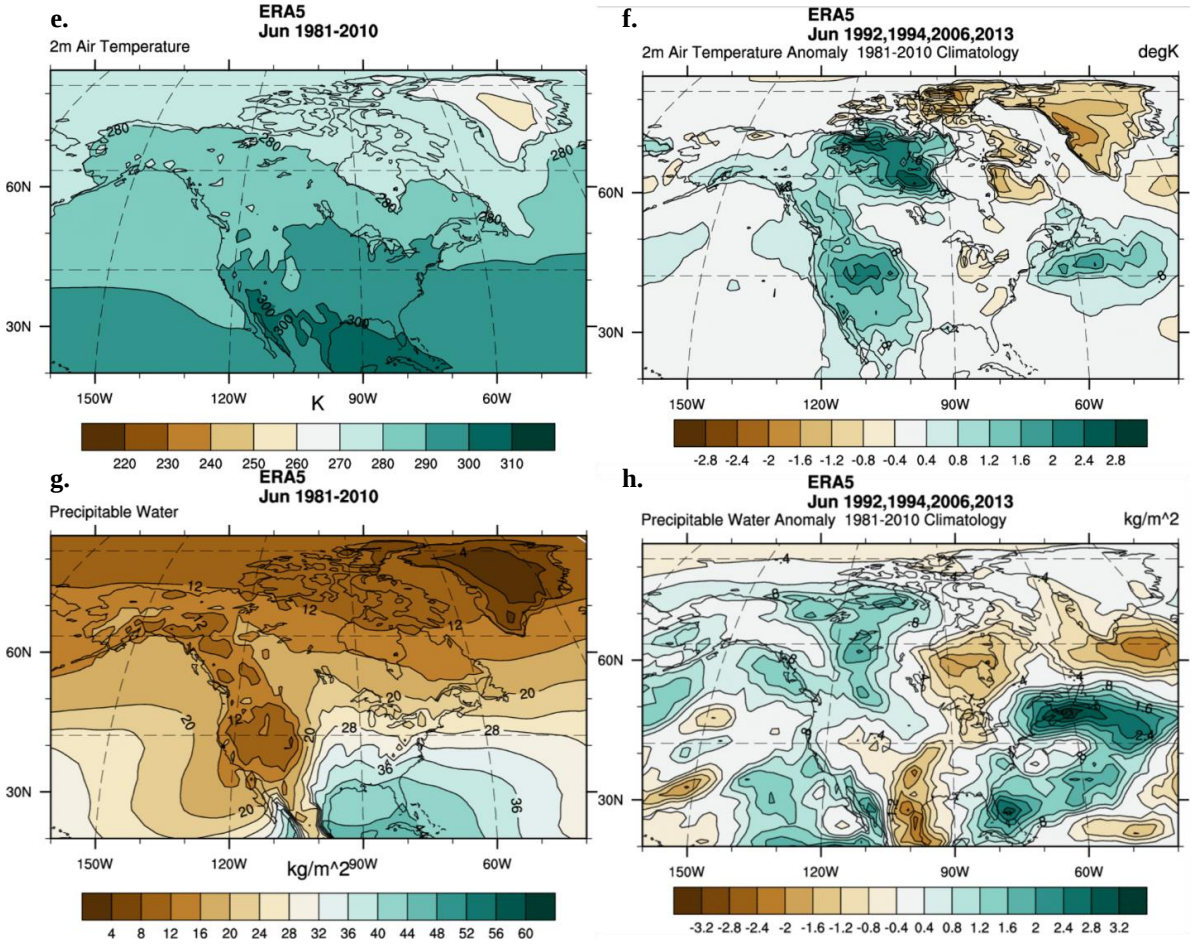

Figure 65. (cont.) Beaufort Sea contemporary June composites for maximum SIE and minimum GBI. The T2m composites are on top with the climatology shown in e) and the composite anomaly shown in f). The PW composites are on the bottom with the climatology shown in g) and the composite anomaly presented in h).

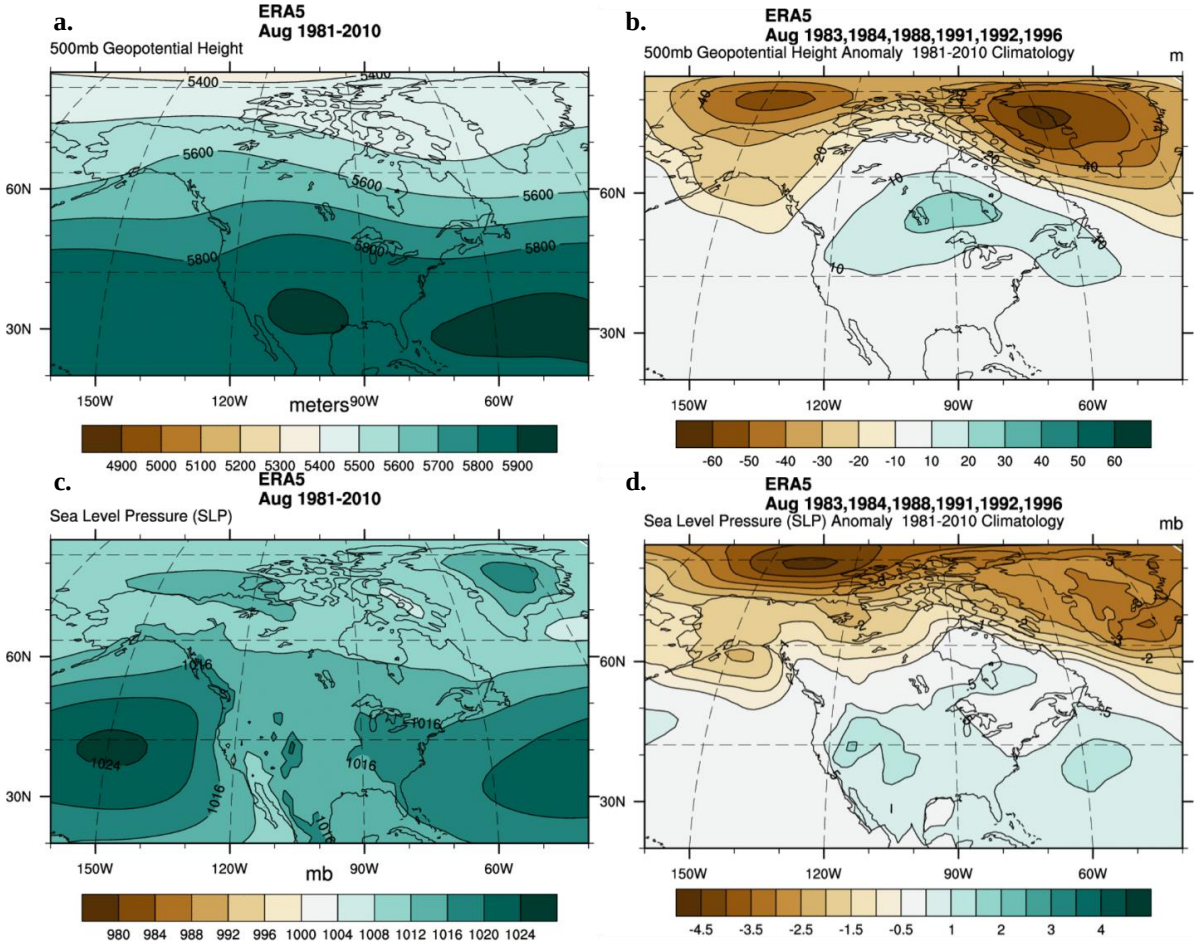

Figure 66. Beaufort Sea contemporary August composites for maximum SIE and minimum GBI. The 500GPH composites are on top with the climatology shown in a) and the composite anomaly shown in b). The MSLP composites are on the bottom with the climatology shown in c) and the composite anomaly presented in d).

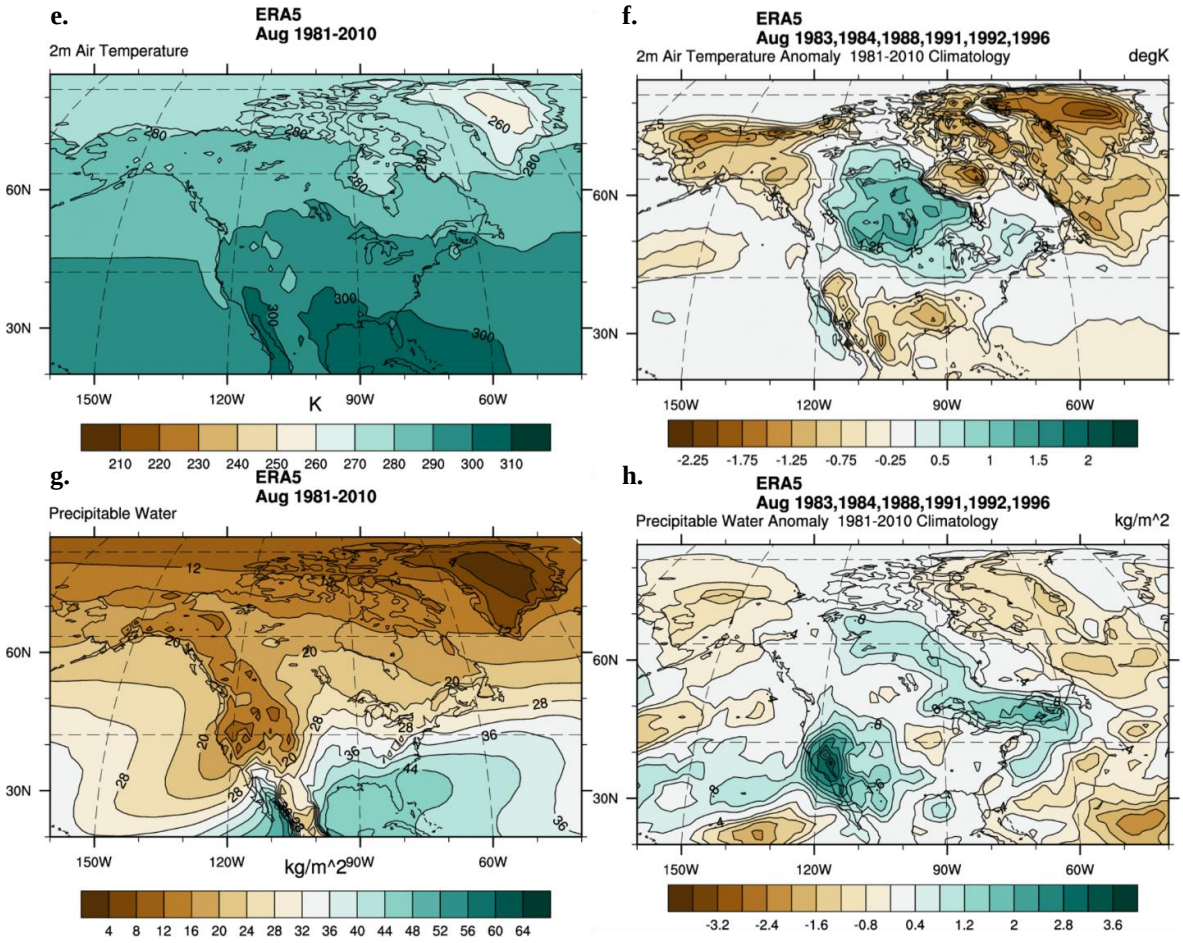

Figure 66. (cont.) Beaufort Sea contemporary August composites for maximum SIE and minimum GBI. The T2m composites are on top with the climatology shown in e) and the composite anomaly shown in f). The PW composites are on the bottom with the climatology shown in g) and the composite anomaly presented in h).

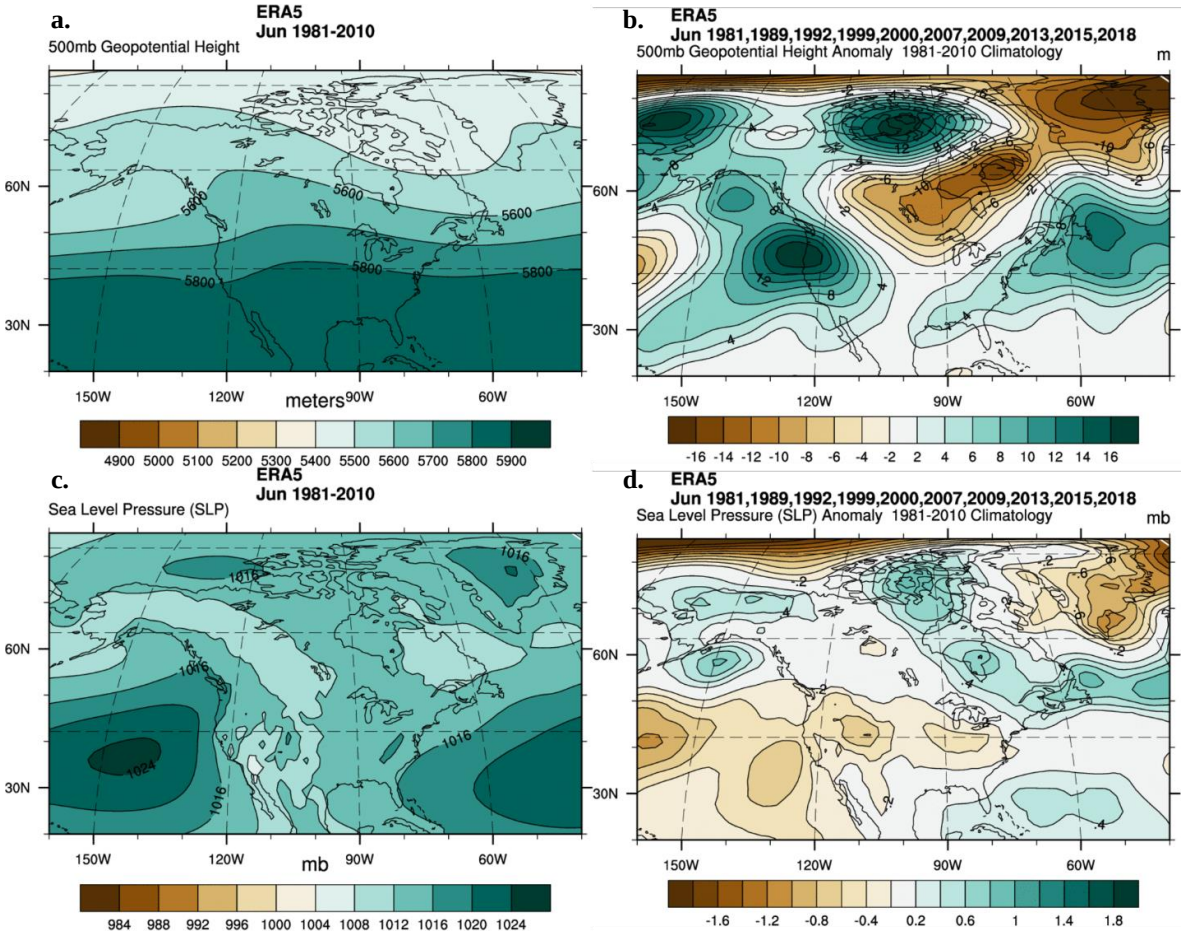

Figure 67. Beaufort Sea lead-1 June composites for maximum SIE and minimum GBI. The 500GPH composites are on top with the climatology shown in a) and the composite anomaly shown in b). The MSLP composites are on the bottom with the climatology shown in c) and the composite anomaly presented in d).

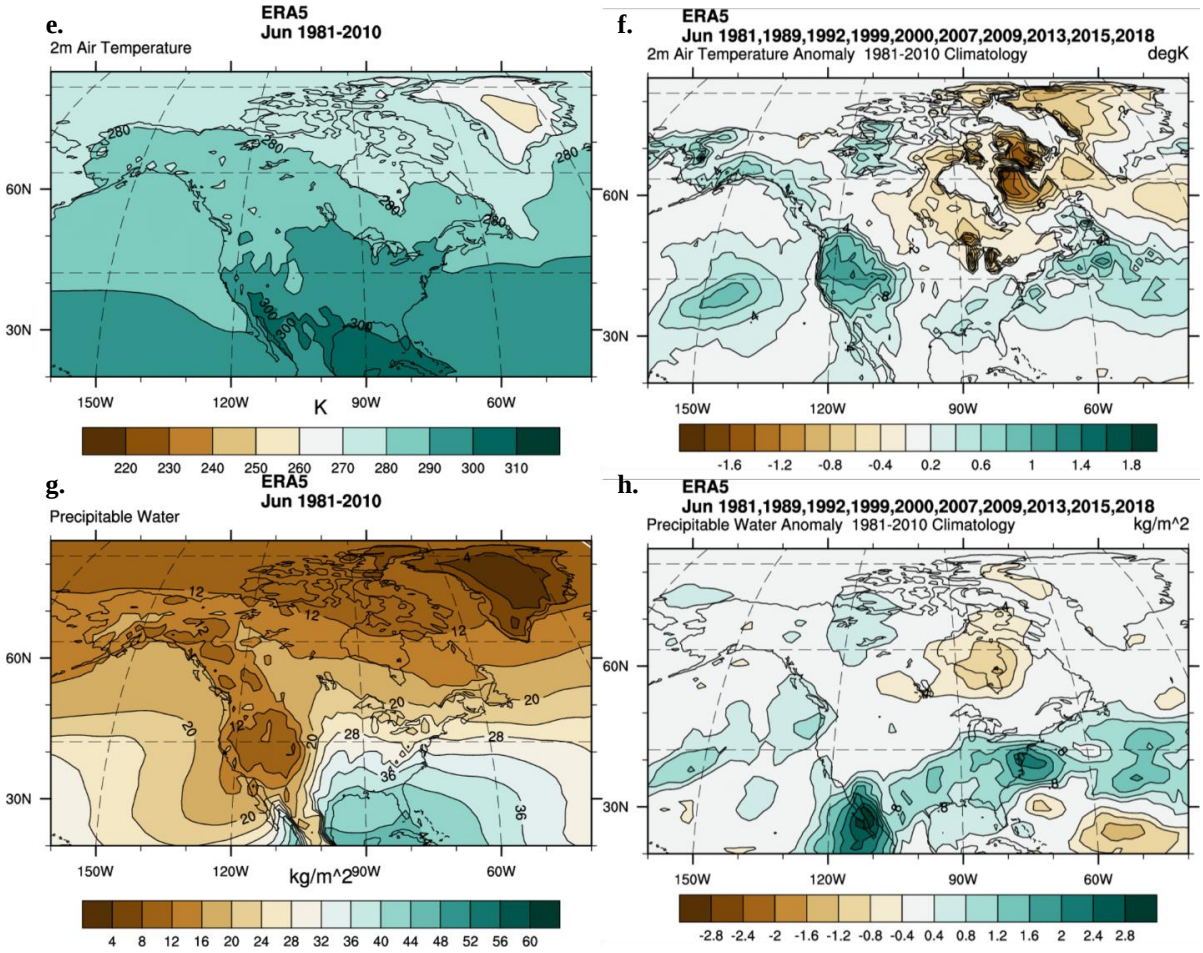

Figure 67. (cont.) Beaufort Sea lead-1 June composites for maximum SIE and minimum GBI. The T2m composites are on top with the climatology shown in e) and the composite anomaly shown in f). The PW composites are on the bottom with the climatology shown in g) and the composite anomaly presented in h).

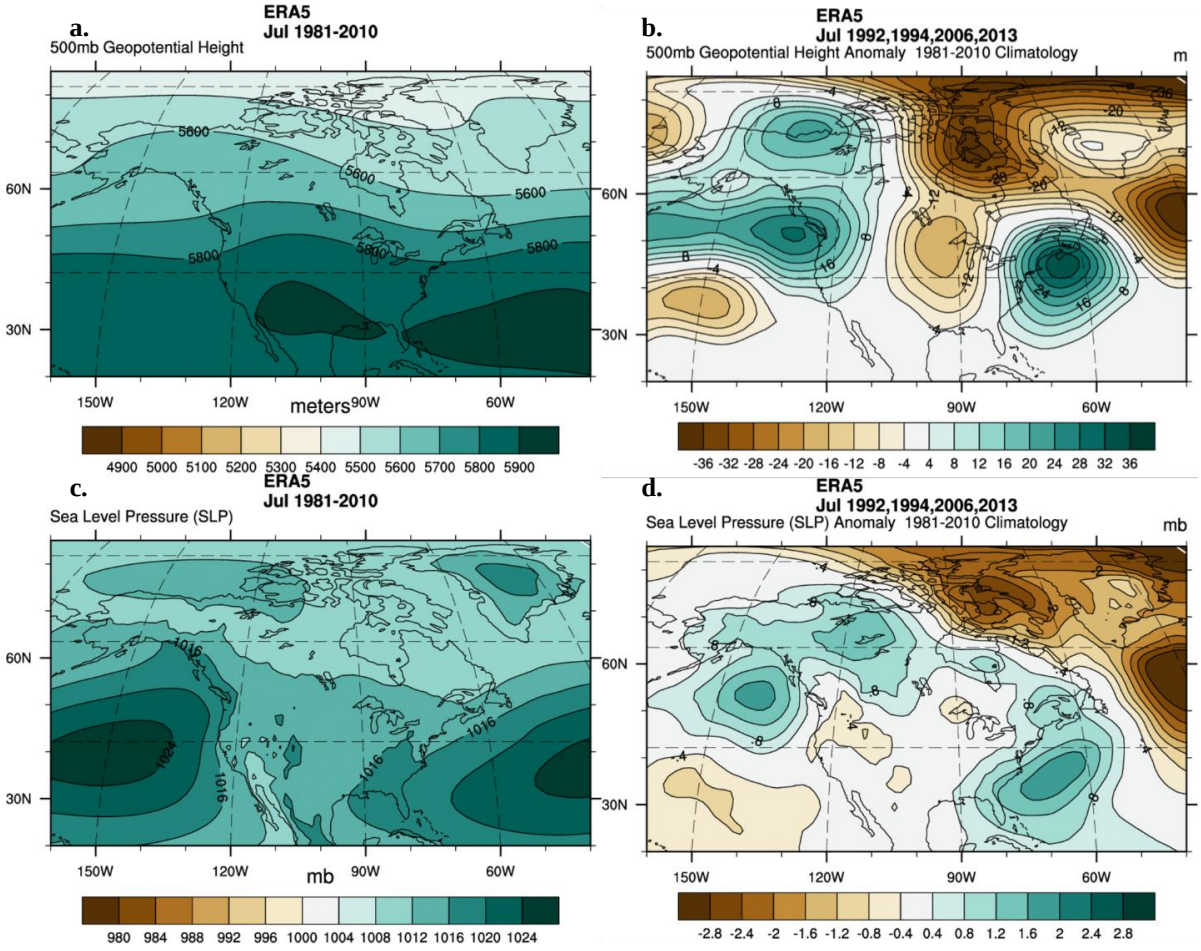

Figure 68. Beaufort Sea lead-1 July composites for maximum SIE and minimum GBI. The 500GPH composites are on top with the climatology shown in a) and the composite anomaly shown in b). The MSLP composites are on the bottom with the climatology shown in c) and the composite anomaly presented in d).

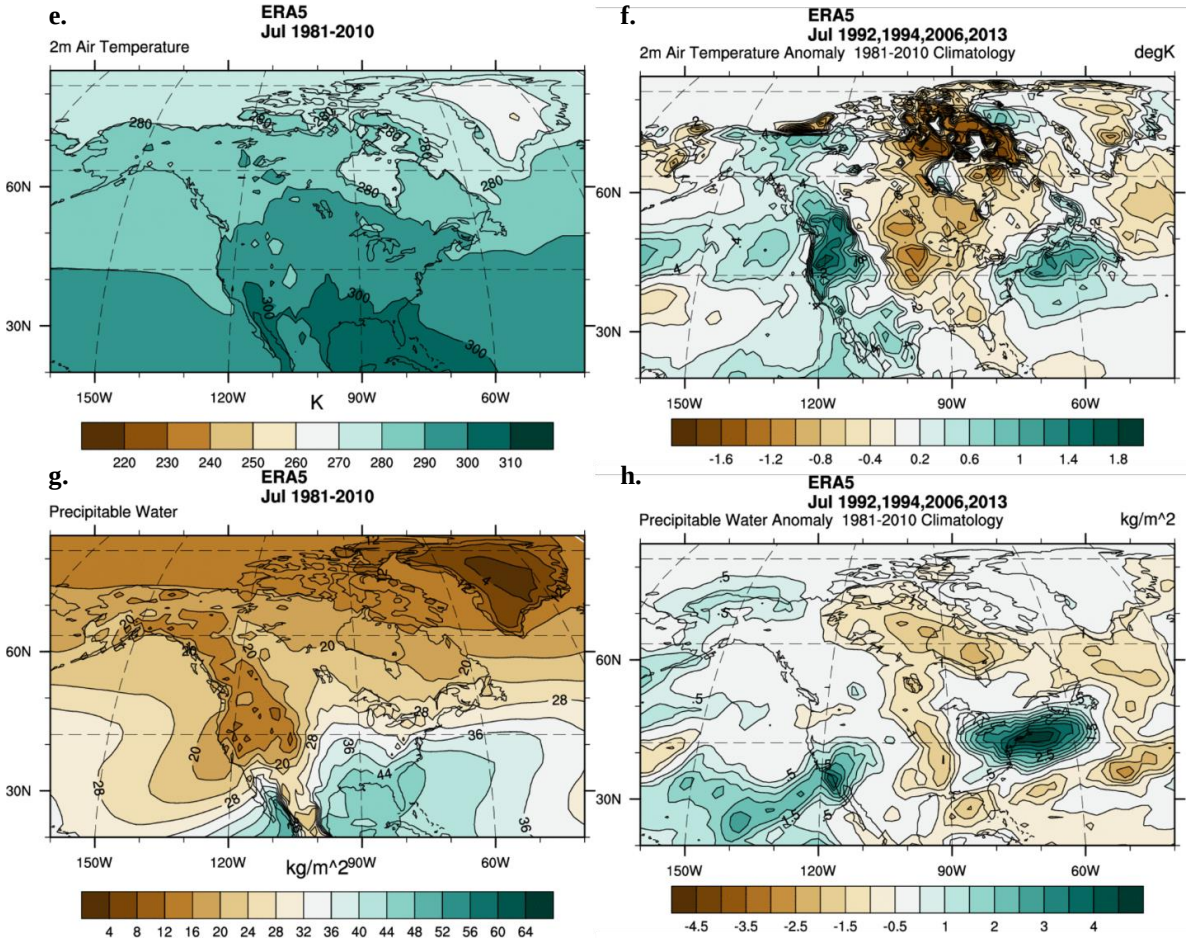

Figure 68. (cont.) Beaufort Sea lead-1 July composites for maximum SIE and minimum GBI. The T2m composites are on top with the climatology shown in e) and the composite anomaly shown in f). The PW composites are on the bottom with the climatology shown in g) and the composite anomaly presented in h).

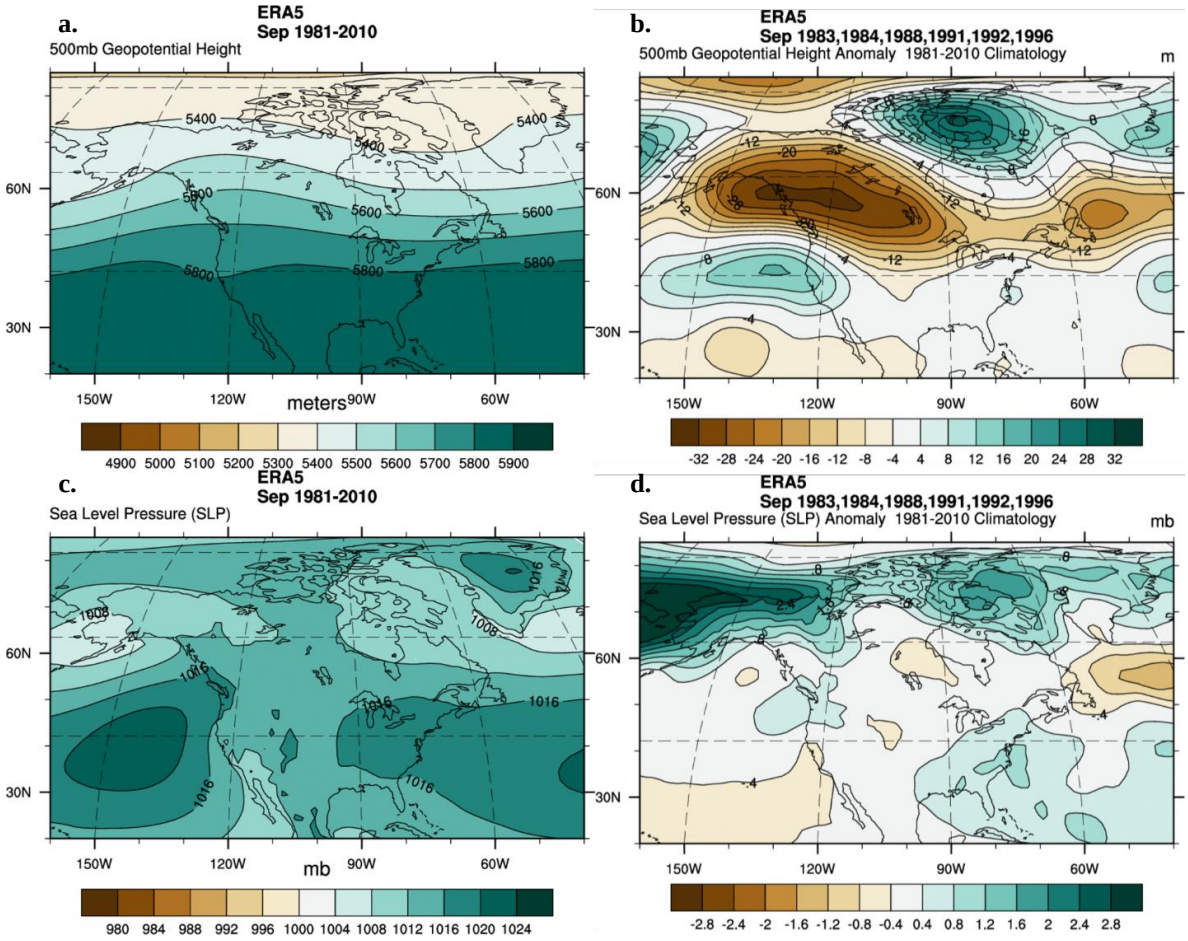

Figure 69. Beaufort Sea lead-1 September composites for maximum SIE and minimum GBI. The 500GPH composites are on top with the climatology shown in a) and the composite anomaly shown in b). The MSLP composites are on the bottom with the climatology shown in c) and the composite anomaly presented in d).

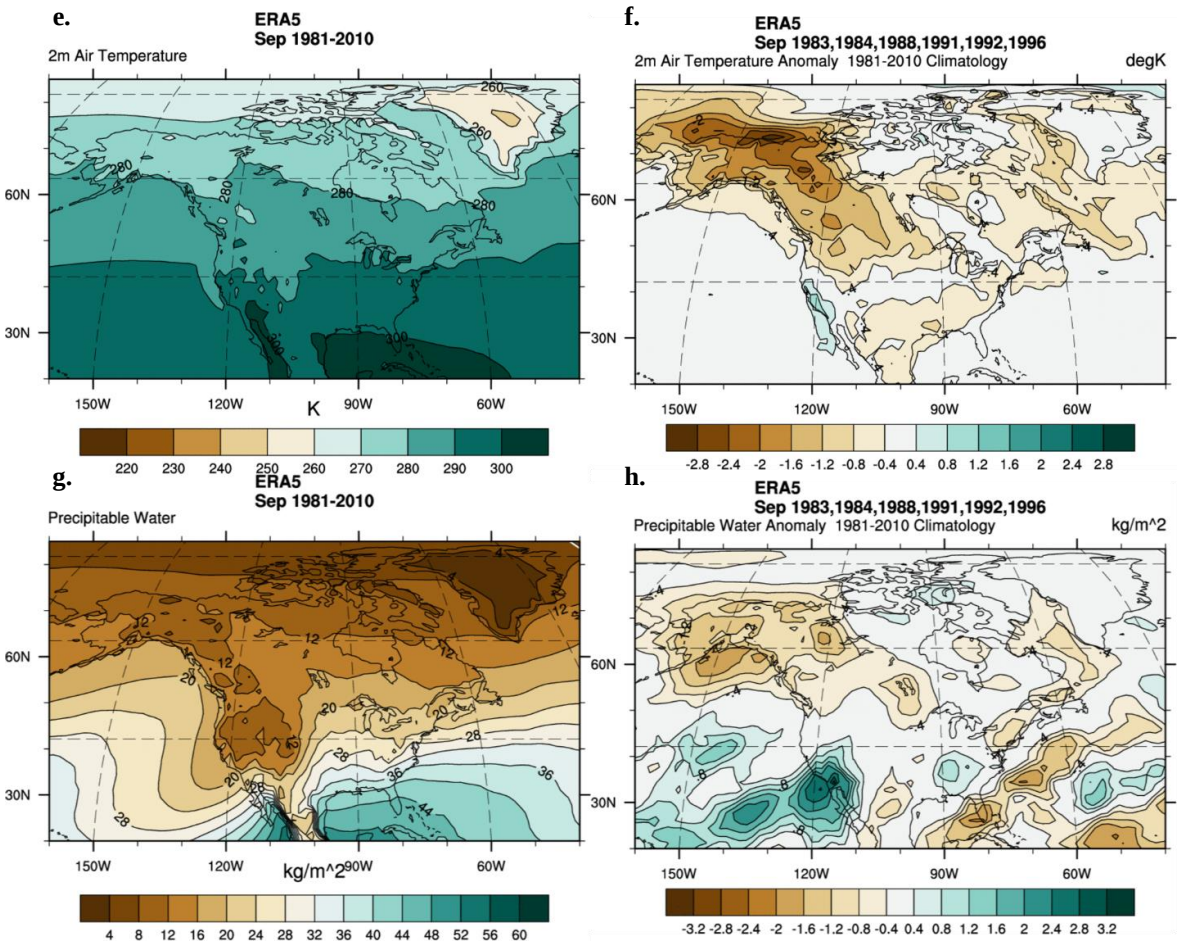

Figure 60. (cont.) Beaufort Sea lead-1 September composites for maximum SIE and minimum GBI. The T2m composites are on top with the climatology shown in e) and the composite anomaly shown in f). The PW composites are on the bottom with the climatology shown in g) and the composite anomaly presented in h).

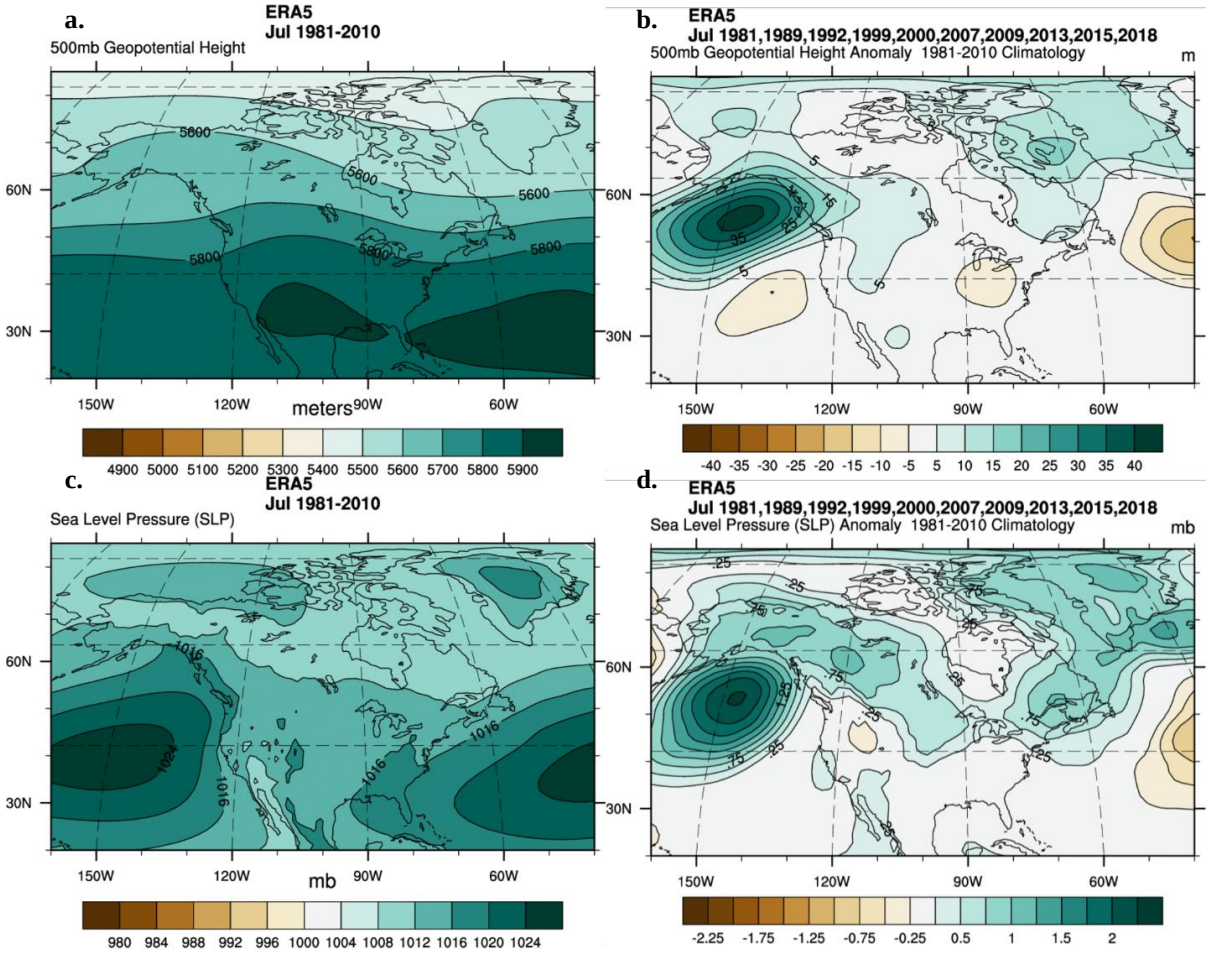

Figure 70. Beaufort Sea lead-2 July composites for maximum SIE and minimum GBI. The 500GPH composites are on top with the climatology shown in a) and the composite anomaly shown in b). The MSLP composites are on the bottom with the climatology shown in c) and the composite anomaly presented in d).

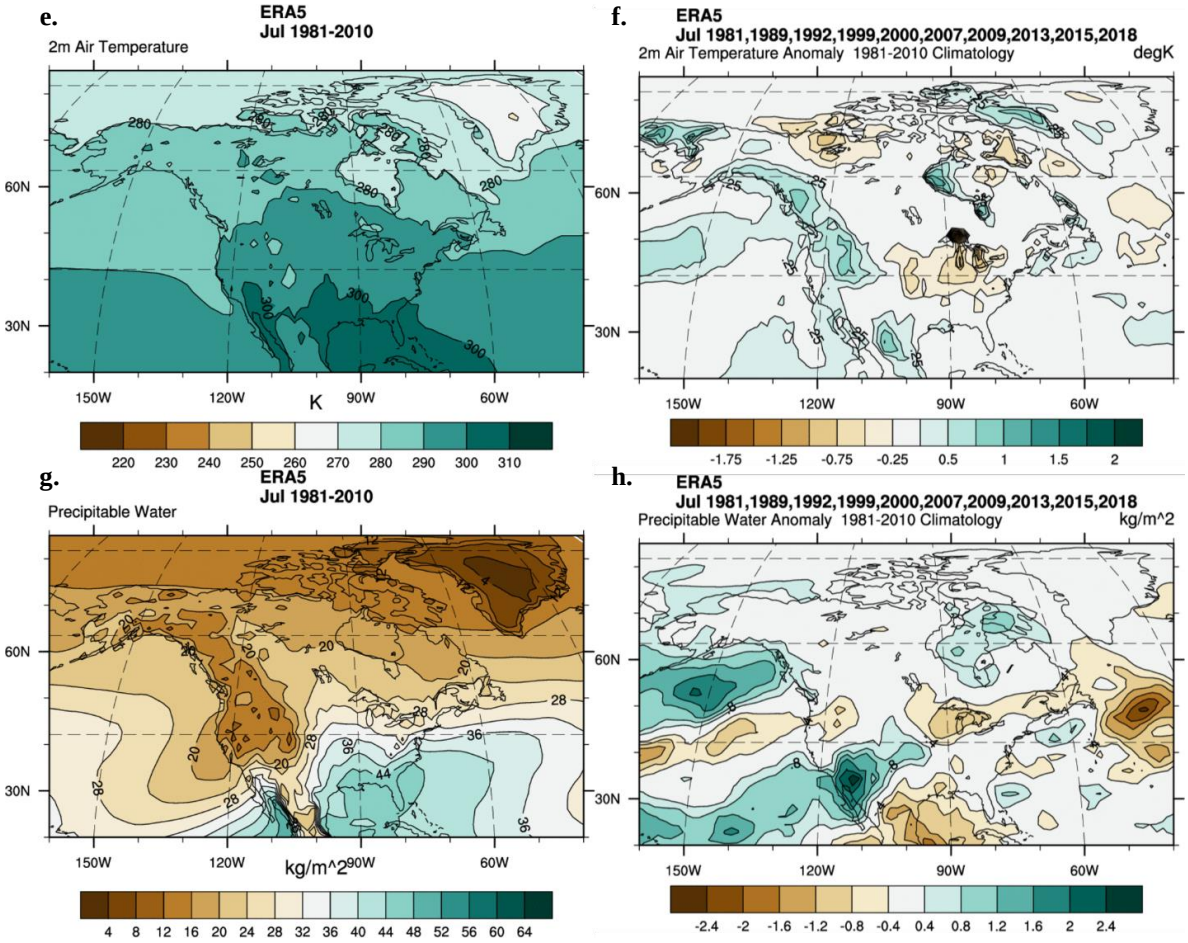

Figure 70. (cont.) Beaufort Sea lead-2 July composites for maximum SIE and minimum GBI. The T2m composites are on top with the climatology shown in e) and the composite anomaly shown in f). The PW composites are on the bottom with the climatology shown in g) and the composite anomaly presented in h).

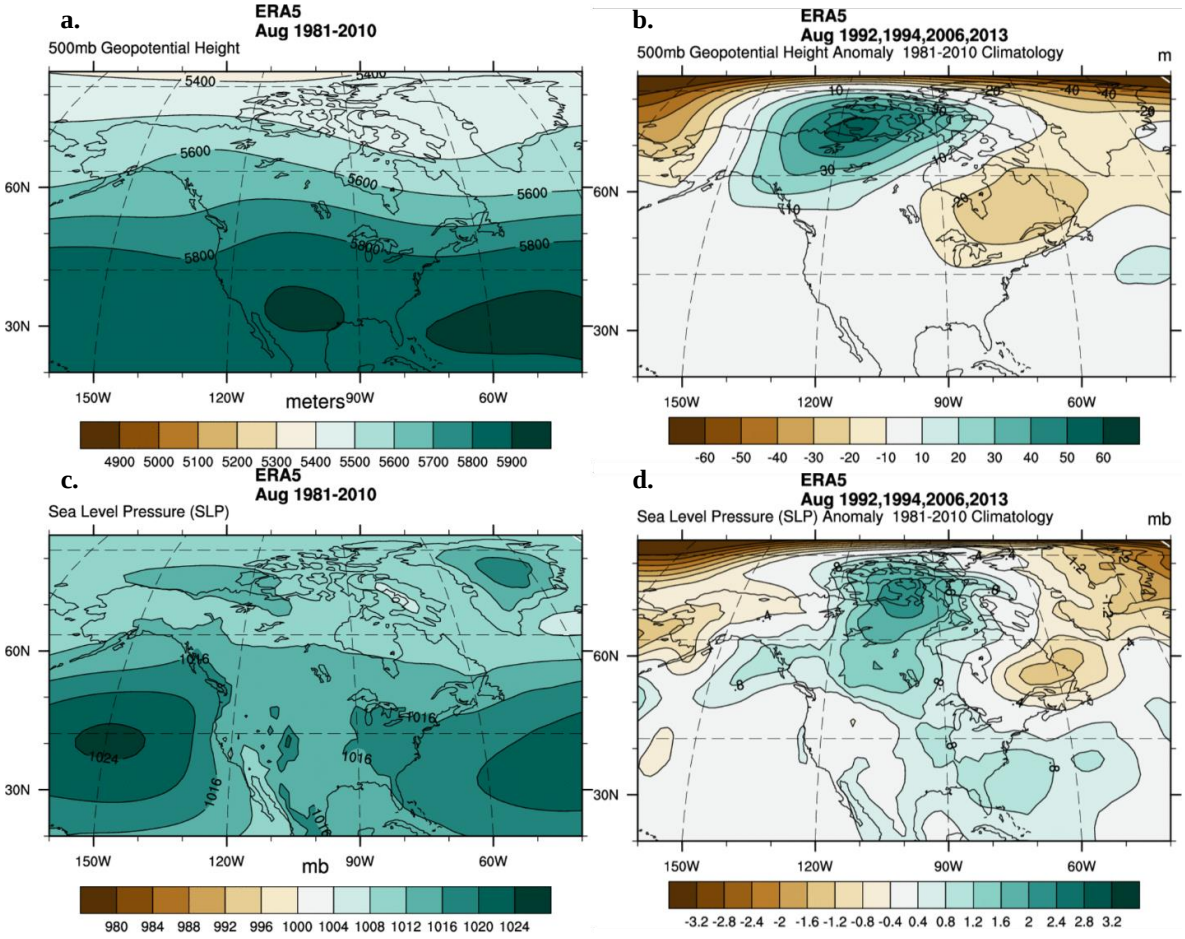

Figure 71. Beaufort Sea lead-2 August composites for maximum SIE and minimum GBI. The 500GPH composites are on top with the climatology shown in a) and the composite anomaly shown in b). The MSLP composites are on the bottom with the climatology shown in c) and the composite anomaly presented in d).

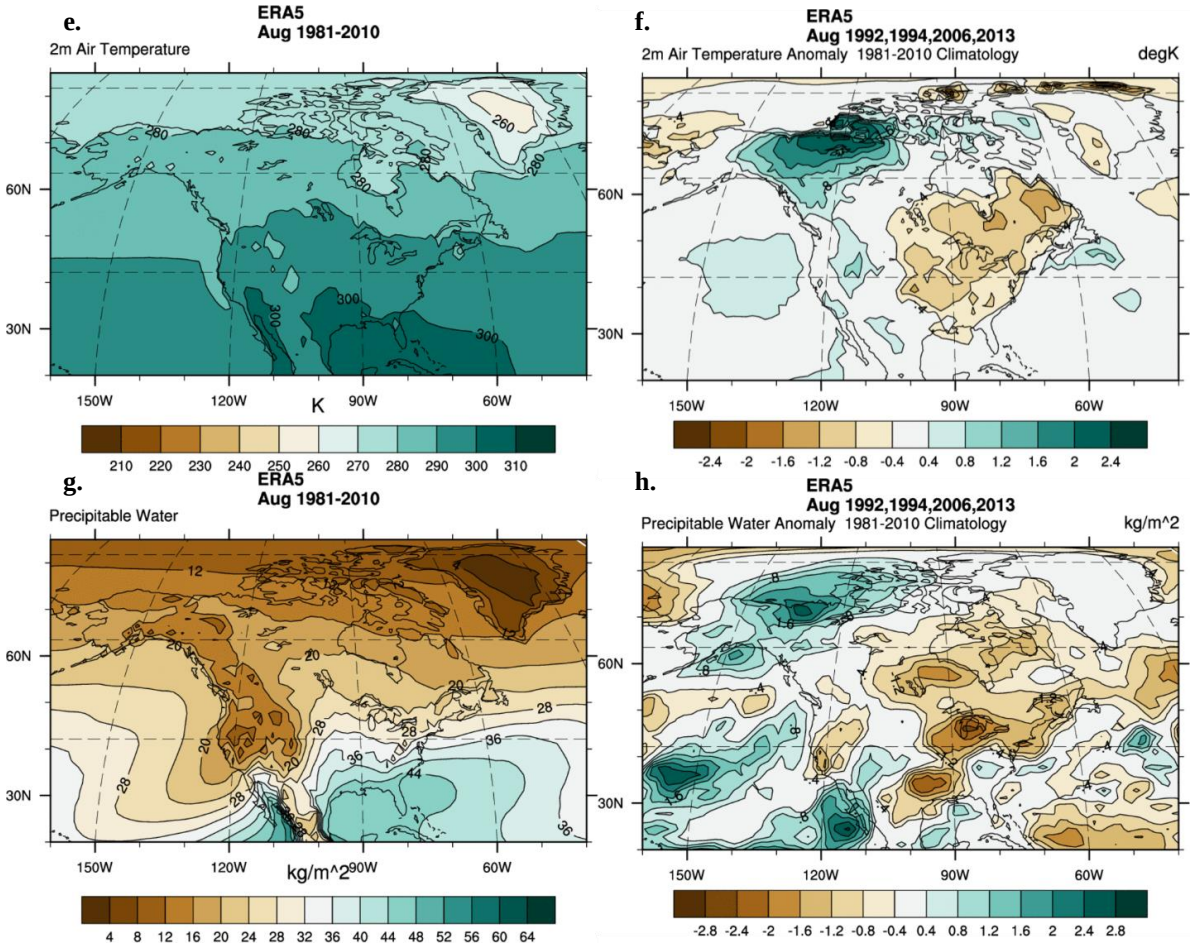

Figure 71. (cont.) Beaufort Sea lead-2 August composites for maximum SIE and minimum GBI. The T2m composites are on top with the climatology shown in e) and the composite anomaly shown in f). The PW composites are on the bottom with the climatology shown in g) and the composite anomaly presented in h).

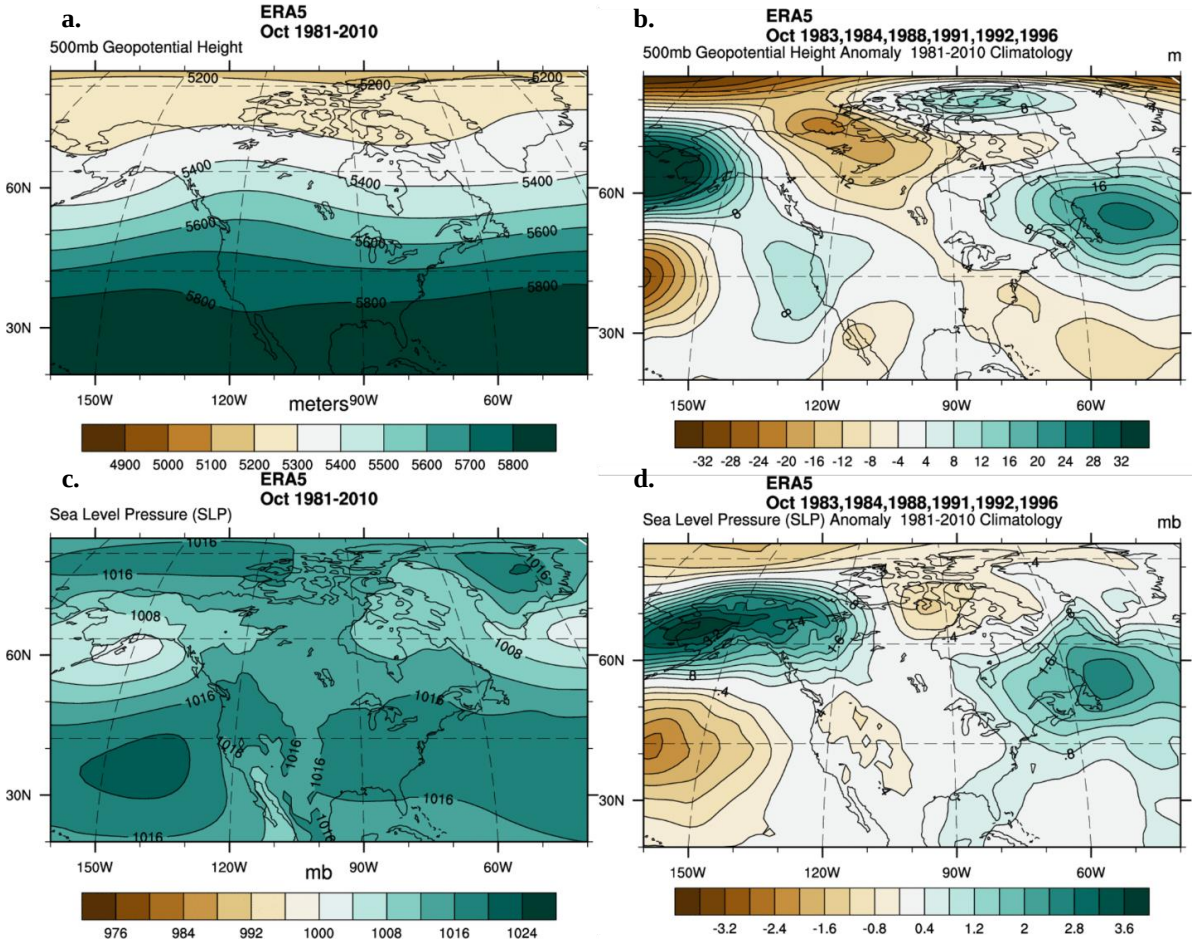

Figure 72. Beaufort Sea lead-2 October composites for maximum SIE and minimum GBI. The 500GPH composites are on top with the climatology shown in a) and the composite anomaly shown in b). The MSLP composites are on the bottom with the climatology shown in c) and the composite anomaly presented in d).

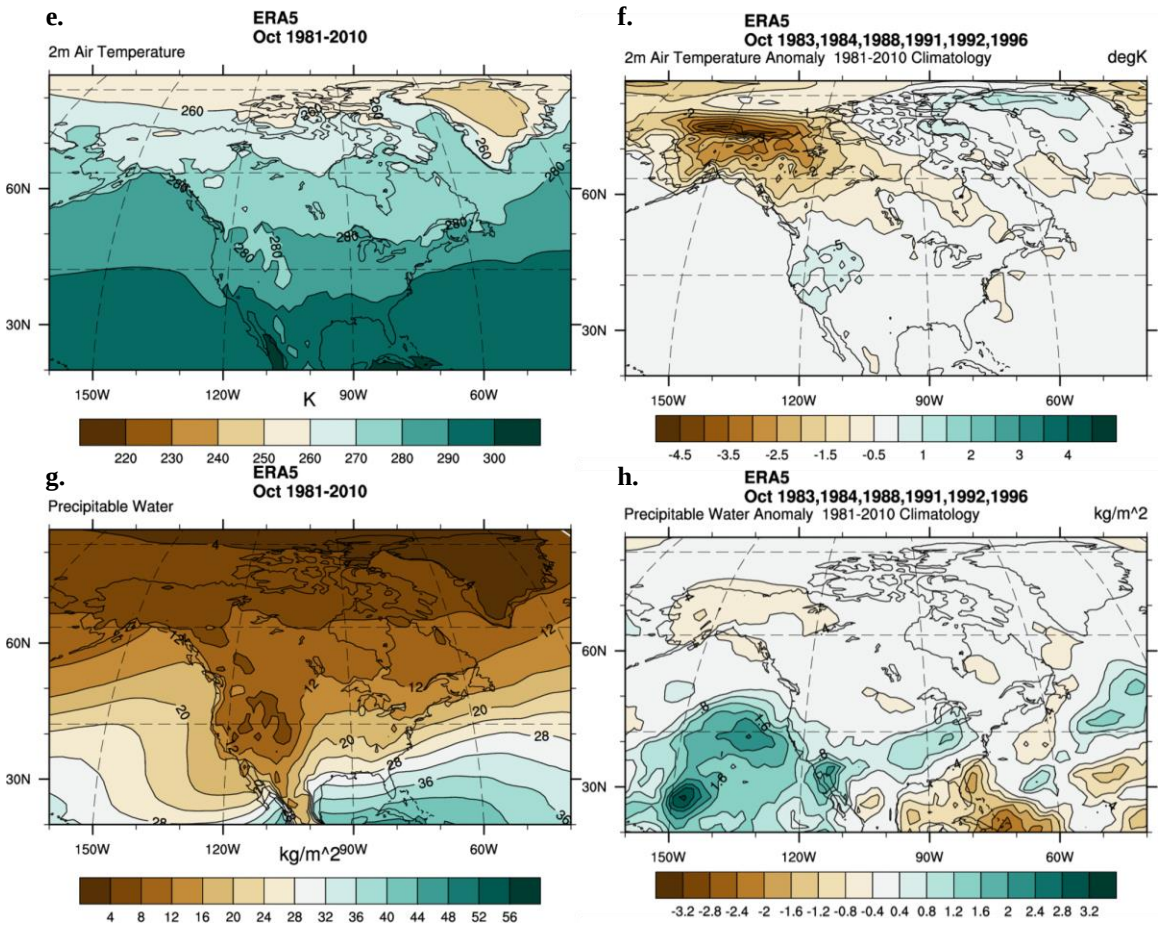

Figure 72. (cont.) Beaufort Sea lead-2 October composites for maximum SIE and minimum GBI. The T2m composites are on top with the climatology shown in e) and the composite anomaly shown in f). The PW composites are on the bottom with the climatology shown in g) and the composite anomaly presented in h).

Table 9. The top 10 values for minimum SIE and maximum GBI for the Beaufort Sea in May, June, and August. Values are listed from highest to lowest. Years of overlap are highlighted, and total counts are shown on the bottom row.

May			
SIE		GBI	
Yr	Min	Yr	Max
2011	931142.48	2010	5479.97
2005	927975.70	2008	5473.09
1991	925551.85	2017	5466.04
2017	925495.16	1993	5451.55
1995	923355.34	2005	5445.83
2008	920877.13	1980	5444.16
2012	917234.96	2006	5441.99
2015	915241.99	1995	5439.65
1998	892792.50	2012	5439.19
2016	822352.69	1997	5420.96
count: 5			

June			
SIE		GBI	
Yr	Min	Yr	Max
1988	865928.82	2012	5581.84
2015	858637.47	1998	5564.49
2005	849406.79	2011	5542.43
1993	835900.36	2007	5541.48
2010	818638.58	2008	5540.48
2017	814085.60	1982	5534.05
2008	812049.36	1997	5519.11
2012	804661.48	1987	5516.73
2016	769860.42	2014	5516.12
1998	674219.32	2016	5511.60
count: 4			

August			
SIE		GBI	
Yr	Min	Yr	Max
2007	616404.54	2010	5571.04
2018	561689.18	2016	5550.43
2010	550331.89	2011	5549.69
2015	522161.77	2014	5542.67
2011	503167.19	1980	5541.61
1998	462102.46	2003	5539.40
2017	354415.14	2012	5539.20
2008	297644.24	2007	5534.71
2016	288741.71	2006	5533.88
2012	213364.93	1987	5524.37
count: 5			

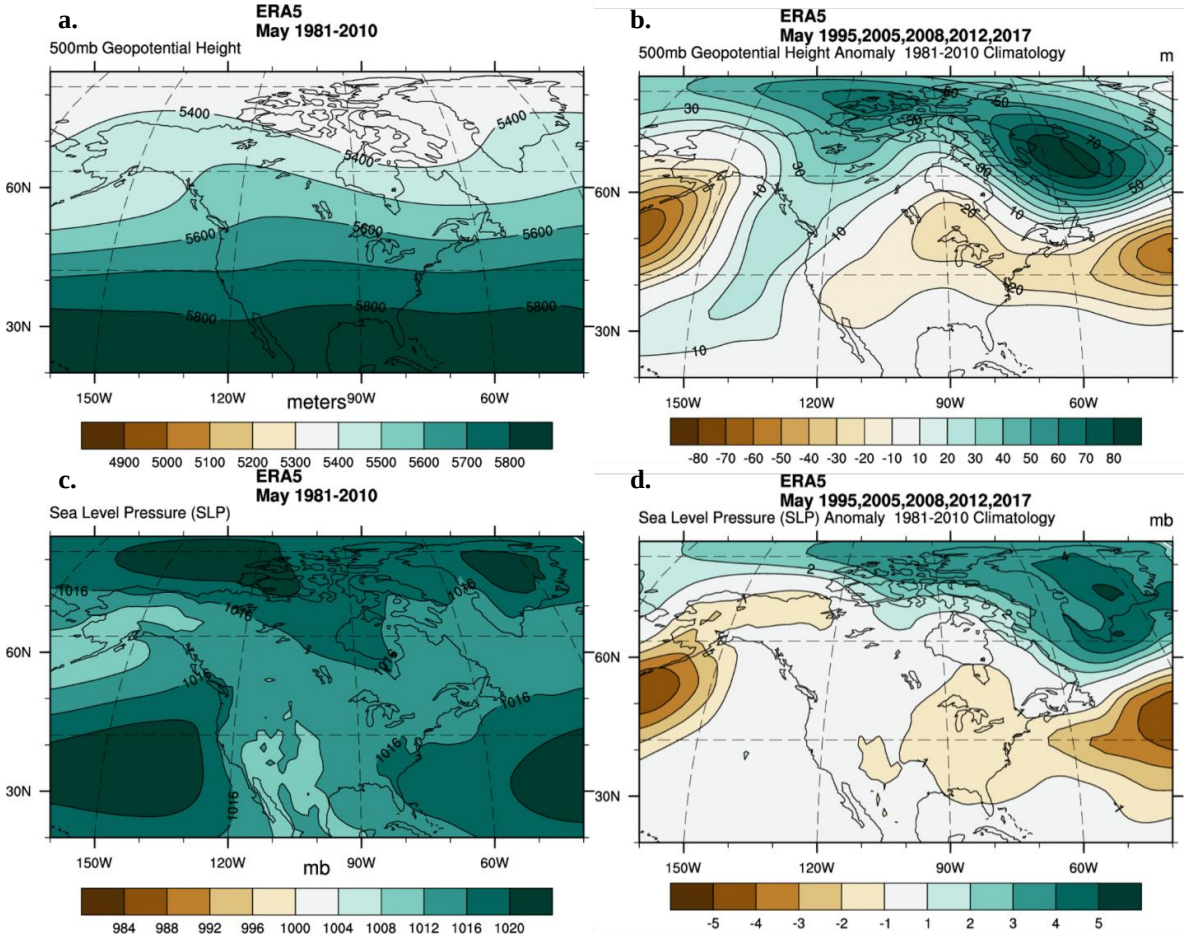

Figure 73. Beaufort Sea contemporary May composites for minimum SIE and maximum GBI. The 500GPH composites are on top with the climatology shown in a) and the composite anomaly shown in b). The MSLP composites are on the bottom with the climatology shown in c) and the composite anomaly presented in d).

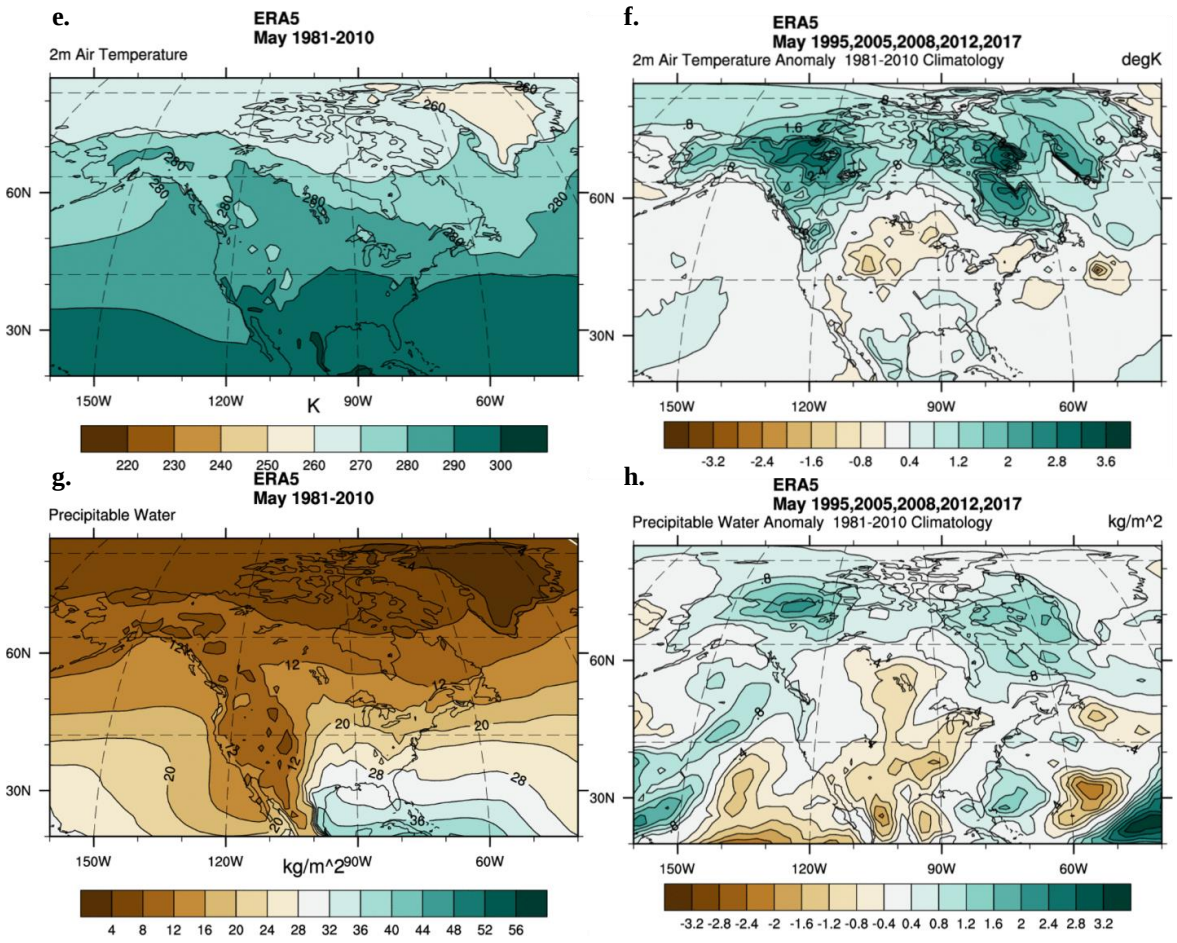

Figure 73. (cont.) Beaufort Sea contemporary May composites for minimum SIE and maximum GBI. The T2m composites are on top with the climatology shown in e) and the composite anomaly shown in f). The PW composites are on the bottom with the climatology shown in g) and the composite anomaly presented in h).

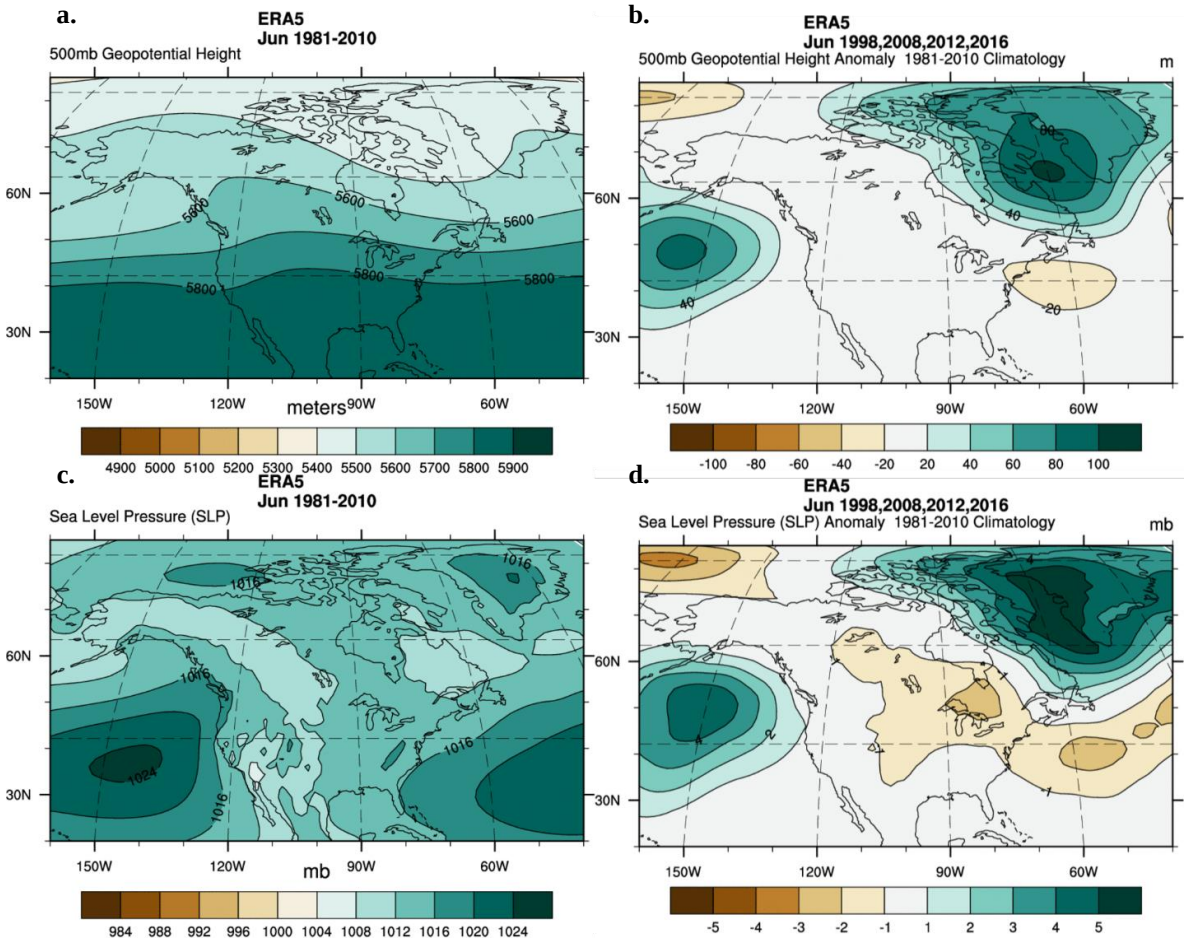

Figure 74. Beaufort Sea contemporary June composites for minimum SIE and maximum GBI. The 500GPH composites are on top with the climatology shown in a) and the composite anomaly shown in b). The MSLP composites are on the bottom with the climatology shown in c) and the composite anomaly presented in d).

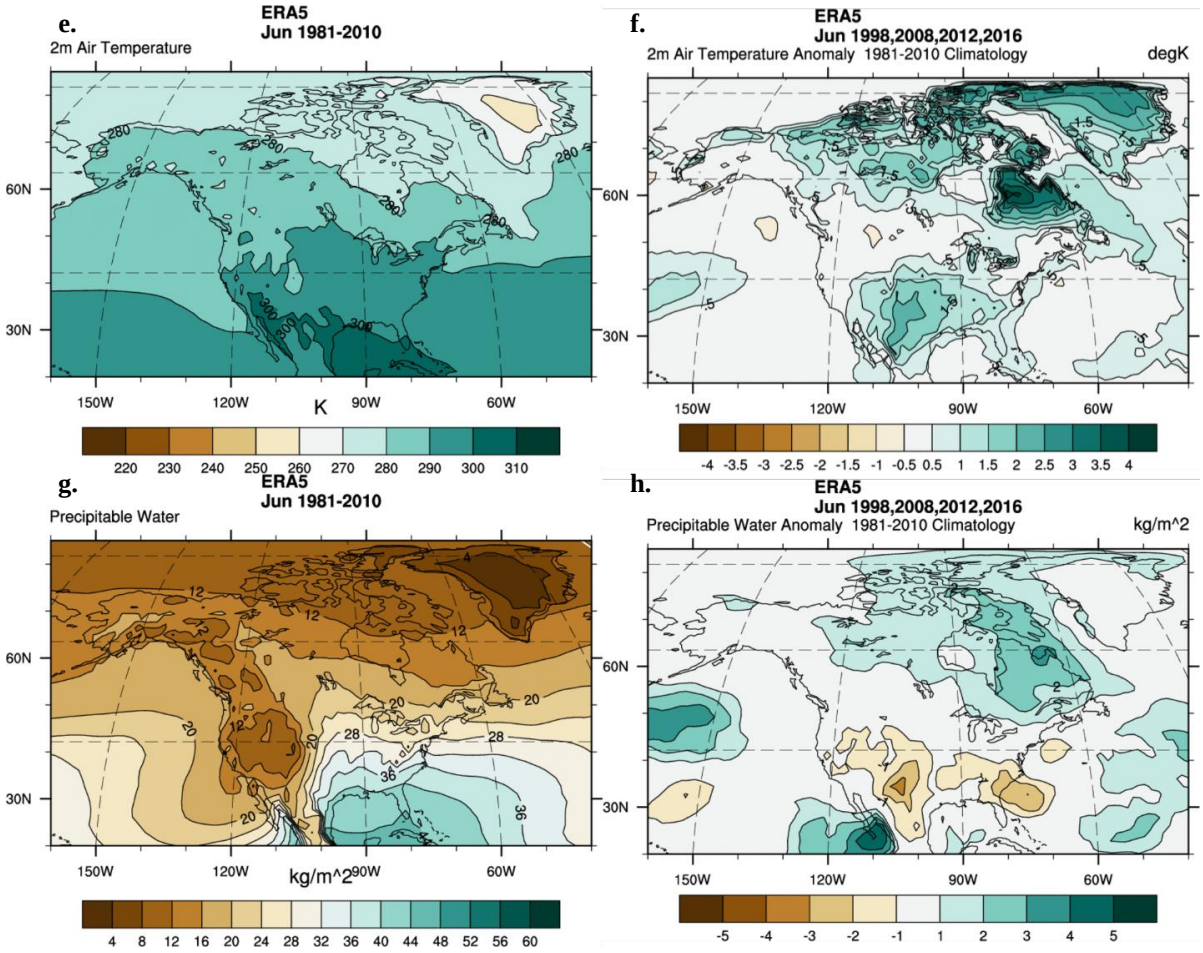

Figure 74. (cont.) Beaufort Sea contemporary June composites for minimum SIE and maximum GBI. The T2m composites are on top with the climatology shown in e) and the composite anomaly shown in f). The PW composites are on the bottom with the climatology shown in g) and the composite anomaly presented in h).

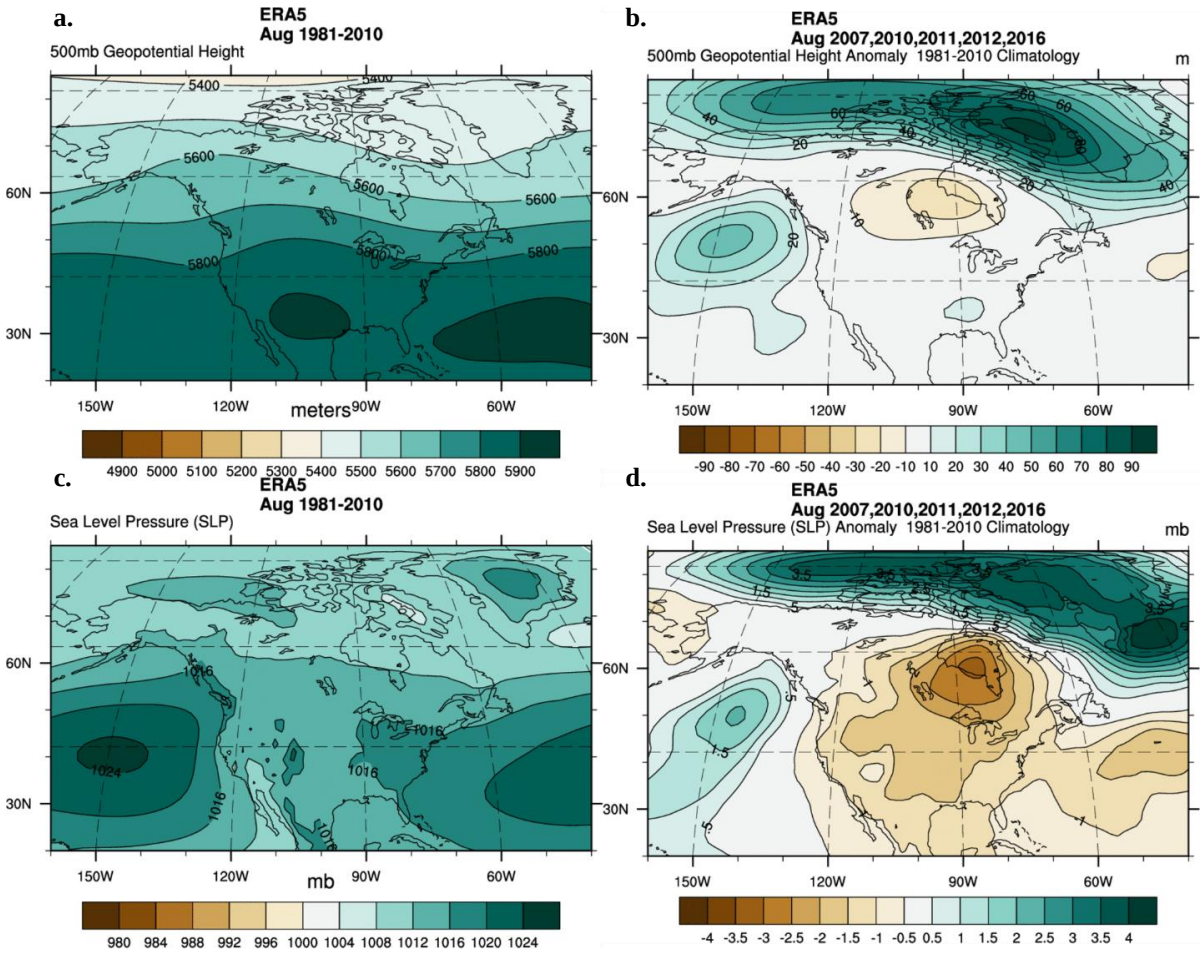

Figure 75. Beaufort Sea contemporary August composites for minimum SIE and maximum GBI. The 500GPH composites are on top with the climatology shown in a) and the composite anomaly shown in b). The MSLP composites are on the bottom with the climatology shown in c) and the composite anomaly presented in d).

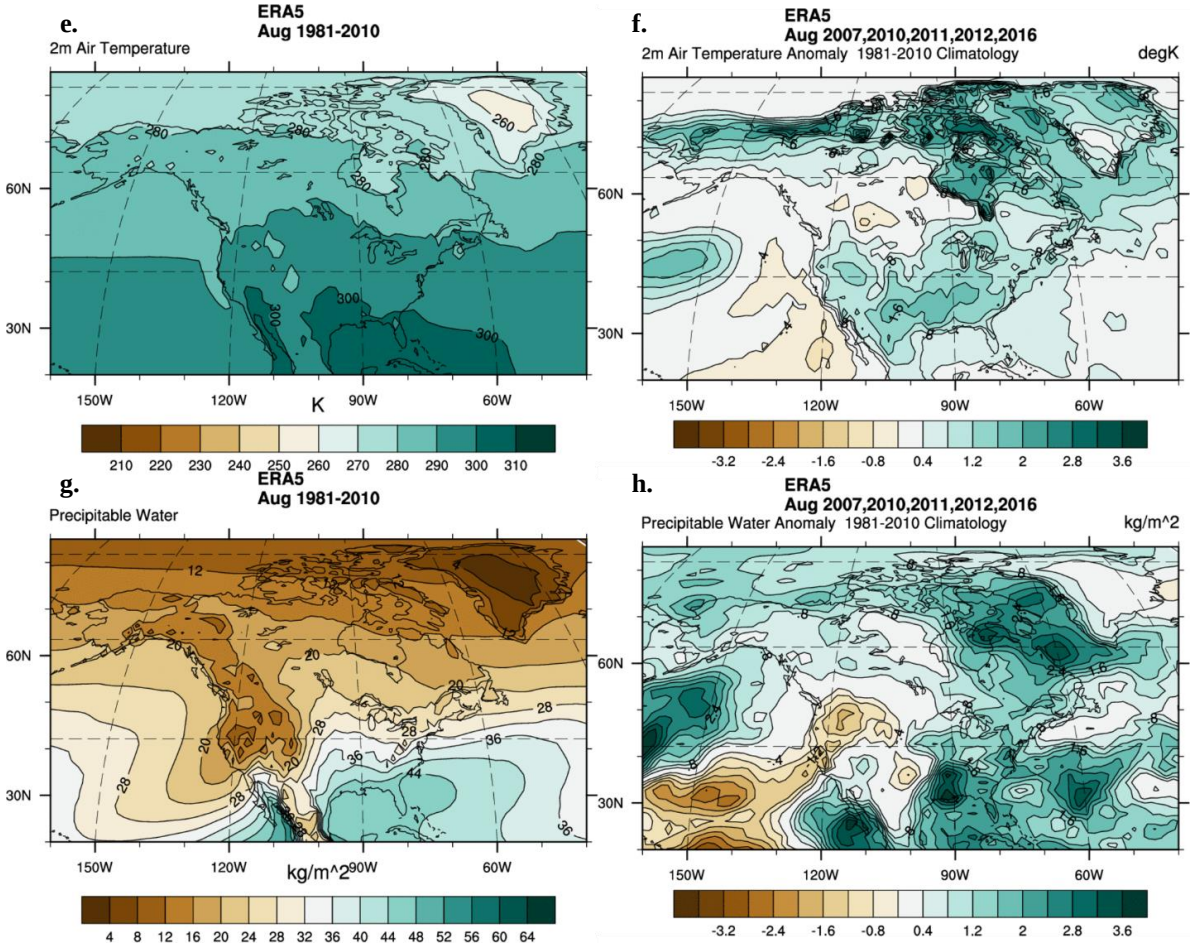

Figure 75. (cont.) Beaufort Sea contemporary August composites for minimum SIE and maximum GBI. The T2m composites are on top with the climatology shown in e) and the composite anomaly shown in f). The PW composites are on the bottom with the climatology shown in g) and the composite anomaly presented in h).

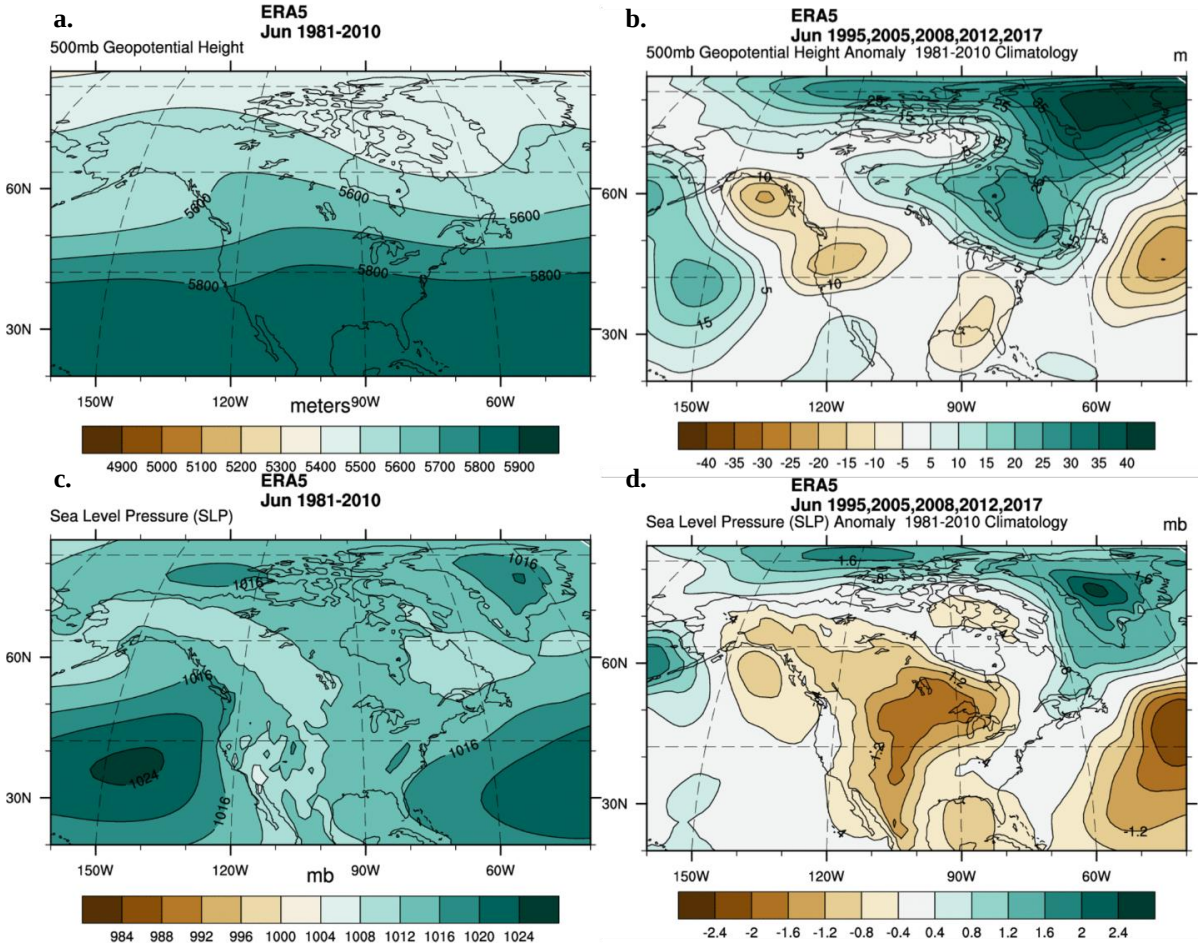

Figure 76. Beaufort Sea lead-1 June composites for minimum SIE and maximum GBI. The 500GPH composites are on top with the climatology shown in a) and the composite anomaly shown in b). The MSLP composites are on the bottom with the climatology shown in c) and the composite anomaly presented in d).

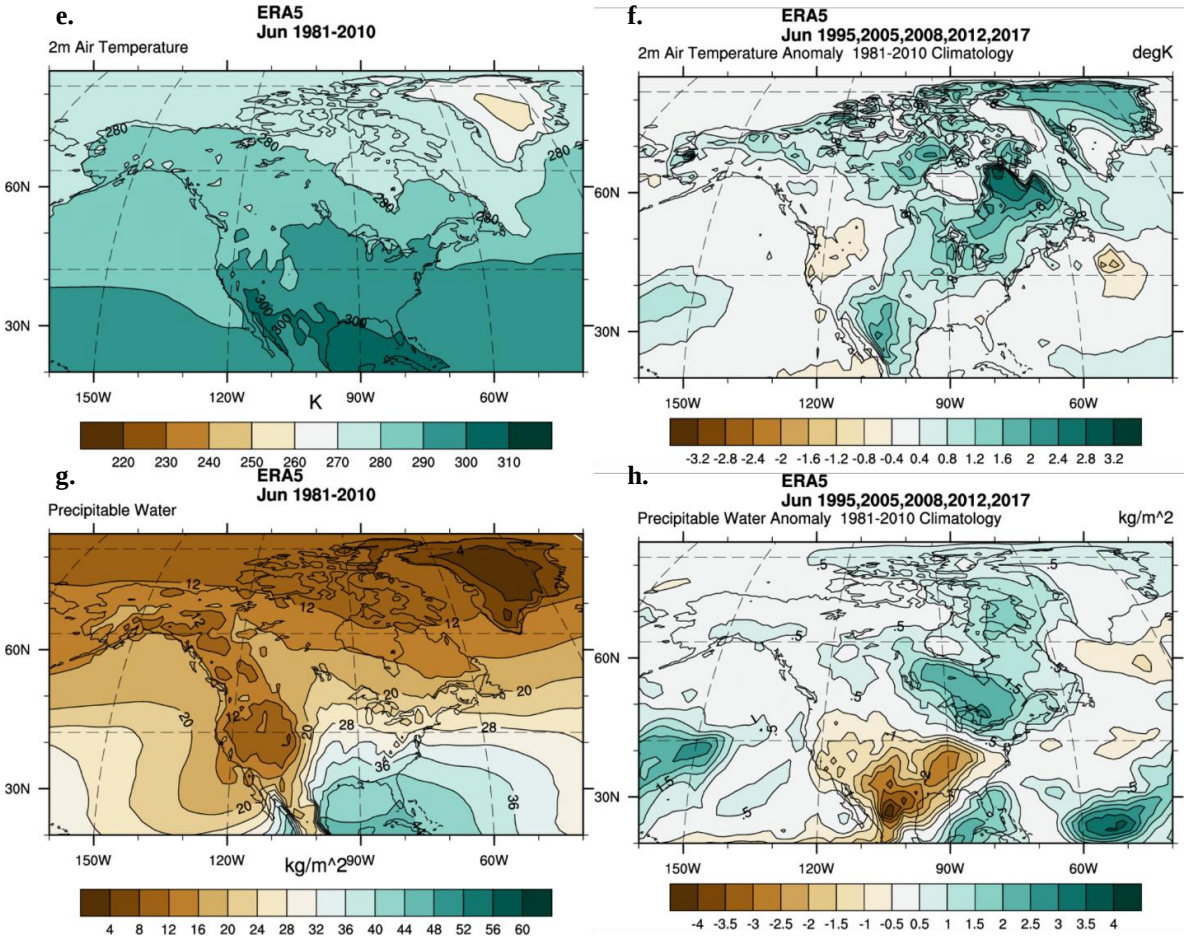

Figure 76. (cont.) Beaufort Sea lead-1 June composites for minimum SIE and maximum GBI. The T2m composites are on top with the climatology shown in e) and the composite anomaly shown in f). The PW composites are on the bottom with the climatology shown in g) and the composite anomaly presented in h).

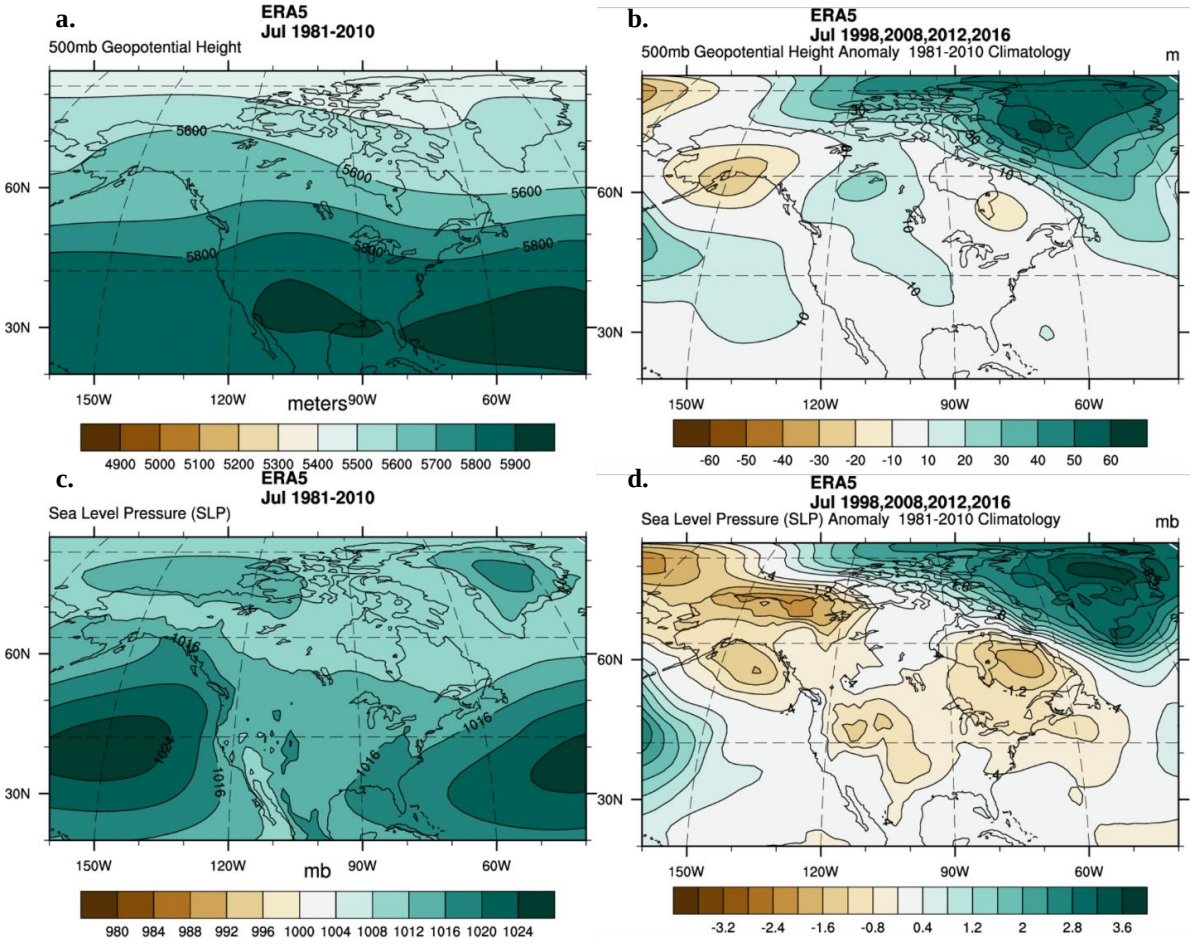

Figure 77. Beaufort Sea lead-1 July composites for minimum SIE and maximum GBI. The 500GPH composites are on top with the climatology shown in a) and the composite anomaly shown in b). The MSLP composites are on the bottom with the climatology shown in c) and the composite anomaly presented in d).

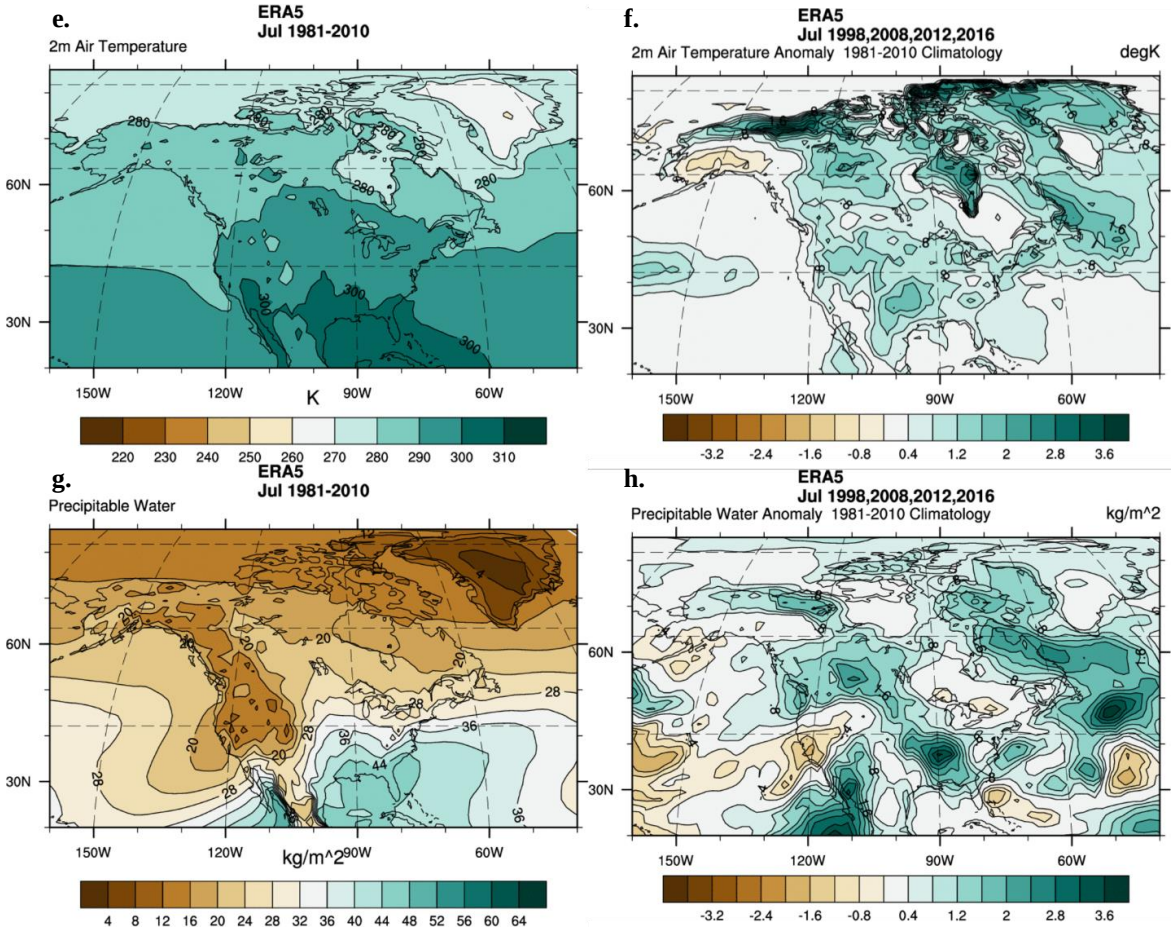

Figure 77. (cont.) Beaufort Sea lead-1 July composites for minimum SIE and maximum GBI. The T2m composites are on top with the climatology shown in e) and the composite anomaly shown in f). The PW composites are on the bottom with the climatology shown in g) and the composite anomaly presented in h).

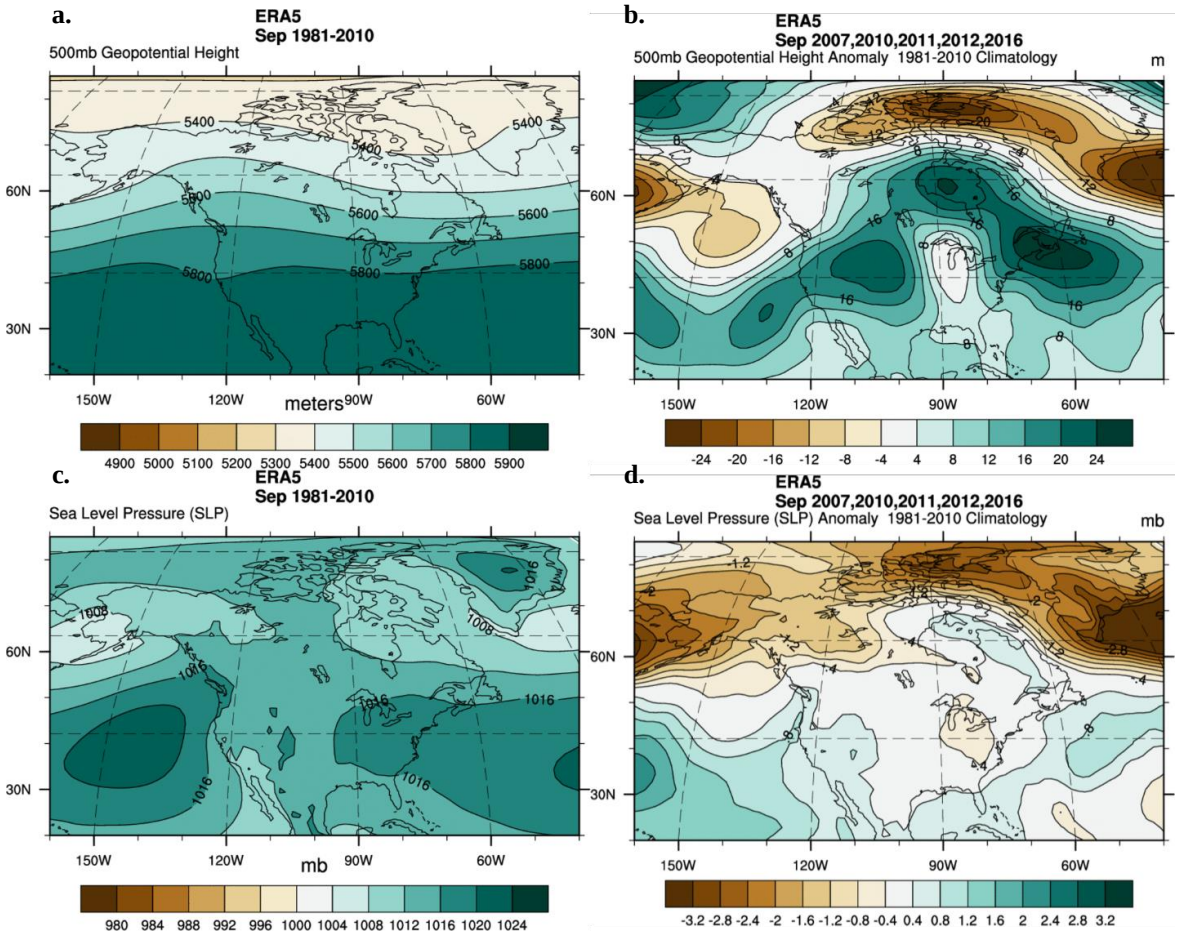

Figure 78. Beaufort Sea lead-1 September composites for minimum SIE and maximum GBI. The 500GPH composites are on top with the climatology shown in a) and the composite anomaly shown in b). The MSLP composites are on the bottom with the climatology shown in c) and the composite anomaly presented in d).

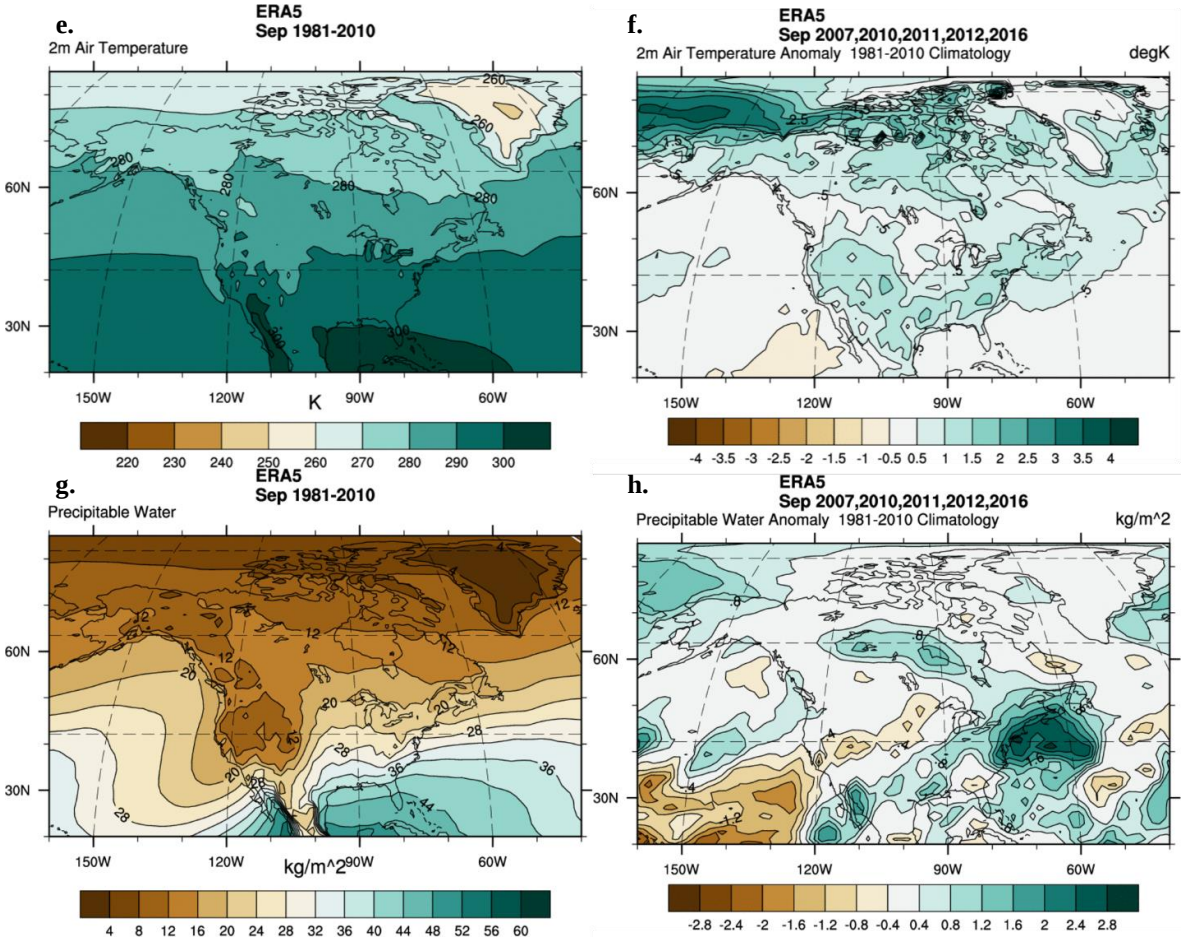

Figure 78. (cont.) Beaufort Sea lead-1 September composites for minimum SIE and maximum GBI. The T2m composites are on top with the climatology shown in e) and the composite anomaly shown in f). The PW composites are on the bottom with the climatology shown in g) and the composite anomaly presented in h).

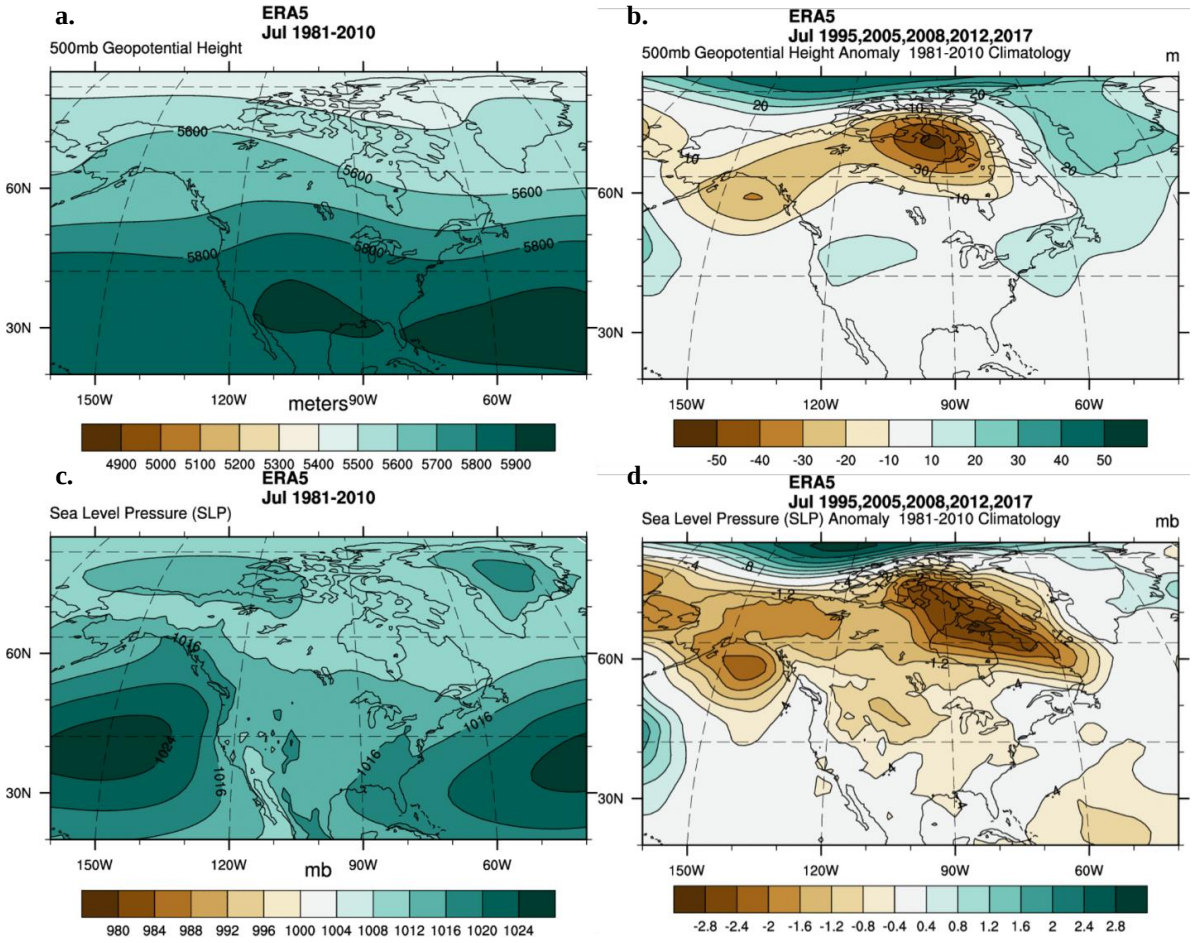

Figure 79. Beaufort Sea lead-2 July composites for minimum SIE and maximum GBI. The 500GPH composites are on top with the climatology shown in a) and the composite anomaly shown in b). The MSLP composites are on the bottom with the climatology shown in c) and the composite anomaly presented in d).

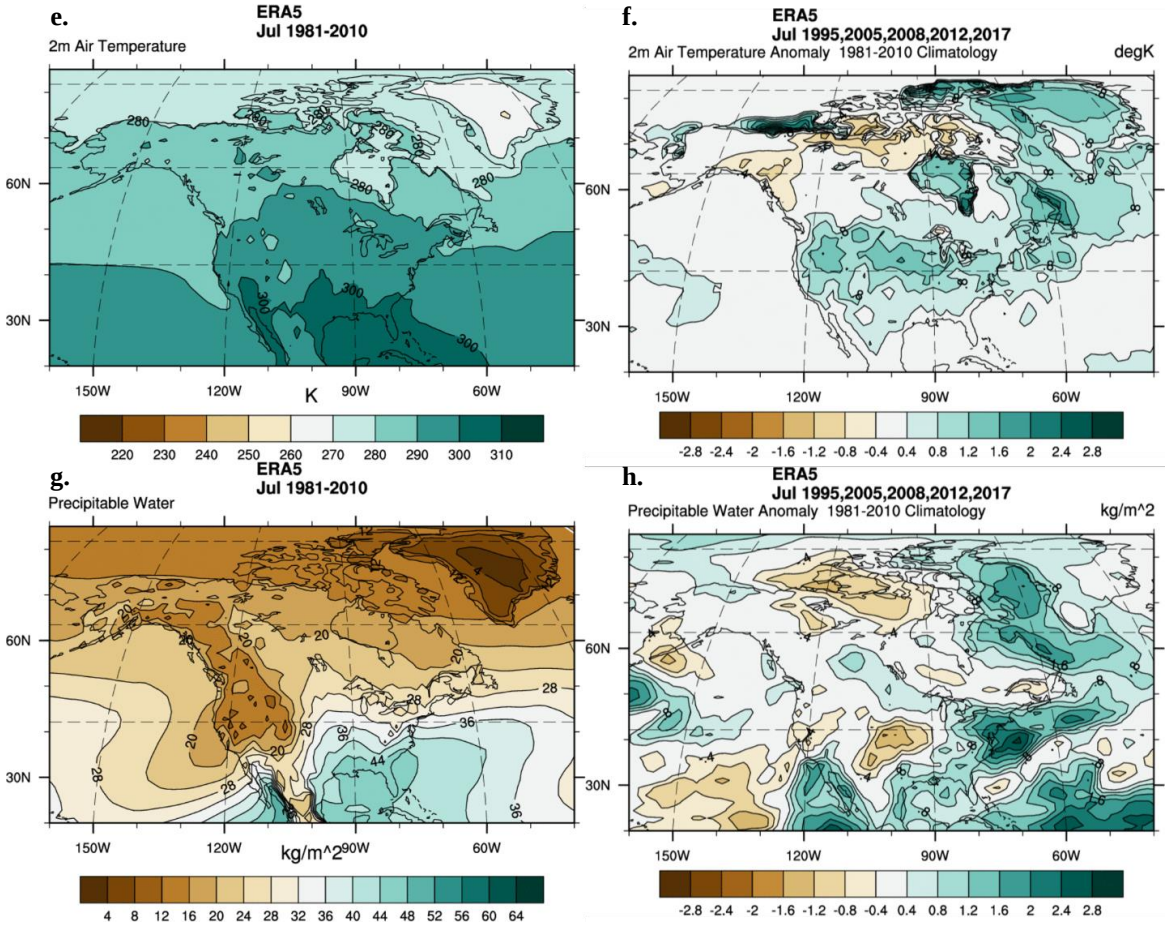

Figure 79. (cont.) Beaufort Sea lead-2 July composites for minimum SIE and maximum GBI. The T2m composites are on top with the climatology shown in e) and the composite anomaly shown in f). The PW composites are on the bottom with the climatology shown in g) and the composite anomaly presented in h).

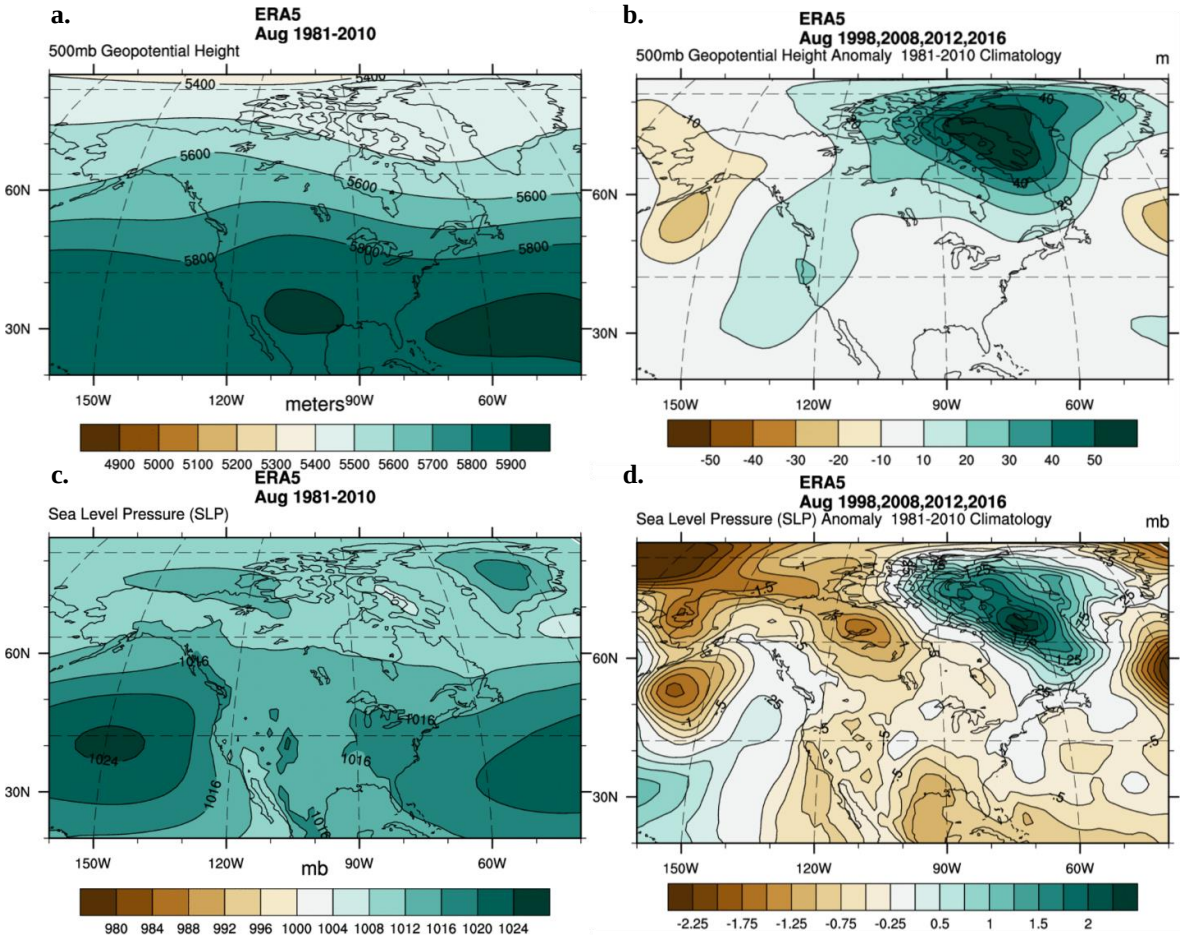

Figure 80. Beaufort Sea lead-2 August composites for minimum SIE and maximum GBI. The 500GPH composites are on top with the climatology shown in a) and the composite anomaly shown in b). The MSLP composites are on the bottom with the climatology shown in c) and the composite anomaly presented in d).

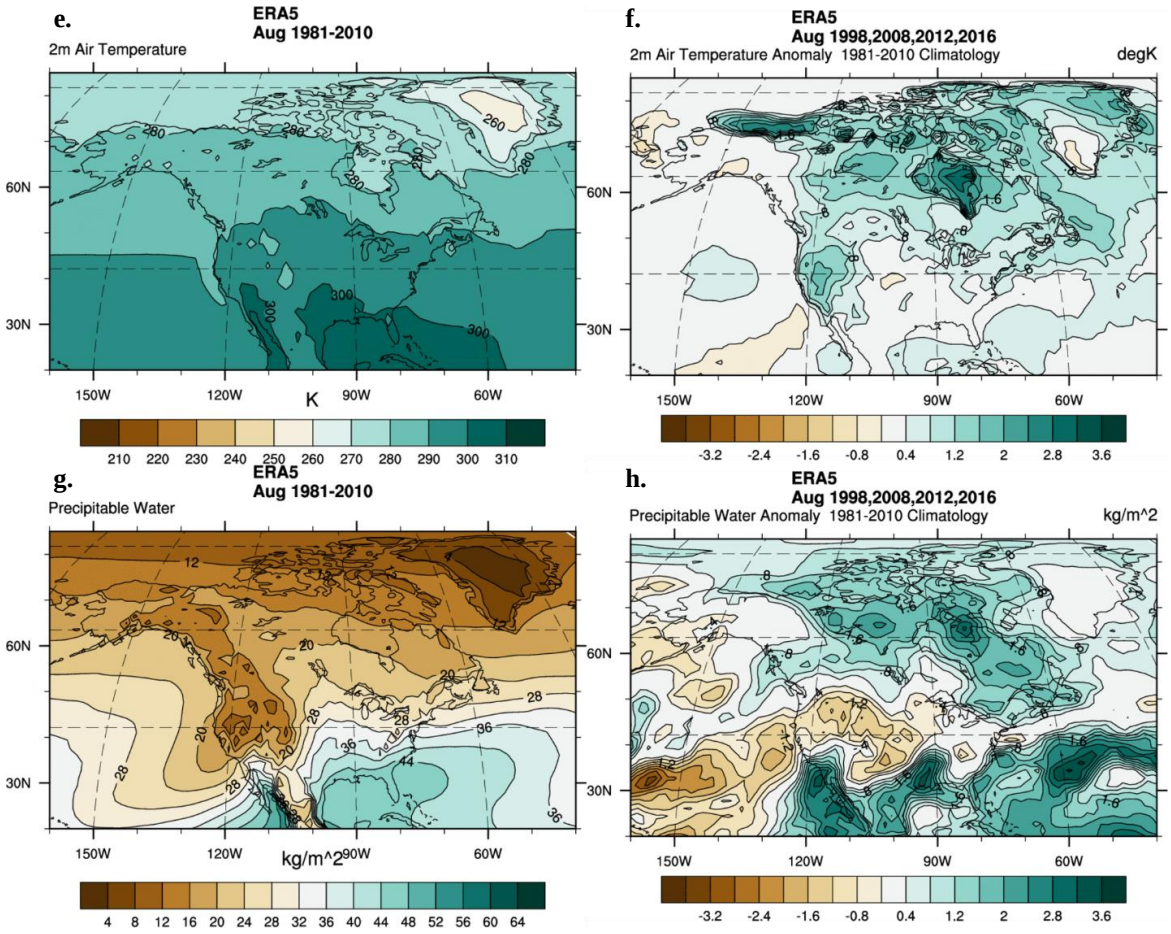

Figure 80. (cont.) Beaufort Sea lead-2 August composites for minimum SIE and maximum GBI. The T2m composites are on top with the climatology shown in e) and the composite anomaly shown in f). The PW composites are on the bottom with the climatology shown in g) and the composite anomaly presented in h).

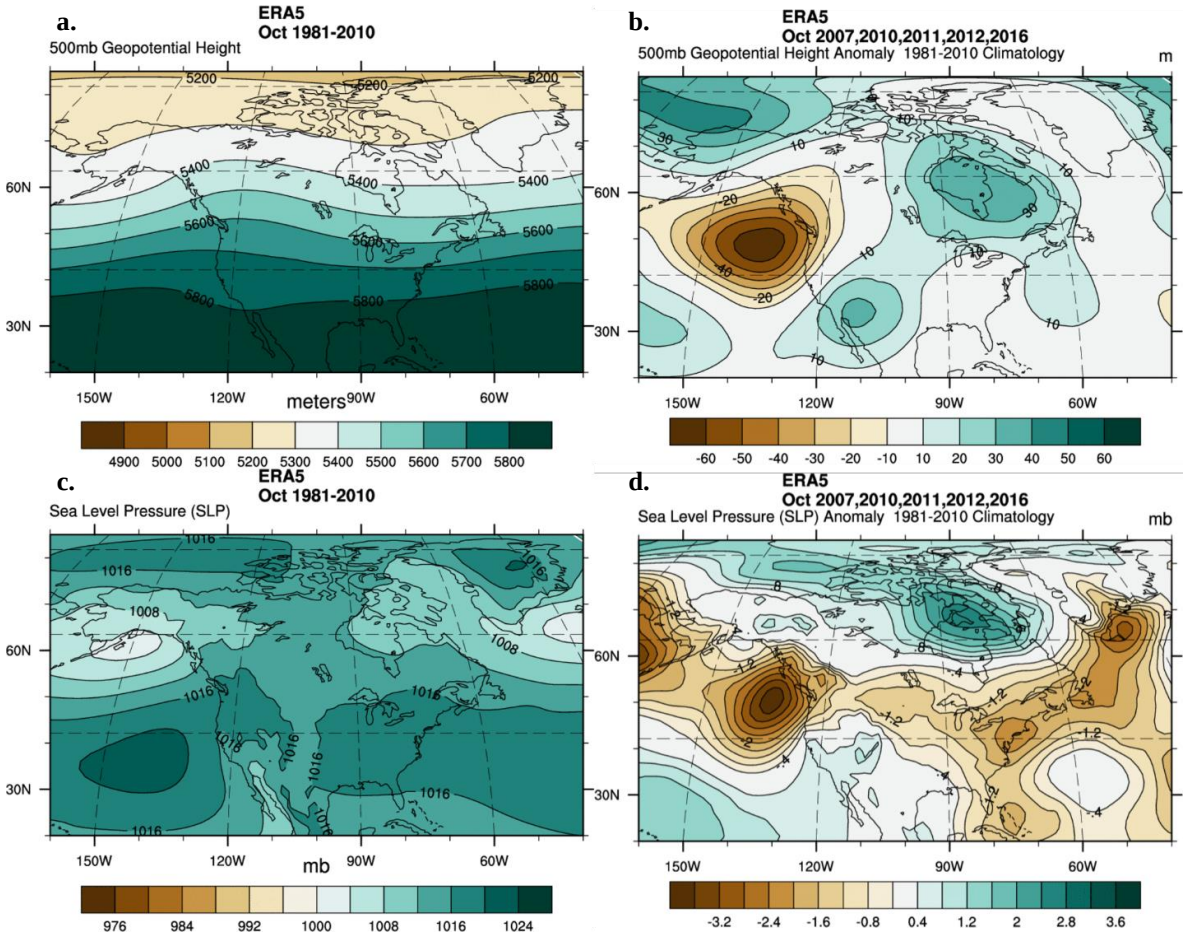

Figure 81. Beaufort Sea lead-2 October composites for minimum SIE and maximum GBI. The 500GPH composites are on top with the climatology shown in a) and the composite anomaly shown in b). The MSLP composites are on the bottom with the climatology shown in c) and the composite anomaly presented in d).

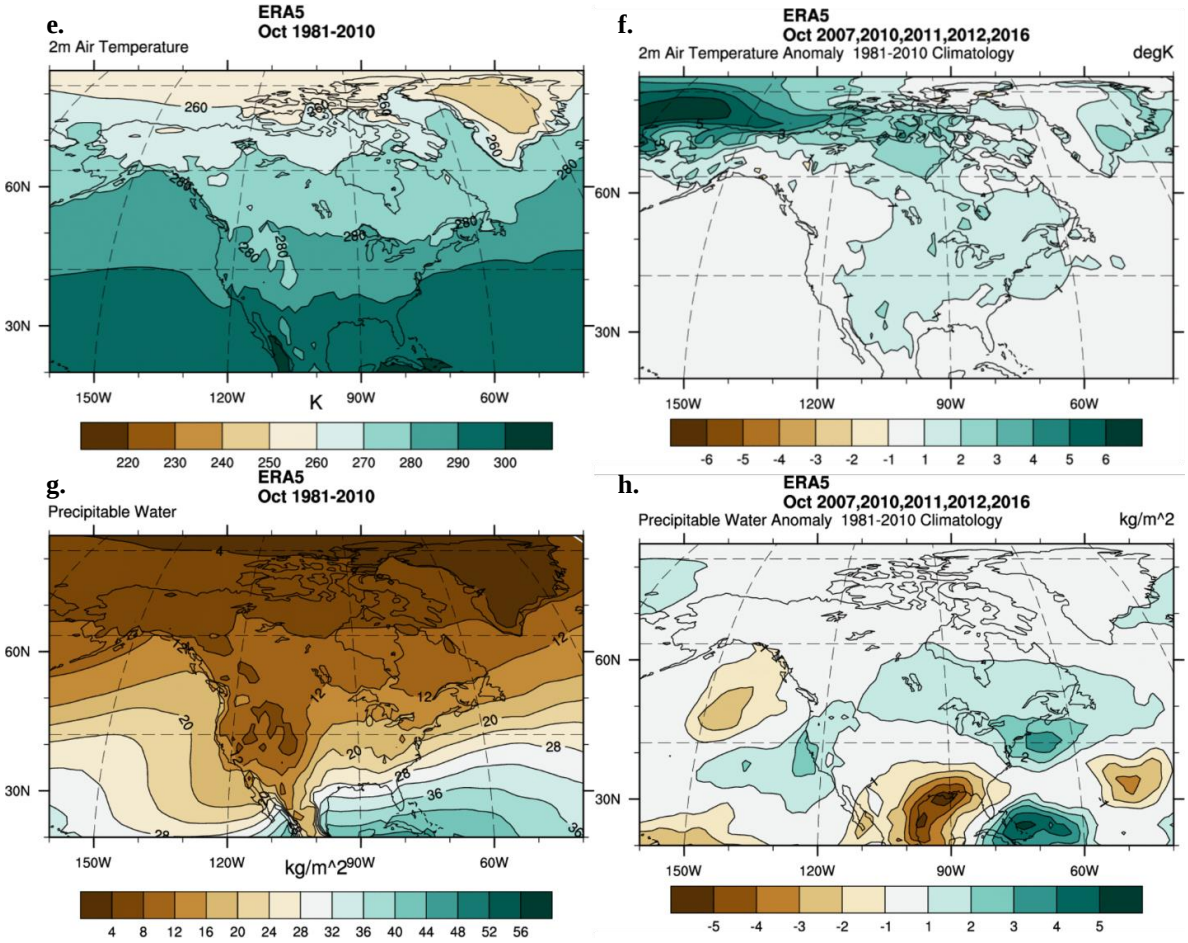

Figure 81. (cont.) Beaufort Sea lead-2 October composites for minimum SIE and maximum GBI. The T2m composites are on top with the climatology shown in e) and the composite anomaly shown in f). The PW composites are on the bottom with the climatology shown in g) and the composite anomaly presented in h).

7. DISCUSSION AND CONCLUSIONS

7.1 DISCUSSION PART 1: MULTIDECADAL CORRELATION ANALYSIS

The time series of the GBI variable revealed an overall increasing trend in most months for the investigated time period, 1979–2018. Other studies have found that the GBI has increased substantially within the modern record (since the late 1990s), and Hanna et al. (2018b) mentioned this was especially true for the GBI for summer months (JJA). The study by Hanna et al. (2018b) notes an accumulation of high GBI values post-2000 in the summer season, but during the month of August in particular. The summer season showed the greatest increase in number of days with GBI >0 at 69.5 and days >1 at 35.6, relative to the mean 1981-2010 climatology of 47.7 and 18.6 days, respectively. In contrast, the winter season showed its record number of days with high GBI values in the 1960s, and the month of January even showed a long-term decline in GBI. In addition, this study showed a general decrease in both SIE and SIA trends within the study period but noted that sea ice has likely had a minimal influence on the increase in the GBI. The largest contributors for blocking enhancement are warm air mass transport and moisture incursion into the Arctic region (Wang et al. 2019). It may be that the combined effects of warm seasonal summer conditions on top of AA create an ideal environment, affecting the strength, duration, and frequency for blocking episodes, which can condition the Greenland region for continued blocking well into the autumn months (SON). This increase in blocking likely coincides with the start or propagation of a positive feedback around the GrIS, affecting the energy budget well into the cold seasons. Ballinger et al. (2018) found that Baffin Bay freeze onset dates and sea surface temperatures (SST) showed strong correlations with autumn blocking episodes and Greenland coastal air temperatures. These findings indicate that recent stronger and more

frequent blocking episodes during the summer months can lead to drastic and more persistent declines in sea ice cover, which for Baffin Bay includes the melting of young ice, warmer ocean SST and warmer T2m, setting up a warmer surface environment even if the atmosphere begins to cool, possibly strengthening future blocking episodes. The combination of lower sea ice and higher instances of atmospheric blocking is causing changes in the Arctic system, though just how far reaching those changes are is still up for debate. This study has allowed for an initial assessment of the extent of temporal associations of such events.

After the various correlation analyses conducted, at least two marginal seas were identified, the Baffin Bay and the Beaufort Sea, which produced more significant monthly correlation results than any of the other marginal seas, though their seasonal associations differed. A study by Onarheim et al. (2018) examined regional Arctic changes in sea ice by looking at various data, sources for SIC and SIE, including historical and modern (satellite derived) data and found that summer sea ice variability was highest for higher latitude marginal seas including the Beaufort Sea, and winter sea ice variability was highest for those marginal seas at lower latitudes including the Baffin Bay. The trends shown in that study hint at seasonal variability between the marginal seas of interest identified in this research, though pan-Arctic loss of sea ice is also noted due to AA.

By far, the correlation test to produce the greatest number of months with significant associations for the Baffin Bay was the lead-1 test for both SIE and SIA, each with the same seven months of significant coefficients (January, February, March, April, August, October, and November), while the contemporary produced four and five months

respectively for SIE (January, March, October, and December) and SIA (January, February, March, October, and December). The Beaufort Sea produced the greatest number of months with significant associations at lead-1 for the SIA data for five months (March, May, June, July, and October), and both the contemporary and lead-2 tests produced significant associations for SIE for three months (May, June, and August). This emphasis on the lead-1 correlation results in the summer months suggests that the conditions of the upper atmosphere have potentially affected the following month's sea ice regimes for both the Baffin Bay and Beaufort Sea by preconditioning the Arctic environment to warmer SST and overlying T2m, which may be associated with the ice-albedo feedback (Wang et al. 2017). With less land and sea ice, exposed surfaces have a lower albedo and reflect a smaller percentage of incoming shortwave radiation (van den Broeke et al. 2017). There also appears to be some persistent seasonality to the significant months for each marginal sea, though the seasons of emphasis differ between them. If current atmospheric conditions lead future ice conditions, this suggests that atmospheric processes driven by anomalously cold or warm episodes can precondition the Arctic environment to influence ice development and retention. Additionally, the correlation results revealed little predictive skill beyond one and two month leads and no predictive skill for lags, similar to Walsh et al. (2019).

The strongest correlation coefficient values for the Baffin Bay were produced in the contemporary analysis including January (raw τ=-0.37; DT τ=-0.41), March (raw τ=-0.42; DT τ=-0.35), October (raw τ=-0.45; DT τ=-0.32), and December (raw τ=-0.41; DT τ=-0.41), at least one month for winter, spring, and autumn. Although the lead-1 results show even more months with significant correlation coefficient values, the

associations appear to be slightly weaker in all months than those same contemporary months that reached significance except for October. In total, lead-1 produced seven months of significant correlations for January (raw τ=-0.38; DT τ=-0.25), February (raw τ=-0.32; DT τ=-0.36), March (raw τ=-0.40; DT τ=-0.31), April (raw τ=-0.34; DT τ=-0.27), August (raw τ=-0.43; DT τ=-0.27), October (raw τ=-0.39; DT τ=-0.38), and November (raw τ=-0.27; DT τ=-0.40). The winter, spring, and autumn seasonality appears again, but there is also a slight summer signal with August GBI showing significant correlation with September SIE. The lead-2 correlations only produced three months of significance (January raw τ=-0.34, DT τ=-0.26; February raw τ=-0.28, DT τ=-0.31; and June raw τ=-0.34, DT τ=-0.24), though again the significance values were mostly weaker than those of the same months within the lead-1 analysis. A slight summer signal appears for June GBI with August SIE. There is clearly a persistent winter signal for sea ice and GBI associations for Baffin Bay, perhaps due to warm SSTs, though autumn and spring show some persistence as well, and the summer signal appears to be the weakest.

As noted, GB has increased in the summer months, which directly affects the areas around the GrIS including Baffin Bay and may be contributing to the association of GBI and sea ice shown in this study. The intensification of already warm summer temperatures brought on by blocking episodes has been shown to interrupt autumn cooling. A study by Ballinger et al. (2018) noted an accumulation of heat during the summer as a contributing factor for increased SST and late freeze during the autumn months. The study also found a linear increase in GPH over Greenland for autumn months. These effects, such as weaker, thinner ice cover, increased T2m, and an overall

weaker temperature gradient, have the potential to disrupt Arctic conditions from the surface to the upper atmosphere. These effects ripple through the Arctic environment, causing further seasonal disruptions in later months, which may be why significant correlations are found from autumn through spring in the contemporary analysis, and why the lead-1 and lead-2 analyses also produced significant associations.

For the Beaufort Sea, significant coefficient values were shown for months in the middle of the year, May, June, and August (end of spring and summer). At lead-1, two of the same three months (May and June) are shown to be significant, and at lead-2 all three of the same months are significant, suggesting that sea ice conditions around the Beaufort region were influenced by atmospheric conditions potentially related to the GB. These results indicate associations from late spring through summer, which may have been strong enough to elicit significant associations one and two months later. Although the summer signal is strongest for the Beaufort Sea, the lead-2 correlation showed August GBI significant with October SIE, hinting at a possible prolonged association, which may grow stronger as sea ice continues to decline.

Few studies have mentioned direct associations with the Beaufort Sea and the GBI; however, another pattern of high pressure that appears around the Beaufort Sea region, especially during years with low sea ice, known as the Beaufort Sea High (BSH), affects the Western Arctic and may be related with the GBI. Although the BSH was not a part of this study, Ballinger et al. (2014) used several automated synoptic climatology methods to analyze the BSH and determined a statistically significant link to the GBI, suggesting the Beaufort Sea may be influenced by atmospheric variability from the Greenland region or vice versa. There might be a different pathway for this association

than that of Baffin Bay, such as large-scale atmospheric phases related to NAO and AO patterns. A study by Hanna et al. (2015), examined the characteristics of the NAO, AO, and GBI and found that although the NAO and AO patterns show significant overlap, the recent summer decline shown for the NAO was not reflected by the AO, which the authors suggest may be caused by a regional mechanism in the North Atlantic and northeastern NA region, i.e. the anticyclonic blocking pattern measured by the GBI. These authors and others note that both NAO and AO phases have become less positive and have even shown some extreme negative phases, which may contribute to the broad high-pressure regime around the Beaufort Sea region (Belleflamme et al. 2015; Stroeve et al. 2017). Overland et al (2012) also found that high pressure blocking over the Greenland region causes more meridional flow for the North Atlantic jet stream, which encourages a more negative phase of the NAO. It has also been suggested by other that negative phases of the NAO can be affected by other planetary phases such as the El Nino Southern Oscillation (ENSO), which dominates the tropical regions of the NH. These phenomena might partially explain how atmospheric conditions above Greenland correlate with Beaufort Sea ice conditions.

Although the correlations within this study focus on relationships between regional sea ice and atmospheric blocking, there are various other factors both local and remote that impact GB formation and maintenance such as large-scale Rossby wave dynamics, rapid cyclogenesis, precursor cyclones, forcing from tropical anomalies, latent heat release, and the topography of the GrIS; but overall, the drivers of blocking are still not well understood (McLeod and Mote 2015; Drouard and Woollings 2018; Hanna et al. 2018b; Woollings et al. 2018). Regardless of the causes, blocking episodes can be

detrimental to an increasingly fragile Arctic climate system. As the time series graphs revealed, steady declines of sea ice have been observed throughout the Arctic in the last four decades, and with warmer global temperatures expected, declines are likely to continue. The sea ice-albedo feedback mechanism is one way by which the Arctic atmosphere and its various marginal seas can become preconditioned to absorb and retain summer solar heat input, and the increasingly rapid decline of sea ice could lead to further destabilization of the Arctic atmosphere. These processes create the conditions that could affect blocking into the autumn months by increasing the local turbulent heat exchange from the ocean-to-atmosphere and increasing upper tropospheric temperature and pressure, thus perpetuating a positive sea ice-heat flux feedback loop.

Apart from those mentioned, few marginal seas produced consistent month-to-month or seasonal correlational associations. Many of the raw data correlation tests showed a very clear emphasis in summer (JJA) monthly coefficient values, yet these associations were almost completely erased when the tests were run for the DT data. This suggests that the general downward trend in sea ice and upward trend in GBI have influenced the strength of the correlations within the raw data. A somewhat clearer association was shown for the DT data in that the influence of the overall change in the trend for each variable are removed while still accounting for the year-to-year variability (Walsh et al. 2019). The DT data highlights the magnitude of changes within the time series; however, the chaotic nature of the climate system also lends to a level of uncertainty in the interpretation of the interannual correlative results.

7.2 DISCUSSION PART 2: MONTHLY COMPOSITE ANALYSIS

7.2.1 BAFFIN BAY ANALYSIS

7.2.1.1 MAXIMUM SIE VERSUS MINIMUM GBI COMPOSITES

The maximum SIE versus minimum GBI composite analyses for the Baffin Bay produced some consistent anomaly patterns for the NA region. The contemporary anomaly maps showed very strong instances of negative anomalies north of 60°N, and when these maps included positive anomalies, they were typically smaller, much weaker, and often located at a lower latitude than the negative anomaly area. Generally, the composite maps showed consistent negative anomaly patterns over the same regions, e.g. over the high Arctic, northern Canada, the CAA, Greenland, and parts of Alaska, with the Greenland region often showing the strongest negative anomalies. These land areas and the bodies of water that surround them have typically shown some of the lowest anomaly values, relative to the mid-latitudes, for all the variables of interest (500GPH, MSLP, T2m, and PW), as per the climatology and anomaly composite maps. Additionally, the 500GPH and MSLP anomaly composites often showed positive anomalies situated off the eastern and western coasts of NA, typically between 30°N and 60°N. These contemporary patterns were fairly consistent for the lead-1 analyses; however, some composite maps began to show divergent patterns at lead-2 such as weaker negative anomalies or slight positive anomalies north of 60°N depending on the month observed.

The contemporary composite maps for January, March, October, and December all showed negative anomalies for the 500GPH variable around Greenland and for much of the upper Arctic, often with a closed area at the center of the negative anomaly, indicating a particularly strong area of low pressure. If the anomaly is closed and

surrounded by closely-spaced isohypses, strong winds are likely around the area as well. These upper level low pressure systems rotate counterclockwise and can strengthen the prevailing westerly winds and move weather eastward. Additionally, this movement can also be strengthened by the presence of a high pressure system when the high is situated south of a low pressure system, as the counterclockwise movement of the low and clockwise movement of the high create the conditions for a pathway of fast flowing air toward the east. The MSLP anomaly maps for the contemporary months reveal similar spatial anomaly patterns to that of the 500GPH, indicating that surface conditions closely align with those of the upper atmosphere. The MSLP climatology maps shown distinct low pressure systems to the east and west of NA, sometimes covering both sea and land areas. Smaller and weaker MSLP anomalies are often situated off the western coast of Canada in the Gulf of Alaska region, where the negative anomalies are at a higher latitude relative to the anomalies of the eastern coast of NA. Strong negative MSLP anomalies are most common around the Greenland area. The strong negative 500GPH and MSLP anomalies also affect T2m and PW for the NA region by diverting the atmospheric flow. The monthly anomaly composites for January (**Figure 40**), March (**Figure 41**), and December (**Figure 43**) are examples of negative 500GPH and SLP above 60°N acting to produce negative T2m and PW anomalies in these same regions. **Figure 40** (January) shows that the strongest negative 500GPH and SLP anomaly areas produced the strongest T2m and PW anomalies around the same areas. Similar patterns are shown for positive 500GPH and SLP acting to produce positive T2m and PW anomalies below 60°N. These patterns can also be found in many other composites as well, not just for the Baffin Bay maximum SIE and minimum GBI contemporary

analysis. Additionally, October (**Figure 42**; a transitional autumn month) shows some more variability in the response of T2m and PW to the 500GPH and MSLP anomalies. Negative T2m and PW anomalies were shown for the US and positive anomalies over parts of western NA including parts of Canada (though these are very weak).

Low pressure systems (with counterclockwise rotation) found in areas of highly negative anomalies can also act to divert the cold, dry air of the Arctic is downward into lower latitude regions, bringing lower temperatures and lower moisture for much of Canada and parts of the US. Much of the southern and eastern US experience positive T2m and PW anomalies; however, these anomalies are contained to the mid-latitudes by the cold, dry air parcels from higher latitudes.

The lead-1 anomaly maps showed similar results as the contemporary composites, with large negative anomalies north of 60°N, but depending on the month and variable, some negative anomalies reach southward into the mid-latitudes. The anomaly MSLP composite for November and anomaly 500GPH composite for January revealed the largest, strongest positives anomalies. The November MSLP extended over much of the Arctic and the highest MSLP anomalies, +2.8 mb, were found over the Beaufort and the Central Arctic Ocean. The January 500GPH showed two large slightly positive anomaly areas with +30 m at their strongest. Overall, the lead-1 analyses did not deviate too much from those anomaly patterns shown in the contemporary analyses.

The lead-2 composites began to exhibit some slight shifts in the spatial coverage of negative and positive anomalies, but this could be more to do with the months observed. For example, the anomaly composite maps for 500GPH and MSLP for the month of May showed some strong positive anomalies north of the 60°N; however, as

evident by the climatology maps for each variable, relatively low 500GPH and MSLP values are less common for the Arctic region in this month, likely due to the seasonal changes bringing increased insolation, and warmer SST and SAT, which reduces the temperature gradient between the Arctic and mid-latitudes.

Consideration must be given to the NAO as blocking episodes are representative of the northern half of its dipole pattern (Mattingly et al., 2015) and Hanna et al. (2018a) suggest negative NAO phases arise from Greenland blocking. Positive phases of the NAO are characterized by strong low and high pressure systems which create a less wavy jet stream, and negative phases are associated with weak low and high pressure systems, which create a wavier jet stream. Low sea ice influences the temperature gradient as well, which lends to the distribution of low and high pressure systems. Although the results of this study do not include consideration for anomalous weather over NA related to NAO phase explicitly, the 500GPH and MSLP variables indicate regional flow patterns, and according to Hanna et al. (2016), the GBI may have a greater influence on regional weather patterns and GrIS melt than broad scale hemispheric patterns such as the NAO.

7.2.1.2 MINIMUM SIE VERSUS MAXIMUM GBI COMPOSITES

The minimum SIE versus maximum GBI composite maps for Baffin Bay showed consistent anomaly patterns, but the types of anomalies tend to be opposite of those shown for maximum SIE versus minimum GBI. In particular, areas where negative anomalies were commonly found within those composite maps for maximum sea ice then became occupied with positive anomaly areas for those years of minimum sea ice. Regions like Baffin Bay, Greenland, the CAA, Canada, and Alaska are subject to positive anomalies for all variables under the minimum sea ice and maximum GBI for the

contemporary, lead-1, and lead-2 composite maps. The large positive anomalies are far more common over Greenland, but the anomalies also extend poleward into the high Arctic. This migration of positive anomalies into the Arctic indicates warmer air masses and the formation of high pressure systems, which are associated with warmer T2m and increased PW. Indeed, the T2m and PW anomaly maps showed large and extensive positive anomalies intruding into the Arctic, which have the potential to exacerbate already low sea ice conditions, in part through turbulent heat fluxes from the atmosphere to the surface (Serreze and Berry 2011; Baggett and Lee 2019). Other studies have also found that warming and moistening of the Arctic atmosphere can provide an energy source for the circulation that may influence the mid-latitudes (Vihma 2014; Blackport and Kushner 2016).

In addition to positive anomalies moving to higher latitudes, it appears negative anomalies have become more common for the mid-latitudes (south of 60°N) for all months (January, March, October, and December). All the variables showed negative anomalies over parts of Canada and the US with some of the strongest anomalies appear over central and eastern US. The 500GPH and MSLP anomaly maps showed consistent negative anomalies stretching from eastern US into the Atlantic Ocean. The movement southward of low pressure systems, south of 60°N, and high pressure systems northward of 60°N latitude can act together to divert the westerly winds backwards, due to rotation of each pressure field (high pressure rotates clockwise, low pressure counterclockwise), if they are strong enough. This disruption to the flow of winds can then affect weather patterns in unusual ways. For example, Mattingly et al. (2015) found that a persistent high pressure ridge from a blocking pattern south of Greenland contributed to the unusual

track of Hurricane Sandy from its eastward track back westward, which devastated parts of the northeastern US in October of 2012. Although hurricanes are common for the mid-latitude region, they typically lose strength as they move along the eastern coast of NA due to colder surface and atmospheric conditions; however, the above average 500GPH and MSLP anomalies they found in parts of Canada along with below average 500GPH and SLP anomalies south of Greenland in the North Atlantic Ocean acted together to steer the hurricane northeastward.

Another study by Cohen et al (2018) analyzed two polar cap indices (one for geopotential height and another for air temperature from the surface to the mid-stratosphere) in conjunction with a winter season severity index for several US cities mostly in the north where snowfall in more common and found a stronger relationship between warmer Arctic episodes and increased frequency of extreme winter weather for those cities in the eastern half of the US. Their results showed a statistically significant and nearly linear relationship for Arctic GPH changes (in the troposphere) and the winter season severity index, that greater GPH surfaces in the Arctic stratosphere are more important than warm stratospheric temperatures in forcing mid-latitude severe winter weather. Although this study does not include the GBI, the winter season severity index is a measure of mid-tropospheric height, and therefore could potentially act as a pathway just as other indices that account for tropospheric changes. In addition to height changes, the positive T2m and PW anomalies shown throughout the Arctic when sea ice is minimal also contribute to increased moisture fluxes with the atmosphere, providing the Arctic with more water vapor, which can eventually fall as precipitation over the high and mid-latitudes depending on the jet stream configuration and prevailing winds (Cohen

et al. 2014). The findings from this study are in line with those studies mentioned, which show more common instances of negative anomalies found over the NA for 500GPH, MSLP, T2m and PW for those years of minimum SIE and maximum GBI.

7.2.2 BEAUFORT SEA ANALYSIS

7.2.2.1 MAXIMUM SIE VERSUS MINIMUM GBI COMPOSITES

The contemporary Beaufort Sea composite analyses for maximum SIE and minimum GBI exhibited similar anomaly patterns to those anomaly patterns shown in the contemporary Baffin Bay composite maps for maximum SIE versus minimum GBI. The months of analysis included May, June and August, yet despite the time of year, all three months showed extensive negative anomaly areas north of 60°N. As found in the anomaly composite maps, the strongest negative anomalies were generally shown over the Greenland region, while August also shows negative anomalies over the Beaufort Sea and Alaska. While the negative anomalies were generally contained north of 60°N, positive anomalies were shown south of 60°N. These positive anomalies covered both land and sea areas, but as with the Baffin Bay composites, they were far weaker than the negative anomalies, and depending on the variable observed, usually smaller in spatial extent.

The lead-1 composite maps for June, July, and September began to reveal more mixed anomaly patterns, perhaps due to the months observed. June and July showed multiple smaller sized 500GPH and MSLP anomaly areas in close proximity to one another (both positive and negative anomalies), which is perhaps a characteristic of the weaker temperature gradient during the summer time allowing for the push of both Arctic air masses and Tropical air masses across the mid-latitude region. Despite some

movement further northward of positive 500GPH and MSLP anomalies, the T2m and PW anomaly areas were mostly still negative for much of the NA continent and Greenland, while not unusually, the eastern and western coasts sometimes showed positive T2m and PW anomalies.

The lead-2 composite maps produced anomalies consistent with seasonal climatological variations. The July anomaly maps showed large positive 500GPH and MSLP anomalies over parts of NA, though the strongest anomaly was situated in the Gulf of Alaska, consistent with summer months from the contemporary and lead-1 results. The July and August T2m and PW anomalies are somewhat mixed, but there are generally more positive anomalies over the western coast of NA and more negative anomalies over the eastern half. The composite years used for July maximum SIE analysis include 1981, 1989, 1992, 1999, 2000, 2007, 2009, 2013, 2015, and 2018, many of these within the last 30 years, which seems counterintuitive to AA; however, it may reveal how impactful minimum GBI is for sea ice within this marginal sea. Therefore, the positive anomalies shown for July may have more to do with the seasonal summer climatology. August and October both showed negative 500GPH and SLP anomalies for the high Arctic region, with some positive anomalies north of 60°N, specifically over the CAA and parts of Alaska. The more mixed anomalies shown for October are likely characteristic of the autumn season acting as a transitional period.

7.2.2.2 MINIMUM SIE VERSUS MAXIMUM GBI COMPOSITES

The Beaufort Sea composite analyses for minimum SIE and maximum GBI exhibited similar anomaly patterns to those anomaly patterns for the minimum SIE and maximum GBI Baffin Bay anomaly composites for all four variables, especially for the

positive anomaly pattern of the 500GPH and MSLP variables. The low sea ice years produced large and strong positive anomalies for all variables north of 60°N, especially over the Baffin Bay and Greenland region for the contemporary, lead-1, and lead-2 composites. The negative anomaly patterns depend on the month observed. May produced negative 500GPH and MSLP anomaly patterns on either side of NA. June showed large positive 500GPH and MSLP anomalies over the Greenland and the Gulf of Alaska region, as well as positive T2m over much of the US and negative PW anomalies for regions of the southern US. The month of August showed very large and strong positive 500GPH and MSLP anomalies in northern Canada, as well as large T2m and PW anomalies over much of the NA continent.

Although the Beaufort composites produced much the same positive anomaly patterns as those of the Baffin Bay, one notable difference is the fewer negative anomalies at the lower latitudes (south of 60°N), and the lack of consistencies found with the Baffin Bay composites. For example, there are more instances where Beaufort Sea minimum SIE and maximum GBI composites produced negative anomalies at higher latitudes, for most of lead-1 and lead-2 maps.

One study by Ballinger et al. (2014) found recent increases in high pressure patterns over the Beaufort Sea for early and middle warm season months, which coincides with those months of significance found in this study. The high pressure systems over the western Arctic region are accompanied by changes in both GPH and MSLP, causing similar migration of positive anomalies southward while positive anomalies tend to coincide with areas where the high pressure systems are found. Although there are few studies directly on the Beaufort Sea's ice regime's effects on

eastern US weather, Kug et al. (2015) used observational data and a climate modeling approach and identified anomalous warming in the East Siberian-Chukchi Sea region (the Beaufort Sea borders the Chukchi Sea) that resulted in severe winter weather for NA. The anomalous warming was accompanied by an anticyclone and a subsequent mid-latitude trough, which provided favorable conditions for northerly air flow and an extremely cold winter.

7.3. CONCLUSIONS

The boreal mid-latitudes are located at a region bordered by northern high-latitude lows and southern subtropical highs, creating the circumstances for extreme weather phenomena; however, evidence suggests that AA has decreased the temperature gradient and therefore affected the movement of winds and weather systems across the region (Francis and Vavrus 2012; Overland and Wang 2016). These disruption to the Arctic system are far reaching, however, the pathways by which Arctic changes can directly affect the mid-latitudes are still uncertain. Sea ice is a key factor for regulation of high latitudes as well as global temperature patterns but has been on the decline for several decades. Without sea ice, the Arctic has experienced increased surface and air temperatures and moisture incursion, which have disrupted seasonal sea ice formation. Along with changes in sea ice are increased instances of blocking episodes, which act to divert westerly air flow. These phenomena may be related and are important to focus on in future observational and modeling studies, particularly at the regional scale as suggested in this thesis work (Chen and Luo 2017; Ye et al. 2018; Dethloff et al. 2019).

This study found the greatest number of statistically significant relationships for

sea ice and GBI within Baffin Bay and the Beaufort Sea, one marginal sea from each of the two sectors (the Atlantic and the Pacific, respectively) of the Arctic. Each of these marginal seas produced several months of significant association and were explored further; however, overall, those seven marginal seas for the Atlantic sector (Baffin Bay, Barents Sea, Canadian Archipelago, Greenland Sea, Hudson Bay, Kara Sea, and the Gulf of St. Lawrence) produced a greater number of statistically significant associations with the GBI, suggesting a potentially stronger relationship than that of the Pacific sector. McKenna et al. (2018) used idealized modeling and a general circulation model to explore sea ice loss for the Atlantic and Pacific sectors and found that the magnitude of the sea ice loss in each of these sectors could determine the influence on the atmospheric response. For moderate magnitude sea ice losses, each of the sectors produced opposite effects on the AO; the Atlantic produced a positive response and Pacific produced a negative response, but large magnitude losses produced a negative AO response for both sectors. The magnitude of the overall change in Arctic sea ice therefore could indicate how frequent, how large, and how intense future atmospheric responses may be, including GB episodes.

The research presented in this study helped to further examine the role of the GBI as a pathway by which the NA continent experiences extreme weather due to changes in sea ice conditions. The statistical correlation tests were able to show some relationships for two marginal seas and various seasons. The results for the Baffin Bay (Beaufort Sea) showed the strongest relationships during the winter, autumn, and spring (summer). The various monthly time association results (contemporary, lead-1, and lead-2 tests) suggests that sea ice may be continuously impacted by the GB pattern during all months of the

year, though the strength of the association varies by marginal sea and season. Those statistically significant months for each marginal sea were explored further using years with extreme sea ice and GBI values and revealed the monthly characteristics of several variables of interest. From the composite maps produced, the physical response to sea ice and GBI conditions were inferred, and it was found that sea ice from both marginal seas were associated with anomalous weather conditions over NA. Specifically, positive 500GPH, MSLP, T2m, and PW anomalies became more common north of 60°N, while negative anomalies for these variables appeared to cover parts of NA, though the strength of these anomalies varied by the month and marginal sea observed. These findings are in line with studies that have looked at the broader NH impacts of sea ice loss producing a warm Arctic-cold continents pattern (Overland et al. 2011; Chen et al. 2018).

The maximum sea ice and minimum GBI years mostly revealed weather anomalies in line with the 1981–2010 climatology maps in terms of the latitudinal positions expected. Negative anomaly areas for all four variables were mostly confined to the Arctic region, with the occasional positive anomaly; however, the atmospheric response to minimum sea ice and maximum GBI seemed to show opposite trends in anomaly patterns, with extensive and much stronger positive anomalies in the Arctic. These changes have altered the surface and atmospheric characteristics of the Arctic, potentially disrupting seasonal patterns.

This study did not account for individual extreme weather phenomena but did assess the reversal of anomaly trends found for regions of NA and Greenland. Cold, dry Arctic air migrating into the mid-latitudes and warm, moist air moving poleward into the Arctic may be a manifestation of an ongoing weakened temperature gradient weakening

the westerly flow of winds, and a wavier jet stream all due to AA. These changes in and of themselves constitute at least a semblance of a teleconnection between the Arctic and mid-latitudes.

This research helped to further advance the GBI as a possible driver of regional weather patterns over NA, specifically anomalous 500GPH, SLP, T2m, and PW. Assessing these variables helped to better assess the potential for anomalous weather conditions for regions of NA that could become more common as sea ice continues to decline and GB continues to increase. Anomalously cold winter weather could cause widespread damage for regions of NA unprepared to endure such conditions, and anomalously low precipitation patterns along with warmer temperatures during the summer can help to create disastrous droughts and economic losses.

Several limitations to this research include the relatively simple statistical approach used to determine associations for sea ice and the GBI, and the lack of modeling to strengthen this relationship. Additionally, the complexity associated with climate dynamics is inherently prohibitive, although assessing initial relationships such as those found with this research can warrant further investigation.

Increased blocking episodes over the North Atlantic region and elsewhere in the NH are still not well understood but have become more common. Continued monitoring and modeling of these phenomena are critical for understanding the processes that may drive Arctic-mid-latitude teleconnections. Blocks cause disruptions to the energy and moisture budget of the Arctic system, which in turn can drive larger anomalous weather events across the mid-latitudes. Future work should attempt to better understand the impact of atmospheric anomalies on sea ice regimes, the blocking life-cycle, and both the

regional and hemispheric impacts that may ensue after anomalous blocking episodes.

APPENDIX SECTION

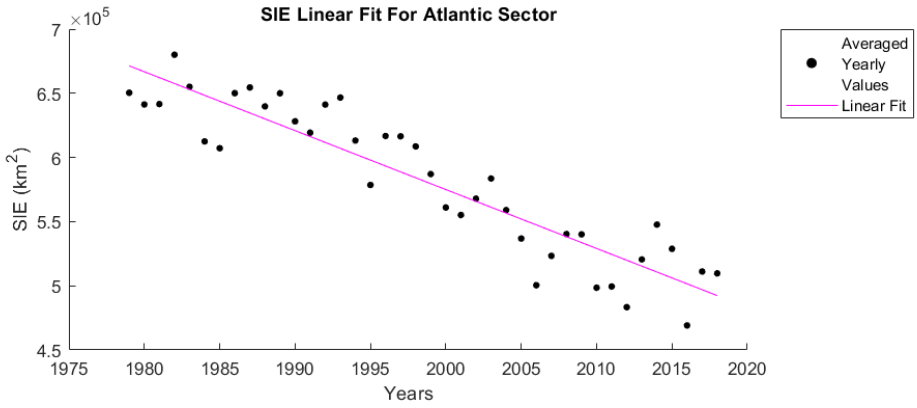

Figure S1. Linear fit for SIE for the Atlantic sector ($y=-4590x+6.8x10^5$; $r^2=0.8$). Yearly values are averaged.

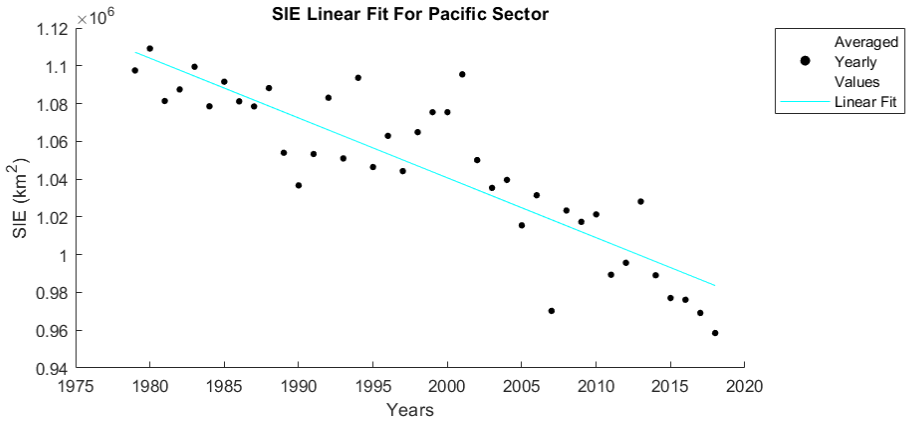

Figure S2. Linear fit for SIE for the Pacific sector ($y=-3168x+1.0x10^6$; $r^2=0.8$). Yearly values are averaged.

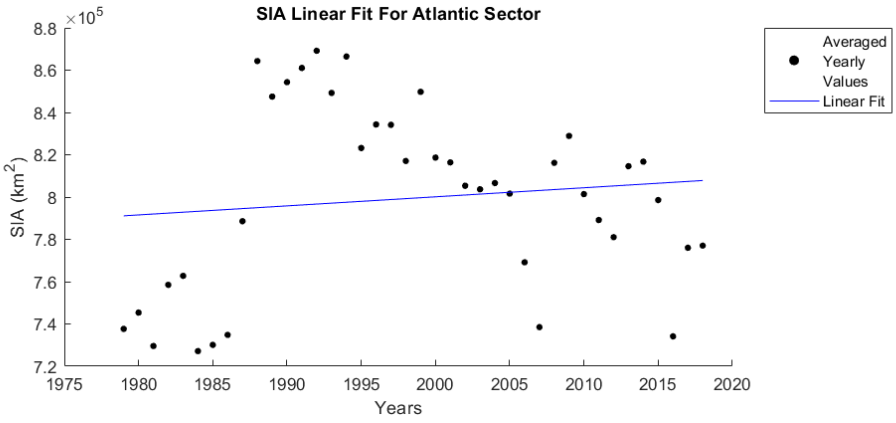

Figure S3. Linear fit for SIA for the Atlantic sector ($y=428x+7.9x10^5$; $r^2=0.01$). Yearly values are averaged.

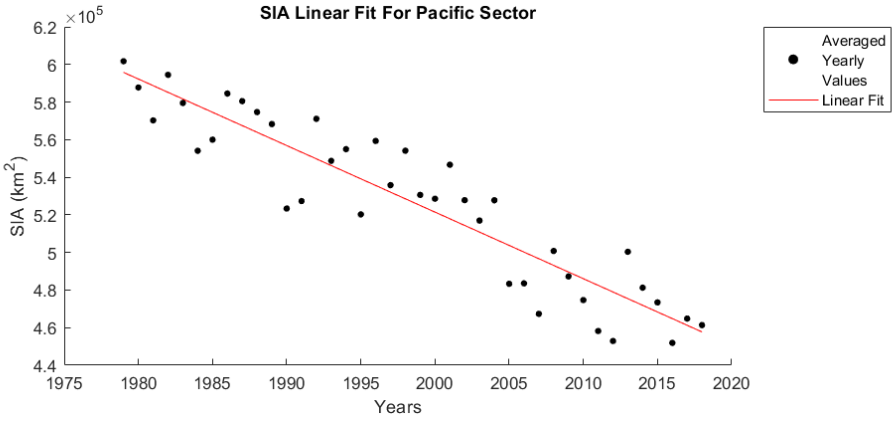

Figure S4. Linear fit for SIA for the Pacific sector ($y=-3540x+6.0x10^5$; $r^2=0.9$). Yearly values are averaged.

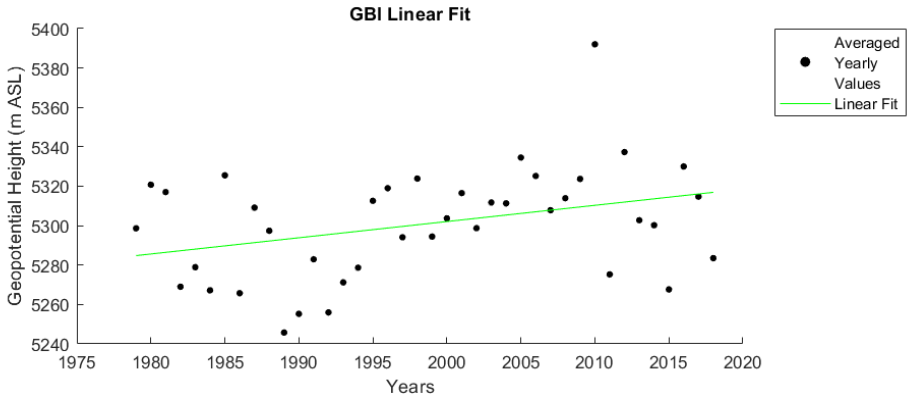

Figure S5. Linear fit for GBI (y=0.8x+5284; r^2=0.1). Yearly values are averaged.

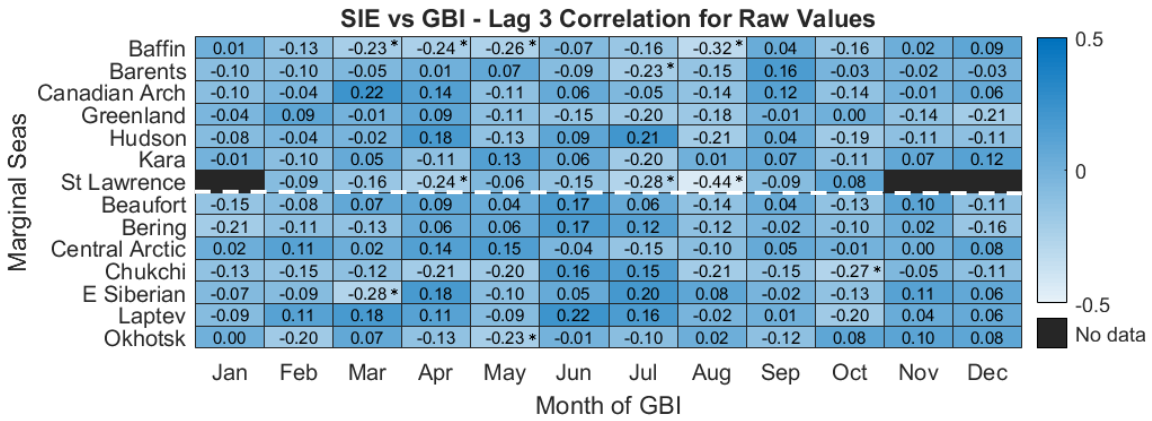

Figure S6. Heatmap showing all correlation coefficients for SIE versus GBI at lag-3 for raw values. SSV are denoted with an asterisk where p≤0.05. The dashed white line divides Atlantic (top) and Pacific (bottom) sectors.

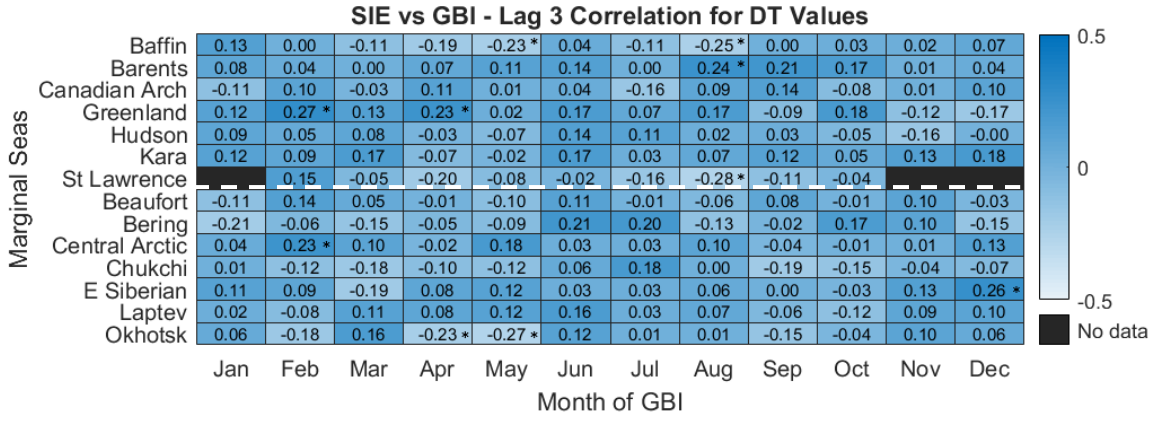

Figure S7. Heatmap showing all correlation coefficients for SIE versus GBI at lag-3 for detrended values. SSV are denoted with an asterisk where p≤0.05. The dashed white line divides Atlantic (top) and Pacific (bottom) sectors.

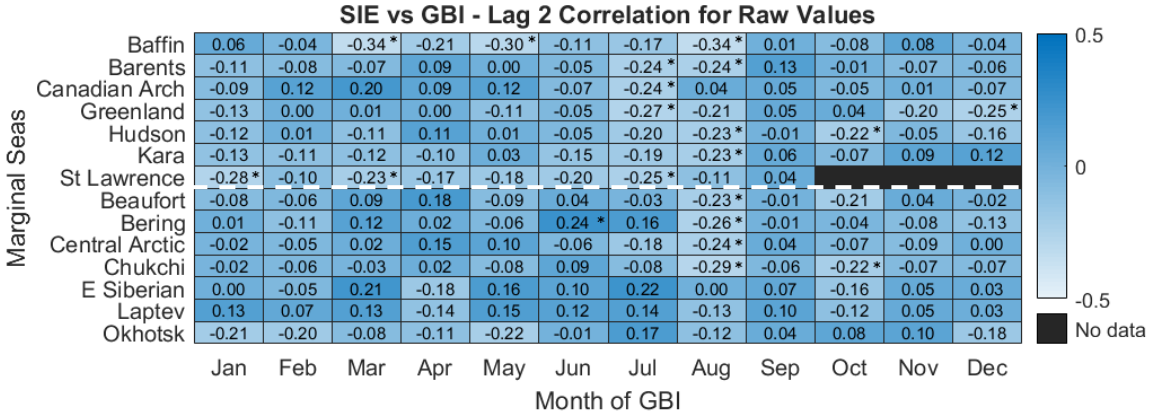

Figure S8. Heatmap showing all correlation coefficients for SIE versus GBI at lag-2 for raw values. SSV are denoted with an asterisk where p≤0.05. The dashed white line divides Atlantic (top) and Pacific (bottom) sectors.

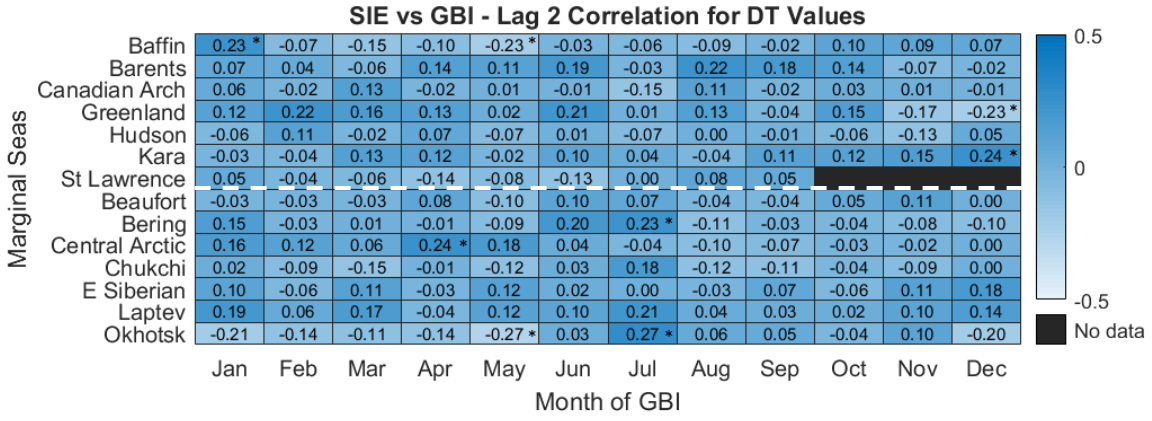

Figure S9. Heatmap showing all correlation coefficients for SIE versus GBI at lag-2 for detrended values. SSV are denoted with an asterisk where p≤0.05. The dashed white line divides Atlantic (top) and Pacific (bottom) sectors.

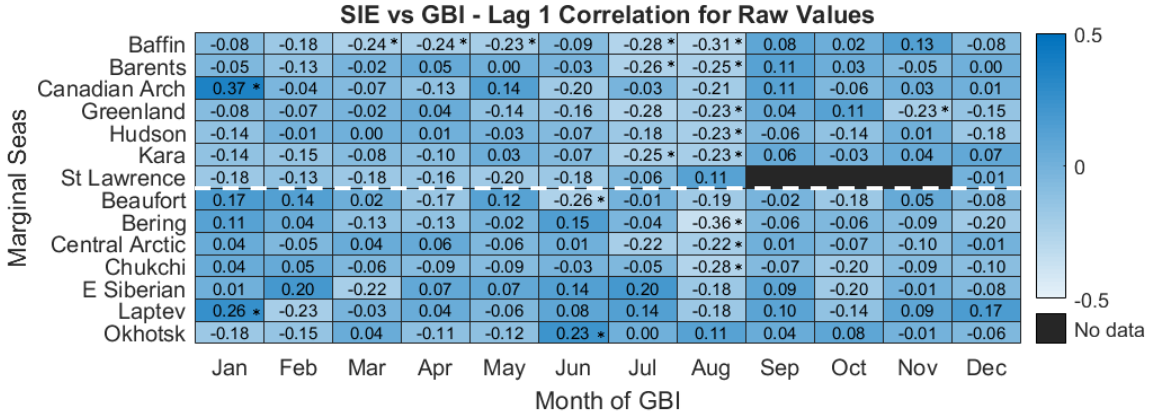

Figure S10. Heatmap showing all correlation coefficients for SIE versus GBI at lag-1 for raw values. SSV are denoted with an asterisk where p≤0.05. The dashed white line divides Atlantic (top) and Pacific (bottom) sectors.

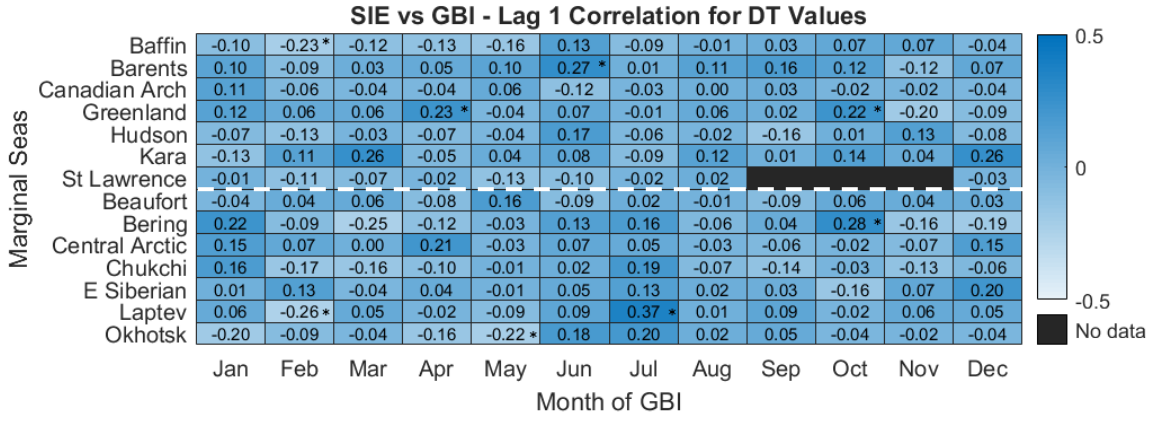

Figure S11. Heatmap showing all correlation coefficients for SIE versus GBI at lag-1 for detrended values. SSV are denoted with an asterisk where p≤0.05. The dashed white line divides Atlantic (top) and Pacific (bottom) sectors.

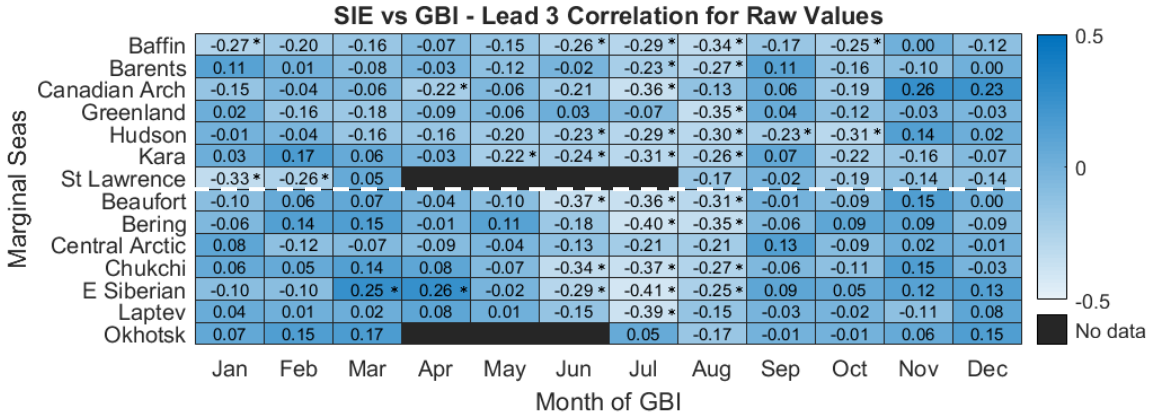

Figure S12. Heatmap showing all correlation coefficients for SIE versus GBI at lead-3 for raw values. SSV are denoted with an asterisk where p≤0.05. The dashed white line divides Atlantic (top) and Pacific (bottom) sectors.

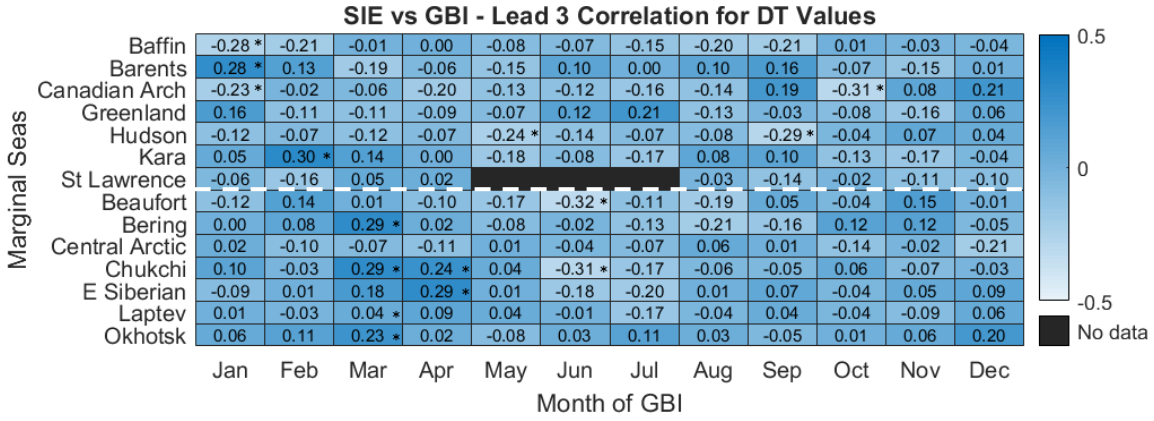

Figure S13. Heatmap showing all correlation coefficients for SIE versus GBI at lead-3 for detrended values. SSV are denoted with an asterisk where p≤0.05. The dashed white line divides Atlantic (top) and Pacific (bottom) sectors.

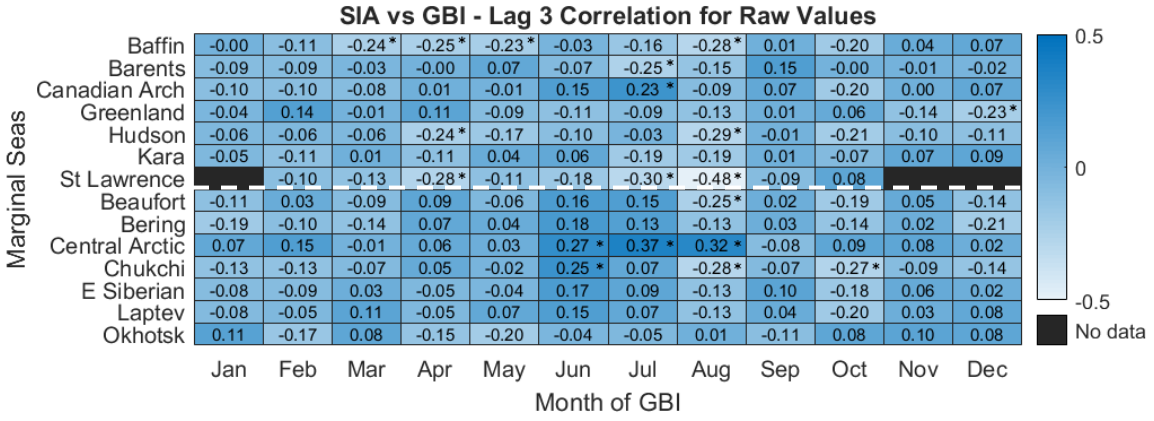

Figure S14. Heatmap showing all correlation coefficients for SIA versus GBI at lag-3 for raw values. SSV are denoted with an asterisk where p≤0.05. The dashed white line divides Atlantic (top) and Pacific (bottom) sectors.

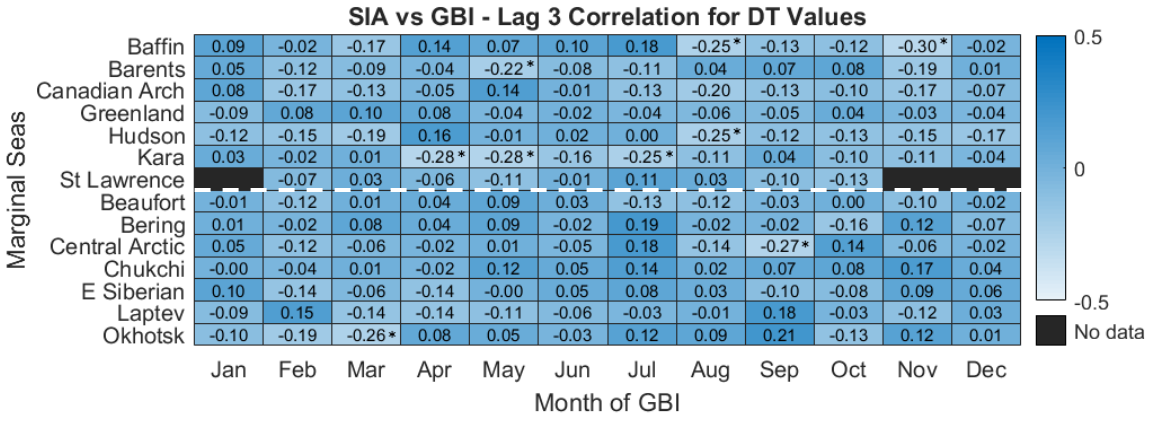

Figure S15. Heatmap showing all correlation coefficients for SIA versus GBI at lag-3 for detrended values. SSV are denoted with an asterisk where p≤0.05. The dashed white line divides Atlantic (top) and Pacific (bottom) sectors.

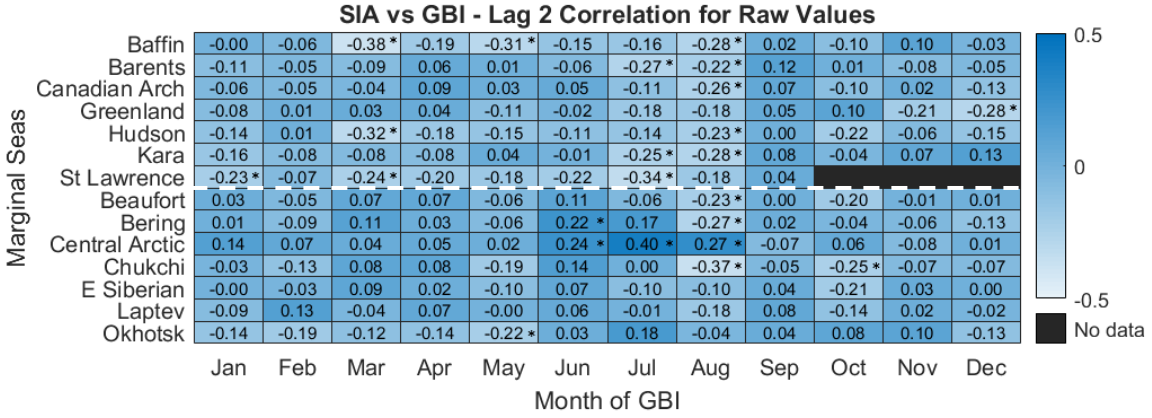

Figure S16. Heatmap showing all correlation coefficients for SIA versus GBI at lag-2 for raw values. SSV are denoted with an asterisk where p≤0.05. The dashed white line divides Atlantic (top) and Pacific (bottom) sectors.

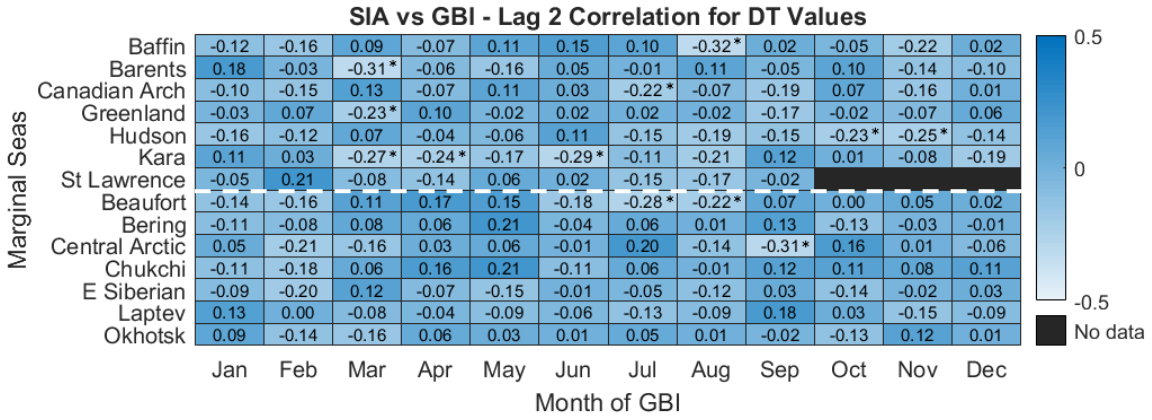

Figure S17. Heatmap showing all correlation coefficients for SIA versus GBI at lag-2 for detrended values. SSV are denoted with an asterisk where p≤0.05. The dashed white line divides Atlantic (top) and Pacific (bottom) sectors.

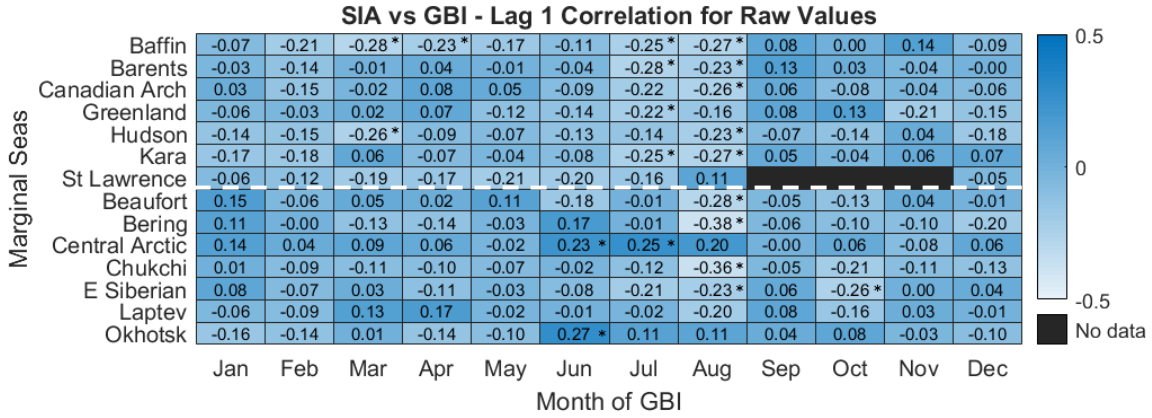

Figure S18. Heatmap showing all correlation coefficients for SIA versus GBI at lag-1 for raw values. SSV are denoted with an asterisk where p≤0.05. The dashed white line divides Atlantic (top) and Pacific (bottom) sectors.

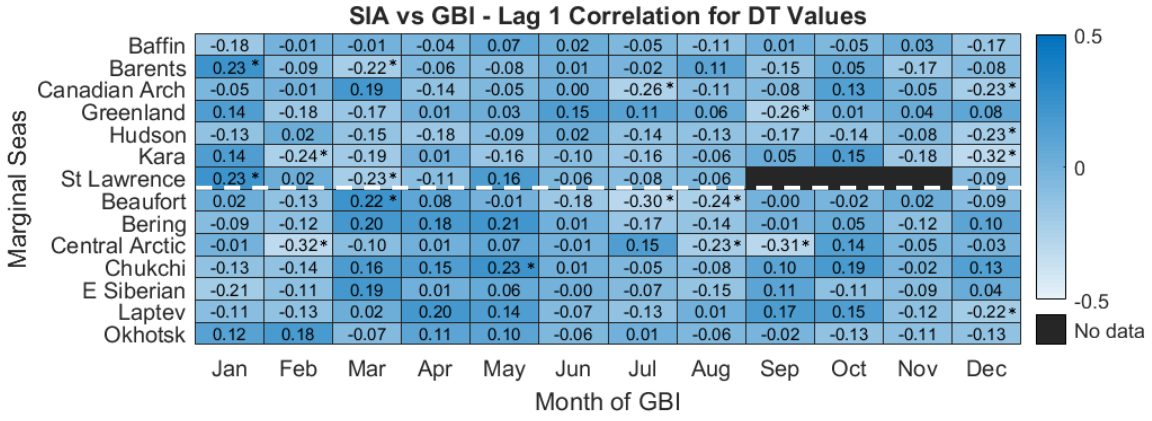

Figure S19. Heatmap showing all correlation coefficients for SIA versus GBI at lag-1 for detrended values. SSV are denoted with an asterisk where p≤0.05. The dashed white line divides Atlantic (top) and Pacific (bottom) sectors.

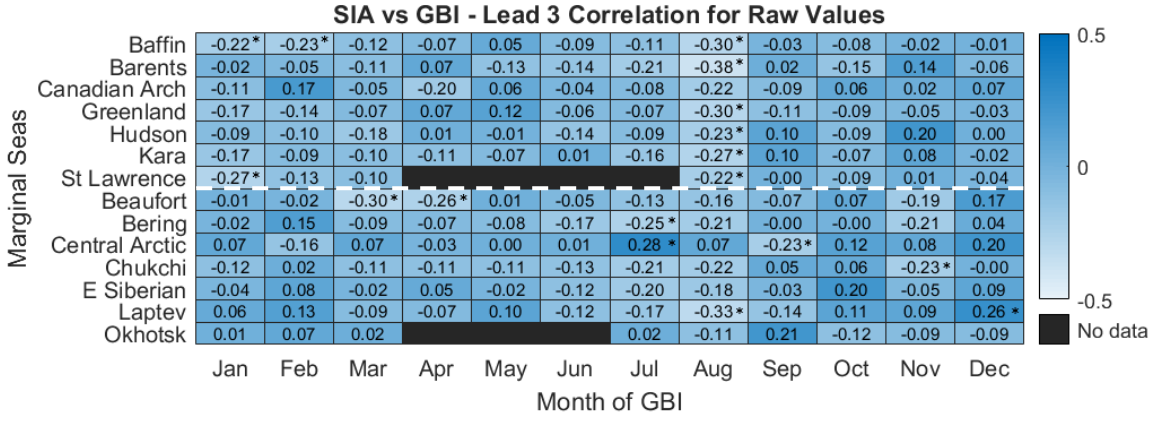

Figure S20. Heatmap showing all correlation coefficients for SIA versus GBI at lead-3 for raw values. SSV are denoted with an asterisk where p≤0.05. The dashed white line divides Atlantic (top) and Pacific (bottom) sectors.

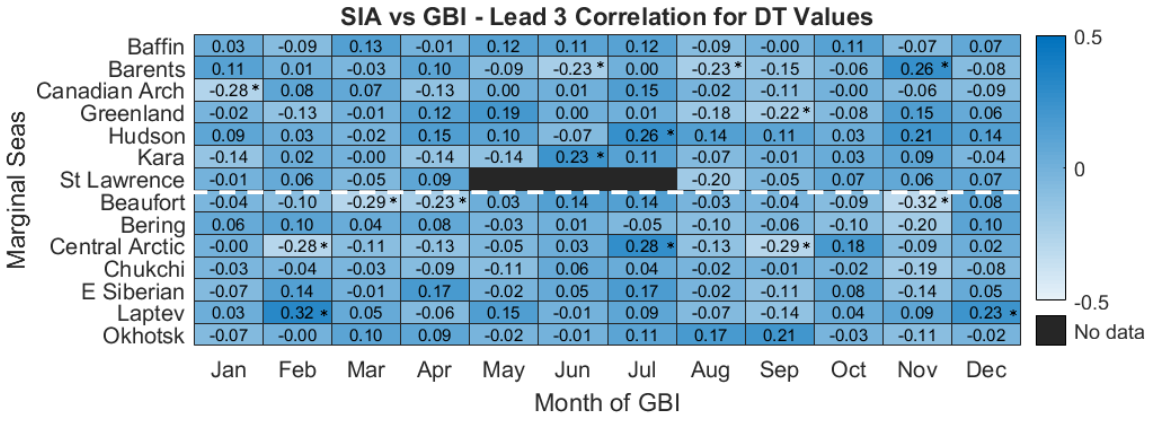

Figure S21. Heatmap showing all correlation coefficients for SIA versus GBI at lead-3 for detrended values. SSV are denoted with an asterisk where $p \leq 0.05$. The dashed white line divides Atlantic (top) and Pacific (bottom) sectors.

LITERATURE CITED

Ballinger, T. J., S. C. Sheridan, and E. Hanna. 2014. Resolving the Beaufort Sea High using synoptic climatological methods. *International Journal of Climatology* 34 (11):3312–3319.

Ballinger, T.J., E. Hanna, R.J. Hall, T.E. Cropper, J. Miller, M.H. Ribergaard, J.E. Overland, and J. L. Hoyer. 2018. Anomalous blocking over Greenland preceded the 2013 extreme early melt of local sea ice. *Annals of Glaciology* 59 (76):181–190.

Ballinger, T.J., E. Hanna, R.J. Hall, J. Miller, M.H. Ribergaard, and J.L. Høyer. 2018. Greenland coastal air temperatures linked to Baffin Bay and Greenland Sea ice conditions during autumn through regional blocking patterns. *Climate Dynamics* 50 (1–2):83–100.

Barnes, E. A., and J. A. Screen. 2015. The impact of Arctic warming on the midlatitude jet-stream: Can it? Has it? Will it? *Wiley Interdisciplinary Reviews: Climate Change* 6 (3):277–286.

Belleflamme, A., X. Fettweis, and M. Erpicum. 2015. Recent summer Arctic atmospheric circulation anomalies in a historical perspective. *Cryosphere* 9 (1):53–64.

Blackport, R., and P. J. Kushner, 2016: The Transient and Equilibrium Climate Response to Rapid Summertime Sea Ice Loss in CCSM4. *J. Climate*, **29**, 401–417.

Bliss, A.C., J.A. Miller, and W.N. Meier. 2017. Comparison of Passive Microwave-Derived Early Melt Onset Records on Arctic Sea Ice. *Remote Sensing*, 9(3), 199.

Bliss, A.C., M. Steele, G. Peng, and W.N. Meier. 2019. Regional variability of Arctic sea ice seasonal change climate indicators from a passive microwave climate data record. *Environmental Research Letters* 14, 045003.

Boland, E.J.D., T.J. Bracegirdle, and E.F. Shuckburgh. 2016. Assessment of sea ice atmosphere links in CMIP5 models. *Climate Dynamics*, 37, 1–20.

Box, J. E., W. T. Colgan, T. R. Christensen, N. M. Schmidt, M. Lund, F.-J. W. Parmentier, R. Brown, U. S. Bhatt, E. S. Euskirchen, V. E. Romanovsky, J. E. Walsh, J. E. Overland, M. Wang, R. W. Corell, W. N. Meier, B. Wouters, S. Mernild, J. Mård, J. Pawlak, and M. S. Olsen. 2019. Key indicators of Arctic climate change: 1971–2017. *Environmental Research Letters* 14 (4):045010.

Brönnimann, S., G. P. Compo, R. Spadin, R. Allan, and W. Adam. 2011. Early ship-based upper-air data and comparison with the Twentieth Century Reanalysis. *Climate of the Past* 7 (1):265–276.

Budikova, D., L. Chechi. 2016. Arctic sea ice and warm season North American extreme surface air temperatures. *Climate Research*, 67:15–29.

Budikova, D., T.W. Ford, and T.J. Ballinger. 2017. Connections between north-central United States summer hydroclimatology and Arctic sea ice variability. *International Journal of Climatology* 37 (12):4434–4450.

Bulygina, O.N., N.M. Arzhanova, and P.Y. Groisman. 2015. Icing conditions over Northern Eurasia in changing climate. *Environmental Research Letters* 10 (2).

Cai, D., M. Dameris, H. Garny, and T. Runde. 2012. Implications of all season Arctic sea-ice anomalies on the stratosphere. *Atmospheric Chemistry and Physics*, 12, 11,819–11,831.

Carr J.R., A. Vieli, and C. Stokes. 2013. Influence of sea ice decline, atmosphere warming, and glacier width on marine-terminating outlet glacier behavior in northwest Greenland at seasonal to interannual time scales. *Journal of Geophysical Research: Earth Surface* 118:1210–1226.

Chen, X., and D. Luo. 2017. Arctic sea ice decline and continental cold anomalies: Upstream and downstream effects of Greenland blocking. *Geophysical Research Letters* 44 (7):3411–3419.

Chen, L., J. Francis, and E. Hanna. 2018. The "Warm-Arctic/Cold-continents" pattern during 1901–2010. *International Journal of Climatology* 38 (14):5245–5254.

Cohen, J., K. Pfeiffer, and J.A. Francis. 2018. Warm Arctic episodes linked with increased frequency of extreme winter weather in the United States. *Nature Communications* 9 (869).

Cohen, J., X. Zhang, J. Francis, T. Jung, R. Kwok, J. Overland, T. J. Ballinger, U. S. Bhatt, H. W. Chen, D. Coumou, S. Feldstein, H. Gu, D. Handorf, G. Henderson, M. Ionita, M. Kretschmer, F. Laliberte, S. Lee, H. W. Linderholm, W. Maslowski, Y. Peings, K. Pfeiffer, I. Rigor, T. Semmler, J. Stroeve, P. C. Taylor, S. Vavrus, T. Vihma, S. Wang, M. Wendisch, Y. Wu, and J. Yoon. 2020. Divergent consensuses on Arctic amplification influence on midlatitude severe winter weather. *Nature Climate Change* 10, 20–29 (2020).

Copernicus Climate Change Service (C3S) (2017): ERA5: Fifth generation of ECMWF atmospheric reanalyses of the global climate . Copernicus Climate Change Service Climate Data Store (CDS), 06/17/2020.

Delhasse, A., C. Kittel, C. Amory, S. Hofer, Di. Van As, R. S. Fausto, and X. Fettweis. 2020. Brief communication: Evaluation of the near-surface climate in ERA5 over the Greenland Ice Sheet. *Cryosphere* 14 (3):957–965.

Dethloff, K., D. Handorf, R. Jaiser, A. Rinke, and P. Klinghammer. 2019. Dynamical mechanisms of Arctic amplification. *Annals of the New York Academy of Sciences* 1436 (1):184–194.

Fetterer, F., K. Knowles, W.N. Meier, M. Savoie, and A.K. Windnagel. 2017. Sea Ice Index, Version 3. g02135. NSIDC: National Snow and Ice Data Center. Boulder, Colorado USA.

Francis, J. A., and S. J. Vavrus. 2012. Evidence linking Arctic amplification to extreme weather in mid-latitudes. *Geophysical Research Letters* 39 (6):1–6.

Gong, T., S. Feldstein, and S. Lee. 2017. The role of downward infrared radiation in the recent arctic winter warming trend. *Journal of Climate* 30 (13):4937–4949.

Hanna, E., S. H. Mernild, J. Cappelen, and K. Steffen. 2012. Recent warming in Greenland in a long-term instrumental (1881-2012) climatic context: I. Evaluation of surface air temperature records. *Environmental Research Letters* 7 (4).

Hanna, E., J. M. Jones, J. Cappelen, S. H. Mernild, L. Wood, K. Steffen, and P. Huybrechts. 2013. The influence of North Atlantic atmospheric and oceanic forcing effects on 1900-2010 Greenland summer climate and ice melt/runoff. *International Journal of Climatology* 33 (4):862–880.

Hanna, E., X. Fettweis, S.H. Mernild, J. Cappelen, M.H. Ribergaard, C.A. Shuman, K. Steffen, L. Wood, and T.L. Mote. 2014. Atmospheric and oceanic climate forcing of the exceptional Greenland ice sheet surface melt in summer 2012. *International Journal of Climatology*, 34, 1022–1037.

Hanna, E., T.E. Cropper, P.D. Jones, A.A. Scaife, and R. Allan. 2015. Recent seasonal asymmetric changes in the NAO (a marked summer decline and increased winter variability) and associated changes in the AO and Greenland blocking index. *International Journal of Climatology*, 35, 2540–2554.

Hanna, E., T.E. Cropper, R.J. Hall, and J. Cappelen. 2016. Greenland blocking index 1851–2015: a regional climate change signal. *International Journal of Climatology*, 36, 4847–4861.

Hanna, E., X. Fettweis, and R. J. Hall. 2018. Brief communication: Recent changes in summer Greenland blocking captured by none of the CMIP5 models. *Cryosphere* 12 (10):3287–3292.

Hanna, E., R.J. Hall, T.E. Cropper, T.J. Ballinger, L. Wake, T. Mote, and J. Cappelen. 2018. Greenland blocking index daily series 1851–2015: Analysis of changes in extremes and links with North Atlantic and UK climate variability and change. *International Journal of Climatology* 38:3546-3564.

Hermann, M., L. Papritz, and H. Wernli. 2020. A Lagrangian analysis of the dynamical and thermodynamic drivers of Greenland melt events during 1979-2017. (April):1–32. [forthcoming].

Hersbach, H., B. Bell, P. Berrisford, S. Hirahara, A. Horányi, J. Muñoz-Sabater, J. Nicolas, C. Peubey, R. Radu, D. Schepers, A. Simmons, C. Soci, S. Abdalla, X. Abellan, G. Balsamo, P. Bechtold, G. Biavati, J. Bidlot, M. Bonavita, G. De Chiara, P. Dahlgren, D. Dee, M. Diamantakis, R. Dragani, J. Flemming, R. Forbes, M. Fuentes, A. Geer, L. Haimberger, S. Healy, R. J. Hogan, E. Hólm, M. Janisková, S. Keeley, P. Laloyaux, P. Lopez, C. Lupu, G. Radnoti, P. de Rosnay, I. Rozum, F. Vamborg, S. Villaume, and J. N. Thépaut. 2020. The ERA5 global reanalysis. *Quarterly Journal of the Royal Meteorological Society* (2019):1–51.

Ipbuker, C. 2004. Numerical evaluation of the Robinson projection. *Cartography and Geographic Information Science* 31 (2):79–88.

IPCC. 2014. Climate Change 2014: Synthesis Report. Contribution of Working Groups I, II and III to the Fifth Assessment Report of the Intergovernmental Panel on Climate Change [Core Writing Team, R.K. Pachauri and L.A. Meyer (eds.)]. IPCC, Geneva, Switzerland.

IPCC. 2019. Summary for Policymakers. In: IPCC Special Report on the Ocean and Cryosphere in a Changing Climate [H.-O. Pörtner, D.C. Roberts, V. Masson-Delmotte, P. Zhai, M. Tignor, E. Poloczanska, K. Mintenbeck, M. Nicolai, A. Okem, J. Petzold, B. Rama, N. Weyer (eds.)]. IPCC, Geneva, Switzerland.

Jensen T.S., J.E. Box, and C.S. Hvidberg. 2016. A sensitivity study of annual area change for Greenland Ice Sheet marine terminating outlet glaciers: 1999–2013. *Journal of Glaciology* 62: 72–81.

Kinnard C, C.M. Zdanowicz, D.A. Fisher, E. Isaksson, A. de Vernal, and L.G. Thompson. 2011. Reconstructed changes in Arctic sea ice over the past 1,450 years. *Nature* 479:509–512.

Kug, J. S., J. H. Jeong, Y. S. Jang, B. M. Kim, C. K. Folland, S. K. Min, and S. W. Son. 2015. Two distinct influences of Arctic warming on cold winters over North America and East Asia. *Nature Geoscience* 8 (10):759–762.

Kwok, R. and D.A. Rothrock. 2009. Decline in Arctic sea ice thickness from submarine and ICESat records: 1958–2008, *Geophysical Research Letters* 36, L15501.

Kwok R. and G.F. Cunningham. 2015 Variability of Arctic sea ice thickness and volume from CryoSat-2. *Philosophical Transactions of the Royal Society A: Mathematical, Physical and Engineering Sciences* 373: 20140157.

Liu J., Z. Chen, J. Francis, M. Song, T. Mote, and Y. Hu. 2016. Has Arctic sea ice loss contributed to increased surface melting of the Greenland Ice Sheet? *Journal of Climate* 29:3373-3386.

Mattingly, K.S., J. T. Mcleod, J.A. Knox, J.M. Shepherd, and T.L. Mote. 2015. A climatological assessment of Greenland blocking conditions associated with the track of Hurricane Sandy and historical North Atlantic hurricanes. *International Journal of Climatology* 35 (5):746–760.

Mattingly, K. S., T. L. Mote, X. Fettweis, D. van As, K. Van Tricht, S. Lhermitte, C. Pettersen, and R. S. Fausto. 2020. Strong Summer Atmospheric Rivers Trigger Greenland Ice Sheet Melt through Spatially Varying Surface Energy Balance and Cloud Regimes. *Journal of Climate*. [forthcoming].

Meleshko, V.P., V.M. Mirvis, V.A. Govorkova, A.V. Baidin, V.M. Kattsov, and T.V. Pavlova. 2018. Is There a Link between Arctic Sea Ice Loss and Increasing Frequency of Extremely Cold Winters in Eurasia and North America? Synthesis of Current Research. *Russian Meteorology and Hydrology* 43 (11):743–755.

Meier, W.N., J. Stroeve, and F. Fetterer. 2007. Whither Arctic sea ice? A clear signal of decline regionally, seasonally and extending beyond the satellite record. *Annals of Glaciology* 46: 428–434.

McKenna, C. M., T. J. Bracegirdle, E. F. Shuckburgh, P. H. Haynes, and M. M. Joshi. 2018. Arctic Sea Ice Loss in Different Regions Leads to Contrasting Northern Hemisphere Impacts. *Geophysical Research Letters* 45 (2):945–954.

McLeod, J.T. and T.L. Mote. 2016. Linking interannual variability in extreme Greenland blocking episodes to the recent increase in summer melting across the Greenland ice sheet. *International Journal of Climatology* 36:1484–1499.

Moon, T. A., I. Overeem, M. Druckenmiller, M. Holland, H. Huntington, G. Kling, A.L. Lovecraft, G. Miller, T. Scambos, C. Schädel, E.A.G. Schuur, E. Trochim, F. Wiese, D. Williams, and G. Wong. 2019. The Expanding Footprint of Rapid Arctic Change. *Earth's Future* 7(3):212–218.

Orsolini, Y.J., R. Senan, R.E. Benestad, and A. Melsom. 2012. Autumn atmospheric response to the 2007 low Arctic sea ice extent in coupled ocean-atmosphere hindcasts. *Climate Dynamics* 38:2437–2448.

Overland, J. E., K. R. Wood, and M. Wang. 2011. Warm Arctic-cold continents: Climate impacts of the newly open arctic sea. *Polar Research* 30 (SUPPL.1).

Overland, J.E. and M. Wang. 2015. Increased variability in early winter subarctic North American atmospheric circulation. *Journal of Climate* 28:7297–7305.

Overland, J. E., and M. Wang. 2016. Recent extreme arctic temperatures are due to a split polar vortex. *Journal of Climate* 29 (15):5609–5616.

Overland, J.E., E. Hanna, S. Hansen-Bauer, J. Kim, J.E. Walsh, M. Wang, U.S. Bhatt, and R.L. Thomas. 2018. Surface Air Temperature [In Arctic Report Card 2018]. National Oceanic and Atmospheric Administration.

Overland, J. E., and M. Wang. 2019. Impact of the winter polar vortex on greater North America. *International Journal of Climatology* 39 (15):5815–5821.

Overland, J.E., E. Hanna, I. Hanssen-Bauer, S.-J. Kim, J.E. Walsh, M. Wang, U.S. Bhatt, R.L. Thoman, and T.J. Ballinger, 2019: Surface air temperature. *NOAA Arctic Report Card 2019*, J. Richter-Menge, M.L. Druckenmiller, and M. Jeffries, Eds., http://www.arctic.noaa.gov/Report-Card.

Petty, A. A., J. C. Stroeve, P. R. Holland, L. N. Boisvert, A. C. Bliss, N. Kimura, and W. N. Meier. 2018. The Arctic sea ice cover of 2016: A year of record-low highs and higher-Than-expected lows. *Cryosphere* 12 (2):433–452.

Richter-Menge, J., M. L. Druckenmiller, and M. Jeffries. 2019. Arctic Report Card 2019. :100. http://www.arctic.noaa.gov/Report-Card.

Scinocca, J.F., M.C. Reader, D.A. Plummer, M. Sigmond, P.J. Kushner, T.G. Shepherd, and R. Ravishankara, 2009. Impact of sudden Arctic sea-ice loss on stratospheric polar ozone recovery. *Geophysical Research Letters*, 36, L24701.

Screen, J.A., I. Simmonds, C. Deser, and R. Tomas. 2013. The atmospheric response to three decades of observed Arctic sea ice loss. *Journal of Climate* 26:1230–1248.

Screen, J.A., J. Francis, D. Entekhabi, J. Jones, J.C. Furtado, J. Cohen, and D. Whittleston. 2014. Recent Arctic amplification and extreme mid-latitude weather. *Nature Geoscience* 7(9):627–637.

Screen, J.A. 2017. Simulated atmospheric response to regional and pan-arctic sea ice loss. *Journal of Climate* 30 (11):3945–3962.

Serreze, M. C., and R. G. Barry, 1988: Synoptic Activity in the Arctic Basin, 1979–85. J. *Climate*, 1, 1276–1295.

Serreze, M.C. and R.G. Barry. 2011. Processes and impacts of Arctic amplification: a research synthesis. *Global and Planetary Change* 77:85–96.

Sheridan, S., and C.C. Lee. 2012. Synoptic climatology and the analysis of atmospheric teleconnections. *Progress in Physical Geography* 36 (4):548–557.

Stroeve, J., and D. Notz. 2018. Changing state of Arctic sea ice across all seasons. *Environmental Research Letters* 13 (10).

Tarek, M., F. P. Brissette, and R. Arsenault. 2020. Evaluation of the ERA5 reanalysis as a potential reference dataset for hydrological modelling over North America. *Hydrology and Earth System Sciences* 24 (5):2527–2544.

Taylor, P.C., B.M. Hegyi, R.C. Boeke, and L.N. Boisvert. 2018. On the increasing importance of air-sea exchanges in a thawing Arctic: A review. *Atmosphere* 9 (2):1–39.

Tedesco, M., and X. Fettweis. 2020. Unprecedented atmospheric conditions (1948-2019) drive the 2019 exceptional melting season over the Greenland ice sheet. *Cryosphere* 14 (4):1209–1223.

Vavrus, J.S. 2018. The Influence of Arctic Amplification on Mid-latitude Weather and Climate. *Current Climate Change Reports* 48:398.

Vihma, T. 2014. Effects of Arctic sea ice decline on weather and climate: a review. *Surveys in Geophysics* 35:1175–1214.

Walsh, J.E. 2014. Intensified warming of the Arctic: causes and impacts on middle latitudes. *Global and Planetary Change* 117:52–63.

Walsh, J.E., F. Fetterer, J.S. Stewart, and W.L. Chapman. 2017. A Database for Depicting Arctic Sea Ice Variations Back to 1850. *Geographical Review* 107:89–107.

Walsh, J.E., J.S. Stewart, and F. Fetterer. 2019. Benchmark seasonal prediction skill estimates based on regional indices. *Cryosphere* 13 (4):1073–1088.

Wang, C., R. M. Graham, K. Wang, S. Gerland, and M. A. Granskog. 2019. Comparison of ERA5 and ERA-Interim near-surface air temperature, snowfall and precipitation over Arctic sea ice: effects on sea ice thermodynamics and evolution. Cryosphere 13 (6):1661–1679.

Wang, Y., F. Huang, and T. Fan. 2017. Spatio-temporal variations of Arctic amplification and their linkage with the Arctic oscillation. *Acta Oceanologica Sinica* 36 (8):42–51.

Wang, S., D. Nath, W. Chen, L. Wang, S. Wang, D. Nath, W. Chen, and L. Wang. 2019. Recent strengthening of Greenland blocking drives summertime surface warming over northern Canada and eastern Siberia. *Journal of Climate*: JCLI-D-18-0410.1.

Wu, R., and Y. Wang. 2020. Comparison of North Atlantic Oscillation-related changes in the North Atlantic sea ice and associated surface quantities on different time scales. *International Journal of Climatology* 40 (5):2686–2701.

Yarnal, B., A.C. Comrie, B. Frakes, and D.P. Brown. 2001. Developments and prospects in synoptic climatology. *International Journal of Climatology* 21 (15):1923–1950.

Ye, K., T. Jung, and T. Semmler. 2018. The Influences of the Arctic Troposphere on the Midlatitude Climate Variability and the Recent Eurasian Cooling. *Journal of Geophysical Research: Atmospheres* 123 (18):10,162-10,184.

Zhang, X., J. E. Walsh, J. Zhang, U. S. Bhatt, and M. Ikeda. 2004. Climatology and interannual variability of Arctic cyclone activity: 1948-2002. *Journal of Climate* 17 (12):2300–2317.